



HAL
open science

Subsurface stress inversion modeling using linear elasticity: sensitivity analysis and applications

Mostfa Lejri

► **To cite this version:**

Mostfa Lejri. Subsurface stress inversion modeling using linear elasticity: sensitivity analysis and applications. Geophysics [physics.geo-ph]. Université de Montpellier, 2015. English. NNT: . tel-01324110

HAL Id: tel-01324110

<https://hal.science/tel-01324110>

Submitted on 31 May 2016

HAL is a multi-disciplinary open access archive for the deposit and dissemination of scientific research documents, whether they are published or not. The documents may come from teaching and research institutions in France or abroad, or from public or private research centers.

L'archive ouverte pluridisciplinaire **HAL**, est destinée au dépôt et à la diffusion de documents scientifiques de niveau recherche, publiés ou non, émanant des établissements d'enseignement et de recherche français ou étrangers, des laboratoires publics ou privés.

Délivré par l'Université de Montpellier

**Préparée au sein de l'école doctorale SIBAGHE
Et de l'équipe de recherche BASSINS**

Spécialité : GEOSCIENCES

Présentée par LEJRI Mostfa (Mustapha)

**SUBSURFACE STRESS INVERSION
MODELING USING LINEAR
ELASTICITY: SENSITIVITY ANALYSIS
AND APPLICATIONS**

Soutenance prévue le 02 Juillet 2015 devant le jury composé de :

Dr. Roger Soliva, Université Montpellier	Directeur de thèse
Dr. Laurent Maerten, Schlumberger	Co-Directeur
Dr. Frantz Maerten, Schlumberger	Co-Directeur
Pr. Olivier Lacombe, Université Paris VI	Rapporteur
Pr. Jean Pierre Gratier, Université de Grenoble	Rapporteur
Pr. Rodolphe Cattin, Université Montpellier	Examineur
Dr. Bertrand Gauthier, Total	Examineur
Dr. Bernard Célérier, Université Montpellier	Examineur



Avant-propos

Cette thèse a été co-financée par une bourse CIFRE (ANRT) et l'entreprise Schlumberger sous l'égide du laboratoire de géosciences de l'université de Montpellier. Elle s'est déroulée en majeure partie au sein des locaux de Schlumberger MpTC à Montpellier.

Le présent manuscrit est constitué de quatre articles scientifiques. Le premier est publié dans la revue *Tectonophysics*, le second est en préparation pour la revue *Tectonophysics*. Les troisième et quatrième articles sont en préparation pour *Structural geology* et le journal de l'AAPG. Par conséquent, le format des chapitres est présenté en anglais sous la forme d'articles scientifiques.

Remerciements

Mon expérience pendant cette thèse CIFRE au sein de Schlumberger a été intellectuellement stimulante et enrichissante au delà des espérances. Cette thèse n'aurait pas été possible sans l'implication et la contribution intellectuelle de plusieurs personnes que ce soit au sein de Schlumberger, de l'université de Montpellier ou dans mon entourage.

Je tiens d'abord à remercier très chaleureusement mes directeurs de thèse Laurent Maerten qui m'a transmis son savoir sur la géologie structurale et m'a appris, à travers son œil expert et une pédagogie exceptionnelle, à raisonner et écrire en tant que scientifique, et Frantz Maerten qui, par son génie et avec beaucoup d'humour, m'a donné goût à la programmation et à la mécanique des failles. Ils ont su m'épauler durant ces années, et m'ont insufflé leur enthousiasme, leur vision et leur passion pour la géologie, la modélisation numérique et la géomécanique. Je remercie au même titre Roger Soliva qui m'a transmis sa passion de la géologie structurale, il a été pour moi un exemple de rigueur dans le travail et m'a guidé tout au long de cette aventure. Plus que des mentors vous avez été de véritables amis.

Je voudrais spécialement remercier Emmanuel Malvesin, qui tout au long de ces années a été un ami, d'un conseil avisé, et un motivateur incontournable, "la fine fleur..." ainsi que Jean Pierre Joonnekindt qui a été un grand soutien, et Nader Salman, un co-leader exceptionnel.

Je remercie bien sûr Alex Wilson, qui a suivi tout mon parcours et œuvré pour mon intégration au sein de Schlumberger. Un grand merci aux collègues à Schlumberger MpTC, et plus particulièrement, Stéphane Bonassies et Christelle Guilermou qui ont œuvré afin que ma thèse se déroule dans les meilleures conditions possibles. J'en profite également pour remercier toutes les personnes qui m'ont soutenu de près ou de loin (dans le désordre): Claire Maerten, Aloïse Chabert pour sa bonne humeur constante, Joan Mouba, Pauline Cornard, Thomas Laverne pour les discussions passionnées, Ezzdine Benabou pour son aide qui a été critique

à la dernière minute, Berangère Guerry et Sarah Macaud pour leurs encouragements, Martin Neumeyer pour sa passion de géologie et les discussions enrichissantes, Naouel Arbi pour son aide et ses encouragements depuis mon arrivée à Schlumberger, Marie LeFranc, Saad Kisra, Fabrice, Paxi, Phil Resor, Mathieu, Terje, Jimmy, Michael, David, Illike, Gayana, Thibault Cavailhes, Marine Dalmasso... Bertrand Gauthier qui a été d'un grand conseil et pour sa confiance en moi lors du workshop à Total, Olivier Lacombe pour m'avoir permis d'approfondir mes connaissances et m'avoir accueilli à L'EGU, Bernard Célérier pour ses conseils et corrections post-soutenance, et Romain Plateaux pour son enthousiasme et sa lecture constructive du manuscrit... vous avez tous été là et je garde de vous un souvenir impérissable.

Merci à Ali Mehez, Fares Bouhlila et Adlène Mallem et qui ont été des frères pour moi durant ces années d'études. Un immense merci à Axelle Riou qui a été présente pour moi à chaque instant. Merci également à Sandrine Riou et Michel Portant, votre présence a été pour moi très importante. Et bien sûr, un grand merci à Marie-France Roch pour son assistance depuis le Master et aux équipes du laboratoire géosciences et particulièrement Michel Serannes pour son suivi et son intransigence. Enfin je remercie les membres de ma famille qui m'ont encouragé depuis le plus jeune âge dans ma passion pour les sciences et en particulier mon père Mohamed Lamine Lejri et ma mère Nejia Lejri à qui je dédie ce travail.

Lejri Mostfa, Juillet 2015

« If i have seen further than others, it is by standing upon the shoulders of giants »

Isaac Newton

Table of Contents

Extended abstract	1
General introduction	5
1.Essence of the thesis	5
2.How are the fractures modeled in the Oil & gas industry?	6
2.1. Existing techniques	6
2.2. Techniques based on geomechanics	7
3.Faults and Fractures	9
3.1. Faults, fault systems and stress field	10
3.2. Fault genesis and tectonic regimes	12
3.3. Fault reactivation	14
3.4. Fault sliding friction	16
3.5. Fractures classification and stress field	18
3.6. Fractures related to faulting	19
3.6.1. Fracture genetically associated to faulting	19
3.6.2. Fracture not genetically associated to faulting	20
4.How to recover paleostresses?	22
4.1. Paleostress estimation using Wallace & Bott type methods	23
The Wallace (1951) and Bott (1959) hypothesis	23
4.1.1. The stress ratio (R)	24
4.1.2. The forward problem	25
4.1.3. Stress inversion problem	26
4.1.4. Stress inversion using slip data	28
4.1.5. Stress inversion using focal mechanisms	31
4.1.6. Stress inversion using calcite twins	34
4.2. Polyphase tectonic events	36
4.2.1. The polyphase data problem	36
4.2.2. Existing methods to separate tectonic phases	37
4.3. Methods based on geomechanics	40
4.3.1. Least squares formulation (Kaven et al., 2011)	40
4.3.2. iBem3D (Maerten et al., 2014)	40
5.Methods (after Maerten et al., 2014)	41
5.1. iBem3D - iterative boundary elements method	42
5.1.1. Far field stress/strain	44
5.1.2. Research applications	44
5.1.3. Industry and engineering applications	50
5.1.4. Latest enhancements	55
5.2. BEM-based stress inversion method	57
5.2.1. Principle of superposition	59
5.2.2. Real time computation	60
5.2.3. Method of Resolution	61
5.2.4. Cost functions	62

5.2.5. Tectonic stress domain	64
6.Problematics of the thesis:	65
References	67
CHAPTER I: Paleostress inversion: A multi-parametric geomechanical evaluation of the Wallace-Bott assumptions	95
Abstract	95
1.Introduction	96
2.Method	99
2.1. Numerical tool	99
2.2. Fault geometry	100
2.3. Tectonic stress	103
2.3. Fault friction	104
2.4. Fault fluid pressure	105
2.5. Traction free surface of the Earth	105
2.6. Poisson's ratio	106
2.7. Non-tested parameters	107
2.8. Mean misfit angle calculation and domain representation	107
3.Results	111
3.1. Effect of fault geometry	111
3.1.1. Single planar fault	111
3.1.2. Intersecting faults	112
3.1.3. Sinusoidal faults	115
3.2. Effect of the traction free surface of the Earth	116
3.3. Effect of Poisson's ratio	117
3.4. Effect of fault friction	118
3.5. Effect of fault fluid pressure	120
4.Discussion	121
4.1. Fault geometry	121
4.2. Traction free surface	125
4.3. Poisson's ratio	125
4.4. Fault friction	126
4.5. Fault fluid pressure	126
4.6. Complementary study	126
5.Conclusions	129
Acknowledgements	131
References	132
CHAPTER II: Accuracy evaluation of both Wallace-Bott and BEM-based paleostress inversion methods	143
Abstract	143
1.Introduction	144
2.Method	147
2.1. Stress inversion methods	147
2.2. Fault geometry	149

2.3. Tectonic stress	150
2.4. Sliding friction	151
2.5. Data sampling	152
2.6. Analysis procedure	152
3. Analyses	155
3.1. Relationship between ω and Δ	155
3.2. Sliding friction effect	158
3.3. Sampling effect	161
4. Chimney Rock case study	162
4.1. Geologic setting and previous models	163
4.2. Fault model configuration	167
4.3. Stress inversions and sampling methodology	168
4.4. Stress inversions accuracy prediction domain	172
5. Discussion	173
5.1. Relationship between ω and Δ	173
5.2. Sliding friction	175
5.3. Data sampling	177
5.4. Chimney rock	177
<i>Stress inversion and sampling</i>	177
<i>Chimney rock fault array evolution</i>	179
<i>Prediction domain</i>	179
6. Conclusions	180
Acknowledgements:	184
Tables	185
Annex	187
References	190
CHAPTER III: Geomechanical paleostress inversion using fracture data: Application to modeling natural fractures in reservoirs	199
Abstract	199
1. Introduction	200
2. Method	204
2.1. Numerical tool	205
2.2. Fault Paleo-Geometry	206
2.3. Paleo tectonic stresses	207
2.3.1. Parameter Space	207
2.3.2. Computation Time	209
2.3.3. Fracture data and cost functions	210
2.3.4. Tectonic stress domain	212
2.3.5. Under-constrained model	213
3. Nash Point outcrop case study	216
3.1. Geological Setting	216

3.2. <i>Paleostress inversion</i>	219
3.2.1. Model configuration	220
3.2.2. Model results	221
3.2.3. Sensitivity to fracture data location	223
3.3. <i>Joint trajectory convergence investigation</i>	225
3.3.1. Contact point model	225
3.3.2. Fluid pressure model	227
4. Les Matelles outcrop case study	229
4.1. <i>Geological Setting</i>	230
4.2. <i>Paleostress inversion</i>	232
4.2.1. Model configuration	232
4.2.2. Model results	233
4.2.3. Sensitivity to 3D fault model geometry	237
4.3. <i>Influence of fault friction</i>	238
5. Oseberg Sør field case study	240
5.1. <i>Geological Setting</i>	241
5.2. <i>Paleostress inversion</i>	242
5.2.1. Model configuration	242
5.2.2. Model Results	244
6. Discussion and conclusions	245
6.1. <i>The method</i>	245
6.2. <i>The Nash Point example</i>	247
6.3. <i>The Matelles example</i>	249
6.4. <i>The Oseberg Sør example</i>	250
6.5. <i>Further applications</i>	251
Acknowledgments	252
References	253
Annex 1:	260
Annex 2:	260
CHAPTER IV: Polyphasic geomechanical stress inversion using undefined fractures mechanical type	265
Abstract	265
1. Introduction	266
<i>The determination of multiple tectonic events</i>	267
<i>The oil industry problem: multiple phases and unknown fracture types.</i>	269
<i>Our approach</i>	270
2. Methods and synthetic models validation	271
<i>Numerical methods</i>	271
2.1.1. BEM	271
2.1.2. Paleostress using Fractures	271
2.1.3. Tectonic stress domain	271
<i>Polyphase stress inversion and type separation</i>	272
<i>Confidence criterion</i>	273
<i>Synthetic model for validation</i>	275
2.1.4. Synthetic Fault Model and generated fractures	275

2.1.5. Data clustering and stress inversion validation	277
2.1.6. Type separation validation	278
3. Case Study: La dalle des Matelles	282
<i>Geological setting</i>	282
<i>Model configuration</i>	286
<i>Model results</i>	287
3.3.1. Known mechanical type	287
3.3.2. Unknown mechanical type	288
3.3.3. Type separation	289
4. Discussion and conclusions	291
Acknowledgements:	292
References:	293
Conclusions	301
<i>Perspectives</i>	303
<i>Benefits for Schlumberger</i>	304

Extended abstract

One of the main challenges in the oil industry is the exploitation of new resources in naturally fractured reservoirs often located in structurally complex areas such as tectonic plate boundaries, mountain ranges or near salt structures. While knowing the present day stress field is important for drilling and borehole stability as well as for the prediction of fractures orientation induced by hydro-fracturing, past stress fields, responsible for the development of natural fractures, are equally important to model fractured reservoirs, essential for an efficient recovery of natural reserves.

Numerical simulations of rock deformation based on continuum mechanics are becoming industry standard in providing efficient means for modeling natural fractures in reservoirs. However, amongst the three key elements essential for a complete geomechanical modeling, which are the structure geometry, the rock properties and the far field loading, the later is the most uncertain and difficult to evaluate. It is referred as the type (normal faults in extensional regime, strike slip faults in wrench regime or reverse faults in compressional regime), orientation and magnitude of the regional or local tectonic stresses that needs to be applied as boundary condition in numerical simulations.

Over the last five decades, methods have been developed to recover the paleostress field from observed fault slip data. These methods, based on the Wallace (1951) and Bott (1959) assumption suggesting that slip direction is parallel to the resolved shear stress on the fault plane, have raised some concerns about its validity from part of the research community. Furthermore, these methods are difficult to apply in the oil and gas industry as fault planes with slickenlines are not observed in well log images and seldom observed in cores.

The goal of this work is to improve the estimation of the paleostress field needed to constrain numerical simulations used for modeling natural fractures in the subsurface. For that purpose I aim at addressing four main questions:

1) How much should we trust the Wallace and Bott assumption for paleostress inversion from fault slip data?

A comparison of the resolved shear stress with slip vectors generated by mechanical models using the Boundary Element Method (BEM) is done. By testing the influence of multiple parameters (geometry, boundary conditions, friction, Poisson's coefficient, half-space, fault fluid pressure), it is shown that faults with complex geometries can yield slip vectors with significant discrepancies with respect to the maximum shear stress resolved on the fault plane under specific boundary conditions. Conversely, the presence of a high sliding friction, allows under certain conditions, to validate the hypothesis of Wallace and Bott.

2) How well paleostress inversion techniques based on the Wallace and Bott assumptions perform compared to new generation technique based on geomechanics?

I then focus on the task of comparing the results of stress inversions based on the assumption of Wallace and Bott (called classical stress inversion methods) to a geomechanical method. For this, a complex fault geometry is used in a sensitivity analysis (boundary conditions, friction, data sampling) to analyze the uncertainty of the results of the two inversion methods. This analysis is then compared to a case study, Chimney Rock (Utah, USA), showing the advantages and drawbacks of the classical stress inversion methods.

3) Can we improve paleostress recovery using other types of data?

Since slip markers on faults are hardly observed in cores or image logs, I use observed natural fracture data as main drivers for the inversion of the paleostress using the new generation technique based on geomechanics. I demonstrate, through various outcrop and subsurface examples, how this can efficiently be done and discuss the advantages and drawbacks of such new technique.

4) How is it possible to solve the polyphase problem when the mechanical fracture type is undefined?

It is sometimes difficult to determine the fracture kinematics observed along wellbores, and very often the studied regions underwent multiple tectonic phases. In this final section I address the problem of data with unknown movement type (joints, faults, stylolites ...) and extend the mechanical stress inversion to the separation of tectonic phases.

General introduction

1. Essence of the thesis

Today, one of the main challenges in the oil industry is the exploitation of new resources in naturally fractured reservoirs often located in structurally complex areas such as plate boundaries, mountain ranges or near salt structures. While the knowledge of present day stress field is important for planning drilling and stability as well as for the prediction of fractures induced by hydro-fracturing, past perturbed stress fields, responsible for the development of natural fractures, is equally important to model fractured reservoirs, essential for an efficient recovery of natural reserves. To solve this issue, numerical models of rock deformation based on continuum mechanics are becoming industry standard in providing efficient means for modeling natural fractures in reservoirs. However, amongst the three key elements essential for a complete geomechanical modeling, which are the structure geometry, the rock behavior and the far field loading, the later is the most uncertain and difficult to evaluate. It is referred as the type (normal, wrench or reverse), orientation and magnitude of the regional or local tectonic stresses that needs to be applied as boundary condition in numerical simulations. Over the last five decades methods have been developed to recover the paleostress field from observed fault slip data. These methods, based on the Wallace (1951) and Bott (1959) main assumption that slip direction is parallel to the resolved shear stress on the fault plane, have raised some concerns about its validity from part of the research community. Furthermore, these methods are difficult to apply in the oil and gas industry as fault planes with slickenlines are not observed in well log images and seldom observed in cores.

The main objective of this thesis is to improve the estimation of the paleostress field needed to constrain numerical simulations used for modeling natural fractures in the subsurface.

2. How are the fractures modeled in the Oil & gas industry?

2.1. Existing techniques

For the last 50 years, several methods have been developed to model natural fractures. The curvature analysis methods are intensively used in the industry to predict fracture orientations and clustering of bent or folded strata (Murray, 1968; Thomas et al., 1974, Lisle, 1994; Fisher and Wilkerson, 2000; Hennings et al., 2000). However, the effect of faulting and layer thickness is ignored and the technique is too sensitive to seismic reflection data acquisition and processing.

The statistical methods, based on the power-law distribution of faults size (Childs et al., 1990; Walsh and Watterson, 1991; Schlische et al., 1996; Sassi et al., 1992; Yielding et al., 1992), on the stochastic clustering process (Munthe et al., 1993; Damsleth, 1998), or, on the hypothetical fractal nature of faulting (Gauthier and Lake, 1993) allow to model fractures in reservoirs. However, although the size distributions are predictable, fracture mechanics is not considered with these techniques and therefore it is more difficult to predict the orientations and location of the fractures

Pioneer work by Hudson (1981) has shown that it could be possible to detect fracture networks through seismic attribute processing (Schoenberg and Sayers, 1995; Neves et al., 2004), and through artificial intelligence algorithms such as the ant-tracking (Pedersen et al. 2005). However, despite the recent advances in seismic reflection techniques and in seismic attribute processing, most of the natural fractures cannot be detected at the current resolution (1 to 25 meters) of the seismic reflection data.

Recently structure restoration methods, have been extended to predict areas that have undergone large strains and to relate the strains to structural heterogeneities such as faults and joints (Hennings et al., 2000; Sanders et al., 2002; Kloppenburg et al., 2003; Sanders et al., 2004). However, as for the previous techniques to model fractures, geometric restoration does not consider rock deformation as a physical phenomenon.

Maerten and Maerten (2006) have demonstrated that adding mechanics to structural restoration could help model natural fractures in reservoirs for some configurations only since these techniques are too dependent on unphysical boundary conditions (Lovely et al., 2012).

2.2. Techniques based on geomechanics

Today, numerical models of rock deformation based on continuum mechanics are becoming industry standard in providing efficient means for modeling natural fractures in reservoirs. Over the past decade, pioneer studies (Maerten, 1999; Bourne et al., 2000) have proved that adding a geomechanical rationale to stochastic techniques improves their predictive capability and leads to more realistic fractured reservoir models. To study stress perturbations near major fault zones, Homberg 1997 used 2D distinct element method (DEM) to compare the principal stress directions to the secondary faults orientation in Jura mountain, also showing that stress perturbations around a single discontinuity decrease as friction increases.

The basic idea is to assume that fractures might develop, whatever the fracturing mechanism, in a heterogeneous stress field which could be caused by faulting, folding or by any other geological processes that would locally perturb the stress field. This could result in both heterogeneous fracture orientation and density. Therefore, the general methodology for using geomechanical methods consists of calculating the stress distribution at the time of fracturing using the available reservoir structure informations such as faults, fractures and folds, the rock type and the tectonic setting that can be characterized by stress or strain magnitude and orientation. Then, the calculated stress fields, perturbed by the main structures, combined with rock failure criteria are used to model natural fracture networks (i.e. orientation, location, and spatial density trends). An instructive 2D illustration of the geomechanically-based methods is exposed in figure 1. It shows a preexisting discontinuity subjected to a load that undergoes shear to create a fault. The stress is perturbed around the fault showing both tensile (light grey) and compressive areas (dark grey). Both the orientation of σ_1 (the most compressive principal stress) and σ_2 (the least compressive principal stress) are perturbed close to the fault. This stress pattern can be compared to outcrop example such as reactivated

preexisting fracture showing branch crack in least compressive areas and stylolites in most compressive areas (Rispoli, 1981), both following the orientation of σ_1 and σ_2 respectively.

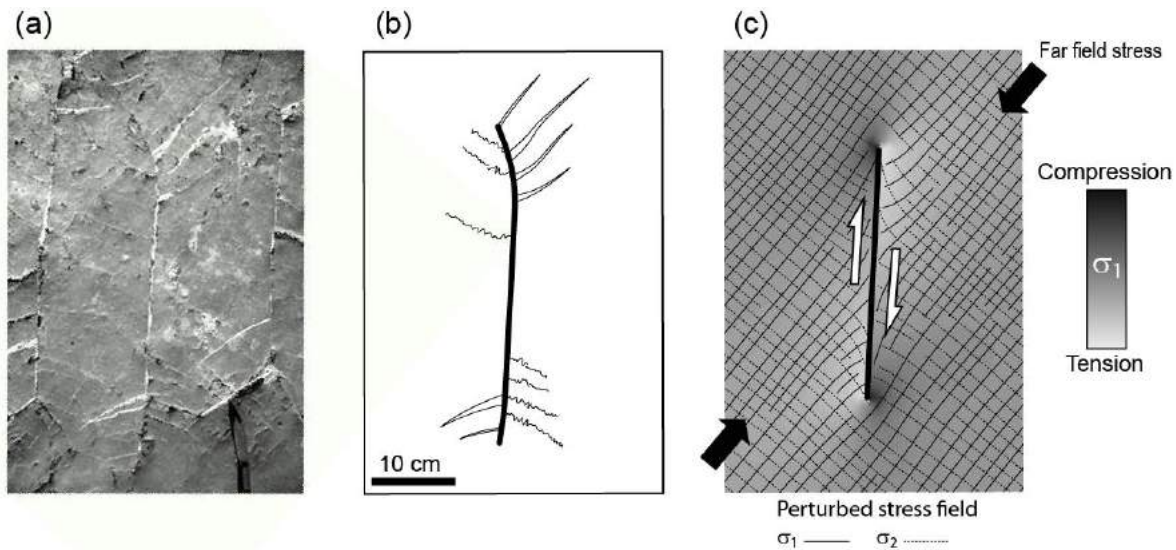


Figure 1. Comparison between (a) photo of secondary features such as tensile cracks and stylolites observed around a reactivated fracture in limestone at Les Matelles, southern France (Rispoli, 1981; Petit and Mattauer, 1995) and (b) its interpretation of observed fractures with (c) stress perturbation computed around a single fault showing σ_1 intensity and orientation.

The method has been successfully applied to both outcrops and reservoirs demonstrating how geomechanics can provide a high degree of predictability of natural fracture networks. For instance, Homberg et al. (2004) used slip inversion and 2D discrete element method (DEM) models to confront the observed secondary faults with the reconstructed the paleostress field. The 3D boundary element method (BEM) has been successfully applied to model subseismic faults (Maerten, 1999; Maerten et al., 2006) in Northern North Sea highly faulted reservoirs as well as the undetected joints in naturally fractured carbonate reservoirs (Bourne et al., 2000) and lately, to compare differential stress magnitude trends revealed by calcite twinning paleopiezometry near a thrust fault tip to the stress magnitudes yielded by a

linear elastic model in Poly3D. Similarly elastic dislocation modeling have been applied to model small-scale fault and fracture network characteristics in normal and reverse fault regimes (Dee et al., 2007).

Three key elements are essential for a complete geomechanical modeling. The first element is the geometry of the subsurface geology called the geological model. Although this is the most important element in geomechanical modeling, it is often oversimplified for technical and/or practical reasons. Geological models should resemble past and/or present day natural structures as much as possible. This includes sedimentary layers, faults, salt diapirs, cavities, folds, or any geological objects. The second element is the stress field, which can be described as the faulting type (normal, wrench, or reverse), orientation and magnitude of the regional or local tectonic stresses through time. This important parameter for the geomechanical modeling is the most difficult to evaluate. While there are techniques for measuring some components of the present day tectonic stress, it is difficult to measure past tectonic stress. These are often partly guessed introducing very high uncertainties in the modeling. Finally, the third element is the rock properties and mechanical behavior. This element of the geomechanical modeling is often the best constrained. Thanks to laboratory testing, we have a fair understanding of the rock properties and behavior. These can be extrapolated in the past using known rules on how the rock evolved (i.e. compaction, porosity, etc.).

In this thesis I focus on the major unknown for natural fracture and present day fracture modeling, which is the far field tectonic stress that we also call the far field boundary conditions in the geomechanical simulation. The tectonic stress estimation is crucial for fracture modeling and existing methods advantages and limitations should be investigated.

3. Faults and Fractures

The proposed work concentrates almost exclusively on the case where faulting is the main driver for stress perturbation that would affect further fracture development. We then make the assumption that in a

growing and active fault system, the orientation of fractures will be influenced by the regional state of stress as well as by the perturbation near large faults.

3.1. Faults, fault systems and stress field

Faults are discontinuities of the rock along which there has been significant shear. We classify faults by how the two rock blocks on either side of a fault move relative to each other.

Throughout the Earth's crust, three faults types are distinguished:

(1) Normal faults, reverse faults and strike-slip faults (figure 2). Normal faults are characteristic of regions undergoing extension (i.e. passive margins). In normal faults, the hanging wall moves downward, relative to the footwall. Normal faults may dip at a variety of angles, but they most typically dip between about 40° and 70°.

(2) Reverse faults are characteristic of regions of compressive shortening of the crust such as subduction zones in active margins or newly formed mountain ranges. For reverse faults, the hanging wall moves up relatively to the footwall. The dip of a reverse fault is generally steep.

(3) Strike-slip faults are usually sub-vertical and the rock blocks moves either or laterally with very little vertical motion. Strike-slip faults with left-lateral motion are called 'sinistral' faults while faults undergoing right-lateral motion are called 'dextral' faults. Each motion sense is defined by the direction of movement of the ground on the opposite side of the fault from an observer.

Transform fault are a special class of strike-slip faults where the latter form a plate boundary, these faults are related to offsets in spreading centers, such as mid-ocean ridges. Transform faults can also be found in continental lithosphere transfer regions such as the San Andreas Fault in the United States. In extensional or compressive regions a mix of normal, strike-slip and reverse faults can be found, for example, Bergerat et al. (1990, 1998), Guðmundsson et al. (1996); Villemin et al. (1994) showed that a mix of normal

faults and strike-slip faults are characteristic of a rifting extensional process. Also, faulting does not necessarily have pure dip slip movement as described above. It is common to have some combination of fault movements occurring, resulting in an oblique slip.

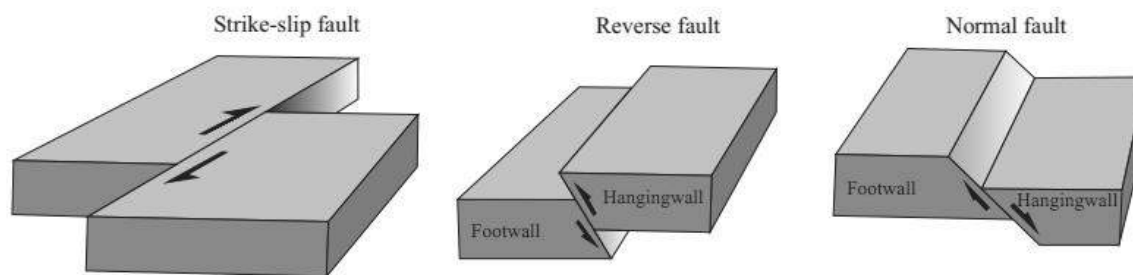


Figure 2. Schematic illustration of Strike-slip, Reverse and Normal faults. Modified from Plateau (2012)

Fault surfaces are characterized by the ratio of length to height (L / H) called shape ratio. Seismic profiles interpretations have shown that fault geometry can be complex (Koledoye et al., 2003; Kattenhorn et al., 2001). Fault growth is controlled by two processes: Propagation at their tip when slip accumulates, or by fault segments coalescence in relay zones (Cartwright et al., 1996).

The analysis of their throw profile of faults (throw distribution observed along faults, from zero at the tip line to a maximum value near its center). During propagation, faults usually accumulate throw proportionally to their size (self-similarity) (Schilsche et al., 1996). The value of the maximum throw (D_{max}) is a function of the length of the fault ($D_{max} \approx 0.03 \cdot L$ in average) but also of its depth ($D_{max} \approx 0.1 \cdot H$) (Soliva et al., 2005; Soliva and Schultz, 2008). For a single fault, the throw profile depends on the 3D geometry of the fault (Schultz and Fossen, 2002; Soliva et al., 2005) and is symmetrical. Numerical modeling in linear elastic media, shows rather elliptical symmetrical curve profiles. Maximum throw versus fault length may deviate from the general trend in the case of fault interaction (Dawers and Anders, 1995; Maerten et al., 1999; Maerten, 2000; Conteras et al., 2000) modifying the throw gradient but also the fault dynamics (Young et al., 2001).

The slip and orientation of the fault planes are associated to the locally perturbed far field stress orientation. However, local stress is not necessarily identical to the far field regional stress. Indeed, faults locally perturb stress fields. These perturbations affect the stress magnitude and orientation related to the displacement on a fault or a fault system.

The perturbation of the stress field is a complex phenomenon, which is the reason why it is often studied using numerical modeling. Numerical models show that stress perturbations at the ends of isolated faults promotes shear failure, thus controlling their propagation (growth). On a fault system, the stress drop due to faults development has been proposed as the phenomenon that controls the fault spacing (Soliva et al., 2006). The perturbed stress establishes the location of the fault initiation and the preferential growth of some of them. Both intersecting faults and overlapping faults are areas where the perturbation of the stress field is high enough to modify the throw profile of the secondary fault segments and their 3D geometry as they propagate (Peacock and Sanderson, 1991; Willemse et al., 1996; Maerten et al., 1999; Maerten, 2000). 3D numerical studies of homogeneous elastic medium on normal fault systems showed that secondary faults with a wide variety of orientations can be explained by stress field perturbations during the same tectonic phase (Maerten et al., 2002; Maerten et al., 2006). The perturbation of the stress field is largely controlled by the 3D geometry of the fault system (Willemse et al., 1996; Kattenhorn et al., 2001; Soliva et al., 2006).

3.2. Fault genesis and tectonic regimes

Triaxial mechanical rock tests highlight the development of fractures under a given state of stress. In such tests, the applied force and displacement are known. Relationship between the fracture system and orientation of the compressive force are obvious. From these results, it is then possible to reconstruct the directions of the forces that generated the creation of a fault system. One of the earliest experiments was conducted by Daubrée (1879), who compared the results with outcrop fracture systems.

Anderson (1905, 1951) was one of the first to present a clear summary of the analysis of faults systems and vein systems in analogy with rock mechanics. The application of these concepts in structural geology permitted to determine the direction of the principal stresses from a conjugate fracture system. To illustrate these concepts, first, it is necessary to consider an isotropic material and a system of newly formed faults. Consider a stress tensor σ defined in the main frame, represented by the matrix:

$$\sigma = \begin{pmatrix} \sigma_1 & 0 & 0 \\ 0 & \sigma_2 & 0 \\ 0 & 0 & \sigma_3 \end{pmatrix} \quad (1)$$

where σ_1 is the maximum principal stress, σ_2 the intermediate stress and σ_3 the minimum compressive stress ($\sigma_1 \geq \sigma_2 \geq \sigma_3$, where compression is positive). The σ_1 axis is the bisector angle of the acute angles of conjugate planes, σ_2 corresponds to the intersection of the two planes and σ_3 is perpendicular to σ_1 and σ_2 . From this geometrical relationship, one can define the tectonic regimes corresponding to a normal, a strike-slip and a reverse fault systems (Figure 2). The permutation between stress regimes can be achieved by a simple rotation around one of the principal stresses axes (Figure 3).

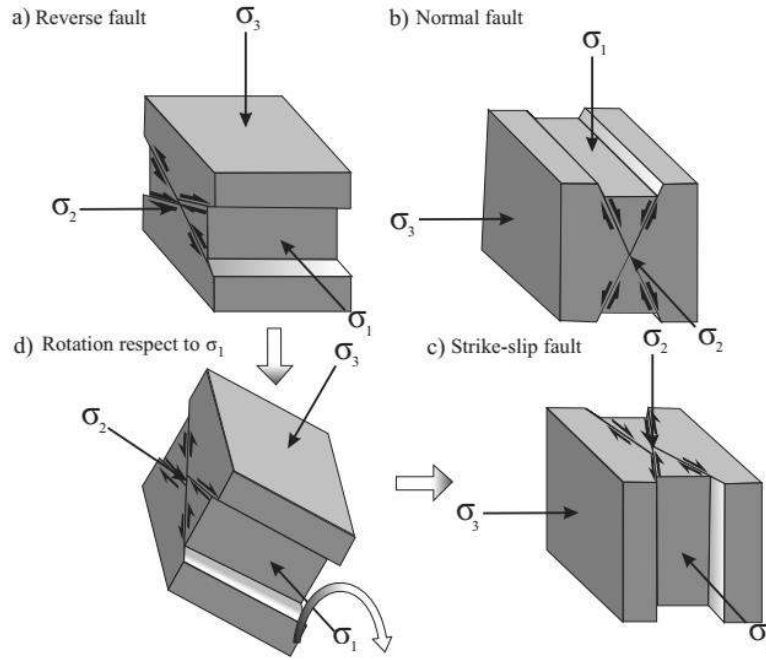


Figure 3. Different fault types and principal stresses. (a) Reverse fault, (b) Normal fault, (c) Strike slip fault, (d) example of bloc rotation around the principal horizontal stress σ_1 axis. After Plateau (2012) from Angelier (1994a).

3.3. Fault reactivation

Consider a traction, denoted \vec{t} (given by the Cauchy formula on the applied stress tensor σ^r), applied at a given point of a fault plane (Figure 4). \vec{t} can be decomposed in two components: the shear stress, denoted $\vec{\tau}$, along the fault plane and the normal stress, denoted \vec{t}_n , normal to the fault plane (Figure 4), such as:

$$\vec{t} = \vec{\tau} + \vec{t}_n \quad (2)$$

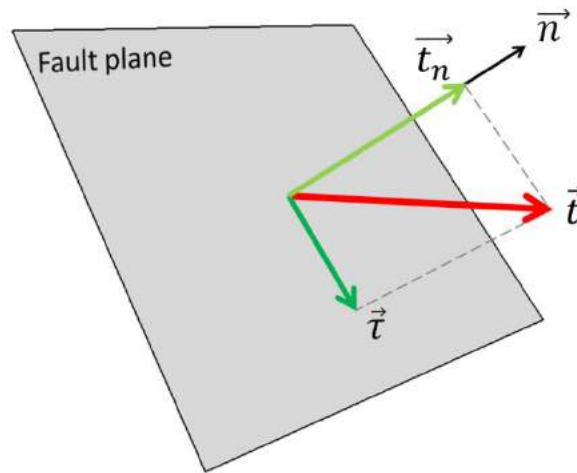


Figure 4. From traction to shear stress. The traction \vec{t} , the shear stress $\vec{\tau}$ and the normal stress \vec{t}_n are illustrated. \vec{n} is for the normal to the fault plane.

Using Mohr-Coulomb (1882) failure criterion and knowing the direction and magnitude of the principal stresses, it is possible to determine the orientation of the failure plane. For example, in the case where stress conditions are optimal (maximizing the difference between the shear stress and frictional resistance) failure should occur when the magnitude of the shear stress τ on a plane is equal to a value of cohesion τ_0 added to a coefficient of friction μ multiplied by the magnitude of the normal stress on the fault plane σ_n . This criterion can be written as follows:

$$\tau = \sigma_n \cdot \mu + \tau_0 \quad (3)$$

Mohr's circle allows to estimate the magnitude τ and σ_n at failure (Figure 5). When the circle defined by σ_1 and σ_3 is tangent to the Mohr failure envelope, which is defined by the friction angle ϕ with $\mu = \tan \phi$ and the material cohesion is τ_0 , the stresses exceed the rock strength and failure occurs (Figure 5). The intersecting point between the failure envelope and the Mohr circle is used to define the shear stress and normal stress magnitudes needed to reach failure, as well as the orientation of the fracture plane (Figure 5). One can thus express τ and σ_n as a function of σ_1 and σ_3 as follows:

$$\tau = \frac{\sigma_1 - \sigma_3}{2} \sin 2\delta \quad (4)$$

$$\sigma_n = \frac{\sigma_1 + \sigma_3}{2} - \frac{\sigma_1 - \sigma_3}{2} \cos 2\delta \quad (5)$$

where δ is the angle between σ_1 and the fault plane

Note that the example above is for optimal failure conditions, where the fracture is newly formed in an isotropic material. This occurs when the rock material has not been deformed or faulted yet. Natural fractures networks show more complex systems having undergone various successive failures under time dependent variations of boundary conditions.

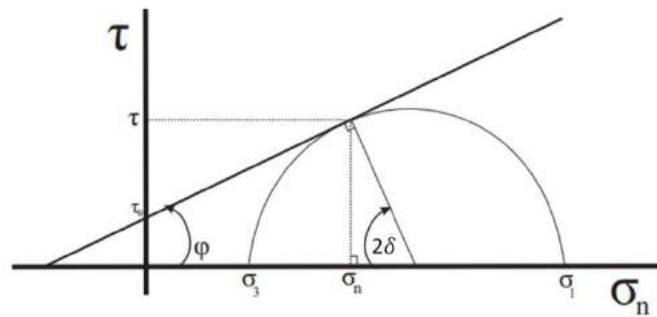


Figure 5. Mohr's circle representation. τ_0 is for the cohesion, ϕ is the friction angle. δ is the angle between σ_1 and the fault plane.

3.4. Fault sliding friction

Friction is the force resisting the relative motion of solid surfaces sliding against each other. Leonardo Da Vinci (1452-1519) pioneered in studying friction. He suggested that friction is dependent on the roughness of the sliding material such that smoother materials will have smaller friction. Similarly, Amontons (1699) suggested that friction was predominately due to the surface irregularities and the force required to lift the weight pressing the surfaces together. Coulomb (1779) suggested that strength due to friction is proportional to compressive force, although for large bodies friction it does not follow exactly this law, which represents the second law of friction. The second law of friction is known as the Amontons-Coulomb Law.

Here, in the context of geological faults reactivation, we distinguish two types of friction:

- 1) Material (internal) friction which is the force resisting motion between the elements strength making up a solid material while it undergoes deformation. It is responsible to faults and fractures initiation.
- 2) Sliding friction which we decompose here in two type: static and dynamic (or kinetic) friction. Static friction is the friction between two solid objects, and is independent of the time (e.g., static friction can prevent an object from sliding along an inclined surface). The coefficient of static friction is usually higher than the coefficient of dynamic friction. Dynamic friction occurs when two objects are moving relative to each other. The coefficient of Dynamic friction is usually lower than the coefficient of static friction at the end of the motion.

The static friction is also defined as an angle such as:

$$\mu = \tan\phi \quad (6)$$

This formula can also be used to calculate μ from empirical measurements of the friction angle.

Byerlee's (1978) law, which is empirically derived from experimental determination of "maximum shear stress" on a wide range of rock types, and stating that the friction coefficients is $0.6 < \mu < 0.85$ (independently of the rock type) for natural sliding surfaces following the relationship (Coulomb's friction law):

$$\tau = \mu\sigma_n + \tau_0 \quad (7)$$

where, τ is the shear stress of a pre-existing fracture, σ_n is the effective normal stress, μ the coefficient of sliding friction, and τ_0 the cohesion of the rock. This relationship provides the coulomb failure envelope within the Mohr-Coulomb Theory (Figure 5).

However, according to many authors, it is inferred a significant decrease in friction as low as $0 < \mu \leq 0.3$ (Zoback and Beroza, 1993; Marone, 2004; Colletini et al. 2009; Reches and Lockner, 2010; Di Toro et al. 2011) is observed for faults reactivation due to fault lubrication during earthquakes, which is much lower than historical values ($\mu = 0.6$ and $\mu = 0.85$) deduced by Beyerlee, (1978).

3.5. Fractures classification and stress field

A fracture is a discontinuity in a rock mass. It can be generated when rock cohesion is lost when applied stress exceeds the rock strength. Fractures can be observed at multiple scales, from kilometric, to microscopic. In this study, we defined 3 natural fracture types (tension fractures, shear fractures and stylolites) based on their development mechanism and their relationship with the orientations of the 3 principal stresses as described in Figure 6.

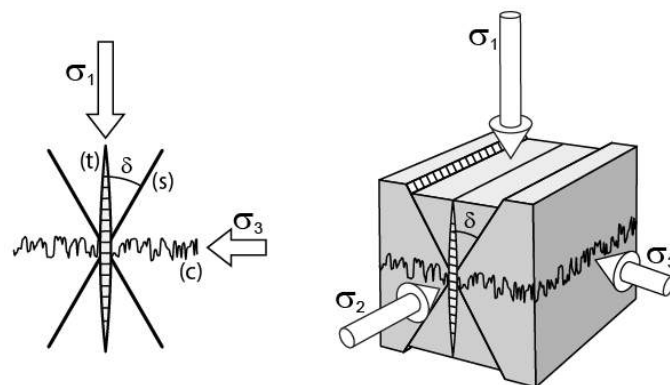


Figure 6. Mechanical fracture types and relationship with principal stresses. (t) Tension fracture (i.e. joint), (c), stylolite) and, (s) Shear fracture (i.e. fault).

Tension fractures form in a direction perpendicular to the potential fracture plane reaches the tensile strength of the rock. Tension fractures show an extension perpendicular to the fracture walls. The most common tensile fractures are the joints but it also includes veins and dikes. Tension fractures form in a plane perpendicular to the least compressive principal stress σ_3 .

Stylolite peaks (or anticracks or closing fractures) form with a compressive stress in a direction perpendicular to the potential fracture plane. Stylolites are very common in carbonates but can also be observed in clastic rocks. Compaction bands will form in a plane perpendicular to the most compressive principal stress σ_1 .

Shear fractures are fractures along which the relative movement is parallel to the fracture walls. The most common shear fractures are the faults but it also includes deformation bands. A shear fracture is one of the two conjugate planes, oriented at acute angles δ on either side of the most compressive principal stress, σ_1 , and with opposite sense of shear direction (see Figure 6). δ is such that:

$$\delta = \frac{\pi}{4} - \frac{\phi}{2}, \quad (8)$$

where ϕ is the angle of rock internal friction.

3.6. Fractures related to faulting

We are distinguishing two types of fractures related to faulting: (i) The fracture that are genetically associated to the faulting and (ii), the fractures that are not genetically associated to the faulting. In both cases the small scale fractures development will be affected by the heterogeneous stress field generated by the active faulting. We therefore make the assumption that in a growing and active fault system, the orientation of fractures will be influenced by the regional tectonic stress as well as by the perturbation of that stress state by nearby larger faults.

3.6.1. Fracture genetically associated to faulting

Here, we consider small scale fracture development related to the faulting mechanism only. In such case fracture initiation, location, density and orientation are directly associated to the perturbed stress field

generated by the active fault. These fractures are generally found near the main fault and especially close to fault tip line as shown in the two examples of Figure 7.

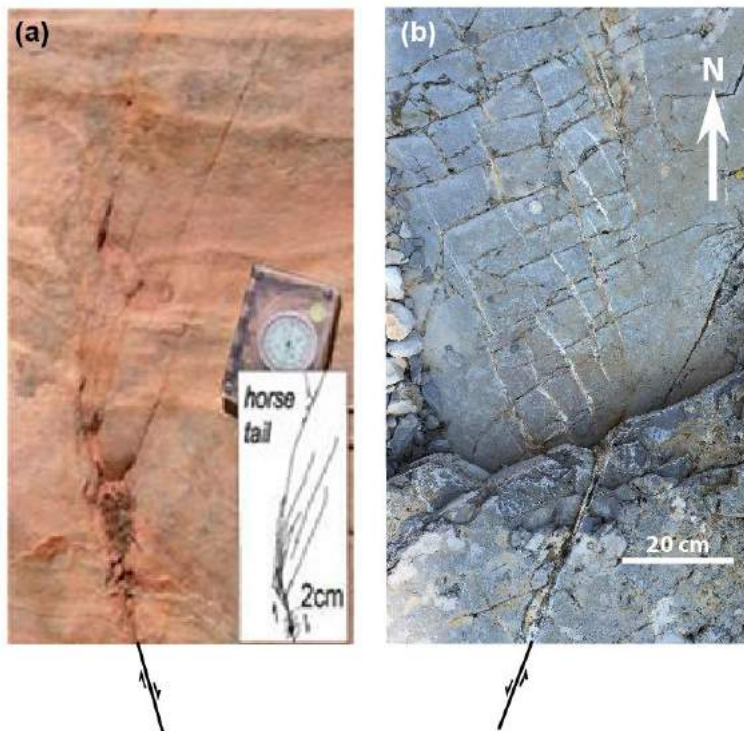


Figure 7: (a) Horsetail-shaped splay joints associated with a left-lateral strike-slip fault (map view) with a couple centimetres offset in sandstone, Valley of Fire State Park, Nevada (from DeJoussineau and Aydin, 2007). (b) Photograph of a strike-slip fault termination showing tail cracks (veins) in limestone at The Matelles, France.

3.6.2. Fracture not genetically associated to faulting

Natural fracturing could have many origins that are not necessarily tectonic. But in any case, natural fracture will develop in the stress field, which could be homogeneous or heterogeneous. Here, we concentrate solely on the assumption that the stress field is heterogeneous because of nearby active faulting. It is important to note that very often only the fracture orientation will be affected by the heterogeneous background stresses as shown in Figure 8 below. Here the joint development mechanism is clearly not the faulting but faulting affects the joint development orientation. In this case faulting does not affect joint density or at least very little.

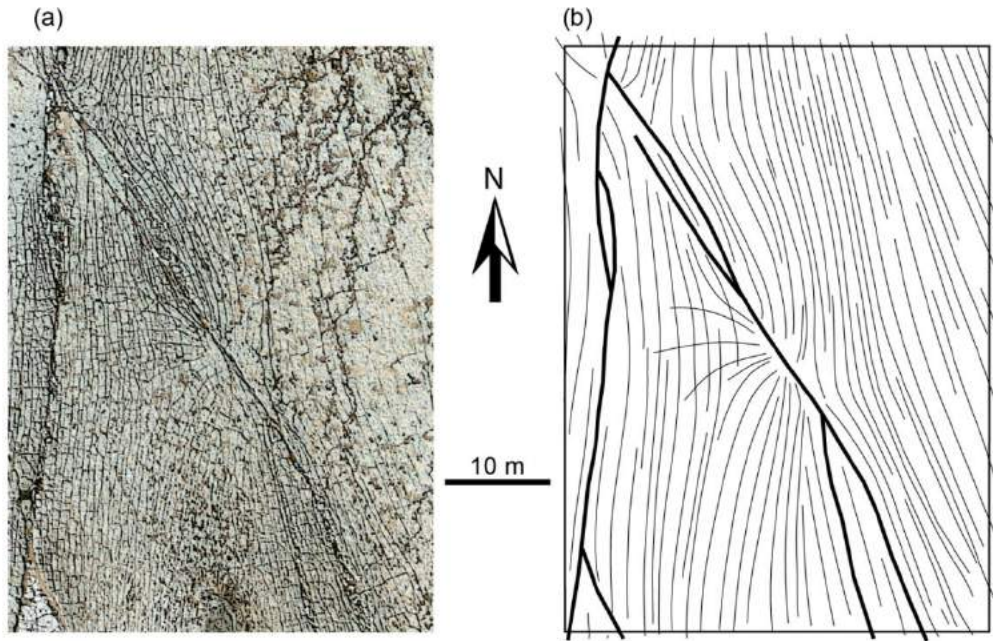


Figure 8: Example from Nash Point, UK. (a) Air photo and (b) interpretation of the outcrop showing fault network (thick black lines) and associated complex pattern of joints (thin black lines). The variability of the joints pattern at Nash Point clearly shows the relationship between the strike slip faults and the development of the joints. Joints appear to have been affected, during their development, by the perturbed stress field caused by slip along faults. Here only the joint orientation seems affected by the faulting, not the density which appears constant.

Very rarely, fracture density will be affected by heterogeneous background stresses as shown in Figure 9. Here the small fault development mechanism is clearly not the main faulting but faulting affect the small fault development density as smaller faults do not develop in the stress shadow around main faults. In this case faulting does not seem to affect small fault orientation.

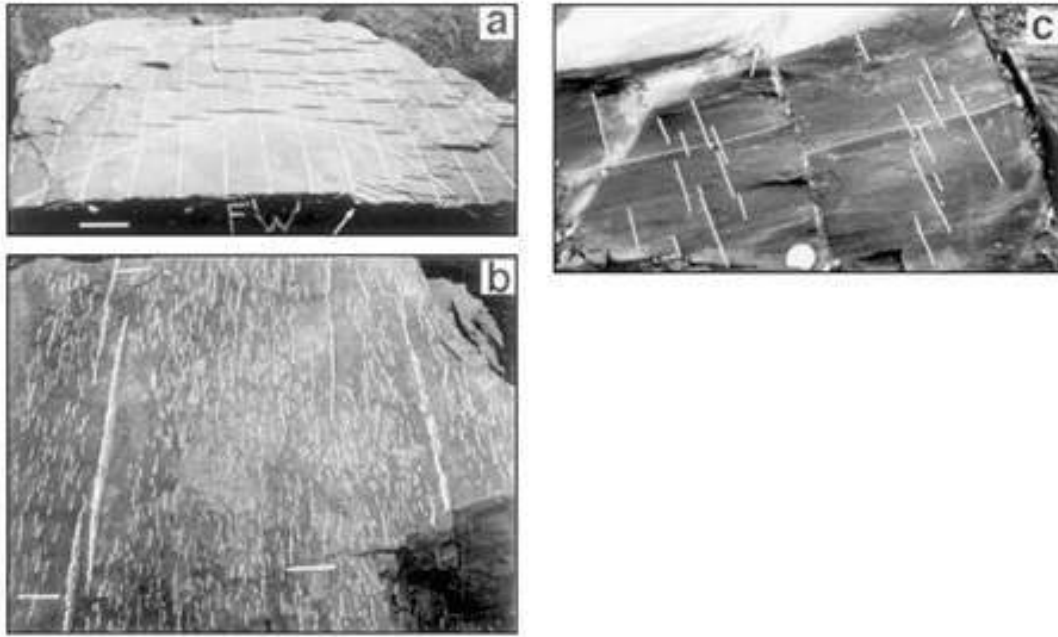


Figure 9: Small faults around larger normal fault (from Ackermann and Schlische, 1997). Here, the anticlustering defining crack shields around the master faults. The shields are ellipsoidal in shape and geometrically similar to the elastic deformation fields of the master faults, and correspond to a critical stress-reduction shadow that prevented the nucleation of smaller faults in the vicinity of the master faults. You can note here that only the small fault density is affected by the main faults, not the orientation.

4. How to recover paleostresses?

Fracture modeling depends on the geological model, which is referred as the geometry of the subsurface geology, the rock mechanical behavior, and the far field stress state at the time of formation of the fractures. The latter parameter is often difficult to estimate especially in the context of complex structure and polyphased tectonic history. Therefore, estimating the so called 'paleostress', which is critical for accurate fracture modeling especially for better characterizing fractured reservoirs, can become very difficult.

4.1. Paleostress estimation using Wallace & Bott type methods

The Wallace (1951) and Bott (1959) hypothesis

Fault systems are created in a given stress regime but are often later reactivated when the stress regime has changed over time or for a different stress regime. For instance, Bergerat (1983) presented a case study of the Rhin Graben (West European rift segment), where Eocene strike-slip faults have been reactivated as normal faults in an Oligocene phase despite their near vertical dip. Similarly, Davatzes et al. (2003) reported that the development of two fault sets at Chimney Rock, Utah (USA) was done during two distinct tectonic phases, while Maerten (2000) highlighted that the slickenlines observed on the two fault sets were produced by the same tectonic event when both fault sets were reactivated. In these two examples, the slip data represents the last phase of slip on the faults. In such a situation, the symmetry relationship between the newly formed conjugate fractures and the optimal principal stress cannot be applied to recover the paleostress tensor. The only way to determine the direction of the principal stresses from slip along reactivated faults is to introduce a relationship between the direction of shear stress and the observed slip (slickenlines). Wallace (1951) studied the variations in the direction and magnitude of the shear stress applied to different fracture plane orientations. He assumed that the orientation of the shear stress and slip should be parallel and have the same direction. Bott (1959) demonstrated that the orientation of the shear stress depends only on the orientation of the principal stresses and on a stress aspect ratio. A common definition of the stress aspect ratio, also called stress ratio R , has been introduced by Angelier (1975) such as :

$$R = \frac{(\sigma_2 - \sigma_3)}{(\sigma_1 - \sigma_3)}, \text{ with } 0 < R < 1 \quad (9)$$

when R increases from 0 to 1, σ_2 increases from σ_3 to σ_1 .

The Wallace (1951) and Bott (1959) assumptions constitute the basis for inversion methods to recover the principal stresses orientation and the stress ratio from fault plane data and slickenlines. To determine the state of stress, it is also necessary to consider that the stress field is assumed to be homogeneous in the rock mass, that faults are planar, that blocks are rigid, that neither stress perturbations nor block rotations along fault surfaces occur and that the stress state is uniform and that all the measured slickenlines were formed synchronously.

4.1.1. The stress ratio (R)

The stress aspect ratio is defined by equation (9) is between 0 and 1. When $R = 0$, the magnitude of σ_2 is identical to that of σ_3 . Conversely, when R is equal to 1 the magnitude of σ_2 is identical to that of σ_1 . These two limits present the case of a uniaxial compression and uniaxial extension, respectively. The concept of stress ellipsoid describes the stress tensor in a point, ellipsoid axes are the principal stresses σ_1 , σ_2 and σ_3 . Figure 10 shows different ellipsoids determined from the magnitude of the principal stresses where the magnitude of σ_2 relatively to σ_1 and σ_3 controls the shape of the ellipsoid.

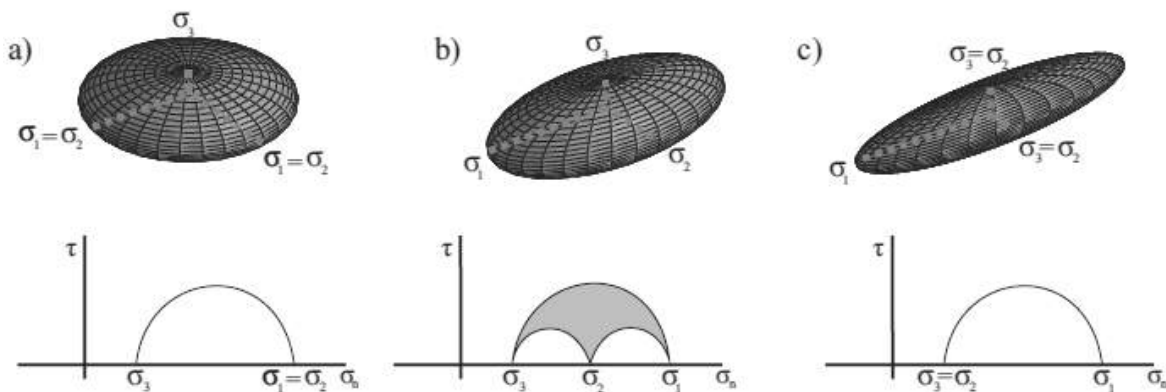


Figure 10. Stress ellipsoids for different values of the stress ratio. Each stress ellipsoid is associated with Mohr circle illustrating the different state of stress at a given point. (a) Oblate ellipsoid with uniaxial extension (b) Triaxial ellipsoid (c) Prolate ellipsoid showing uniaxial compression. After Plateau (2012)

The oblate ellipsoid (Figure 10.a) shows an uniaxial extension case. The intermediate ellipsoid (Figure 10.b) shows a triaxial condition, and the prolate ellipsoid (Figure 10.c) shows an uniaxial compression. The stress ratio can also be illustrated by the Mohr representation (Figure 5).

Depending on which of the principal stresses is vertical, $\sigma_v = \sigma_1$, $\sigma_v = \sigma_2$ or $\sigma_v = \sigma_3$, the three tectonic regimes, normal, strike-slip and reverse, can be described respectively (Anderson, 1951). The permutation of one of the horizontal principal stress axes with the vertical one allows switching from one tectonic regime to another. Furthermore, depending on the relative magnitudes of the intermediate principal stresses, σ_2 , with respect to the two other principal stresses, σ_1 and σ_3 , each tectonic regime can vary continuously from radial to axial.

4.1.2. The forward problem

It is possible to predict the orientation of slip on arbitrary fault plane based on a given stress tensor. The stress tensor has 6 degrees of freedom. It is possible to reduce the number of unknowns since the shear stress direction depends on the orientation of the principal stresses and R (Bott, 1959). We can thus reduce the tensor T to a reduced tensor denoted T^r by removing the isotropic portion of T and a scaling factor (not affecting the direction of τ). Thus the tensor can be characterized by four parameters, which describe the orientation of the three principal stresses (σ_1 , σ_2 and σ_3) and R the stress ratio. This can be simplified even further to a 2D parameter space (θ is the clockwise angle between the North and the orientation of the maximum principal horizontal stress) if we consider that at least one principal stress is vertical (Anderson, 1951).

We can thus calculate the orientation of the shear stress on a fault plane using the reduced stress tensor. The applied stress σ^r is established by the Cauchy formula:

$$\vec{t} = \sigma^r \cdot \vec{n} \quad (10)$$

$$\vec{\sigma}_n = (\vec{t} \cdot \vec{n})\vec{n} \quad (11)$$

The shear stress can thus be written as :

$$\vec{\tau} = \vec{t} - \vec{\sigma}_n \quad (12)$$

4.1.3. Stress inversion problem

Inversion problem consists in finding model parameters that better explain the observed data. In the case of paleostress, the observed data are fault systems with slip directions and the model is associated with stress tensor. In the classical inversion methods, the fault system and the stress tensor are fundamentally linked by the Wallace & Bott hypothesis. The inverse problem is defined by four parameters which are related to the orientation of the principal stresses and the stress ratio R . The observed data are slickenlines along fault planes. Among the inverse methods, there are two major types of algorithms to determine the stress tensor that better fits a faults data set: grid search and least square methods.

The difference between these two types of methods can be illustrated by analogy to the best line passing through a cloud of points in a graph (x, y). After selecting a first adjustment criterion the first approach (Grid search method) is to try a large number of lines and determine for each of them the correlation with the point cloud. To ensure that all the solutions are tried, one needs to systematically vary the two parameters controlling the line (slope and intercept parameters of the line). That consists on exploring a 2D space of the two parameters to ensure that we find the line that better adjusts to the point cloud. Covering the full 2D space can be tedious, thus Monte Carlo method has been used in order to speed up the searching process (Etchecopar et al, 1981 and Etchecopar, 1984). An alternative approach is to use regression to directly determine the best fitting line. To do this, we use an equation containing the sum of the point deviation from a general line. Using the partial differentiation, it is possible to derive a mathematical function which expresses the slope and intercept for the line that minimizes the deviations. The latter method is equivalent to a least square inversion method and is less consuming in terms of

computation time as it does not require repetitive tests. These two approaches require a criterion for determining the best fitting stress tensor with the data. The most intuitive criterion is to use the angle ω between the calculated shear stress τ and the observed slip vector (Figure 11). It is common to determine the stress tensor that produces the lowest ω between the model and the observed data.

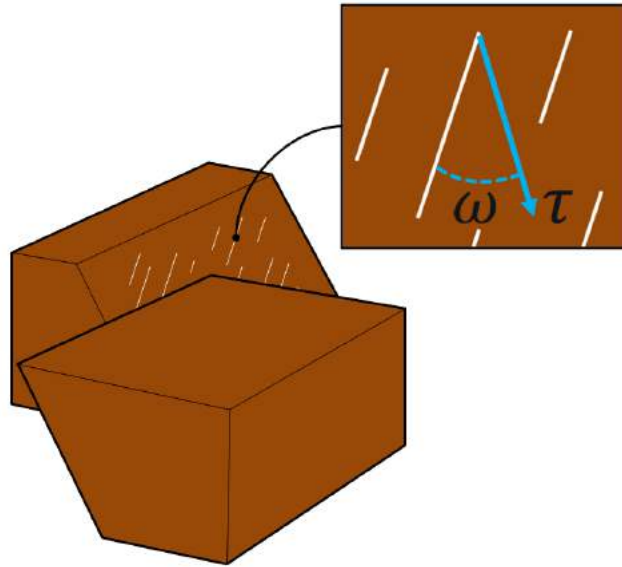


Figure 11. The misfit angle between the slickenline (white lines) and the shear stress resolved to the fault plane. τ is for the shear stress and ω is for the misfit angle between the slickenline and τ .

A commonly used minimization function takes the square sum of the misfit between the data and the theoretical model. Angelier (1984) and Michael (1984) defined it as follow:

$$M_1 = \sum_{k=1}^{k=K} (s - \tau)^2 \quad (13)$$

$$M_2 = \sum_{k=1}^{k=K} (\tau_{max} s - \tau)^2 \quad (14)$$

where τ_{max} is the maximum value of the shear stress for the considered stress tensor, and k represents each data faults or focal mechanisms.

Note here that M_1 (Angelier 1984; Michael, 1984) and M_2 (Angelier, 1990, 1991) criteria tend to maximize τ (close to 1). These criteria are considered as hybrids since they combine both an angle criterion and the Tresca failure criterion, where τ must be sufficient (or maximum) to generate slip on all considered fault planes. Both the INVDIR program, created by Angelier (1990), and the inversion program created by Micheal (1984), use these M_1 and M_2 criteria.

Once the reduced stress tensor that minimizes the misfit between observed data and the model is recovered, most classical inversion methods require identifying the data that are not explained by the stress tensor. This can be measured by the angle ω (Figure 11). When ω is high ($\omega > 30^\circ$) the retrieved tensor hardly explains this observed data. It may then be necessary to remove this data and to rerun an inversion since the data set has changed.

Some more sophisticated criteria than the simple ω have been created. For example, Angelier (1990, 2002) described a ratio which takes into account τ_{max} and ω . After the stress tensor has been found, a retrospective study can help verify that it satisfies a friction law. This can be done by inspecting the data on the Mohr (1882) representation by determining if they are below or above the frictional reactivation line (Angelier, 1983, 1989, 1994b; Célérier, 1988; Etchecopar, 1984; Etchecopar & Mattauer 1988; Fleischmann & Nemčok, 1991; Gephart & Forsyth, 1984). Michael (1987a) for his part developed a 'bootstrap' method for sampling the data set multiple times and thus run a stress inversion on each sample.

The main difficulty of the inverse problem is related to the heterogeneity of the observed data, leading to a multiple possible solutions.

4.1.4. Stress inversion using slip data

For the last five decades, the far field tectonic stress has been recovered through stress inversion techniques. All commonly accepted stress inversion methods use the simple but central Wallace (1951) & Bott (1959) assumptions (WB). Many algorithms based on WB assumptions have been developed to perform

stress inversion (Carey and Brunier, 1974; Angelier, 1975 and 1979a; Etchecopar et al., 1981; Gephart and Forsyth, 1984; Michael 1984; Lisle, 1992 and 1998; Yamaji, 2000; Delvaux and Sperner, 2003; Celerier, 2006) mostly using slickenlines, and quickly adapted for focal mechanisms (Ellsworth and Zhonghuai, 1980; Carey-Gailhardis and Mercier, 1987, 1992; Gephart, 1990a, 1990b; Gephart and Forsyth, 1984; Julien and Cornet, 1987; Mercier and Carey-Gailhardis, 1989; Michael, 1987b; Vasseur et al., 1983; Angelier, 1984; 2002a, 2002b; Lund and Slunga, 1999) and calcite twinnings (Turner, 1953, 1962; Nissen, 1964; Spang, 1972; Laurent et al., 1981, 1990; Dietrich and Song, 1984; Pfiffner and Burkhard, 1987; Lacombe and Laurent, 1996; Nemcok et al. 1999).

Many stress inversion programs have been created, these methods are either graphical inversions, like the well-known Right Dihedron method originally developed by Angelier and Mechler (1977) and improved by Delvaux and Sperner (2003), direct inversion methods using least square minimization (Carey-Gailhardis & Mercier, 1987; Angelier, 1991; Sperner et al., 1993) or iterative algorithms such as Monte Carlo techniques that test a wide range of possible tensors (Etchecopar et al. 1981) or grid search methods (Gephart 1990b; Hardcastle & Hills 1991; Unruh et al. 1996). It was also shown that the paleostress could be determined using fracture planes which do not bear slip lines on their surface (Angelier, 1994; Dunne & Hancock, 1994; Delvaux and Sperner, 2003).

However, the basic WB hypothesis is questionable, since Hancock (1985) and Petit (1987) studied evidences of local stress perturbations in microstructures, while others (Twiss and Geffel, 1990; Twiss et al., 1991; Pascal, 1998) observed block rotations along fault surfaces. Gapais et al., (2000) showed two examples of faulted regions to illustrate the spatial variability of fault-slip data either due to local complications at the edges of fault blocks, or to complex kinematic conditions at regional boundaries. These questions lead to ask as to what extent WB assumptions are verified when used for stress inversion.

Debates have been initiated by Pollard et al. (1993) and Dupin et al. (1993) who checked the validity of the WB assumptions by using mechanical modeling methods (i.e. taken into consideration internal deformation of faulted blocks and local stress perturbation between faults). According to the results of Dupin et al. (1993), the discrepancy angle between mechanical and WB predicted slickenlines reaches 47° for intersecting faults. Pollard et al. (1993) predicted a maximum of 37° discrepancy angle for fault interaction and a 10° misfit angle caused by fault tip geometry.

Later, Nieto-Samaniego and Alaniz-Alvarez (1997) proposed that the slickenlines should be parallel to the intersection line and therefore could deviate from the resolved shear stress orientation. Maerten (2000) explored the consequences of varying geometry of intersecting faults on slip directions using 3D boundary element methods (Thomas, 1993; Maerten et al., 2014). He concluded that significant deviations are expected close to fault intersections where the misfit angle can reach values greater than 50° . This result has been confirmed by field observations along the Chimney Rock fault array in Utah, USA (Maerten, 2000). Xu et al. (2013) compared observed fault striations in the San Miguelito Range with the fault interaction model of Maerten (2000) and found that the slickenlines patterns are consistent with the geomechanical model. The majority of the slickenlines is not parallel to the resolved shear regional stress but is consistent with local stress perturbations caused by fault mechanical interaction.

Another approach was used by Pascal (2002) using 3D distinct element method (Cundall, 1971 and 1988) to demonstrate that the differences between WB and mechanical models are negligible due to the implication of the sliding friction, which reduces the misfit angle between resolved shear stress and slip vector.

More recently, Kaven et al. (2011) pointed out that even if the stress inversion results are similar, WB type inversions perform poorly for limited ranges of slickenline orientations when compared to their proposed mechanical stress inversion method. Furthermore, Lisle (2013) showed from simple models, that

any stress field anisotropy such as that arising from 3D fault geometry, can lead to a significant angular difference between the directions of maximum shear stress and the slip direction predicted by the WB assumptions.

Thus, studies conducted with classical stress inversion methods do not fully take into account the full range of stress boundary conditions (i.e. stress tensor principal directions and stress ratio), fault and material properties (i.e. friction coefficient and Poisson's ratio) as well as the effect of traction free Earth surface (i.e. half-space). Methods of paleostress analysis have, by necessity, incorporated a significant degree of flexibility with respect to the implementation of the WB assumptions.

Another concern is that, although high misfit angle are expected, no stress inversion techniques based on the debatable WB assumptions have been tested on these specific configurations. Indeed, it has never been shown that a low mean misfit angle correlates to a fair stress inversion result, and inversely, that a high misfit angle correlates to an incorrect stress inversion result using the WB assumptions.

4.1.5. Stress inversion using focal mechanisms

In seismology, a fault is defined both in space (coordinates) and in time. Focal mechanisms characteristics depend on both the stress drop during the quake and the orientation of the stresses applied on it. In fact, during an earthquake only a portion of fault is reactivated. Each point of the reactivated fault surface generates a stress that is integrated during the duration of the earthquake on the reactivated fault surface. This allows deducing the amplitude of elastic waves at a distance r from the fault. It is important to determine this function because it is the only data that can be obtained (by seismograms). The seismic moment (Aki & Richards, 1980) is described in the fault referential such as:

$$m_{0ij} = G(\Delta u_i + \Delta u_j n_i)A \quad (15)$$

Where G is the shear modulus, Δ_u the motion vector averaged over the entire area (A) of the active fault, n_j and n_i are the normal vectors to the fault in its own referential. Rotating the referential of the fault in a geographical referential x , y and z gives the seismic moment tensor:

$$M = M_0 \begin{pmatrix} m_{xx} & m_{xy} & m_{xz} \\ m_{yx} & m_{yy} & m_{yz} \\ m_{zx} & m_{zy} & m_{zz} \end{pmatrix} \quad (16)$$

where M_0 is the seismic moment modulus (absolute magnitude). The m terms of the seismic moment tensor are expressed according to three angles: the plane dip, its azimuth and the rake of the sliding vector along a nodal plane for double couple focal mechanisms.

It is shown that this tensor is symmetrical and admits two perpendicular nodal planes as a solution (Aki & Richards, 1980). The two nodal planes define four quadrants (Figure 12). One nodal plane corresponds to the actual fault plane (Figure 12 F1) while the other nodal plane is fictitious (Figure 12 F2). These two nodal planes thus form the double couple focal mechanism introduced by Honda & Masatsuka (1952) and Honda et al. (1956).

The eigenvectors of the seismic moment tensor are the P axis, bisecting the dilatational dihedral, and the T axis, bisecting the compressive dihedral. The third eigenvector is the B axis intersecting both nodal planes. Aki & Richards (1980) defined the orientation of a nodal plane by its strike (0° to 360°), dip (from 0° to 90°) and the rake of the slip vector (from -180° to 180°). Double couple focal mechanisms can be represented as beach balls (Figure 12).

The B axis or null axis is at the intersection of the two nodal planes. The plane containing the P and T axes as well as the slip vector was defined by Arthaud (1969) as the plane of motion Figure 12.

Since one of the two nodal planes is the fault plane and slip vector is defined by the rake (similarity with the faults and slickenlines), it is then possible to use the WB hypothesis for a population of double couple focal mechanisms to get the associated stress tensor.

As the theoretical tangential stress cannot be aligned with the rake of the two nodal planes at once, except if a principal stress is parallel to the axis B or if the considered stress tensor has an axial symmetry such as R is close to its minimum or maximum (Gephart, 1985), one must choose the fault plane between the two nodal planes. There are different methods to choose the nodal plane. The most common approach is to calculate the difference between the slip vector and the theoretical shear stress orientation for both nodal planes of the same focal mechanism, and select the one that will produce the smallest misfit (Gephart & Forsyth, 1984; Gephart, 1990; Julien & Cornet, 1987; Mercier and Gailhardis Carey, 1989). It is also possible to choose the nodal plane that best fulfills a friction criterion (Slunga & Lund, 1999). An alternative is to randomly select the nodal plane when a sufficient number of focal mechanisms are available (Michael, 1987a; Hardebeck & Michael, 2006; Angelier, 2002b).

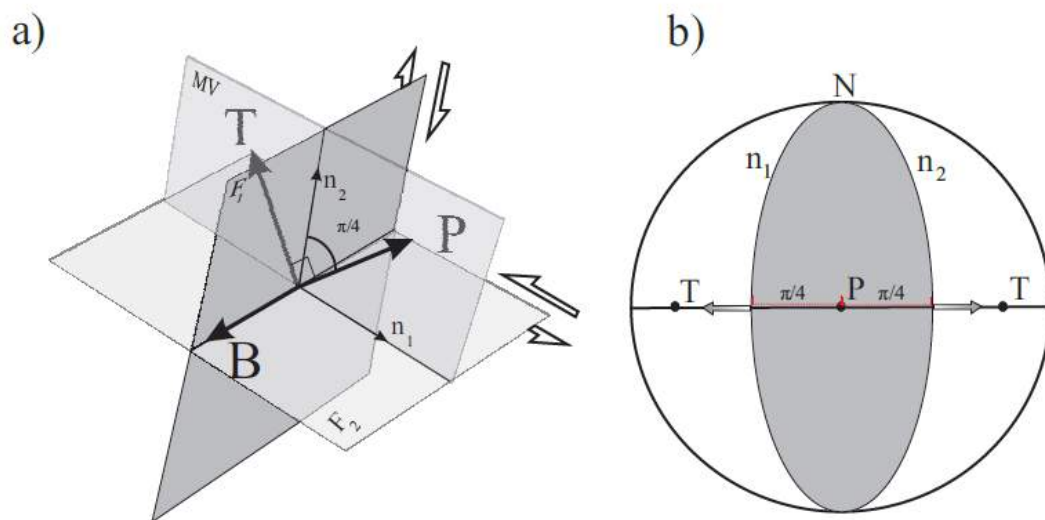


Figure 12. Focal mechanisms geometry and representation.(a) The plan of movement is noted MV , the sismological P , B , T axis are represented by black arrows, n_1 and n_2 are the normal vectors to the nodal planes F_1 and F_2 respectively. (b) A normal

fault type beach ball representation of a focal mechanism in a stereographic projection (lower hemisphere), the P T axis are noted by black points. After Arthaud (1969)

4.1.6. Stress inversion using calcite twins

Turner (1953) showed that analyzing twinning in calcite grains may lead to the orientation of the principal stresses responsible for the crystalline deformation. The possible use of mechanical twinning in calcite as an indicator of differential stresses ($\sigma_1 - \sigma_3$) has also been discussed in both a theoretical and experimental context (Friedman and Heard, 1974; Jamison and Spang, 1976; Tullis, 1980; Spiers and Rutter, 1984; Rowe and Rutter, 1990).

In the same manner as for fault slip data, introducing inverse methods to analyze calcite twinning orientations allows to determine stress tensors that satisfy the twinning criterion (Etchecopar, 1984; Lacombe et al., 1994; Laurent et al., 1981, 1990; Tourneret and Laurent, 1990). Figure 13 summarizes the geometry of calcite twinning on the *e* plane. For more details, see Cahn (1954), Carter and Raleigh (1969), Friedman (1967) and Barber and Wenk (1979).

Twinning occurs at low temperature when the applied shear stress magnitude (τ_s) reaches a threshold. Considering *e* plane of twinning and *s* the glide line (analogous to the slip along a fault), the twinning criterion is:

$$\tau_s \geq \tau_0 \quad (17)$$

where τ_0 is the shear stress threshold that is experimentally calibrated (Lacombe and Laurent, 1996; Laurent et al., 2000). Because this criterion involves the magnitude of shear stress (in the case of fault slip data, only its orientation is needed) it constrains 5 instead of 4 parameters of the stress tensor. These 5 parameters are those that define the deviatoric stress tensor.

The solution deviatoric stress tensor is required to satisfy not only Eq. (17) for each twinned planes but also:

$$\tau_s < \tau_0 \quad (18)$$

The inversion of polyphase data is addressed by a combination of dihedra and clustering methods by Nemcok et al. (1999).

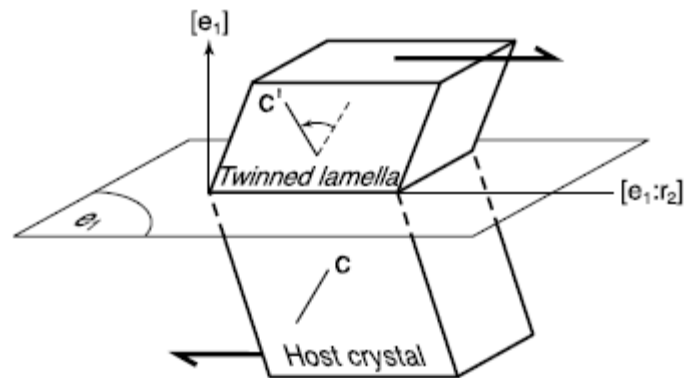


Figure 13. Geometry of twinning on the e planes in calcite. Schematic drawing of one e_1 twinned lamella. C is the optical axis, i.e. the ternary axis of symmetry of the calcite host crystal. The normal to the plane of twinning is e_1 ; the direction of twinning is $[e_1:r_2]$; the imposed sense of shear is indicated by the arrows: by convention, this sense is defined as positive. After twinning, the twinned lamella, which is generally very thin (about a portion of micron), is symmetrical of the host crystal with respect to the twin plane e_1 ; C_0 is the optical axis of the twinned lamella. Note that the optical axis ($C \pm C_0$) rotates in the opposite direction to the lamella. After Laurent et al., 2000

It is important to note that in many case studies, stress inversion using calcite twins is in agreement with fault slip analyses. In Amrouch et al. (2010), paleostress and paleostrain inversion using calcite twin results are in good agreement with similar analyses using surrounding joints and veins as well as slip measured along secondary faults throughout the Sheep Mountain Anticline fold. Homberg (2004) used similar results

from slip and calcite twins for stress inversion to constrain a forward model of the stress orientations around the Pontarilier Fault Zone active fault strands.

Also, in Lacombe (2001) and Lacombe et al. (1993, 1996a, 1996b, 2007) combination of stress inversion for slip along faults and calcite for twin has proven efficient to characterize both stress orientations and magnitudes during development of fold-thrust belts. These results tend to validate the WB based stress inversion methods.

4.2. Polyphase tectonic events

4.2.1. The polyphase data problem

Natural fractures orientation is mechanically linked to the state of stress at the time of their formation. Also, structurally complex reservoir might have undergone multiple tectonic phases over time. Each tectonic phase can be linked to a fracture set. It is therefore important to know and separate paleostress fields in order to better predict fracture orientations.

Evidence such as the reactivation of fault planes, faults with heterogeneous orientations of slip (Hardcastle and Hills, 1991) are common in nature and are not compatible with a single stress tensor. Fault-slip data that can only be explained by more than one stress tensor have been commonly called heterogeneous.

Traditional monophasic techniques can easily lead to spurious solutions, in most cases the inversion may yield an artifact stress tensor that is not really compatible with any of the homogenous subsets, but is a compromise between many subsets (Carey, 1979; Delvaux and Sperner, 2003; Hardcastle, 1989; Nemcok and Lisle, 1995; Shan et al., 2003; Sperner and Zweigel, 2010).

Figure 14 shows how the automated separation of a data set with two clusters results in three subsets, all of them representing only parts of the two clusters of the original data set. In the 2D example of Figure 14

this can easily be done by separating the data of the two clusters into different subsets. The manual separation of fault-slip data is not so straightforward.

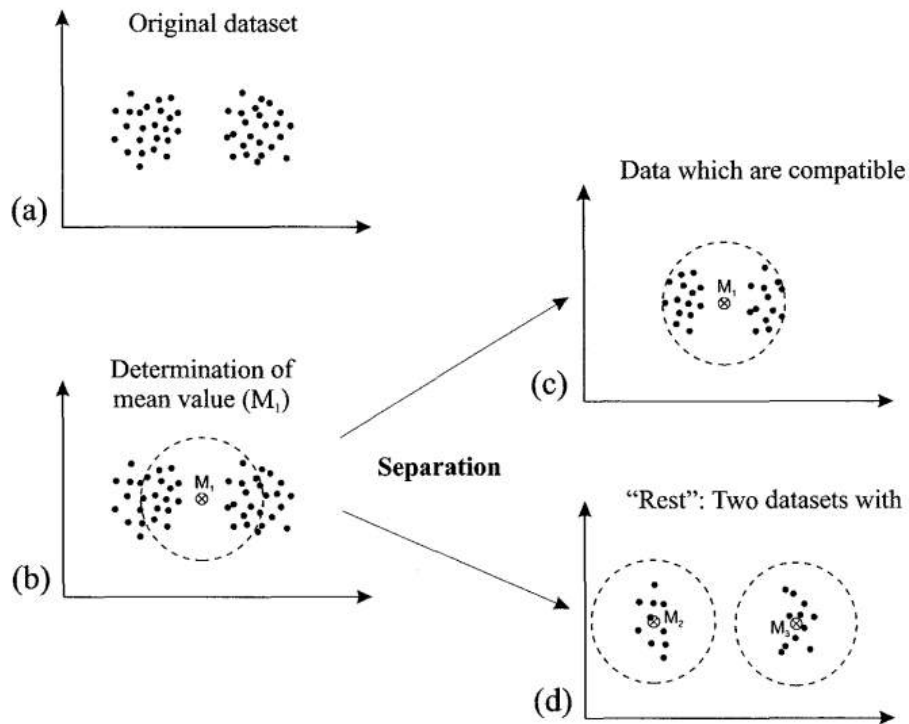


Figure 14. Separation of a synthetic dataset into subsets using an automated procedure. The original dataset (a) shows two clusters. The calculated mean M_1 (b) is a compromise between the two clusters. (c) separation of the data that fits with M_1 solution. (d) Separation of the data into two subsets according to the deviation from M_2 and M_3 . After Delvaux (2003)

4.2.2. Existing methods to separate tectonic phases

To address a clustering problem in the taxonomy field, a numerical iterative method based on dynamic cluster analysis was developed by Diday (1971) in order to separate heterogeneous set of medical data into subsets. This method was employed by Angelier and Manousiss (1980) to analyze the dynamics of faulting as it could separate fault slip data into subsets corresponding to different stress tensors.

Since then, several methods have been developed for separating stresses from heterogeneous fault-slip data, e.g. Angelier (1979a), Etchecopar et al. (1981), Armijo et al. (1982), Huang (1988) and Galindo-Zaldivar

and Gonzalez-Lodeiro (1988). A detailed analysis of most of these methods was presented by Angelier (1994). Recently, new methods, such as that based on cluster analysis (Nemcok and Lisle, 1995), the graphical procedure of Fry (1999), or the multiple inverse method (Yamaji, 2000), have been proposed for analyzing heterogeneous fault-slip data sets.

Following the tentative classification proposed by Celerier et al., 2012, we can distinguish four methodologies that have been investigated to deal with heterogeneous datasets (see Célérier et al., 2012 for a complete description):

(1) Methods that clusterize slip data by analyzing its compatibility before inversion;

(2) Methods that search stress tensors that explain a part of the dataset solely;

(3) Methods that use an altered the misfit function so that it integrates the data clustering during the minimization process;

(4) Methods that compute the stress tensor for each fault slip data and try to minimize the resulting variety of stress tensor variation.

The first category includes clustering of data that yield similar misfits with various trial stress tensors using the right-dihedral (Carey and Vergely, 1992; Mercier and Carey-Gailhardis, 1989; Nemcok et al., 1999). Another intuitive ways to separate heterogeneous data into subsets is to represent the slip data in two dimensional graphic analysis. This representation requires that one of the principal stress directions is vertical, simplifying the 4D problem into a 2D problem. Clustering can therefore be achieved using the γ -R method of Simón-Gómez (1986), or the spherical plot version (Fry, 1992), or its superposition of a modified Breddin's graph to a rake versus strike plot of the data (Célérier and Séranne, 2001).

In the second category, one of the earliest and simplest approaches is to compute the misfit function solely for the subsets (of size N) with the smallest misfits, with N usually chosen as a percentage of the data

(Etchecopar, 1984; Etchecopar et al., 1981). A more recent approach is to clusterize the data into subsets of size N and systematically run stress inversion (Yamaji, 2000). A third approach is to spot the stress tensors that minimize the misfit below a chosen threshold for N data (Etchecopar, 1984; Etchecopar and Mattauer, 1988; Hardcastle, 1989; Hardcastle and Hills, 1991; Vasseur et al., 1983; Yamaji, 2003).

In the third category, a misfit function that reduces the influence of outliers is used (Gephart and Forsyth (1984); Etchecopar and Mattauer (1988); Gephart (1990a,b); Yamaji (2000); Angelier (2002a,b); Will and Powell (1991), Delvaux and Sperner (2003) , Yamaji (2003)). A similar, yet radical approach to reduce the influence of a large subset of outliers that are related to secondary phases, is to modulate the misfit criteria by a function that cuts it when it becomes large (Angelier, 1979a, 1984, 1991a; Angelier and Manoussis, 1980, Yamaji, 2003), or in the hard division scheme of Shan et al. (2003, 2004), or a Gaussian Function (Zalohar and Vrabec, 2007).

The fourth category is similar to the γ -R method (Simón Gómez, 1986). It consists on exploring stress tensor orientations for each slip data and to compute the stress ratio R so that it matches the observed slip direction. Therefore, the solution tensors are those with the least variation on a subset of the data (Armijo and Cisternas, 1978; Armijo et al., 1982; Galindo-Zaldívar and González-Lodeiro, 1988; Phan-Trong, 1993).

Liesa and Lisle (2004) and Lisle and Vandycke (1996) compared multiple polyphase methods (applied the γ -R, the dihedral, the direct inversion (Angelier and Goguel, 1979; Sperner et al., 1993), as well as Etchecopar et al. (1981), Nemcok and Lisle, (1995), and Yamaji's (2000) methods) on the polyphase Ogmire data set. They showed that these methods may lead to spurious solutions as well as artifact stress tensors. Following Angelier's (1984), Delvaux and Sperner's (2003), and Sperner and Zweigel's (2004) opinion, they suggest that the geologist expertise is critical and that relying on automatic polyphase methods only is likely to be unsuccessful.

Although several numerical methods have been used for clustering fractures orientations (Shanley and Mahtab, 1976; Pecher, 1989; Hammah and Curran, 1998; Peel et al., 2001) and paleostress for dikes and veins using a Bingham distribution (Yamaji and Sato, 2011) or calcite twins using the right-dihedra clustering method (Nemcok and Lisle., 1995) have been used, these methods have not yet been used on heterogeneous data with multiple fracture types (as observed in nature) especially when the fracture mechanical type is undefined.

4.3. Methods based on geomechanics

4.3.1. Least squares formulation (Kaven et al., 2011)

Kaven et al. (2011) proposed a new method based on Poly3D (Thomas, 1993; Maerten et al., 2014) that incorporates the effects of mechanical interaction of the entire fault or fault system, and solves the complete mechanical problem. The method requires knowledge of the fault geometry and information on at least one slip vector component along portions of the known fault geometry. However, when all planes are of similar orientation one may expect singularities (wrong stress values), making the Kaven et al. (2011) method spurious (Lovely et al., 2014). Also, stress inversion using Kaven et al. (2011) method is limited to the use of slip data only since the involved equations are expressed along active fault planes solely. Consequently, observed data other than fault slip, cannot be taken into account, which in the case of fracture modeling, is a critical limitation.

4.3.2. iBem3D (Maerten et al., 2014)

To address the lack of geomechanical modeling in geological simulations, Maerten et al. (2010), Maerten (2010) and Maerten et al. (2014) developed iBem3D (former Poly3D initially developed by Thomas (1993)), a numerical tool based on innovative iterative 3D BEM.

In addition Maerten (2010, Ch.9), Maerten and Maerten (2011) and Maerten et al. (2015) have developed a new generation of paleostress analysis using iBem3D technology that solves the main

limitations of the Kaven et al. (2011) method and allows the use any kind of deformation data (slickenlines, joints and veins, shear fractures, deformation bands and faults, stylolites and compaction bands, inSAR data, GPS data, fold hinges,...). This method runs thousands of simulations covering the range of all possible tectonic stress configurations. Then, for each simulation, it compares attributes of the modeled stresses with the observed slip orientation or fracture geometry. Finally, the simulations that give the best fit with observed fracture data, can be analyzed, sorted and selected. Because of its versatility, ease of use and fast computing capabilities, I used iBem3D method in this thesis as the reference geomechanical stress inversion method that is described below under the Methods section.

So far, iBem3D models use an elastic, homogeneous, and isotropic media. Although heterogeneity between geological layers can be added at the cost of much lower performances, iBem3D does not allow to model different mechanical behaviors such as plasticity and viscosity. Therefore, the deformation close to the fault into the damage zone or within fault drags, in areas where stress concentration exceeded the plastic threshold, or, near deformation occurring at high depth, will not be modeled with iBem3D.

Another limitation is that since fractures are not systematically linked to active faulting, the use of fracture data to constrain a BEM-based stress inversion cannot not always be applicable. Indeed, natural fractures can be formed in a continuous media with no active faults, and some fracture clusters can be related to folding, elastic rebound or even the overburden induced stress.

5. Methods (after Maerten et al., 2014)

Most analytical solutions to continuum mechanics problems are limited to simple geometries. To solve problems with more complex geometries, computer-aided numerical methods have been developed. These methods can be categorized into two main types: differential methods and integral methods. The finite element method (FEM) is a differential method that was developed in the 1950's and is one of the most

commonly used numerical methods today. Since its development, other differential methods, including the boundary element method (BEM), have been developed to solve different types of problems.

Among the available numerical methods (e.g., Finite Element Method, Distinct Element Method, Finite Difference, ...), we chose the Boundary Element Method (BEM) as it simplifies the model building and is free from boundary effects.

5.1. iBem3D - iterative boundary elements method

iBem3D is a C++ and modular 3D boundary element computer program based on the theory of angular dislocations for modeling three dimensional (3D) discontinuities in an elastic, heterogeneous, isotropic whole- or half-space. For 20 years it has been used in 150 scientific publications, here we present the basic formulation of the method, how it has been enhanced as well as some important applications. A full description of the formulation is found in Maerten et al. (2014).

The main advantage of using this formulation, for describing geological objects such as faults, resides in the possibility of modeling complex geometries without gaps and overlaps between adjacent triangular dislocation elements, which is a significant shortcoming of models using rectangular dislocation elements. Industrial applications include subseismic fault modeling, fractured reservoir modeling, interpretation and validation of fault connectivity and reservoir compartmentalization, depleted area and fault reactivation, and pressurized wellbore stability. Academic applications include earthquake and volcano monitoring, hazard mitigation, and slope stability modeling.

iBem3D calculates the displacements, strains, and stresses in an elastic whole- or half- space by planar triangular-shaped elements of displacement discontinuity. These elements are constructed by superposition of angular dislocations following the method described by Jeyakumaran et al. (1992), and later by Thomas (1993). The elastic fields around the elements are derived from the solution for a single angular dislocation in an elastic half-space or whole-space (Yoffe, 1960; Comninou and Dundurs, 1975). A triangular element

may represent some portion of a fracture or fault surface across which the discontinuity in displacement is approximately constant. Several triangular dislocation elements can be used to model faults or fractures, some can even be joined to form a closed surface that may represent either a finite elastic body or a void in an otherwise infinite or semi-infinite elastic body. This superposition provides the means to model complex 3D geological structures with boundaries and shapes that are not possible to model effectively with the rectangular surface that has been extensively used in dislocation modeling of faults and fractures in the earth (Okada, 1985, 1992). Attempts to model curved surfaces with rectangular elements, except in the simplest cases, result in gaps and overlaps. In contrast, Figure 15 shows how a complex 3D fault surface can be approximated using triangular elements with no gaps or overlaps. The discretization of a 3D fault surface into triangular boundary elements allows the construction of a surface with any desired tipline and shape. Boundary conditions (i.e., constant displacement over each element or tractions at the center of each element) are prescribed according to the local coordinate system attached to the element (Figure 15). Additionally, remote stresses and/or strains can be prescribed. Output at observation points (black dots in Figure 15) can be displacement, strain, stress, principal strain and principal stress (Figure 15).

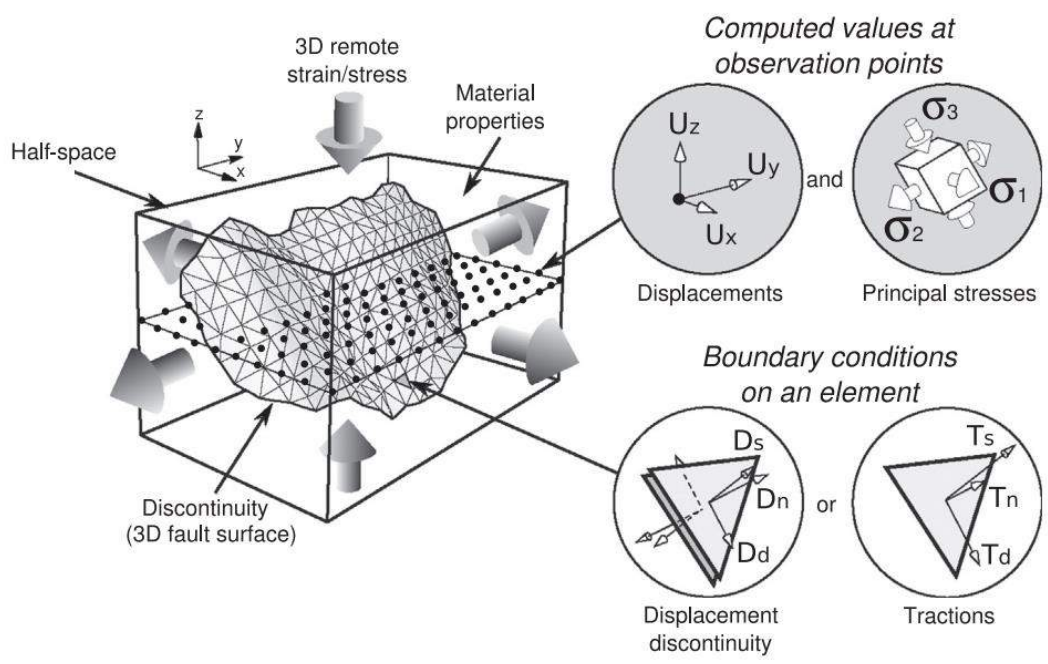


Figure 15 Construction of a complex fault geometry using triangular elements and schematic representation of a surrounding observation grid. Boundary conditions on triangular elements are a combination of displacement and traction defined in the element coordinate system. The element coordinate system is such that the x- and y-axes are along the dip- and strike-directions, respectively. The z-axis is aligned with the normal of the element. At each observation point, displacement, strain, and stress can be computed as a post process. Also shown is the 3D remote strain or stress. After Maerten et al., (2014).

5.1.1. Far field stress/strain

Boundary conditions are prescribed for each triangular element of the model based upon the stress field, σ^R , that exists throughout the rock mass before any slip or opening of the elements. This remote stress is applied to the model by prescribing boundary conditions that are the tractions resolved from this remote stress on the elements using Cauchy's formula (Eq. 10). Then, one uses (Eq. 19) to solve the system.

$$\{\mathbf{t}\} = [\mathbf{T}]\{\mathbf{b}\} \quad (19)$$

where $\{\mathbf{t}\}$ is the column of the initially prescribed traction vectors, $[\mathbf{T}]$ is a dense matrix of traction influence coefficients, and $\{\mathbf{b}\}$ is the column of the unknown Burgers vectors.

Given the far field remote stress, σ^R , and the normal n of an element, e , the initial traction for this element is given by $\mathbf{t} = -\sigma^R \mathbf{n}$. Therefore, the initial traction boundary vector for a given element opposes the prescribed resolved far field stress onto this element, leading to equilibrium. If a remote strain, ϵ^R , is prescribed, one first calculates the corresponding remote stress, σ^R , using Hooke's law and then proceeds as above.

5.1.2. Research applications

Teaching

Computational science methods are often used to investigate and illustrate complex geological phenomena. To provide geology students with opportunities to both visualize and explore such phenomena,

several teachers among them Dr. Linda Reinen (2008) and Dr. Michele Cooke have incorporated the program Poly3D/iBem3D into their undergraduate Structural Geology course.

Fracture mechanics

A major and straightforward use of elastic dislocations is to study fracture mechanics. Since its first version, the program has been used to understand the mechanics of (i) natural fault propagation (Willemse and Pollard, 2000), (ii) echelon normal fault arrays (Willemse et al., 1996; Willemse, 1997; Crider, 2001), (iii) intersecting faults (Maerten et al., 1999; Maerten, 2000), (iv) secondary fracture development (Martel and Boger, 1998; Kattenhorn et al., 2000; Bourne and Willemse, 2001; Soliva et al., 2010), (v) orthogonal cross joints (Bai et al., 2002) (Figure 16), and (vi) normal fault linkage (Crider and Pollard, 1998) and spacing (Soliva et al., 2006).

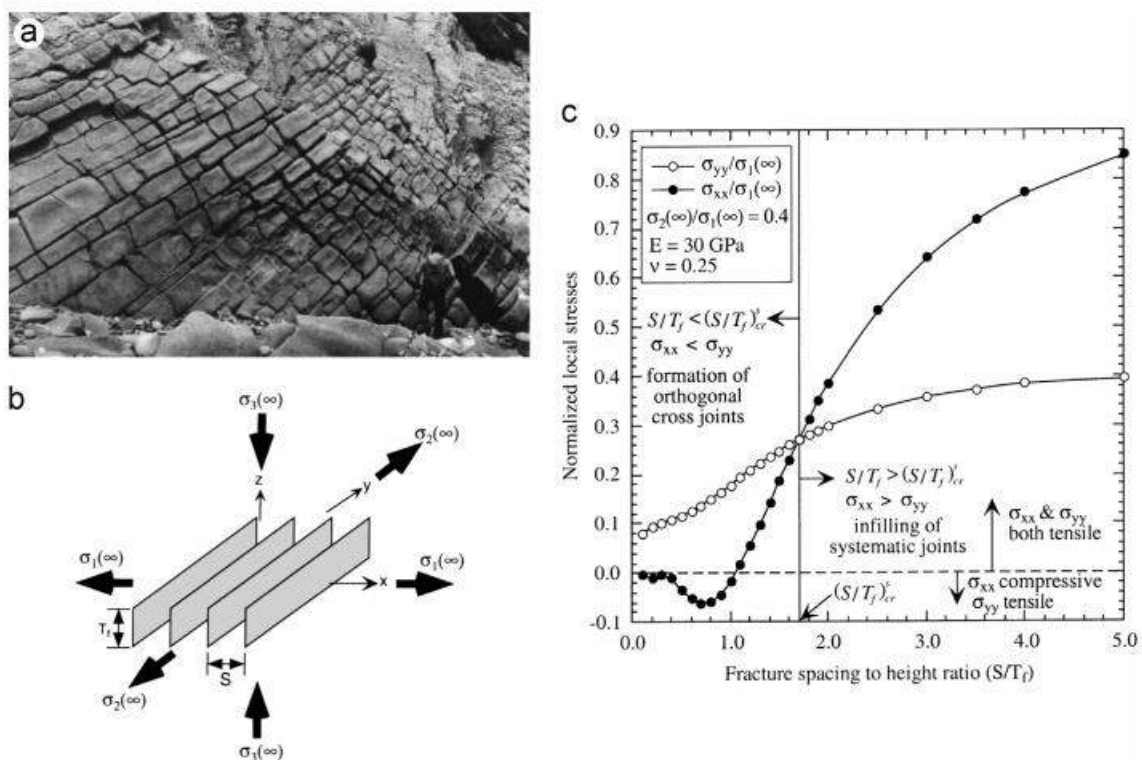


Figure 16. (a) Orthogonal cross joints in a steeply inclined carbonate bed from the Monterey Formation, California. (b) Model configuration with four fractures of the same dimension placed in the whole space of homogeneous, isotropic, and elastic

medium. (c) Results of local stress switch between adjacent equally spaced fractures. The sign convention used here is that tensile stresses are positive and compressive stresses are negative. Figure modified from Bai et al. (2002)

Structural geology

Understanding geological structures and processes normally requires the combination of geological observations from outcrop, core, air photographs, or industry data such as seismic reflection data, with idealized numerical models of rock deformation based on continuum mechanics. Elastic models are often used because they are computationally simple and adequately explain some deformation observed in nature. For instance, faults are modeled as 3D surfaces of displacement discontinuity in a homogeneous, isotropic, linear elastic material. This provides a first-order understanding of how faults accommodate slip, interact, concentrate stress, and deform the surrounding rock mass. Perhaps of greatest importance is the fact that the solutions to the elastic boundary value problem comply with Newton's laws of motion, and they have an explicitly defined constitutive law relating stress and strain in three dimensions. Therefore, geologists have used the program to understand observed geological structures such as fault-related folding and associated secondary fractures (Savage and Cooke, 2003; Bellahsen et al., 2006; White and Crider, 2006; Allward-Fiore, 2006; Mynatt et al., 2007; Shackleton and Cooke, 2007; Hilley et al., 2010), deformation associated with thrust faults (Griffith and Cooke, 2004; Olson and Cooke, 2005), strike-slip faults (Brankman and Aydin, 2004), and normal faults (Resor, 2003; Grant and Kattenhorn, 2004; Soliva et al., 2008; Marshall and Cooke, 2008; Meigs et al., 2008). Figure 17 illustrates how mapped displacement profiles along overlapping faults in Vallo di Diano, Italy, have been geomechanically reproduced using linear elasticity (Soliva et al., 2008).

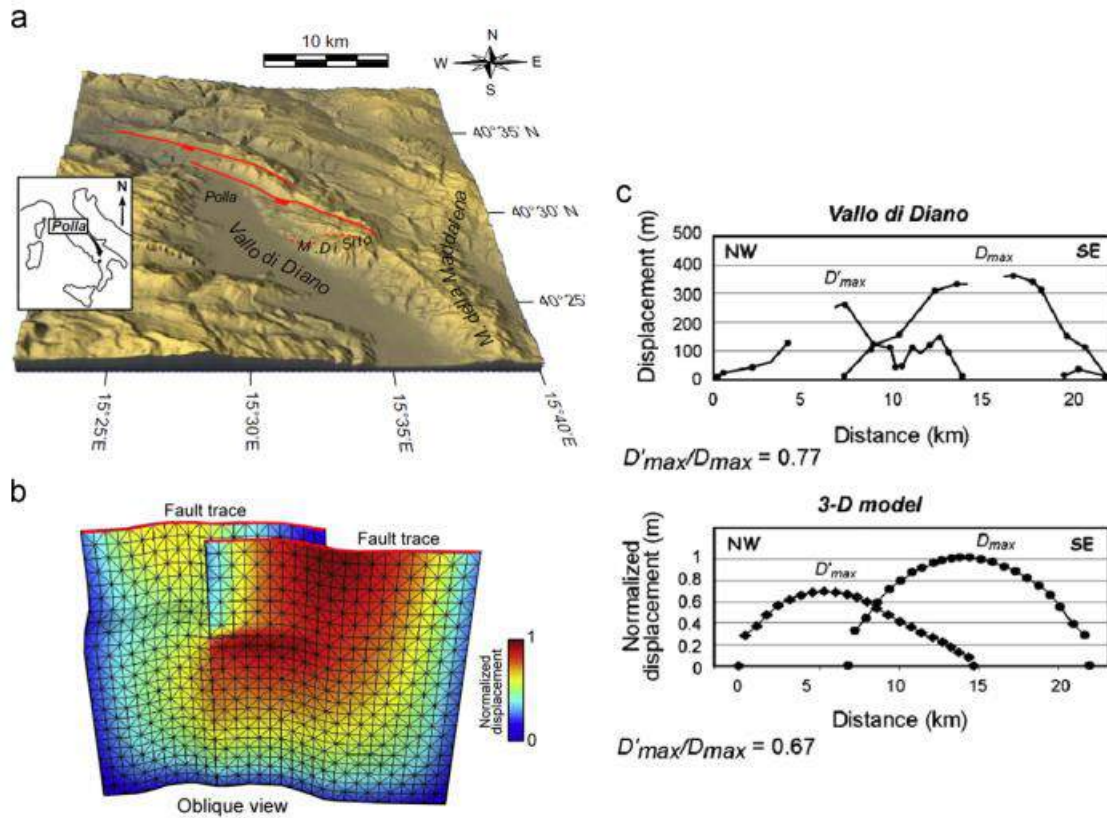


Figure 17 (a) Location and overview of the Vallo di Diano segmented normal fault zone on a digital elevation model. The overlapping normal fault segments are mapped with red lines at the base of the fault scarps. (b) 3D view of the fault surface, the mesh used in the model, and computed displacement distribution. (c) Comparison between Earth's surface scarp topography profiles and displacement computed at the surface in the model. Figure modified from Soliva et al. (2008).

Active tectonics and earthquakes

The increasing availability of spatially rich geodetic data, specifically dense GPS networks and InSAR, offers researchers opportunities to construct increasingly complex geometric and kinematic models of earthquake ruptures. These high-quality data now available to geophysicists and geologists are not fully exploited in forward and inversion procedures when using geomechanical methods based on rectangular dislocation segments (Okada, 1985; Johnson et al., 2001; Jónsson et al., 2002). Indeed, these methods, which tend to oversimplify fault geometries, can lead to inconsistencies when inverting for slip on earthquake faults, and they preclude a more complete understanding of the role of fault geometry in the earthquake

process. With the use of angular dislocations (Comninou and Dundurs, 1975; Thomas, 1993; Maerten et al., 2005), discontinuities can be discretized into triangular elements allowing for the construction of 3D fault surfaces that more closely approximate curvilinear surfaces and curved tiplines without introducing overlaps or gaps, consistent with the full extent of available data. The strengths of this method have been successfully demonstrated for (i) simulating stress transfer from one rupture to nearby faults (Price and Bürgmann, 2002; Muller et al., 2003; Muller and Aydin, 2004; Muller et al., 2006), (ii) modeling stress distribution around active faults (Fielding et al., 2004; Lovely et al., 2009; Fielding et al., 2009), (iii) appraising different rupture geometries (Rigo et al., 2004; Muller and Aydin, 2005; Akoglu et al., 2006; Marshall and Cooke, 2008; Dair and Cooke, 2009), (iv) modeling rupture slip distribution (Burgmann et al., 2000; Schmidt et al., 2005; Kreemer et al., 2006; Zhang et al., 2008; Cheng et al., 2009), and (v) using slip inversion to model coseismic deformation associated with recent earthquakes as illustrated in Figure 18 (Maerten et al., 2005; Resor et al., 2005; Cakir et al., 2006).

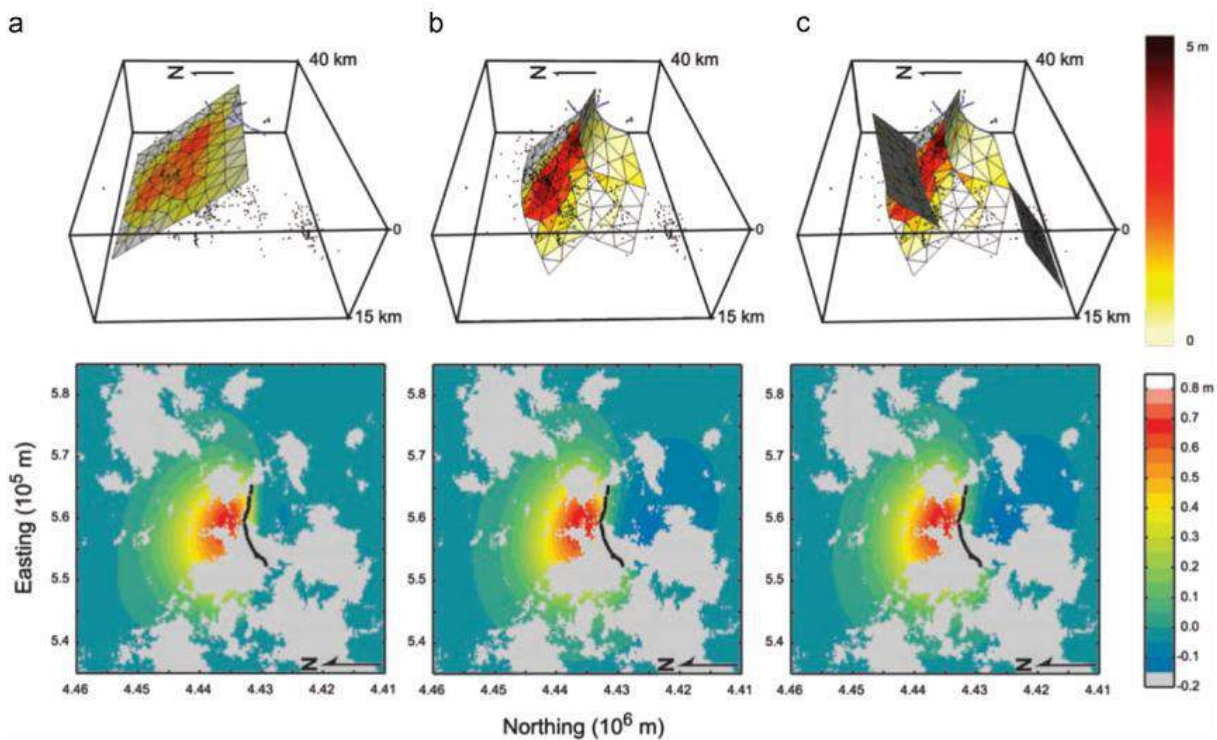


Figure 18. Inversion results of the 1995 Kozani–Grevena earthquake, Greece, for three models: (a) the best-fit planar model from nonlinear inversion, (b) a three-fault model including major fault segments interpreted from aftershock hypocenters and surface ruptures, and (c) a five-fault model including two antithetic faults also interpreted from aftershock distributions. For each model, two images are presented: (top) an oblique view of the model looking toward the east with the slip distribution calculated from linear inversion of InSAR data, aftershock hypocenters, and surface rupture traces; (bottom) the results of the forward model illustrating predicted surface deformation (range change) with areas of no InSAR data in gray. Figure modified from Resor et al. (2005).

Volcanos

Swelling or collapse of volcanos is often related to magma migration within and outside the magma chamber. Therefore, analyzing the ground surface deformation along the flanks of volcanos over time can provide very good insight on the potential eruptions. GPS networks, InSAR data, and microseismic data are commonly used to study volcanic activity. Similarly, the same geomechanical tools based on elastic dislocation can be used to model magma activity and potential interaction with nearby faults or dikes as illustrated in Figure 19 (Cailleau et al., 2007; Diez et al., 2005; Klügel et al., 2005; Lundgren and Lu, 2006; Walter and Amelung, 2006, 2007; Walter, 2007; Yun et al., 2006).

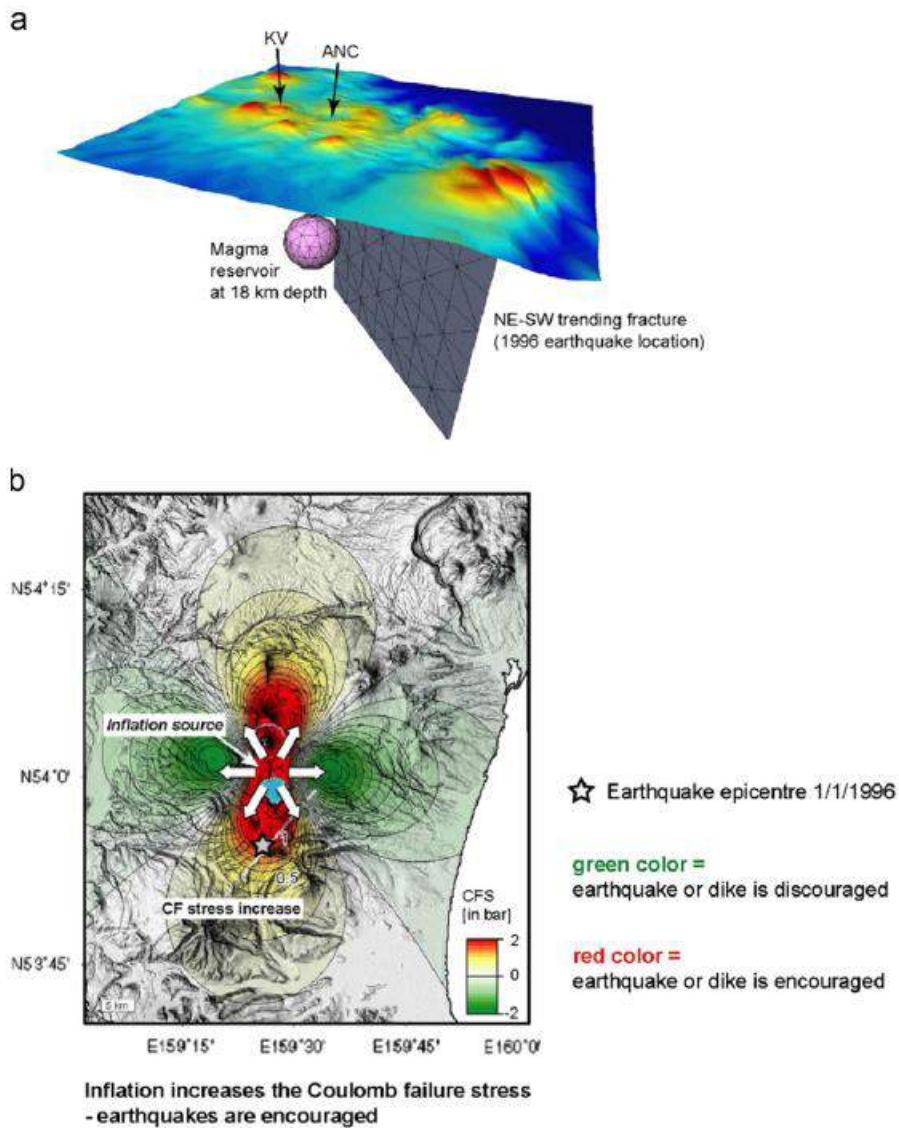


Figure 19. 1996 Earthquake-eruption sequence at the Karymsky Volcanic Group, Kamchatka. (a) Numerical model construction. Perspective view of the boundary element model setup. (b) Modeling results. Model simulation of inflation of a deep magma reservoir. Coulomb failure stress change (CFS) calculated at faults parallel to the NESW (N040) fracture system (red ¼ faults brought closer to failure, indicating CFS increases; green ¼ CFS decreases). Faulting is triggered in exactly the area of the 1996 earthquake main shock. Inflation therefore triggered this earthquake. Figure modified from Walter (2007).

5.1.3. Industry and engineering applications

Subsurface fault interpretation

Complex geological structures, where the interpretation of faults is challenging because high-quality images cannot be obtained, are known to be potentially good hydrocarbon reserves. As an example, spatial continuity and linkage of faults may substantially affect fluid flow either by compartmentalizing the reservoir or by increasing the tortuosity of flow pathways, whether the faults act as seals or conduits. In such context, it is essential to check the consistency of the subsurface structural interpretations as they will improve reservoir flow simulation models and, in turn, significantly reduce the number of wells required to drain reserves. Maerten (1999) and Maerten et al. (2000) demonstrate how geomechanical models based on elastic dislocation can be applied to improve the subsurface interpretation understanding and obtain more realistic reservoir models. They have developed a method to infer, in three dimensions, the fault tipline geometry below the seismic resolution as well as potential fault linkage. A 3D numerical model of the faulted reservoir and its surroundings is constructed using seismic interpretation. Such a model, combined with an appropriate set of boundary conditions, is used to compute the fault slip distribution as well as vertical displacement field. By comparing the interpreted fault slip distribution with the computed slip distribution adjacent to potential intersection lines, the geomechanical models can constrain the geometry of the faults as well as the location of the intersection line between faults (Figure 20). The interpreted structure contour map and theoretical displacement field also are compared to constrain the fault geometry.

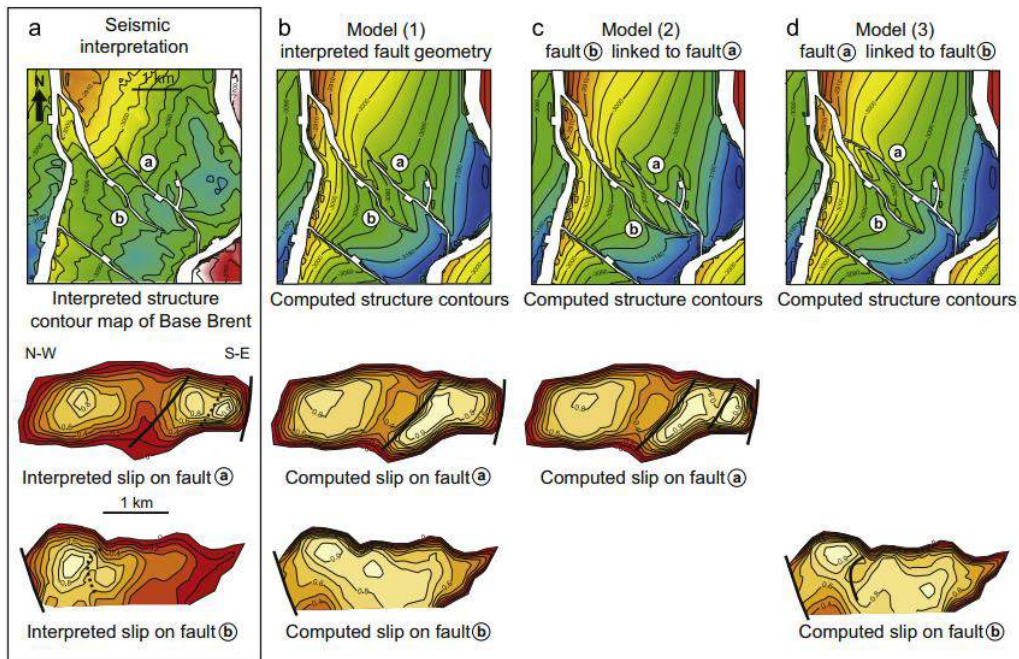


Figure 20. Analysis of the Oseberg reservoir compartmentalization, northern North Sea. (a) Interpreted structure contour map and normalized contoured slip distribution on faults a and b. (b) Computed vertical displacement field and normalized slip distribution on faults a and b from a first model using the interpreted fault geometries. (c) Computed values from a second model using fault b linked to fault a. (d) Computed values from a third model with fault a linked to fault b. Qualitative and quantitative comparisons suggest that fault b is likely to be linked to fault a. Figure modified from Maerten (1999).

Subsurface small-scale fracture modeling

Natural fractures such as small-scale faults and joints are known to be capable of significantly altering the flow of hydrocarbons, either during the migration from the source to the reservoir rock or during production of the reservoir. Therefore, understanding and quantifying the spatial and temporal development of these features, as well as their properties (e.g., geometry, throw, aperture, permeability, etc.), can have great economic impact on the recovery of natural reserves. During the past 10 years, to address these economic issues, methods based on elastic dislocation have been developed. These methods take into account the mechanical concepts and the fundamental physical laws that govern fracture development in order to realistically model the spatial and temporal development of structural heterogeneities. It consists on calculating the stress distribution at the time of fracturing, using the available

reservoir structure data – such as faults, fractures, folds – and rock properties and the tectonic setting that can be characterized by stress or strain magnitude and orientation. Then, the calculated stress fields, perturbed by the main structures, combined with rock failure criteria are used to model natural fracture networks (i.e., type, orientation, location, and spatial density). Applications to both outcrops (Kattenhorn et al., 2000; Bourne and Willemse, 2001; Davatzes et al., 2005) and reservoirs (Maerten et al., 1999; Maerten, 1999; Bourne et al., 2000; Maerten et al., 2002, 2006) demonstrate how geomechanics can provide a high degree of predictability of natural fracture networks. Both Igeoss Poly3D and iBem3D have been successfully applied to model subseismic faults (Maerten,1999; Maerten et al., 2006) in northern North Sea highly faulted reservoirs (Figure 21) as well as undetected joints in naturally fractured carbonate reservoirs (Bourne and Willemse, 2001).

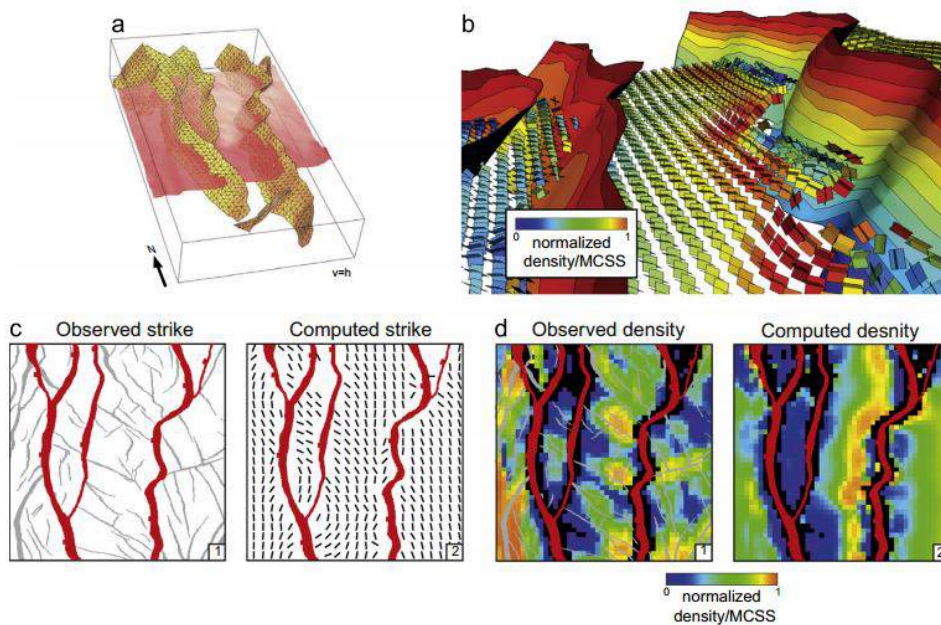


Figure 21 Subseismic fault modeling of the Oseberg reservoir, northern North Sea. (a) 3D view of the model mesh made of triangular elements. Base Brent horizon (red) used as observation surface. (b) 3D visualization of the predicted failure planes at observation points. Conjugate planes represent the two Coulomb failure planes color coded by the magnitude of the normalized MCSS. (c) Comparison between observed and computed fault strike. (1) Fault map. (2) Computed fault strike using the major approximately north–south (gray) faults and a remote loading with a N80E direction of extension. (d) Comparison between observed and computed fault densities. (1) Density of the observed Upper Jurassic (black) faults. (2) Computed fault density. All densities are normalized. Figure modified from Maerten (1999).

Perturbed stress field and fracture reactivation

Fracture reactivation can have a significant effect on flow properties. The two main factors that allow quantitative modeling of fracture reactivation are the geometry of preexisting natural fractures and the present day stress fields. The latter can have different origins but it is always caused by local deformation such as the one observed around active faults, cavities, wellbores, and salt formations for instance. As a direct application of elastic dislocation, Tamagawa and Pollard (2008) show that in the Yufutsu field, Japan, nonproductive wells were drilled in the area where the regional stress state prevails, and the most productive well penetrates the area near the tips of active faults, where stress concentrations lead to enhancements of permeability by opening or shearing of fractures.

Risk assessment

The design of roads, dams, tunnels, and underground repositories to safely store waste requires the conservative assessment of risks that landslides, fracture reactivation, and earthquakes might pose. With that in mind, researchers and engineers have efficiently used geomechanics and elastic dislocation to study landslides from a theoretical aspect (Martel, 2004) and to evaluate slope instability of the Corinth Canal, Greece, that resulted from nearby fault activation (Tselentis and Gkika, 2005). Over the past decade, Igeoss Poly3D and iBem3D have been used to evaluate the potential risk of fracture reactivation over time, during glacial loading and unloading cycles, at the Olkiluoto high-level nuclear waste repository site, Finland (La Pointe et al., 2002; Soliva et al., 2010).

5.1.4. Latest enhancements

Heterogeneous material

Solutions for heterogeneous elastic materials can be formulated using triangulated interfaces between regions (Maerten and Maerten, 2008). An interface is defined as a doubly triangulated surface (one for each region), perfectly coincident but with opposite normals. Each region is characterized by a homogeneous and isotropic material but the elastic moduli may be different in each. The interface between two different regions transmits the mechanical influence of one region on the other by computing the corresponding Burgers vectors for two adjacent elements on the interface using continuity and equilibrium conditions prescribed in the global coordinate system:

$$\begin{cases} u_1^- = u_2^- & (\text{continuity conditions}) \\ t_1 + t_2 = 0 & (\text{equilibrium conditions}) \end{cases} \quad (20)$$

In (20), u_1^- and t_1 , part of region 1, represent the displacement computed on the negative side of each element and the traction, respectively. This formulation leads to separate models for each region that are linked through the continuity and equilibrium conditions at the interface (Maerten and Maerten, 2008). Heterogeneous materials will not be used in this thesis as it is expensive in terms of computation time.

Friction and non-interpenetration

Friction and non-interpenetration present a subset of inequality constraints on traction and displacement, respectively, for the general contact problem in mechanics. While solving such problems, different algorithms can be used to incorporate these constraints. The most popular ones are the Lagrange multipliers, the penalty method and the complementarity problem (Wriggers, 2002). However, these methods incorporate either new equations into the system, artificial parameters, or the necessity to explicitly construct the system matrix. In Maerten et al. (2010), we used another technique based on successive corrections of the solution. Compared with other techniques of contact management, this new

simple methodology, which does not use any incremental trial and error procedure, brings more flexibility and makes the system more stable and less subject to round-off errors, without significant computational overhead. The incorporation of inequality constraints on traction and displacement now extends the existing wide range of applications of iBem3D. For example, static friction can be used to model the cohesive end zone (CEZ) (or zones of increased frictional strength) of a fault (Martel, 1997; Davatzes and Aydin, 2003; Cooke, 1997), where greater friction reduces slip so that a (nonphysical) infinite stress state is avoided. This enhancement also can be used to study frictional behaviors when faults or opening fractures approach interfaces separating regions of different material properties (Maerten and Maerten, 2008), or to understand the role of static friction on fracture orientation in extensional relays along strike-slip faults (Soliva et al., 2010).

Linear slip inversion

Retrieving the slip distribution on 3D faults, given measurements of ground displacements (e.g., from global positioning system (GPS) or synthetic aperture radar interferometry (InSAR)), associated with tectonic events such as earthquakes is of great interest. 3D indirect boundary element methods are a good candidate for the inversion. Usually, a weighted least-squares approach combined with a Tikhonov regularization is used (Johnson et al., 2001; Maerten et al., 2005). Then, the system has to be solved with a constrained solver to reach a realistic solution. Constraints allow the slip components to be inverted to be either negative or positive. In Maerten et al. (2005), they extend the forward formulation to linear slip inversion and show that using such a formulation is more precise than using rectangular elements (Okada, 1985). For instance, gaps and overlaps between adjacent elements, which lead to numerical artifacts, do not exist on triangulated discontinuities. Consequently, this technique more precisely captures information close to the fault elements.

Optimization

Because the interface is decomposed into pairs of perfectly coincident discontinuities with opposite normal, the number of unknowns when working with heterogeneous materials grows rapidly. As a result, solving the system of equations requires a huge amount of memory to store the dense system matrix, and a long computation time. Furthermore, post-processing at observation points can require lengthy computational time. Maerten (2010a) described the H Matrix (Hackbusch, 1999) combined with the adaptive cross approximation (Bebendorf, 2000; Bebendorf et al., 2008; Bebendorf and Rjasanow, 2003) to significantly reduce the memory needed to store the dense matrix and the time needed to solve the system of equations. This technique is also applied to the postprocessing at observation points, drastically decreasing the computational time. Furthermore, Maerten (2010a) shows that this optimization can easily be parallelized on multicore architectures.

5.2. *BEM-based stress inversion method*

In typical forward model problems, the equilibrium equations are solved using the applied remote stress, yielding the slip distributions over the model faults and the resulting local stress, strain, and displacement fields around the model faults (e.g. Pollard et al., 1993; Burgmann et al., 1994; Willemsse et al., 1996; Maerten et al., 1999; Madden et al., 2013). The fault geometries are explicitly defined and boundary conditions are prescribed in terms of tractions or displacement discontinuities. For example, Anderson (1942) calculates and interprets the stress perturbations near a model fault using the solution of Inglis (1913) for a highly eccentric elliptical hole in an elastic plate. Maerten et al. (2002) use mechanical models based on the boundary element method to study the relationship between secondary faults and the perturbed stress due to slip along larger, primary faults in the North Sea.

However, the main unknown for such forward model problems are the paleo tectonic stresses that need to be applied to the model. It is always difficult to estimate both the orientation and the relative magnitude of these tectonic stresses. In addition, calibration with available fault slip data and/or fracture data measured along wellbore for instance, is often time consuming as the process is not automatized. We are

thus often tempted to neglect that part of the process by guessing the paleo tectonic stresses and not fully using on available data.

To fill this important gap we have developed a new generation of paleostress analysis using iBem3D technology, which is an extension of Maerten et al. (2015) for focal mechanisms but using fracture data. The theoretical steps to recover paleo tectonic stress are to run thousands of simulations covering the range of all possible tectonic stress configurations. Then, for each simulation we compare the modeled slip vector with observed slickenlines along faults or attributes of the modeled stresses with the observed fracture characteristics. Finally, we analyze, sort and select the simulations that give the best fit with observed data. However, three main problems need to be solved in order to make the technique valuable: (i) The dimension of parameter space for covering the range of all possible tectonic stress configurations needs to be decreased, (ii) the computation time must be optimized as running thousands of geomechanical simulations would take days and (iii), the analysis of the results must be efficient and automatized.

A model composed of multiple fault surfaces is subject to a constant and uniform remote stress tensor, σ_R .

According to Lisle et al. (2006) and as predicted by Anderson (1951), one of the principal stress directions must be vertical. therefore, the resolved shear tractions on faults if they are allowed only to slip (i.e., no volume change), σ_R is defined such as:

$$\sigma_R = R_\theta \begin{bmatrix} \sigma_h - \sigma_v & \\ & \sigma_H - \sigma_v \end{bmatrix} R_\theta^T \quad (21)$$

Here, R_θ is the rotation matrix around the vertical axis (clockwise) with $\theta \in [0, \pi]$, σ_H and σ_h are the magnitudes of maximum and minimum horizontal compressive stress oriented with respect to the y-axis (North), and σ_v is the vertical stress.

Using σ_1 , σ_2 and σ_3 while continuing to assume an Andersonian faulting regime with one vertical principal stress, factoring with $(\sigma_1 - \sigma_3)$, and introducing the stress ratio $R = (\sigma_2 - \sigma_3) / (\sigma_1 - \sigma_3) \in [0,1]$, (21) becomes:

$$\sigma_R = \begin{cases} (\sigma_1 - \sigma_3)R_\theta \begin{bmatrix} -1 & \\ & R - 1 \end{bmatrix} R_\theta^T & \text{for normal regime} \\ (\sigma_1 - \sigma_3)R_\theta \begin{bmatrix} -R & \\ & 1 - R \end{bmatrix} R_\theta^T & \text{for wrench regime} \\ (\sigma_1 - \sigma_3)R_\theta \begin{bmatrix} R & \\ & 1 \end{bmatrix} R_\theta^T & \text{for reverse regime} \end{cases} \quad (22)$$

Because the stress ratio R varies from 0 to 1 for the three tectonic stress regimes, we define, for practical reasons, the stress ratio \bar{R} such as:

$$\begin{cases} \text{Normal } \bar{R} = R \in [0,1] \\ \text{Wrench } \bar{R} = 2 - R \in [1,2] \\ \text{Reverse } \bar{R} = 2 + R \in [2,3] \end{cases} \quad (23)$$

Here, depending on which of the principal stresses is vertical, we can cover the normal, wrench and reverse regimes with $\sigma_v = \sigma_1$, $\sigma_v = \sigma_2$ and $\sigma_v = \sigma_3$ respectively, with only one parameter that varies from 0 to 3 continuously. The orientation θ of the maximum principal horizontal stress defined clockwise from North is also tested. Consequently, any Andersonian remote stress is now entirely defined by the two parameters, θ and \bar{R} .

5.2.1. Principle of superposition

The key idea of the technique is to reduce the computation time using the principle of superposition (Brillouin, 1946), a well-known principle in linear elasticity. It allows recovering the displacement, strain and stress at any observation point P using pre-computed specific values from three linearly independent simulations. This principle stipulates that a given value σ^t can be entirely determined by a linear combination of independent solutions such that:

$$\sigma^t = \sum_{i=1}^3 \alpha_i(\theta, \bar{R}) \cdot \sigma_i^t, \quad (24)$$

where σ^t is the tectonic stress, $\alpha_i(\theta, \bar{R})$ are scalar coefficients and σ_i^t are the linearly independent pre-computed tectonic stresses.

Here, the three scalars ($\alpha_1, \alpha_2, \alpha_3$) are enough to cover the full range of tectonic stresses. Suppose that for each linearly independent tectonic stress $\sigma_R^{(i)} \in [1,3]$, applied to a model, we compute and store the corresponding total stress tensor, $\sigma_P^{(i)}$ (the total stress is defined as the imposed tectonic stress plus the perturbations caused by the slipping faults (Crouch and Starfield, 1983)), at a fracture location, P. Then, the total stress tensor at P due to the tectonic stress defined by $\sigma_R(\alpha) = \sum_i \alpha_i \sigma_R^{(i)}$ ($\alpha_i \in \mathbb{R}$) will be $\sigma_P = \sum_i \alpha_i \sigma_P^{(i)}$, involving only 18 multiplications. As shown previously, any reduced Andersonian tectonic stress is entirely defined by only two parameters, θ and \bar{R} . Although we are inverting for these two parameters, we need to perform three simulations at initialization.

Using the principle of superposition does not require re-computing the unknown displacement discontinuities on triangular elements, making possible to perform many simulations in few seconds (i.e. 50,000 in a couple of minutes). Therefore, if measurements of geological features are known at some given locations such as displacement, strain and/or stress, fractures orientation or secondary fault planes, which formed in the vicinity of major active faults, then it is possible to recover the triple ($\alpha_1, \alpha_2, \alpha_3$) and therefore the tectonic stress σ^t and the corresponding tectonic regime (Maerten et al., 2015).

5.2.2. Real time computation

Changing σ_R usually requires re-computing the entire model in order to determine the corresponding unknown displacement distributions on faults. Then, at any observation point P , the total stress is determined as a superposition of the tectonic stress σ_R and the stress changes due to fault slip from

mechanical interactions between faults. For a model with n triangular elements, computing the total stress at P requires first solving for the unknown displacement on these elements (for which the complexity is of $O(n^2)$), and then approximately $350n$ multiplications using the standard method. In contrast, using the principle of superposition does not require re-computing the unknown slip vectors and the total stress at P . Only 18 multiplications and 12 additions are needed. The complexity is independent of the number of triangular elements within the model and is consequently constant in computation time.

5.2.3. Method of Resolution

A Monte Carlo method (Hammersley and Handscomb, 1975; Rubinstein, 1981) is used to find the parameters $(\alpha_1, \alpha_2, \alpha_3)$ that minimize the misfit between observed and modeled data. Though $(\alpha_1, \alpha_2, \alpha_3)$ is a 3D parameter-space, it can be reduced to 2D, namely, the parameters θ and \bar{R} , as explained earlier (see Algorithm 1).

A simple sampling method can be executed by considering a 2D rectangular domain for which the x-axis and y-axis correspond to $\bar{R} \in [0,3]$ and $\theta \in [0, \pi]$, respectively. A total of n_s stress regimes are randomly selected from this 2D-domain and the average cost, d , over all P is determined for each selected regime. A refinement is created around the stress regime with the minimum cost d and the procedure is repeated with the smaller domain. Algorithm 1 depicts a simplified version of the procedure, for which there is no refinement. The sampling method presented here can be optimized by various techniques (McKay et al., 1979), but these optimizations are not necessary, due to the reasonable computational time of a few seconds.

To see the benefit of the principle of superposition combined with a Monte Carlo method, relative to a naive method, we take a model composed of 3,000 triangular elements as an example. For one simulation following the naïve method, the model takes approximately 30 seconds to compute the displacement on

faults and 5 seconds to compute the total stress at 200 points. Consequently, running 20,000 simulations takes 8 days, whereas 40 seconds are needed using the principal of superposition.

Algorithm 1: Remote stress regime

Input: 3D Fault geometries

Input: Dataset (fault slip and/or fracture orientations ...)

Output: $\sigma_{\mathbf{R}}$ // the estimated remote stress

Initialization: Compute 3 simulations with faults using 3 linearly independent $\sigma_{\mathbf{R}}^{(i)}$ ($1 \leq i \leq 3$). Store the resulting slip vectors on faults and the strain, stress and displacement at each point P as necessary.

Let $c = 1$ // initial cost

Let $\bar{\alpha} = (0, 0, 0)$ // initial ($\alpha = \sigma$) solution

for $k = 1$ to n_s **do**

Randomly generate $\bar{R} \in [0, 3]$

Randomly generate $\theta \in [0, \pi]$

Convert $(\theta, \bar{R}) \in \mathfrak{R}^2$ to $\alpha \in \mathfrak{R}^3$ using (7) and (6)

// Compute d , the average cost over P :

$d = \text{cost}(\alpha, \text{data set})$

if $d \leq c$ **then**

$\bar{\alpha} = \alpha$

$c = d$

end

end

$\sigma_{\mathbf{R}} = \sum_{i=1}^3 \bar{\alpha}_i \sigma_{\mathbf{R}}^{(i)}$

5.2.4. Cost functions

When we use a Monte Carlo method to find the parameters $(\alpha_1, \alpha_2, \alpha_3)$, we need to minimize some cost functions given three independent far field stresses. The cost functions must be as simple as possible as we do not want add extra computation time to the overall process. In the present study we constrain the paleostress inversion with observed fault slickenlines and fracture data exclusively.

Fault slip vector

For a given tectonic stress defined by θ and \bar{R} , the minimum cost for slip vectors, C_{slip} , is such that

$$C_{slip} = \frac{1 - (\bar{\tau} \cdot \bar{a})}{2} \quad (25)$$

where C_{slip} is defined between 0 and 1, $\vec{\tau}$ is the shear stress and \vec{d} the slip vector.

Using this cost function, $C_{slip} = 0$ if the vectors are collinear, $C_{slip} = 0.5$ when orthogonal and $C_{slip} = 1$ when opposed in sense.

Fractures

The cost is normalized for the 3 fracture types and varies from 0 and 1. A cost of 0 means a perfect match between observed fractures orientation and local computed stresses, while a cost of 1 means the worst match.

For a given tectonic stress defined by θ and \bar{R} , the minimum cost for tension fractures, $C_{tension}$, is such that the computed local minimum principal stress, $\vec{\sigma}_3$, is aligned with the normal \vec{n} of the observed tension fracture plane:

$$C_{tension} = 1 - (\vec{\sigma}_3 \cdot \vec{n})^2 \quad (26)$$

For stylolites, the minimum cost, $C_{stylolite}$, is such that the computed local maximum principal stress, σ_1 , is aligned with the normal \vec{n} of the observed stylolite plane:

$$C_{stylolite} = 1 - (\vec{\sigma}_1 \cdot \vec{n})^2 \quad (27)$$

For shear fractures, the minimum cost C_{shear} , is such that the computed local minimum principal stress, σ_3 , is at angle ϕ (friction angle) from the normal \vec{n} of the observed shear fracture plane:

$$C_{shear} = \left| (\vec{\sigma}_3 \cdot \vec{n})^2 - \frac{1}{2}(1 + \sin \phi) \right| \quad (28)$$

The 3 types of fractures can be combined and the total cost for one simulation will be the average cost of all observed fractures used to constrain the inversion. Each fracture data or data type can be weighted according to a user defined confidence criterion.

It is interesting to highlight that cost functions can be written for any observed deformation or stress measurements such as fault throw, GPS data, InSAR data, micro-seismicity or breakout orientations.

5.2.5. Tectonic stress domain

To better visualize and analyze the results of one paleostress inversion, which consists of thousands of simulations, we introduce the tectonic stress domain (Lejri et al., 2015), a 2D graph (see Figure 22) for which the x-axis is the stress ratio \bar{R} , and the y-axis is the orientation (θ) of the maximum horizontal stress according to the North. A point in the domain represents one simulation that is color coded with respect to the computed cost which goes from 0 to 1. As we can have numerous observed data, the color symbolizes the mean cost of all the used data. For a given model, the inversion procedure will try to find the best solutions (\bar{R}, θ) by minimizing the cost functions. These will be highlighted in the tectonic stress domain with warm colors (see Figure 22). The optimum simulation (lowest cost), which will be the result of paleostress inversion, includes the orientation and relative magnitude of the paleo-tectonic regime as well as the style (normal, wrench or reverse fault regime).

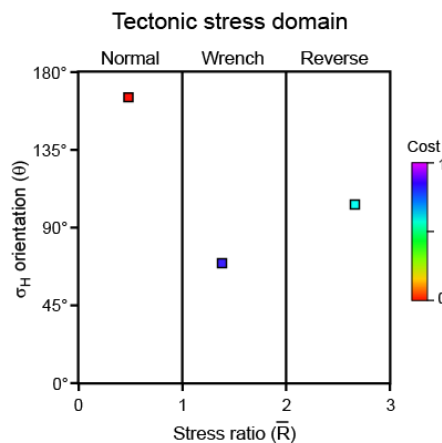


Figure 22: Example of a tectonic stress domain. The x-axis is the stress ratio, \bar{R} , and the y-axis is the orientation, θ , of the maximum horizontal stress according to the North. A point in the domain represents one simulation that is color coded with respect to the computed cost which goes from 0 to 1.

When filled with all the simulations a tectonic stress domain can look like the one on Figure 23, highlighting the areas with best solution (warm areas) and those with the poorest solution (blue areas).

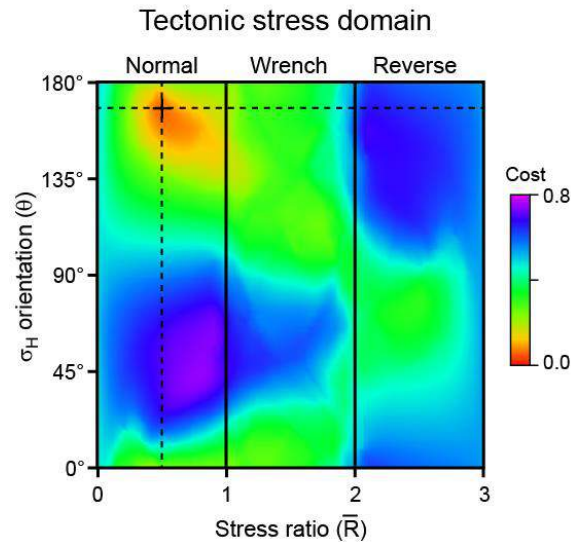


Figure 23. Example of a filled tectonic stress domain.

6. Problematics of the thesis:

The main goal of this thesis is to improve the geomechanical stress inversion technique using fractures observed along wellbores, in order to enhance fracture modeling in reservoirs. For that purpose I aimed at answering four main questions:

1- How much should we trust the Wallace and Bott assumptions for paleostress inversion from fault slip data?

A comparison of slip vectors generated with mechanical modeling using the Boundary Element Method (BEM) with the resolved shear stress is performed. By testing the influence of multiple parameters (geometry, boundary conditions, friction, Poisson's coefficient, half-space, fault fluid pressure), it is shown that complex geometry faults subject to specific boundary conditions can yield slip vectors with significant

discrepancies with the shear stress resolved on the fault plane. Conversely, the presence of a high sliding friction, allows under certain conditions, to validate the WB hypothesis.

2- How well paleostress inversion techniques based on the Wallace and Bott assumptions perform compare to new generation technique based on geomechanics?

I then focus on the task to compare the results of stress inversions based on the WB assumptions (called classical stress inversion methods) to a geomechanical method. For this, complex fault geometry is used in a sensitivity analysis (boundary conditions, friction, data sampling) to analyze the uncertainty of the results of the two inversion methods. This analysis is then compared to a case study, Chimney Rock (Utah, USA), showing the advantages and disadvantages of the classical stress inversion methods.

3- Can we improve paleostress recovery using other types of data?

Since slip markers on faults are hardly observed in core or image log, I intended to use observed natural fracture data as main drivers for the inversion of the paleostress using new generation technique based on geomechanics. I demonstrate, through various outcrop and subsurface examples, how this can efficiently be done and discuss the advantages and drawbacks of such new technique.

4- How is it possible to solve the poly-tectonic phase problem when the mechanical fracture type is undefined?

It is sometimes difficult to determine the fracture kinematics observed along wellbores, and very often the studied regions underwent multiple tectonic phases. In this final section I aim at addressing the problem of data with unknown kinematic (joints, faults, stylolites ...) and extend the mechanical stress inversion to the separation of tectonic phases.

References

- Ackermann, R.V., Schlische, R.W., 1997. Anticlustering of small normal faults around larger faults. *Geology* 25, 1127–1130.
- Aki, K., & P. G. Richards, *Quantitative seismology : Theory and methods*, W.H. Freeman (San Francisco, Calif.-USA), 1, 557, 1980.
- Akoglu, A.M., Cakir, Z., Meghraoui, M., Belabbes, S., El Alami, S.O., Ergintav, S., Akyuz, H.S., 2006. The 1994–2004 Al Hoceima (Morocco) earthquake sequence: conjugate fault ruptures deduced from insar. *Earth Planet. Sci. Lett.* 252, 467–480.
- Allward-Fiore, P., 2006. 3D Characterization and Mechanics of Brittle Deformation in Thrust Fault Related Folds (Ph.D. thesis). Stanford University, CA, USA.
- Amonton G., 1699. *Histoire de l'Académie Royale des Sciences avec les Mémoires de Mathématique et de Physique*, p.206.
- Amrouch, K., Lacombe, O., Bellahsen, N., Daniel, J.-M., Callot, J.P., 2010. Stress/strain patterns, kinematics and deformation mechanisms in a basement-cored anticline: Sheep Mountain anticline (Wyoming, USA). *Tectonics* 29, TC1005
- Anderson, E. M., The dynamics of faulting, *Transactions of the Edinburgh Geological Society*, 8, 387–402, 1905.
- Anderson, E.M., 1942. *The Dynamics Of Faulting And Dyke Formation With Applications To Britain*, first ed. Oliver & Boyd, Edinburgh.
- Anderson, E.M., 1951. *The Dynamics of Faulting and Dyke Formation with Applications to Britain*, 2nd Edition. Oliver and Boyd, Edinburgh.
- Angelier, J., 1975. Sur l'analyse de mesures recueillies dans des sites faillés : l'utilité d'une confrontation entre les méthodes dynamiques et cinématiques, *Comptes Rendus de l'Académie des Sciences-Series IIA - Earth and Planetary Science*, D281, 1805–1808.

- Angelier, J., 1979. Determination of the mean principal directions of stresses for a given fault population. *Tectonophysics* 56, T17–T26.
- Angelier, J., Analyses qualitative et quantitative des populations de jeux de failles., *Bulletin de la Société Géologique de France*, 5, 661–672, 1983.
- Angelier, J., 1984. Tectonic analysis of fault slip data sets, *Journal of Geophysical Research*, 89, 5835–5848,
- Angelier, J., 1989. From orientation to magnitudes in paleostress determinations using fault slip data, *Journal of Structural Geology*, 11 (1-2), 37–50.
- Angelier, J., 1990. Inversion of field data in fault tectonics to obtain the regional stress — III. A new rapid direct inversion method by analytical means. *Geophysical Journal International* 103 (2), 363–376.
- Angelier, J., 1991a. Inversion directe et recherche 4-D: comparaison physique et mathématique de deux modes de détermination des tenseurs des paléocontraintes en tectonique de failles. *C. R. Acad. Sci., Série II* 312 (10), 1213–1218.
- Angelier, J., 1991b. Un élément nouveau dans la détermination des états de contrainte en tectonique cassante. Les plans de défaut non-cisaillants, ou “non-failles”. *C. R. Acad. Sci., Série II* 314 (4), 381–386.
- Angelier, J., 1994. Paleostress Determinations. In: Hancock, P.L. (Ed.), *Continental Deformations*. Pergamon Press, Tarrytown, N.Y., pp. 53e100.
- Angelier, J., 1994a. Failles, non-failles et structures de pression/tension dans l'inversion des données de tectonique cassante en termes de tenseurs des contraintes. *Bull. Soc. géol. de France*. 165 (3), 211–220.
- Angelier, J., 1994b. Fault slip analysis and palaeostress reconstruction. In: Hancock, P.L. (Ed.), *Continental Deformation*. Pergamon Press, Oxford, pp. 53–100.
- Angelier, J., 2002a. Détermination du tenseur des contraintes par inversion de mécanismes au foyer de séismes sans choix de plans nodaux. *Comptes Rendus Geoscience* 334 (1), 73–80.
- Angelier, J., 2002b. Inversion of earthquake focal mechanisms to obtain the seismotectonic stress IV — a new method free of choice among nodal planes. *Geophysical Journal International* 150 (3), 588–609.

- Angelier, J., Goguel, J., 1979. Sur une méthode simple de détermination des axes principaux des contraintes pour une population de failles. C. R. Acad. Sci. Série D 288, 307–310.
- Angelier, J., & S. Manoussis, 1980. Classification automatique et distinction des phases superposées en tectonique de failles, C. R. Acad. Sci. série D, 290, 651–654.
- Angelier J., Mechler P., 1977. Sur une méthode graphique de recherche des contraintes principales également utilisable en tectonique et en séismologie : la méthode des dièdres droits. – Bull. Soc. géol. Fr. XIX (6), 1309-1318.
- Armijo, R., & A. Cisternas, 1978. Un problème inverse en microtectonique cassante, C. R. Acad. Sci. série D, pp. 595–598
- Armijo, R., Carey, E., Cisternas, A., 1982. The inverse problem in microtectonics and the separation of tectonic phases. Tectonophysics 82, 145–160.
- Arthaud, F., 1969. Méthode de détermination graphique des directions de raccourcissement, d'allongement et intermédiaire d'une population de failles. Bull. Soc. géol. De France 7 (XI), 729–737.
- Bai, T., Maerten, L., Gross, M.R., Aydin, A., 2002. Orthogonal cross joints: do they imply a regional stress rotation?. J. Struct. Geol. 24, 77–88.
- Barber, D.J., Wenk, H.R., 1979. Deformation twinning in calcite, dolomite and other rhombohedral carbonates. Phys. Chem. Miner. 5, 141-165.
- Bebendorf, M., Rjasanow, S., 2003. Adaptive low-rank approximation of collocation matrices. Computing 86(4), 1–24.
- Bebendorf, M. (Ed.), 2008. Hierarchical Matrices, A Means to Efficiently Solve Elliptic Boundary Value Problems. Springer, Berlin, Heidelberg.
- Bebendorf, M., 2000. Approximation of boundary element matrices. Numer. Math. 86 (4), 565–589.
- Bellahsen, N., Allward-Fiore, P., Pollard, D.D., 2006. From spatial variation of fracture patterns to fold kinematics : a geomechanical approach. Geophys. Res. Lett. 33, L02301.

- Bergerat, F., Paléo-contraintes et évolution tectonique paléogène du fossé Rhéna, Comptes Rendus de l'Académie des Sciences, Paris, série II, 297, 77–80, 1983.
- Bergerat, F., & J. Angelier, 1998. Fault systems and paleostresses in the Vestfirðir Peninsula. Relationships with the tertiary paleo-rifts of Skagi and Snaefells, *Geodinamica Acta*, 11 (2-3), 105–118.
- Byerlee, James D., 1978. "Friction of Rocks". *Pure and Applied Geophysics* 116 (4-5): 615–626.
- Bott, M.H.P., 1959. The mechanics of oblique slip faulting. *Geological Magazine* 96, 109–117.
- Bourne, S. J., and E. J. M. Willemse, 2001, Elastic stress control on the pattern of tensile fracturing around a small fault network at Nash Point, UK: *Journal of Structural Geology*, v. 23, p. 1753-1770.
- Bourne, S. J., Rijkels, L., Stephenson, B. J., Willemse, E. J. M., 2000, Predictive modeling of naturally fractured reservoirs using geomechanics and flow simulation: *GeoArabia*, v. 6, p. 27-42.
- Brankman, C.M., Aydin, A., 2004. Uplift and contractional deformation along a segmented strike-slip fault system: the Garganopromontory, Southern Italy. *J. Struct. Geol.* 26, 807–824.
- Brillouin, L., 1946, *Wave propagation in Periodic Structures: Electric Filters and Crystal Lattices*, McGraw–Hill, New York, 255 p.
- Burg, J.-P., Célérier, B., Chaudhry, M.N., Ghazanfar, M., Gnehm, F., Schnellmann, M., 2005. Fault analysis and paleostress evolution in large strain regions: methodological and geological discussion of the southeastern Himalayan fold-and-thrust belt in Pakistan. *J. Asian Earth. Sci.* 24, 445–467.
- Bürgmann, R., Pollard, D., Martel, S., 1994. Slip distributions on faults: effects of stress gradients, inelastic deformation, heterogeneous host-rock stiffness, and fault interaction. *Journal of Structural Geology* 16, 1675-1688.
- Bürgmann, R., Schmidt, D.A., Nadeau, R.M., D'Alessio, M., Fielding, E.J., Lawrence, S., Manaker, D., McEvilly, T., Murray, M.H., 2000. Earth quake potential along the northern Hayward fault. *Science* 289, 1178–1182.
- Cahn, R.W., 1954. Twinned crystals. *Advances in physics. Philos. Mag.* 3, 363-445.

- Cailleau, B., LaFemina, P.C., Dixon, T.H., 2007. Stress accumulation between volcanoes: an explanation for intra-arc earth quakes in Nicaragua?. *Geophys. J. Int.* 169, 1132–1138.
- Cakir, Z., Meghraoui, M., Akoglu, A.M., Jabour, N., Belabbes, S., Ait-Brahim, L., 2006. Surface deformation associated with the mw6.4, February 24, 2004 Al Hoceima (Morocco) earth quake deduced from insar : implication for the active tectonics along North Africa. *Bull. Seismol. Soc. Am.* 96, 59–68.
- Carey, E., Brunier, B., 1974. Analyse théorique et numérique d'un modèle mécanique élémentaire appliqué à l'étude d'une population de failles. – *C. R. Acad. Sci., D*, 279, 891-894.
- Carey, E., Vergely, P., 1992. Graphical analysis of fault kinematics and focal mechanisms of earthquake in terms of stress; the right dihedral method, use and pitfalls. *Annales Tectonicae VI* (1), 3–9.
- Carey, E., 1979. Recherche des directions principales de contraintes associées au jeu d'une population de failles. *Revue de Géographie physique et de Géologie dynamique* 21 (1), 57–66.
- Carey-Gailhardis, E., Mercier, J.L., 1987. A numerical method for determining the state of stress using focal mechanisms of earthquake populations: application to Tibetan teleseisms and microseismicity of southern Peru. *Earth and Planetary Science Letters* 82 (1–2), 165–179.
- Carey-Gailhardis, E., Mercier, J., 1992. Regional state of stress, fault kinematics and adjustments of blocks in a fractured body of rock: application to the microseismicity of the Rhine graben. *Journal of Structural Geology* 14 (8–9), 1007–1017.
- Carter, N.L., Raleigh, C.B., 1969. Principal stress directions from plastic flow in crystals. *Geological Society of America Bulletin* 80 (7), 1231–1264.
- Cartwright, J. A., C. Mansfield, B. Trudgill (1996), The growth of normal fault by segment linkage, in *modern Developments, in Structural Interpretation, Validation and Modeling*, edited by P. G. Buchanan and D. A. Nieuwland, *Geol. Soc. Spec. Publ.*, 99, p. 163-177.
- Celerier, B., Etchecopar, A., Bergerat, F., Vergely, P., Arthaud, F., Laurent, P., 2012. Inferring stress from faulting: from early concepts to inverse methods. *Tectonophysics*, Volume 581, 18 December 2012, Pages 206-219

- C  lerier, B., Seranne, M., 2001. Breddin's graph for tectonic regimes. *J. Struct. Geol.* 23, 789-801
- Celerier B., 1988. How much does slip on a reactivated fault plane constrain the stress tensor? *Tectonics* 7, 1257-1278.
- Celerier, B., 2006. FSA version 28.8: Fault & stress analysis software, in: Editor (Eds.), <http://www.pages-perso-bernard-celerier.univ-montp2.fr/software/dcmt/fsa/fsa.html>.
- Cheng, L.-W., Lee, J.-C., Hu, J.C., Chen, H.-Y., 2009. Coseismic and post seismic slip distribution of the 2003 mw6.5 Chengkung earth quake in Eastern Taiwan: elastic modeling from inversion of gps data. *Tectonophysics* 466, 335–343.
- Childs, C., J. J. Walsh, and J. Watterson, 1990, A method for estimation of the density of fault displacements below the limits of seismic resolution in reservoir formations, in G. Trotman, eds., *North Sea oil and gas reservoirs: The Norwegian Institute of Technology, Liverpool*, v. 2.
- Chinnery, M.A., 1963. The stress change that accompany strike-slip faulting. *Bulletin of the Seismological Society of America* 53 (5), 921–932.
- Chinnery, M., 1961. The deformation of the ground around surface faults. *Bull. Seismol. Soc. Am.* 51, 355–372.
- Colletini, C., Niemeijer, A., Viti, C., and Marone, C., 2009. Fault zone fabric and fault weakness. *Nature* 462, 907-910, doi: 10.1038/nature 08585.
- Comninou, M., Dundurs, J., 1975. The angular dislocation in a half space. *J. Elast.* 5 (3), 203–216.
- Contreras, J., M. H. Anders, C. H. Scholtz (2000), Growth of normal fault system: observation from the Lake Malawi basin of the east African rift, *Journal of Structural Geology*, v. 22, p. 159-168.
- Cooke, M., 1997. Fracture localization along faults with spatially varying friction. *J. Geophys. Res.* 22, 425–434.
- Coulomb, C. A., 1779. *Th  orie des machines simples, en ayant   gard au frottement de leurs parties et    la roideur des cordages*
- Crider, J.G., Pollard, D. D., 1998. Fault linkage : three-dimensional mechanical interaction between echelon normal faults. *J. Geophys. Res.* 103, 24, 373–24, 391.

- Crider, J., 2001. Oblique slip and the geometry of normal fault linkage: mechanics and a case study from the basin and range in Oregon. *J. Struct. Geol.* 23, 1997–2009.
- Crouch, S.L., Starfield, A.M. (Eds.), 1983. *Boundary Element Methods in Solid Mechanics*. George Allen and Unwin, London.
- Cundall, P.A., 1988. Formulation of a three dimensional distinct element model: Part I. A scheme to detect and represent contacts in a system composed of many polyhedral blocks. *Int. J. Rock Mech. Min. Sci. Geomech. Abstr.* 25, 107-116.
- Cundall, P.A., 1971. A computer model for simulating progressive large scale movement in blocky rock systems. *International Symposium on Rock Mechanics*. International Society of Rock Mechanics, Nancy, p. II-8.
- Dair, L., Cooke, M.L., 2009. San Andreas fault topology through the San Geronimo pass, California. *Geology* 37, 119–122.
- Damsleth, E., V. Sangolt, and G. Aamodt, 1998, Subseismic faults can seriously affect fluid flow - a stochastic modelling case study: SPE 49024, p. 1-11.
- Daubrée, M., 1879. Application de la méthode expérimentale à l'étude des déformations et des cassures terrestres, *Bulletin de la Société Géologique de France*, 3, 108–141,
- Davatzes, N.C., Aydin, A., 2003. The formation of conjugate normal fault systems in folded sandstone by sequential jointing and shearing. *J. Geophys. Res.* 108.
- Davatzes, N.C., Aydin, A., and Eichhubl, P., 2003, Overprinting faulting mechanisms during the development of multiple fault sets in sandstone, Chimney Rock fault array, Utah, USA: *Tectonophysics*, v. 363, p. 1–18
- Davatzes, N. C., Eichhubl, P., Aydin, A., 2005. Structural evolution of fault zones in sandstone by multiple deformation mechanisms: Moab fault, south east Utah. *Geol. Soc. Am. Bull.* 117, 135–148
- Dawers, N. H., M. H. Anders, 1995. Displacement-length scaling and fault linkage, *Journal of Structural Geology*, v. 17, 5, p. 607-614.

- Dee, S.J., Yielding, G., Freeman, B., Healy, D., Kuszniir, N.J., Grant, N., Andellis, P., 2007, Elastic dislocation modelling for prediction of small-scale fault and fracture network characteristics, in Lonergan, L., Jolly, R. H., Rawnsley, K., and Sanderson, D.J. eds., *Fractured Reservoirs: Geological Society of London, Special Publication 270*, p. 139–155.
- De Jossineau, G., Aydin, A., 2007. The evolution of the damage zone with fault growth in sandstone and its multiscale characteristics. *Journal of Geophysical Research* 112.
- Delvaux, D., Sperner, B., 2003. Stress tensor inversion from fault kinematic indicators and focal mechanism data: the TENSOR program. In: Nieuwland, D. (Ed.), *New Insights into Structural Interpretation and Modelling*, 212. Geological Society, London, Special Publication, pp. 75-100.
- Di Toro G., Han R., Hirose T., De Paola N., Nielsen S., Mizoguchi K., Ferri F., Cocco M., Shimamoto T. 2011. Fault lubrication during earthquakes. *Nature*, 471(7339): 494–498.
- Diday, E., 1971, Une nouvelle methode en classification automatique de formes : la méthode des nuées dynamiques : *Rev. Star. Appl.* v. XIX. no. 2, p. 19-33.
- Dietrich, D., Song, H., 1984. Calcite fabrics in a natural shear environment, the Helvetic nappes of western Switzerland. *Journal of Structural Geology* 6 (1–2), 19–32.
- Diez, M., LaFemina, P.C., Connor, C.B., Strauch, W., Tenorio, V., 2005. Evidence for static stress changes triggering the 1999 eruption of Cerro Negro volcano, Nicaragua and regional aftershock sequences. *Geophys. Res. Lett.* 32, L04309
- Dunne, W.M., Hancock, P.L., 1994. Palaeostress analysis of small-scale brittle structures. In: Hancock, P.L. (Ed.), *Continental Deformation*. Pergamon Press, Oxford, pp. 101–120.
- Dupin, J.M., Sassi, W., Angelier, J., 1993. Homogeneous stress hypothesis and actual fault slip: a distinct element analysis. *J. Struct. Geol.* 15, 1033-1043.
- Ellsworth, W., Zhonghuai, X., 1980. Determination of the stress tensor from focal mechanism data. *Eos, Transactions, American Geophysical Union* 61 (46, abstract T127), 1117.

- Etchecopar, A., & M. Mattuer, 1988. Méthodes dynamiques d'analyse des populations de failles, *Bulletin de la Société Géologique de France*, 2, 289–302.
- Etchecopar, A., Vasseur, G., Daignieres, M., 1981. An inverse problem in microtectonics for the determination of stress tensors from fault striation analysis. *J. Struct. Geol.* 3, 51-65.
- Etchecopar, A., 1984. Étude des états de contrainte en tectonique cassante et simulations de déformations plastiques (approche mathématique). Thèse d'État. Ph.D. thesis, Université des Sciences et Techniques du Languedoc.
- Fielding, E.J., Wright, T.J., Muller, J.R., Parsons, B.E., Walker, R., 2004. Aseismic deformation of a fold-and-thrust belt imaged by synthetic aperture radar interferometry near Shahdad, south east Iran. *Geology* 32, 577–580.
- Fielding, E.J., Lundgren, P., Burgmann, R., Funning, G.J., 2009. Shallow fault-zone dilatancy recovery after the 2003 Bam earthquake in Iran. *Nature* 458, 64–68.
- Fischer, M. P., and M. S. Wilkerson, 2000. Predicting the orientation of joints from fold shape: Results of pseudo-three-dimensional modeling and curvature analysis: *Geology*, v. 28, p. 15-18.
- Fleischmann, K. H., & M. Nemcok, 1991. Paleostress inversion of fault-slip data using the shear stress solution of means, *Tectonophysics*, 196, 195–202.
- Friedman, M., 1967. Description of rocks and rock masses with a view to their physical and mechanical behavior. *Proceedings of the 1st International Congress on Rock Mechanics*, vol. 3, pp. 182±197.
- Friedman, M., Heard, H.C., 1974. Principal stress ratio in Cretaceous limestones from Texas Gulf Coast. *Bull. Am. Assoc. Petrol. Geol.* 58, 71±78.
- Fry, N., 1999. Striated faults: visual appreciation of their constraint on possible paleostress tensors. *Journal of Structural Geology* 21, 7–21.
- Fry, N., 1992. Stress ratio determinations from striated faults: a spherical plot for cases of near-vertical principal stress. *Journal of Structural Geology* 14 (10), 1121–1131.

- Galindo-Zaldívar, J., González-Lodeiro, F., 1988. Faulting phase differentiation by means of computer search on a grid pattern. *Annales Tectonicae* II 2, 90–97.
- Gapais, D., Cobbold, P.R., Bourgeois, O., Rouby, D., de Urreiztieta, M., 2000. Tectonic significance of fault slip data. *J. Struct. Geol.* v22,7:881-888.
- Gauthier, B. D. M., and S. D. Lake, 1993, Probabilistic modeling of faults below the limit of seismic resolution in Pelican Field, North Sea, offshore United Kingdom: *AAPG Bulletin*, v. 77, p. 761-776.
- Gephart, J.W., Forsyth, D.W., 1984. An improved method for determining the regional stress tensor using earthquake focal mechanism data: application to the San Fernando earthquake sequence. *Journal of Geophysical Research* 89 (B11), 9305–9320.
- Gephart, J.W., 1990a. FMSI: a Fortran program for inverting fault/slickenside and earthquake focal mechanism data to obtain the regional stress tensor. *Computers & Geosciences* 16 (7), 953–989.
- Gephart, J.W., 1990b. Stress and the direction of slip on fault planes. *Tectonics* 9 (4), 845–858.
- Gephart, J. W., Forsyth, D. W., 1984. An improved method for determining the regional stress tensor using earthquake focal mechanisms data: Application to the San Fernando earthquake sequence, *J. Geophys. Res.*, 89, 9305-9320.
- Gephart, J. W., 1985. Principal stress directions and the ambiguity in fault plane identification from focal mechanisms, *Bulletin of the Seismological Society of America*, 75 (2), 621–625.
- Grant, J. V., & S. A. Kattenhorn, 2004. Evolution of vertical faults at an extensional plate boundary, Southwest Iceland, *Journal of Structural Geology*, 26, 537–557.
- Griffith, W.A., Cooke, M.L., 2004. Mechanical validation of the three-dimensional intersection geometry between the Puente hills blind-thrust system and the Whittier fault, Los Angeles, California. *Bull. Seismol. Soc. Am.* 94, 493–505.
- Guðmundsson, Á., F. Bergerat, & J. Angelier, 1996. Off-rift and rift-zone palaeostresses in Northwest Iceland, *Tectonophysics*, 255 (3-4), 211–228.

- Hackbusch, W., 1999. A sparse matrix arithmetic based on H-matrices: part 1: introduction to H-matrices. *Computing* 62, 89–108.
- Hammah, R.E., Curran, J.H., 1998. Fuzzy cluster algorithm for the automatic identification of joint sets. *International Journal of Rock Mechanics and Mining Sciences* 35, 889–905.
- Hammersley, J. M. and Handscomb, D. C., 1975. *Monte Carlo Methods*. Fletcher, Norwich, England.
- Hancock, P.L., 1985. Brittle microtectonics: principles and practice *J. Struct. Geol.* V7, 3:347–457.
- Hardcastle, K.C., Hills, L.S., 1991. BRUTE3 and SELECT: Quick Basic 4 programs for determination of stress tensor configuration and separation of heterogeneous populations of fault-slip data. *Computers & Geosciences*, 17, 23–43.
- Hardcastle, K.C., 1989. Possible paleostress tensor configurations derived from fault–slip data in eastern Vermont and western New Hampshire. *Tectonics* 8 (2), 265–284.
- Hardebeck, J. L., & A. J. Michael, 2006. Damped regional-scale stress inversions: Methodology and examples for southern California and the Coalinga aftershock sequence, *Journal of Geophysical Research*, 111 (B11), 1–11.
- Hennings, P. H., J. E. Olson, and L. B. Thompson, 2000, Combining outcrop data and threedimensional structural models to characterize fractured reservoirs: an example from Wyoming: *American Association of Petroleum Geologists Bulletin*, v. 84, p. 830–849.
- Hilley, G.E., Mynatt, I., Pollard, D.D., 2010. Structural geometry of Raplee ridge monocline and thrust fault image during inverse boundary element modeling and alsm data. *J. Struct. Geol.* 32, 45–58.
- Homberg, C., Angelier, J., Bergerat, F., Lacombe, O., 2004. Using stress deflections to identify slip events in fault systems. *Earth and Planetary Sciences Letters* 217, 409–424.
- Homberg, C., J. Hu, J. Angelier, F. Bergerat, & O. Lacombe, 1997. Characterization of stress perturbations near major fault zones: insights from 2-D distinct-element numerical modeling and field studies (Jura mountains), *Journal of Structural Geology*, 19 (5), 703–718.

- Honda, H., & A. Masatsuka, 1952. On the mechanism of the earthquakes and the stresses producing them in Japan and its vicinity. Science reports of the Tohoku University Ser. 5., Geophysics, 4, 42–60.
- Honda, H., A. Masatsuka, & K. Emura. On the mechanism of the earthquakes and the stresses producing them in Japan and its vicinity (second paper). Science reports of the Hohoku University, Geophysics, 8, 186–205, 1956.
- Hu, J.-C., Angelier, J., 2004. Stress permutations: three-dimensional distinct element analysis accounts for a common phenomenon in brittle tectonics. J. Geophys. Res. 109.
- Huang, Q., 1988. Computer-based method to separate heterogeneous sets of fault-slip data into sub-sets. Journal of Structural Geology 10, 225-237.
- Hudson, J.A., 1981, Wave speeds and attenuation of elastic material containing cracks: Geophysics journal of the Royal Astronomical Society 64, 133-150.
- Inglis, C., 1913. Stresses in a plate due to the presence of cracks and sharp corners. Transactions of the Institution of Naval Architects. 55, 219-230.
- Jamison, W.R., Spang, J.H., 1976. Use of calcite twin lamellae to infer differential stress. Geol. Soc. Am. Bull. 87, 868-872.
- Jeyakumaran, M., Rudnicki, J.W., Keer, L.M., 1992. Modeling slip zones with triangular dislocation elements. Bull. Seismol. Soc. Am. 82, 2153–2169.
- Johnson, K., Y. Hsu, P. Segall, and S. Yu (2001). Fault geometry and slip distribution of the 1999 Chi-Chi, Taiwan, earthquake imaged from inversion of GPS data, Geophys. Res. Lett. 28, 2285–2288.
- Jónsson, S., Zebker, H., Segall, P., Amelung, F., 2002. Fault slip distribution of the 1999 Mw 7.1 Hector mine, California, earthquake, estimated from satellite radar and GPS measurements. Bull. Seismol. Soc. Am. 92, 1377–1389.
- Julien, P., & F. H. 1980. Cornet, Stress determination from aftershocks of the Campania-Lucania earthquake of November 23, Annales Geophysicae, 5B, 289–300, 1987.

- Kattenhorn, S., Aydin, A., Pollard, D., 2000. Joints at high angles to normal fault strike: an explanation using 3d numerical model of fault perturbed stress field. *J. Struct. Geol.* 22, 1–23.
- Kattenhorn, S. A., D. D. Pollard, 2001. Integrated 3-D seismic data, field analogs and mechanical models in the analysis of segmented normal faults in the With Farm oil field, southern England, United Kingdom, *AAPG Bulletin*, Vol 85, 7, p. 1183-1210.
- Kaven J.O., Maerten F., Pollard, D.D., 2011. Mechanical analysis of fault slip data: Implications for paleostress analysis. *J. Struct. Geol.* 33, 78-91.
- Kloppenburg, A., J. C. Alzate, and G. R. Charry, 2003, Building a discrete fracture network based on the deformation history: A case study from the Guaduas Field, Colombia: Extended abstract for the VIII Simposio Bolivariano, Cartagena, Colombia.
- Klügel, A., Walter, T.R., Schwarz, S., Geldmacher, J., 2005. Gravitational spreading causes en-echelon diking along a rift zone of Madeira archipelago: an experimental approach and implications for magma transport. *Bull. Volcanol.* 68, 37–46.
- Koledoye, A.B., Aydin, A., May, E., 2003. A new process-based methodology for analysis of shale smear along normal faults in Niger Delta. *American Association of Petroleum Geologists Bulletin*, v. 87, p. 445-463.
- Kreemer, C., Blewitt, G., Maerten, F., 2006. Co- and post seismic deformation of the 28 March 2005 Nias mw 8.7 earthquake from continuous gps data. *Geophys. Res. Lett.* 33, L07307.
- La Pointe, P., Cladouhos, T., Follin, S., 2002. Development, application, and evaluation of a methodology to estimate distributed slip on fractures due to future earthquakes for nuclear waste repository performance assessment. *Bull. Seis-mol. Soc. Am.* 92, 923–944.
- Lacombe, O., 2001. Paleostress magnitudes associated with development of mountain belts: Insights from tectonic analyses of calcite twins in the Taiwan Foothills. *Tectonics* 20 (6), 840–849.

- Lacombe, O., Laurent, P., 1996. Determination of deviatoric stress tensors based on inversion of calcite twin data from experimentally deformed monophase samples: preliminary results. *Tectonophysics* 255 (3–4), 189–202.
- Lacombe, O., J. Angelier, and P. Laurent, 1993. Calcite twins as markers of recent compressional events in an active orogen: The reefal limestones of southern Taiwan as a case study, *C. R. Acad. Sci., Ser. II*, 316, 1805 – 1813.
- Lacombe, O., Laurent, P., 1996. Determination of deviatoric stress tensors based on inversion of calcite twin data from experimentally deformed monophase samples: preliminary results. *Tectonophysics* 255 (3–4), 189–202.
- Lacombe, O., Laurent, P., Rocher, M., 1996b. Magnitude of the pyrenean deviatoric stresses in the north pyrenean foreland. *C. R. Acad. Sci. Paris, Ser. II* 322, 229–235.
- Lacombe, O., K. Amrouch, F. Mouthereau, and L. Dissez 2007. Calcite twinning constraints on late Neogene stress patterns and deformation mechanisms in the active Zagros collision belt, *Geology*, 35(3), 263 – 266
- Lacombe, O., Laurent, P., Angelier, J., 1994. Calcite twins as a key to paleostresses in sedimentary basins: preliminary results from drill cores of the Paris basin. In: Roure, F.(Ed.), *Peri-Tethyan Platforms*. Technip, Paris, pp. 197–210.
- Laurent, P., Bernard, P., Vasseur, G., Etchecopar, A., 1981. Stress tensor determination from the study of e twins in calcite: a linear programming method. *Tectonophysics* 78 (1–4), 651–660.
- Laurent, P., Tourneret, C., Laborde, O., 1990. Determining deviatoric stress tensors from calcite twins: applications to monophased synthetic and natural polycrystals. *Tectonics* 9 (3), 379–389.
- Laurent, P., Kern, H., Lacombe, O., 2000. Determination of deviatoric stress tensors based on inversion of calcite twin data from experimentally deformed monophase samples. Part II. Axial and triaxial stress experiments. *Tectonophysics* 327 (1–2), 131–148.

- Liesa, C., & R. J. Lisle, 2004. Reliability of methods to separate stress tensors from heterogeneous fault-slip data, *Journal of Structural Geology*, 26, 559–572.
- Lisle, R.J., 2013. A critical look at the Wallace-Bott hypothesis in fault-slip analysis. *Bull. Soc. géol. Fr.*, 184, 4-5, 299-306.
- Lisle, R.J., 1998. Simple graphical constructions for the direction of shear. *J. Struct. Geol.*, 20, 969-973.
- Lisle, R. J., & S. Vandycke, 1996. Separation of multiple stress events by fault striation analysis : an example from Variscan and younger structures at Ogmere, South Wales, *Journal of Geological Society*, 153 (6), 945.
- Lisle, R.J., Orife, T.O., Arlegui, L., Liesa, C., Srivastava, D.C., 2006. Favoured states of palaeostress in the earth's crust: evidence from fault-slip data. *J. Struct. Geol.* 28 (6), 1051–1066.
- Lisle, R.J., 1992. New method of estimating regional stress orientations: applications to focal mechanism data of recent British earthquakes. *Geophys. J. Internat.*, 110, 276-282.
- Lisle, R., 1994, Detection of zones of abnormal strains in structures using Gaussian curvature analysis; *AAPG bulletin*, v. 78 (12), p. 1811-1819.
- Lovely, P.J., Pollard, D.D., Mutlu, O., 2009. Regions of reduced static stress drop near fault tips for large strike-slip earthquakes. *Bull. Seismol. Soc. Am.* 99, 1691–1704.
- Lovely, P., Flodin, E., Guzowski, C., Maerten, F., and Pollard, D. D., 2012, Pitfalls among the promises of mechanics-based restoration: Addressing implications of unphysical boundary conditions: *Journal of Structural Geology*, v. 41, p. 47-63.
- Lovely, P., Flodin, E., Guzowski, C., Maerten, F., and Pollard, D. D., 2012, Pitfalls among the promises of mechanics-based restoration: Addressing implications of unphysical boundary conditions: *Journal of Structural Geology*, v. 41, p. 47-63.
- Lund, B., Slunga, R., 1999. Stress tensor inversion using detailed micro earthquake information and stability constraints: application to Ölfus in southwest Iceland. *Journal of Geophysical Research* 104 (B7), 14947–14964.

- Lundgren, P., Lu, Z., 2006. Inflation model of Uz on Caldera, Kamchatka, constrained by satellite radar interferometry observations. *Geophys. Res. Lett.* 33, L06301.
- Madden, E. H., F. Maerten, and D. D. Pollard (2013), Mechanics of nonplanar faults at extensional steps with application to the 1992 M 7.3 Landers, California, earthquake, *J. Geophys. Res.*, 118.
- Maerten, L., 1999, Mechanical interaction of intersecting normal faults: theory, field examples and applications: Ph.D. thesis, Stanford University, Stanford, California, U.S.A., p. 167.
- Maerten, L., 2000. Variations in slip on intersecting normal faults: implications for paleostress inversion. *J. Geophys. Res.* 270, 197–206.
- Maerten, F., 2010a. Adaptive cross-approximation applied to the solution of system of equations and post-processing for 3D elastostatic problems using the boundary element method. *Engineering Analysis with Boundary Elements* 34 (5), 483-491.
- Maerten, L., Maerten, F., 2006, Chronologique modeling of faulted and fractured reservoirs using geomechanically based restoration: Technique and industry applications: American Association of Petroleum Geologist Bulletin, v. 90, p. 1201-1226.
- Maerten, F., Maerten, L., 2008. Iterative 3d bem solver on complex faults geometry using angular dislocation approach in heterogeneous, isotropic elastic whole or half-space. In: Brebbia (Ed.), *Boundary Elements and Other Mesh Reduction Methods XXX*, WIT Press, Southampton, UK, pp. 201–208.
- Maerten, F., and L. Maerten, 2011, Stress and fracture modeling using the principle of superposition, Slb Patent declaration and assignment for docket no. 94.0276
- Maerten, L., Pollard, D.D., Karpuz, R., 2000. How to constrain 3-D fault continuity and linkage using reflection seismic data: a geomechanical approach. *American Association of Petroleum Geologists Bulletin* 84, 1311–1324.
- Maerten, L., Pollard, D. D., Gillespie, P., 2002, Effects of local stress perturbation on secondary fault development: *Journal of Structural Geology*, v. 24, p. 145-153.

- Maerten, F., Maerten, L., and Pollard, D. D., 2014, iBem3D, a three-dimensional iterative boundary element method using angular dislocations for modeling geologic structures: *Computers and Geosciences*, v. 72, p. 1-17.
- Maerten F., Madden, B., Pollard, D. D., Maerten, L., 2015, Accounting for fault mechanics in the inversion of geophysical data for the tectonic driving stress: Application to the 1992 Landers, California earthquake, Submitted to JGR.
- Maerten, F., Resor, P.G., Pollard, D.D., Maerten, L., 2005. Inverting for slip on threedimensional fault surfaces using angular dislocations. *Bulletin of the Seismological Society of America* 95, 1654e1665.
- Maerten, L., Willemse, E.J.M., Pollard, D.D., Rawnsley, K., 1999. Slip distribution on intersecting normal faults. *Journal of Structural Geology* 21, 259–271.
- Maerten, L., Gillespie, P., Daniel, J.-M., 2006, 3-D geomechanical modeling for constraint of subseismic fault simulation: *American Association of Petroleum Geologists*, v. 90, p. 1337-1358.
- Marone C., 2004. Earthquake science: faults greased at high speed. *Nature*, 427(6973):405-6.
- Marshall, S.T.,Cooke, M.L., 2008.Effects of nonplanar fault topology and mechanical interaction on fault-slip distributions in the Ventura basin,California.*Bull. Seismol. Soc.Am.*98,1113–1127.
- Martel, S.J., Boger, W.A., 1998. Geometry and mechanics of the secondary fracturing around small three-dimensional faults in granitic rock. *Journal of Geophysical Research* 103,21299-21308
- Martel, S.,1997.Effects of cohesive zones on small faults and implications for secondary fracturing and fault trace geometry. *J. Struct. Geol.* 19,835–847.
- Martel, S.J.,2004.Mechanics of landslide in itiation as a shear fracture phenomenon. *Marine Geol.*203,319–339.
- McKay, M. D., R. J. Beckman, a 889 nd W. J. Conover (1979), A comparison of three methods for selecting values of input variables in analysis of output from a computer code. *Technometrics*, 21, 239–245.
- Meigs, A.J.,Cooke,M.L.,Marshall,S.T.,2008.Using vertical rock uplift patterns to constrain the three-dimensional fault configuration in the Los Angeles basin. *Bull. Seismol.Soc.Am.*98,106–123.

- Mercier, J., & E. Carey-Gailhardis, 1989. Regional state of stress and characteristic fault kinematics instabilities shown by aftershock sequences : the aftershock sequences of the 1978 Thessaloniki (Greece) and 1980 Campania-Lucania (Italia) earthquakes as examples, *Earth and Planetary Science Letters*, 92(2), 247–264.
- Michael, A. J., 1984. Determination of Stress From Slip Data : Faults and Folds, *Journal of Geophysical Research*, 89 (B13), 11,517–11,526.
- Michael, A., 1987a. Stress rotation during the Coalinga aftershock sequence. *Journal of Geophysical Research* 92 (B8), 7963–7979.
- Michael, A., 1987b. Use of focal mechanisms to determine stress: a control study. *Journal of Geophysical Research* 92 (B1), 357–368.
- Mohr, O., 1882. Über die Darstellung des Spannungszustandes eines Korper-elementes, *Civilingenieur*, 28, 113–156.
- Muller, J.R., Aydin, A., 2004. Rupture progression along discontinuous oblique fault sets: implications for the karadere rupture segment of the 1999 Izmit earth-quake, and future rupture in the Sea of Marmara. *Tectonophysics* 391, 283–302.
- Muller, J.R., Aydin, A., 2005. Using geomechanical modeling to constrain the fault geometry within the Marmara sea, Turkey. *J. Geophys. Res.* 110, B03407.
- Muller, J. R., Aydin, A. and Maerten F., 2003, Investigating the transition between the 1967 Mudurnu Valley and 1999 Izmit earthquakes along the North Anatolian fault with static stress changes. *Geophysical Journal International* 154, 471-482.
- Muller, J.R., Aydin, A., Wright, T.J., 2006. Using an elastic dislocation model to investigate static coulomb stress change scenarios for earthquake ruptures in the eastern Marmara sea region, Turkey. In: Buiter, S.J.H., Schreurs, G. (Eds). *Analogue and Numerical Modelling of Crustal-Scale Processes*, vol. 253, Geological Society, London, Special Publications, pp. 397–414.

- Munthe, K.L., H. Omre, L. Holden, E. Damsleth, K. Heffer, T. S. Olsen, and J. Watterson, 1993, Subseismic faults in reservoir description and simulation: SPE 26500, p. 843-850.
- Murray, G. H., 1968, Quantitative fracture study-Sanish Pool, McKenzie County, North Dakota: American Association of Petroleum Geologists Bulletin, v. 52, p. 57-65.
- Mynatt, I., Hilley, G., Pollard, D.D., 2007. Inferring fault characteristics using fold geometry constrained by airborne lasers with mapping at Raplee ridge, Utah. *Geophys. Res. Lett.* 34, L16315.
- Nemcok, M., Lisle, R.J., 1995. A stress inversion procedure for polyphase fault/slip data sets. *J. Struct. Geol.*, 17, 1445-1457.
- Nemcok, M., Kovac, D., Lisle, R.J., 1999. A stress inversion procedure for polyphase calcite twin and fault/slip data sets. *Journal of Structural Geology* 21 (6), 597–611.
- Neves, F.A., Zahrani, M.S., Brekcamp, S.W., 2004, Detection of potential fractures and small faults using seismic attributes: The Leading Edge, Society of Exploration Geophysicists, September, p. 903-906.
- Nieto-Samaniego, A. F., and Alaniz-Alvarez, S. A., 1997, Origin and tectonic interpretation of multiple fault patterns: *Tectonophysics*, v. 270, p. 197-206.
- Nissen, H.U., 1964. Dynamic and kinematic analysis of deformed crinoid stems in a quartz graywacke. *Journal of Geology* 72, 346-368.
- Okada, Y., 1985. Surface deformation due to shear and tensile faults in a half-space. *Bull. Seismol. Soc. Am.* 75, 1135–1154
- Okada, Y., 1992. Internal deformation due to shear and tensile faults in a half-space. *Bull. Seismol. Soc. Am.* 82, 1018–1040.
- Olson, E.L., Cooke, M.L., 2005. Application of three fault growth criteria to the Puente hills thrust system, Los Angeles, California, USA. *J. Struct. Geol.* 27, 1765–1777.
- Pascal C., 2002. Interaction of faults and perturbation of slip: influence of anisotropic stress states in the presence of fault friction and comparison between Wallace–Bott and 3D Distinct Element models. *Tectonophysics* 356, 307–322.

- Pascal, C., 1998. Etude mécanique et modélisation de la fracturation en extension, application au domaine de la Mer du Nord. Unpublished PhD thesis, Sciences de la Terre, Univ. P. M. Curie, Paris, 410pp.
- Peacock, D. C., & D. Sanderson, 1991. Displacements, segment linkage and relay ramps in normal fault zones, *Journal of Structural Geology*, 13, 721–733.
- Pecher, A., 1989. SCHMIDTMAC: a program to display and analyze directional data. *Computers and Geosciences* 15, 1315-1326.
- Pedersen, S. I., T. Skov, T. Randen and L., Sonneland, 2005, Automatic Fault Extraction Using Artificial Ants, in Armin Iske and Trygve Randen (eds.), *Mathematical Methods and Modelling in Hydrocarbon Exploration and Production*, Springer Verlag, Berlin/Heidelberg, DE, pp. 107-116.
- Peel, D., Whiten, W.J., McLachlan, G.J., 2001. Fitting mixtures of Kent distributions to aid in joint set identification. *Journal of the American Statistical Association* 96, 566-573.
- Petit, J.-P., 1987. Criteria for the sense of movement on fault surfaces in brittle rocks. *J. Struct. Geol.*, 9, 597-608.
- Petit, J.-P., Mattauer, M., 1995. Palaeostress superimposition deduced from mesoscale structures in limestone: the Matelles exposure, Languedoc, France. *Journal of Structural Geology* 17, 245–256.
- Pfiffner, O.A., Burkhard, M., 1987. Determination of paleo-stress axes orientations from fault, twin and earthquake data. *Ann. Tecton* 1, 48-57.
- Phan-Trong, T., 1993. An inverse problem for the determination of the stress tensor from polyphased fault sets and earthquake focal mechanisms. *Tectonophysics* 224 (4), 393–411.
- Plateau, R., 2012. Architecture et mécanismes du rift islandais dans la région du Vatnajökull. Thèse. Université de Nice-Sophia Antipolis.
- Pollard, D.D., Saltzer, S.D., Rubin, A.M., 1993. Stress inversion methods: are they based on faulty assumptions. *J. Struct. Geol.*, 15, 1045-1054.

- Price, E., Bürgmann, R., 2002. Interactions between the landers and Hector Mine, California, earthquakes from space geodesy, boundary element modeling, and time-dependent friction. *Bull. Seismol. Soc. Am.* 92, 1450–1469.
- Reches Z., Lockner D. A., 2010. Fault weakening and earthquake instability by powder lubrication *Nature* 467, 452–455.
- Reinen, L.A., 2008. Numerical Models for Exploration and Visualization of Complex Geological Phenomena in an Undergraduate Structural Geology Course. *American Geophysical Union, Fall Meeting*, vol. 89(53), pp. ED53A-0582
- Resor, P.G., Pollard, D.D., Wright, T.J., Beroza, G.C., 2005. Integrating high-precision aftershock locations and geodetic observations to model coseismic deformation associated with the 1995 Kozani-Grevena earthquake, Greece. *J. Geophys. Res.* 110, B09402.
- Resor, P.G., 2003. Deformation Associated with Continental Normal Faults (Ph.D. thesis) Stanford University, CA, USA.
- Rigo, A., De Chabaliér, J.-B., Meyer, B., Armijo, R., 2004. The 1995 Kozani-Grevena (northern Greece) earthquake revisited: an improved faulting model from synthetic aperture radar interferometry. *Geophys. J. Int.* 157, 727–736.
- Rispoli, R., 1981. Stress fields about strike-slip faults inferred from stylolites and tension gashes: *Tectonophysics*, 75, p. 29-36.
- Rowe, K.J., Rutter, E.H., 1990. Paleostress estimation using calcite twinning: experimental calibration and application to nature. *Journal of Structural Geology* 12, 1–18.
- Rubinstein, R. Y. 1981. *Simulation and the Monte Carlo Method*. John Wiley and Sons, Inc.
- Sanders, C., M. Bonora, E. Kozłowski, and C. Sylwan, 2002. From 2D to 4D fracture network model, structural modeling of a complex thrust trap: A case study from the Tarija Basin, Argentina: *SPE, ISRM78184*, p. 1-8.

- Sanders, C., M. Bonora, D. Richards, E. Kozlowski, C. Sylwan, and M. Cohen, 2004, Kinematic structural restorations and discrete fracture modeling of a thrust trap: a case study from the Tarija Basin, Argentina: *Marine and Petroleum Geology*, v. 21, p. 845-855.
- Sassi, W., S. E. Livera, and B. P. R. Caline, 1992, Reservoir compartmentalization by faults in Cormorant Block IV, U.K, in R. M. Larsen, N.P.S., eds., *Structural and tectonic modeling and its application to petroleum geology*, v. 1, p. 147-156.
- Savage, H.M., Cooke, M.L., 2003. Can flat-ramp-flat geometry be inferred from fold shape? *J. Struct. Geol.* 25, 2023–2034.
- Schlische, R. W., S. S. Young, R. V. Ackermann, and A. Gupta, 1996, Geometry and scaling relations of a population of very small rift-related normal faults: *Geology*, v. 24, p. 683-686.
- Schmidt, D.A., Burgmann, R., Nadeau, R.M., D'Alessio, M., 2005. Distribution of aseismic slip rate on the Hayward fault inferred from seismic and geodetic data. *J. Geophys. Res.* 110, 1–15.
- Schoenberg, M., and Sayers, C.M., 1995, Seismic anisotropy of fractured rock: *Geophysics*, 60, pp. 204-211.
- Schultz, R.A., Fossen, H., 2002. Displacement-length scaling in three dimensions: The importance of aspect ratio and application to deformation bands. *Journal of Structural Geology* 24, 1389–1411.
- Shackleton, R., Cooke, M.L., 2007. Is plane-strain a valid assumption in non-cylindrical fault-cored folds? *J. Struct. Geol.* 29, 1229–1240.
- Shan, Y., Suen, H., Lin, G., 2003. Separation of polyphase fault/slip data: an objective function algorithm based on hard division. *Journal of Structural Geology* 25 (6), 829–840.
- Shan, Y., Li, Z., Lin, G., 2004. A stress inversion procedure for automatic recognition of polyphase fault/slip data sets. *Journal of Structural Geology* 26 (5), 919–925.
- Shanley, R.J., Mahtab, M.A., 1976. Delineation and analysis of clusters in orientation data. *Mathematical Geology* 8, 9-23
- Simon-Gomez 1986 Analysis of a gradual change in stress regime (example from the eastern Iberian Chain, Spain). *Tectonophysics*, 124, 37-53.

- Soliva, R., Schultz, R.A., 2008. Distributed and localized faulting in extensional settings: insight from the North Ethiopian Rift–Afar transition area. *Tectonics* 27, TC2003,
- Soliva, R., Benedicto, A., 2005. Geometry, scaling relations and spacing of vertically restricted normal faults. *Journal of Structural Geology* 27 (2), 317e325.
- Soliva,R.,Benedicto,A.,Maerten,L.,2006.Spacing and linkage of confined faults: the importance of mechanical thickness.*J.Geophys.Res.*111.
- Soliva,R.,Benedicto,A.,Schultz,R.A.,Maerten,L.,Micarelli,L.,2008.Displacement and interaction of normal fault segments branched at depth: implications for fault growth and potential earth quake rupture size.*J.Struct.Geol.*30, 1288–1299.
- Soliva, R., Maerten, F., Petit, J.-P., and Auzias, V., 2010. Field evidences for the role of static friction on fracture orientation in extensional relays along strike-slip faults ; comparison with photoelasticity and 3D numerical modelling. *J. Struct. Geol.* 32, 1721–1731.
- Spang, J.H., 1972. Numerical method for dynamic analysis of calcite twin lamellae. *Geological Society of America Bulletin* 83 (2), 467–472.
- Sperner, B., & P. Zweigel, , 2010. A plea for more caution in fault-slip analysis, *Tectonophysics*, 482 ((1-4)), 29–41.
- Sperner, B., Ratschbacher, L., Ott, R., 1993. Fault-striae analysis: a Turbo Pascal program package for graphical presentation and reduced stress tensor calculation. *Computers & Geosciences* 19 (9), 1361–1388.
- Spiers, C.J. and Rutter, E.H., 1984. A calcite twinning palaeopiezometer. In: Henderson (Editor). *Progress in Experimental Petrology*. N.E.R.C Publ. Ser. D25, pp. 241-245.
- Tamagawa,T.,Pollard,D.D.,2008.Fracture permeability created by perturbed stress fields around active faults in a fractured basement reservoir. *Am. Assoc. Petrol. Geol.* 92,743–764.

- Thomas, A., J.-L. Mallet, and F. De Beaucourt, 1974, Une Methode analytique de localisation des accidents structuraux dans un massif rocheux: Proceedings of the Congress of the International Society for Rock Mechanics, p. 625-630.
- Thomas, A.L., 1993. Poly3D: a three-dimensional, polygonal-element, displacement discontinuity boundary element computer program with applications to fractures, faults, and cavities in the Earth's crust. M.S. thesis, Stanford University, California.
- Tibaldi, A., 1998. Effects of topography on surface fault geometry and kinematics: examples from the Alps, Italy and Tien Shan, Kazakstan. *Geomorphology* 24, 225– 243.
- Tourneret, C., Laurent, P., 1990. Paleo-stress orientations from calcite twins in the north Pyrenean foreland, determined by the Etchecopar inverse method. *Tectonophysics* 180 (2–4), 287–302.
- Tselentis, G.-A., Gkika, F., 2005. Boundary elements lobe instability modeling of Corinth canal, Greece, due to nearby faults activation. *Coast. Eng.* 78, 313–322.
- Tullis, T.E., 1980. The use of mechanical twinning in minerals as a measure of shear stress magnitudes. *J. Geophys. Res.* 85, 6263-6268.
- Turner, F.J., 1953. Nature and dynamic interpretation of deformation lamellae in calcite of three marbles. *American Journal of Science* 251, 276±298.
- Turner, F.J., 1962. "Compression" and "tension" axes deducted from {0112} twinning in calcite. *Journal of Geophysical Research* 67, 1660.
- Twiss, R.J., Geffel, M.J., 1990. Curved slickenfibers: a new brittle shear sense indicator with application to a sheared serpentinite. *J. Struct. Geol.*, 12, 173-183.
- Twiss, R.J., Protzman, G.M., Hurst, S.D., 1991. Theory of slickenline patterns based on the velocity gradient tensor and microrotation. *Tectonophysics* 186 (3–4), 215–239.
- Unruh, J. R., Twiss, R. J. & Hauksson, E. 1996. Seismogenic deformation field in the Mojave block and implications for tectonics of the eastern California shear zone. *Journal of Geophysical Research*, 101, 8335-8361.

- Vasseur, G., A. Etchecopar, & H. Philip, Stress state inferred from multiple focal mechanisms, *Annales Geophysicae*, 1, 291–298, 1983.
- Villemin, T., F. Bergerat, J. Angelier, & C. Lacasse, 1994. Brittle deformation and fracture patterns on oceanic rift shoulders : the Esja peninsula , SW Iceland, *Journal of Structural Geology*, 16 (12), 1654–1994.
- Wallace, R.E., 1951. Geometry of shearing stress and relation to faulting. *J. Geol.*, 59, 118-130.
- Wallace, R.E., Morris, H.T., 1986. Characteristics of faults and shear zones in deep mines. *Pure Appl. Geophys.* 124. 107-126.
- Walsh, J.J., Watterson, J., 1991. Geometric and kinematic coherence and scale effects in normal fault systems. In: Roberts, A.M., Yielding, G., Freeman, B. (Eds.), *The Geometry of Normal Faults*. Special Publication of the Geological Society, London 56, pp. 193±203.
- Walter, T.R., Amelung, F., 2007. Volcanic eruptions following m 9 mega thrust earth quakes: implications for the Sumatra–Andaman volcanoes. *Geology* 35, 539–542.
- Walter, T.R., Amelung, F., 2006. Volcano–earthquake interaction at Mauna Loa volcano, Hawaii. *J. Geophys. Res.* 111, B05204.
- Walter, T.R., 2007. How a tectonic earthquake may wake up volcanoes: stress transfer during the 1996 earthquake - eruption sequence at the Karymsky volcanic group, Kamchatka. *Earth Planet. Sci. Lett.* 264, 347–359.
- White, I.R., Crider, J.G., 2006. Extensional fault-propagation folds: mechanical models and observations from the Modoc plateau, north eastern California. *J. Struct. Geol.* 28, 1352–1370.
- Will, T.M., Powell, R., 1991. A robust approach to the calculation of paleostress fields from fault plane data. *Journal of Structural Geology* 13, 813–821.
- Willemsse, E.J.M., Pollard, D.D., 2000. Normal fault growth: evolution of tip line shapes and slip distribution. In: Lehner, F.K., Urai, J.L. (Eds.), *Aspects of Tectonic Faulting*. Springer-Verlag, Berlin, pp. 193–226.
- Willemsse, J.M., Pollard, D.D., Aydin, A., 1996. Three-dimensional analyses of slip distribution on normal fault arrays with consequences for fault scaling. *J. Struct. Geol.* 18, 295-309.

- Willemsse, J.M.,1997.Segmented normal faults: correspondence between three- dimensional mechanical models and field data.J.Geophys.Res.102,675–692.
- Wriggers,P., 2002. Computational Contact Mechanics. J. WileyandSons, NewYork.
- Xu S., Nieto-Samaniego A.F., Alaniz-Álvarez. S.A., 2013. Origin of superimposed and curved slickenlines in San Miguelito range, Central México. *GeologicaActa*, 11(1), 103-112.
- Yamaji, A., 2000. The multiple inverse method: a new technique to separate stresses from heterogeneous fault-slip data. *J. Struct. Geol.*, 22, 441-452.
- Yamaji, a., 2003. Are the solutions of stress inversion correct ? Visualization of their reliability and the separation of stresses from heterogeneous fault-slip data, *Journal of Structural Geology*, 25, 241–252.
- Yamaji, A., Sato, K., 2011. Clustering of fracture orientations using a mixed Bingham distribution and its application to paleostress analysis from dike or vein orientations. *Journal of Structural Geology* 33 (7), 1148–1157.
- Yamaji, A., Otsubo, M., Sato, K., 2006. Paleostress analysis using the Hough transform for separating stresses from heterogeneous fault–slip data. *Journal of Structural Geology* 28 (6), 980–990.
- Yielding, G., J. J. Walsh, and J. Watterson, 1992, The prediction of small-scale faulting in reservoirs: First Break, v. 10, p. 449-460.
- Yoffe, E., 1960. The angular dislocation. *Phil. Mag.* 5,161–175.
- Young, M.J., Gawthorpe, R.L., Hardy, S., 2001. Growth and linkage of a segmented normal fault zone; the late Jurassic Murchinson–Statfjord North Fault, northern North Sea. *Journal of Structural Geology* 23, 1933–1952.
- Yun,S.H.,Segall,P.,Zebker,H.,2006.Constraints on magma chamber geometry at Sierra Negra volcano,Galapagos islands, basedoninsarobservations. *J. Volcanol.Geotherm.Res.*150,232–243.
- Zalohar, J., Vrabec, M., 2007. Paleostress analysis of heterogeneous fault–slip data: the Gauss method. *Journal of Structural Geology* 29 (11), 1798–1810.

Zhang, L., Wu, J. C., Ge, L. L., Ding, X. L., Chen, Y. L., 2008. Determining fault slip distribution of the Chi-Chi Taiwan earthquake with gps and insar data using triangular dislocation elements. *J. Geodyn.* 45.

Zoback, M. D., and G. C. Beroza (1993), Evidence for near-frictionless faulting in the 1989 (M 6.9) Loma Prieta, California, earthquake and its aftershocks, *Geology*, 21, 181–185.

CHAPTER I: Paleostress inversion: A multi-parametric geomechanical evaluation of the Wallace-Bott assumptions

Mostfa Lejri^{1,2}, Frantz Maerten¹, Laurent Maerten¹, Roger Soliva²

¹Schlumberger – MpTC, Parc Euromédecine, 340 rue Louis Pasteur, 34790 Grabels, France

²Géosciences Montpellier, Université Montpellier 2, Place E. Bataillon, 34095 Montpellier cedex 5, France

Accepted in Tectonophysics.

Key words: stress inversion, geomechanics, Wallace-Bott, friction, fault striation, tectonic stress states, boundary element method

Abstract

Wallace (1951) and Bott (1959) were the first to introduce the idea that the slip on each fault surface has the same direction and sense as the maximum shear stress resolved on that surface. However, this simplified hypothesis is questionable since fault mechanical interactions may induce slip reorientations. Earlier numerical geomechanical models confirmed that the slickenlines (slip vectors) are not necessarily parallel to the maximum resolved shear stress but are consistent with local stress perturbations. This leads us to ask as to what extent the Wallace and Bott simplifications are reliable as a basis hypothesis for stress inversion from fault slip data. Here, a geomechanical multi-parametric study using a 3D boundary element method, covering (i) fault geometries such as intersected faults or corrugated fault surfaces, (ii) the full range of Andersonian state of stress, (iii) fault friction, (iv) fault fluid pressure, (v) half space effect and (vi), rock properties, is performed in order to understand the effect of each parameter on the misfit angle between geomechanical slip vectors and the resolved shear stresses. It is shown that significant misfit angles can be found under specific configurations invalidating the Wallace and Bott assumptions, even though fault friction tends to minimize the misfit. We therefore conclude that in such cases, stress inversions based on fault slip data should be interpreted with care.

1. Introduction

Faulting of the brittle crust can only occur in the presence of a driving stress, which often is of tectonic origin. Its estimation is therefore essential for a better understanding of the regional tectonic history, earthquake physics, seismic hazard assessment as well as for a better exploitation of natural reserves (Célérier et al., 2012). For this purpose, stress inversion methods have been developed during the last three decades for estimating the state of stress either using focal mechanisms or fault slip measurements.

Nowadays, all commonly accepted stress inversion methods use the simple but central Wallace (1951) and Bott (1959) assumptions, which stipulate that when faulting occurred, the shear stress resolved onto the fault plane is parallel to the slip vector and thus could be used to determine the stress tensor. In 1959, Bott demonstrated that the striation line orientation on a given reactivated plane of weakness depends only on the orientation of the principal stresses, the stress ratio and the normal of the plane. In addition, Wallace-Bott (WB) assumptions assumes that faults are planar, that blocks are rigid, that neither stress perturbations nor block rotations along fault surfaces occur and that the applied stress state is uniform.

It eventually became clear that observed striations along fault planes (Angelier, 1994; Célérier et al., 2012; Lacombe, 2012; Lisle, 2013) could be used to invert for paleostress but also with the recognition that the reliability of the inversion is strongly dependent on the hypothesis used. The earliest methods based on this hypothesis, developed by Arthaud (1969), Carey and Brunier (1974) and Angelier (1975), led to the generalization of the fault-slip analysis discipline (Angelier and Mechler, 1977; Etchecopar, 1984; Simon-Gómez, 1986; Reches, 1987; Angelier, 1990; Hardcastle and Hills, 1991; Nemcok and Lisle, 1995; Wallbrecher et al., 1996; Célérier et al., 2013). Many algorithms based on WB assumptions have been developed to perform stress inversion (Carey and Brunier, 1974; Angelier, 1975 and 1979; Etchecopar et al., 1981; Gephart and Forsyth, 1984; Michael 1984; Celerier, 1988; Lisle, 1992 and 1998; Yamaji, 2000; Delvaux and Sperner, 2003; Žalohar and Vrabec, 2007; Hansen, 2013) and successful applications in numerous regional studies

consolidated the strength of these assumptions (e.g. Mattauer and Mercier, 1980; Letouzey and Tremolière, 1980; Zoback et al., 1981; Angelier et al., 1985; Barrier and Angelier, 1986; Letouzey, 1986; Bergerat, 1987; Mercier et al., 1989; Huchon et al., 1991; Lacombe et al., 1990; Vandycke et al., 1991; Lacombe et al., 2001; Liesa and Simon, 2009).

However, one of the main limitations, which is rarely reported, is that the WB assumptions assume that all the slickenlines measured were created synchronously, which is typically not true. Once a fault underwent slip, the stress can rotate for the next slip on the nearby fault. Furthermore, this basic hypothesis is also questionable, since Wallace and Morris (1986) and Tibaldi (1998) reported that observed geometrical complexity of fault surfaces and fault networks may induce heterogeneity in fault slip directions. Hancock (1985) and Petit (1987) studied evidences of local stress perturbations in microstructures, while others (Twiss and Geffel, 1990; Twiss et al., 1991; Pascal, 1998) observed block rotations along fault surfaces. Gapais et al., (2000) showed two examples of faulted regions to illustrate the spatial variability of fault-slip data either due to local complications at the edges of fault blocks, or to complex kinematic conditions at regional boundaries. These findings question about the extent that the WB simplifications are reliable when used for stress inversion.

Debates have been initiated by Pollard et al. (1993) and Dupin et al. (1993) who checked the validity of the WB assumptions by using mechanical modeling methods (i.e. taken into consideration internal deformation of faulted blocks and local stress perturbation between faults). According to the results of Dupin et al. (1993), the discrepancy angle between mechanical and WB predicted slickenlines reaches 47° for intersecting faults. Pollard et al. (1993) predicted a maximum of 37° discrepancy angle for fault interaction and a 10° misfit angle caused by fault tip geometry.

Later, Nieto-Samaniego and Alaniz-Alvarez (1997) proposed that the slickenlines on a restricted fault surface should be parallel to the intersection line and therefore could deviate from the resolved shear stress

orientation. Maerten (2000) explored the consequences of varying geometry of intersecting faults on slip directions using 3D boundary element methods (Thomas, 1993; Maerten et al., 2014). He concluded that significant deviations are expected close to fault intersections and for which the misfit angle can reach values greater than 50°. This result has been confirmed by field observations along the Chimney Rock fault array in Utah, USA (Maerten, 2000). Xu et al. (2013) compared observed fault striations in the San Miguelito Range with the fault interaction model of Maerten (2000) and found that the slickenlines patterns are consistent with the geomechanical model. The majority of the slickenlines is not parallel to the resolved shear stress but is consistent with stress perturbations caused by fault mechanical interaction.

Another approach was used by Pascal (2002) using 3D distinct element method (Cundall, 1971 and 1988) to demonstrate that the differences between WB and mechanical models are negligible due to the implication of the sliding friction, which reduces the misfit angle between resolved shear stress and slip vector. The two fault models used by Pascal (2002) under three stress states with a constant friction coefficient ($\mu = 0.58$) show little angular discrepancy. Therefore, Pascal (2002) concluded that the friction effect leads to a reduction of slip perturbation, which validates the WB assumptions for tested geometries and boundary conditions.

More recently, Kaven et al. (2011) pointed out that even if the stress inversion results are similar, WB type inversions perform poorly for limited ranges of slickenline orientations when compared to their proposed mechanical stress inversion method. Furthermore, Lisle (2013) showed from simple models, that any stress field anisotropy such as that arising from 3D fault geometry, can lead to a significant angular difference between the directions of maximum shear stress and the slip direction predicted by the WB assumptions. Thus, studies conducted with classical stress inversion methods do not fully take into account the full range of stress boundary conditions (i.e. stress tensor principal directions and stress ratio), fault and material properties (i.e. friction coefficient and Poisson's ratio) as well as the effect of traction free Earth

surface (i.e. half-space). Methods of paleostress analysis have, by necessity, incorporated a significant degree of flexibility with respect to the implementation of the WB assumptions.

In this paper, a multi-parametric study, covering variation in fault geometry, the full range of Andersonian state of stress, multiple friction coefficients, fluid pressure, the half space effect and Poisson's ratio variation, is performed in order to understand the effect of each parameter on the misfit angle between geomechanical slip vector and resolved shear stress. It is shown that significant misfit, which could invalidate the WB assumptions, is to be expected for specific configurations.

2. Method

2.1. Numerical tool

To evaluate the consistency of the WB based stress inversion methods, a comparison between resolved shear stress and mechanical slip vector computed from 3D numerical simulations is performed. In order to test the influence of fault geometries, friction coefficient, Poisson's ratio, and tectonic stress conditions, iBem3D, a boundary element method (BEM) for elastic isotropic and heterogeneous half-space (Thomas, 1993; Maerten et al., 2014), formerly called Poly3D, is used through a scripting language. For our purpose, this code is fast enough (Maerten, 2010a), avoids boundary effects as in Finite Element or Discrete Element methods, and allows the use of fault friction, which has been implemented using a Gauss-Seidel iterative solver with inequality constraints (Maerten et al., 2010b). This methodology for implementing friction (Maerten et al., 2010b) appears to be stable and less subject to round off errors compared to other techniques (Lagrange multipliers, Penalty methods, or complementary problem). Although heterogeneous and anisotropic sliding friction distribution can be used, we employ a constant friction for the whole sliding fault surface, making the results easier to analyze and comprehend. Another advantage of this numerical method is that fault surfaces are discretized using three dimensional triangulated meshes, allowing complex fault geometries and fast model construction. As a result, modeled faults will mechanically interact and slide

in response to the applied 3D tectonic stress, rock properties and fault friction. The result of the simulation, which is of interest to us, is the heterogeneous slip orientation along the fault planes.

We assume that the discrepancy between resolved shear stress orientation (WB assumptions) and computed slip vector is caused by the mechanical interactions between adjacent or intersecting faults. Here, we test the parameters that may influence these mechanical interactions. For all simulations done in the coming sections, when a parameter is not tested, its default value is given in Table 2. Furthermore, to facilitate the reading of this paper we have listed and defined all variables and parameters in Table 1.

2.2. Fault geometry

A generally accepted parameter controlling fault mechanical interaction is the fault geometry. With that respect, Dupin et al. (1993), Pollard et al. (1993), Maerten (2000) and Lisle (2013) have tested several fault configurations. Maerten (2000) tested the effect of intersecting normal faults with different strike angles under an uniaxial vertical remote stress ($\bar{R} = 0$) and reported that when the angle between the strike of the two faults is near 30° , the discrepancy angle between the resolved shear stress and the computed slip vector reaches 50° close to the fault intersection line. Xu et al. (2013) observed the same discrepancy on similar pair of intersecting normal faults with 300° and 340° strike directions. Lisle (2013) suggested that the slip directions associated with contemporaneous sliding on a non-orthogonal pairs of planes will violate the WB assumptions.

Following the earlier studies on the influence of fault geometry on the misfit angle between slip vectors and resolved shear traction vectors (Dupin et al., 1993; Pollard et al., 1993; Maerten, 2000; Pascal, 2002; Kaven et al., 2011; Resor and Meer, 2009; Lisle, 2013), planar faults, intersected faults and sinusoidal faults have been investigated.

In this study, analyzing the mean misfit for complex fault geometries can be a difficult task. We therefore need to understand its behavior for a single planar elliptical fault. The planar elliptical fault used in this study has an aspect ratio of 2 and a friction coefficient of 0.3. We study here different dip angles ($\beta = 0^\circ$ to 90°).

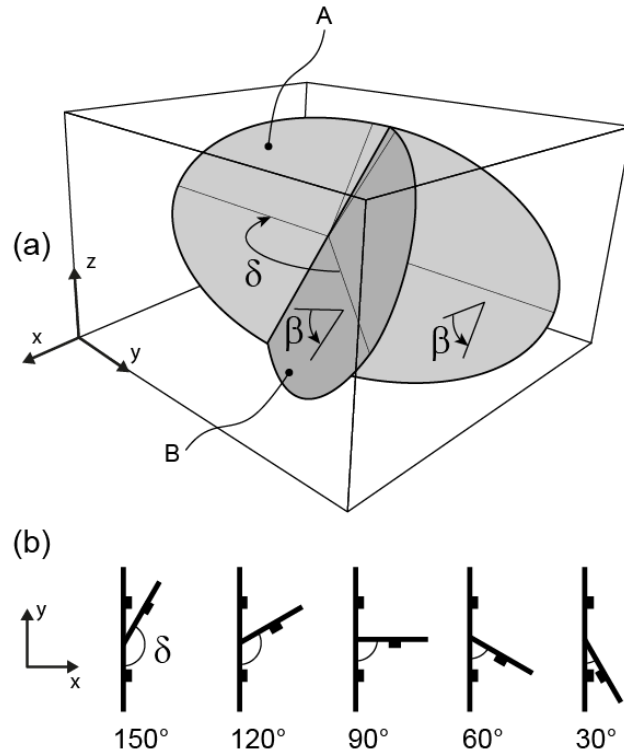


Figure 1. 3D BEM geometry model of intersecting faults. (a) 3D view of one fault model, and (b) different intersecting fault patterns where the angle between the strike of 2 intersecting faults, δ , varies from 30° to 150° . The dip angle, β , of the two faults, defined by the dip line and the horizontal line, is 60° .

We adopt the same geometry as in Maerten (2000) (Figure 1), which consists of two normal faults, (A) the main fault and (B) the secondary fault, dipping at $\beta = 60^\circ$ with an elliptical tip line and an aspect ratio of 2, defined by the ratio of the horizontal length over the fault dip dimension. This relative average aspect ratio is commonly observed for isolated normal fault (Rippon, 1985; Barnett et al, 1987; Walsh et al. 1989; Nicol et al., 1996). Fault A truncates fault B, and both faults are linked at their centers with an oblique

intersection line. δ is defined by the angle between the strike lines of the faults (Figure 1). Here δ varies from 30° to 150° with a 30° increment. $\delta = 30^\circ$ and $\delta = 150^\circ$ are considered to be acute angles between the faults, while 90° angle is typical of orthogonal fault system geometry, whereas $\delta = 0^\circ$ and $\delta = 180^\circ$ faults are equivalent to single planar fault geometry. Reverse and wrench fault configuration are also tested (Figure 10)

Finally, we tested corrugated fault geometries (Lisle, 2013). Some natural faults present sinusoidal surfaces like the Flowers Pit Fault, Oregon (Sagy and Brodsky, 2009; Sagy et al., 2007), the sub vertical strike-slip faults in the central Sierra Nevada, California, (Griffith et al., 2009) and the Arkitsa fault surface with 1 to 5 m corrugations (Resor and Meer, 2009). The 3D undulations of the fault surface (Power et al., 1987; Lee and Bruhn, 1996) are thought to be influential in term of mechanical behavior of slip during its reactivation (Marshall and Morris, 2012; Chester and Chester, 2000; Saucier et al., 1992). In order to evaluate this hypothesis, Resor (2009) used observations from the Arkista normal fault in central Greece and observed a misfit angle of 4.8° in comparison to those predicted by the remote stress tensor determined by the *Fault and Stress Analysis software* (Celerier, 2006) based on WB assumptions. On the same idea, Lisle (2013) tested a 3D model with linear corrugations made of planar fault segments (with $\mu = 0.58$ and Cohesion = 0) and found that the slip direction is not always parallel to the maximum resolved shear stress direction. Following these observations, a second geometric configuration has been studied. It includes corrugated faults with increasing amplitude to wavelength ratio (Am), which is given by the formulation of Ritz and Pollard (2012), and Marshall and Morris (2012). It consists of a normal fault with a sinusoidal geometry (Figure 2), dipping at 60° with an aspect ratio of 2 and amplitude to wavelength ratio Am . Here, Am varies from 0.1 to 0.5. In order to avoid aliasing effects of a coarse mesh on the geometry, hence on the results, we used homogeneous and densely triangulated surfaces such that the number of triangular elements along the wavelength is 35.

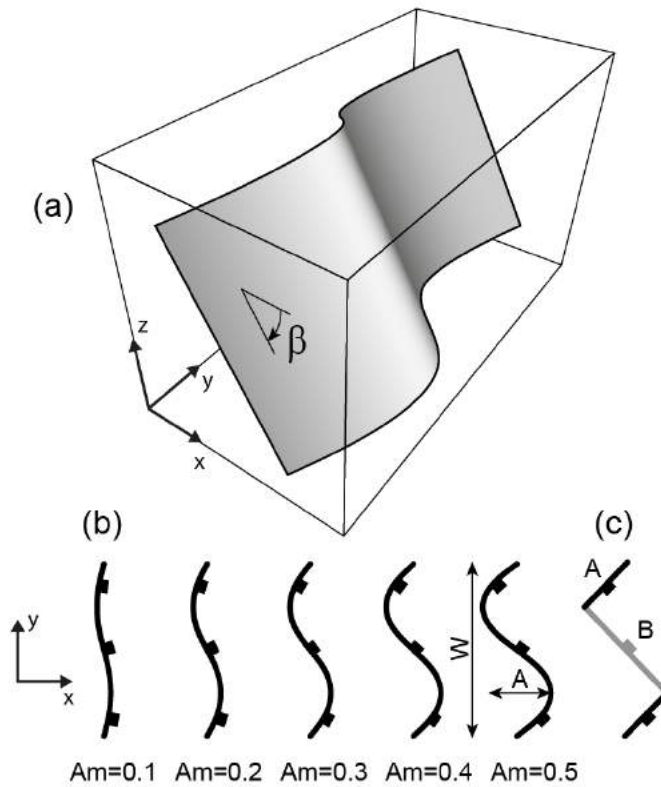


Figure 2. 3D BEM geometry model of corrugated faults. (a) 3D view of one fault model, and (b) different corrugated fault geometry where amplitude to wavelength ratio, $Am=A/W$, varies from 0.1 to 0.5. The dip angle, β , of the fault, defined by the dip line and the horizontal line, is 60° .

2.3. Tectonic stress

Another important parameter to test is the tectonic stress. According to Lisle et al. (2006) and as predicted by Anderson (1951), one of the principal stress directions must be vertical for a flat Earth. Therefore, we chose to use only Andersonian tectonic stresses where one of the principal stresses is vertical, which allows a better determination and understanding of the results.

To our knowledge, no studies have explored, in depth, the effect of all possible Andersonian tectonic stresses on both the slip distribution and the slip vectors along interacting faults. As opposed to Maerten (2000), Pascal (2002) and Lisle (2013), where limited tectonic stresses have been used, here we employ the full range of possible Andersonian stresses and orientations in order to investigate heterogeneous fault slip orientation.

Depending on which of the principal stresses is vertical, $\sigma_v = \sigma_1$, $\sigma_v = \sigma_2$ or $\sigma_v = \sigma_3$, the three tectonic regimes, normal, wrench and reverse, can be described respectively. The permutation of one of the horizontal principal stress axes with the vertical one allows switching from one tectonic regime to another. Furthermore, depending on the relative magnitudes of the intermediate principal stresses, σ_2 , with respect to the two other principal stresses, σ_1 and σ_3 , each tectonic regime can vary continuously from radial to axial. All these information are included in the stress ratio R , which also describes the shape of the stress ellipsoid. R is defined by:

$$R = \frac{(\sigma_2 - \sigma_3)}{(\sigma_1 - \sigma_3)}, \text{ with } 0 < R < 1 \quad (1)$$

When R increases from 0 to 1, σ_2 increases from σ_3 to σ_1 .

Because the stress ratio R varies from 0 to 1 for the three tectonic stress regimes, we define, for practical reasons, the stress ratio \bar{R} such as:

$$\left\{ \begin{array}{l} \text{Normal } \bar{R} = R \in [0,1] \\ \text{Wrench } \bar{R} = 2 - R \in [1,2] \\ \text{Reverse } \bar{R} = 2 + R \in [2,3] \end{array} \right\} \quad (2)$$

Here, depending on which of the principal stresses is vertical, we can cover the normal, wrench and reverse regimes with $\sigma_v = \sigma_1$, $\sigma_v = \sigma_2$ and $\sigma_v = \sigma_3$ respectively, with only one parameter that varies from 0 to 3 continuously. The orientation θ of the maximum principal horizontal stress defined clockwise from North is also tested.

2.3. Fault friction

A parameter that can have a strong effect on the degree of fault mechanical interactions, hence heterogeneous slip vector distribution, is the sliding friction (Soliva et al., 2010). Pascal (2002) showed that even with intersecting faults, therefore potentially highly interacting fault (Maerten, 2000), the WB

assumption is still valid when friction is high. However, results are based on a single two intersecting fault configuration with a unique coefficient of friction ($\mu = 0.58$). Similarly, Lisle and Srivastava (2004) observed, from a compilation of 228 stress analyses, patterns strikingly similar to those predicted by a frictional model for fault reactivation, validating the WB assumptions using frictional fault reactivation. Further exploration with other friction coefficients is considered here, and values of 0, 0.3, 0.6 and 0.9 are used for all simulations (see Table 2).

2.4. Fault fluid pressure

In high water pressure conditions, fluid pressure P reduces the effective normal stress σ_n on a fault plane and consequently may affect both the slip magnitude and the slip vector orientation. So, an increase in fluid pressure could be regarded as a decrease in an equivalent sliding friction. However, excess in fluid pressure cannot be modeled solely using an equivalent friction as this would mean using negative friction. We therefore analyze the effect of fault fluid pressure on the misfit angle between resolved the shear stresses and the slip vectors with the simple direct use of fluid pressure inside the modeled faults. The applied pressure has been normalized against the magnitude of the applied maximum principal stress, σ_1 , and three values for the normalized pressure have been investigated, 0.3, .6 and 0.9. For this set of simulations, we also consider three special cases for which σ_3/σ_1 equals 0, 0.3 and 0.6 since P has no effect on the misfit when $P \leq \sigma_3$.

2.5. Traction free surface of the Earth

Faults can be reactivated in the deep crust or in the subsurface where confinement is weak. A traction free surface of the Earth can modify the slip distribution on faults. Barton (1973) and Hoek and Bray (1981) and Zoback (1985) suggested that stress field anisotropy is likely to be more important at shallow burial environments with weak confinement. Consequently, we decided to investigate the effect of half space on

the slip vector distribution and compare the results with the whole space condition on a north striking, 60°E dipping half-elliptical fault (see Figure 3).

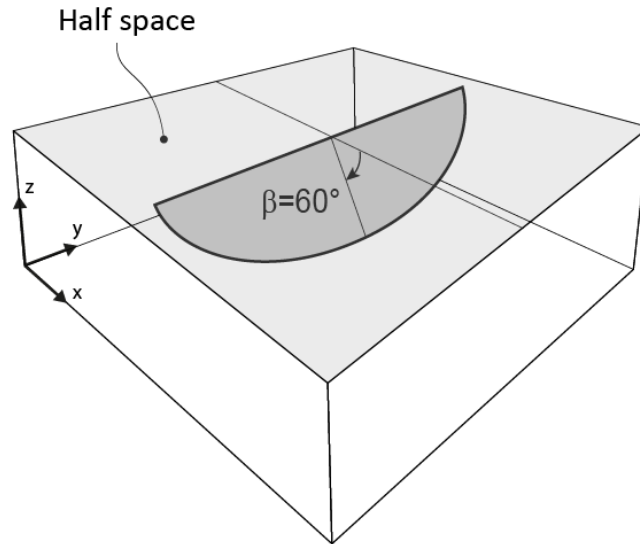


Figure 3. 3D BEM geometry of planar semi-elliptical fault in contact with the traction free surface of the Earth (half space option). The dip angle, β , of the fault, defined by the dip line and the horizontal line, is 60°.

2.6. *Poisson's ratio*

Other parameters that have been rarely investigated with respect to fault slip distributions are the elastic properties of rock. Since Young modulus will only affect stress magnitudes for homogeneous and isotropic materials, and therefore fault slip magnitude (Bourne and Willemse, 2001), it will not affect slip vector. It is therefore not studied here. However, Poisson's ratio can have an effect on perturbed stress distribution, hence we estimated that it was necessary to quantify its effect on the fault slip vector distribution. We chose to study the effect of Poisson's ratio within the range of allowable limits for elastic materials ($\nu=0.01$, $\nu =0.25$ and $\nu =0.49$), the rationale for testing the extreme values being for a purely parametric standpoint.

2.7. Non-tested parameters

Although it is recognized that heterogeneous rock properties, pore pressure, fault opening, cohesion, temperature and plasticity effects could also affect fault mechanical interactions (hence heterogeneous slip vector distribution), these parameters have not been investigated in this study. In the case of opening along the fault plane caused by high fluid pressure inside the fault, fibrous minerals can grow in voids and be interpreted as displacement indicators (Lisle, 2013). Faults are assumed to be cohesionless at relatively shallow depths (Byerlee, 1978) thus cohesion is set to zero and is not tested. In the earth's crust, temperature gradient and rock heterogeneity may have an impact on heterogeneous nature of the mechanical properties (Kocabas, 2004). In order to keep the results easy to analyze, the medium surrounding the faults is considered homogeneous and isotropic, while neglecting crust temperature gradient effects. Finally, it is reasonable to think that rocks around sliding discontinuities (i.e. faults) may undergo plastic deformation. Local impact of plasticity on mechanical slickenline directions and displacement magnitudes for frictional faults can be an important variable to assess. Although the uniform shear strength and uniform remote stress result in large slip gradients near tip line, in this study, large-scale fault reactivations are supposed to take place in a simple-elastic upper-crust material. Indeed, inelastic or plastic deformations, as well as cohesive zones, have little effect on the distribution of slip over the majority of faults (Willemsse et al., 1996; Maerten, 2000). Therefore, plastic behavior is not taken into account in the present study.

2.8. Mean misfit angle calculation and domain representation

In order to compute the misfit angle between the resolved shear stress and the mechanically derived slip vector, a multi-parametric tool capable of running and analyzing thousands of simulations integrating both the WB assumptions and the geomechanical models was created.

The basis of all paleostress inversion techniques is that the direction of the shear traction $\vec{\tau}$ on the fault plane tends to be parallel to the slip vector \vec{u} . The value of $\vec{\tau}$ is found by subtracting the normal traction from the total traction:

$$\vec{\tau} = \sigma \cdot \vec{n} - [(\sigma \cdot \vec{n})\vec{n}]\vec{n}, \quad (3)$$

where σ is the tectonic stress and \vec{n} is the fault plane normal.

According to the WB assumptions, shear traction vectors are used to define slip vectors, and therefore striation line orientations. In the BEM simulations used in this study, shear traction vectors are used as initial boundary values along 3D discontinuities (i.e. faults). These initial shear traction vectors will make the faults slip according to the equilibrium equation:

$$G\vec{u} + \vec{\tau} = 0 \quad (4)$$

where G is the matrix of Green's functions that relates the slip to the traction for triangular elements. For \vec{u} to be similar to $\vec{\tau}$, G needs to be an identity matrix. In a mechanical model, this condition is never met since G is related to the fault geometry and material properties (Maerten et al., 2014).

If we consider a fault surface made of triangular elements, then for a given element, we define the misfit angle ω (Figure 4) as:

$$\omega = \cos^{-1}|\vec{\tau} \cdot \vec{u}| \quad (5)$$

in which $\vec{\tau}$ and \vec{u} are normalized and \cdot represents the dot product.

We also define the mean misfit angle, $\bar{\omega}$ on a fault as the mean of all constitutive element misfit angles on the fault. This is done without weighting each misfit by the element area because the triangular mesh used is homogeneous with a maximum of a $\pm 3\%$ area difference between elements.

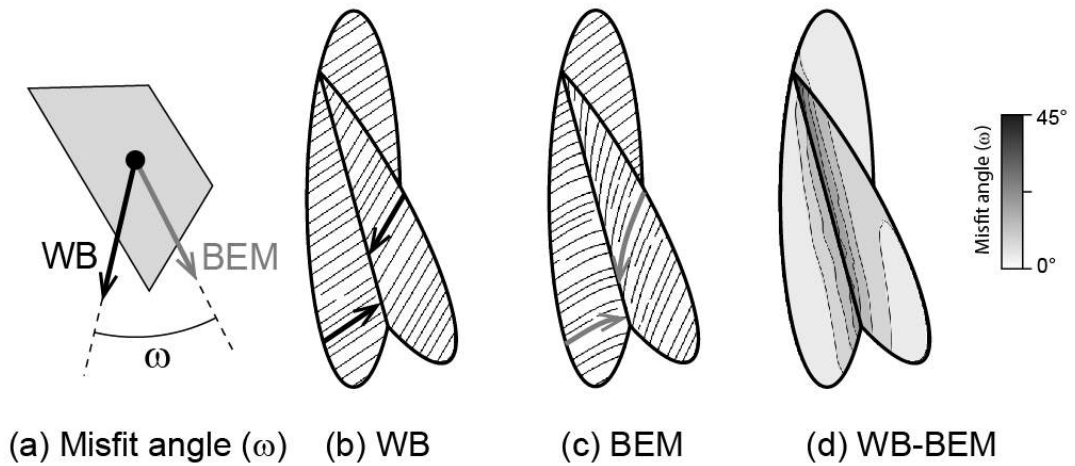


Figure 4. Misfit angle (ω) between resolved shear stress (WB) and computed slip vector (BEM). (a) A simple representation of ω reported to a unit element. (b) and (c) are predicted slip vectors from WB assumption and from BEM simulation respectively. (d) Distribution of ω along the intersected fault model.

The mean misfit angle domain ($\bar{\omega}$ domain) (see Figure 5a), used to analyze the multi-parametric simulations, is a 2D parameter space that covers the full Andersonian tectonic configurations. As an example, the $\bar{\omega}$ domain highlighted in Figure 5a is from two intersecting faults where the angle between the fault strikes is 30° and the friction coefficient is 0.3. The x-axis represents the stress ratio \bar{R} , whereas the y-axis is the orientation θ of the maximum principal horizontal stress defined clockwise according to the North. For a given tectonic stress, $\sigma(\bar{R}, \theta)$, represented by point P in Figure 5a, $\bar{\omega}$ is computed and reported in the 2D domain as a color coded point. The same procedure is repeated for each point of the $\bar{\omega}$ domain until the entire parameter space is covered. The $\bar{\omega}$ domain is covered with a resolution of 100×100 , which makes a total of 10,000 geomechanical simulations per domain.

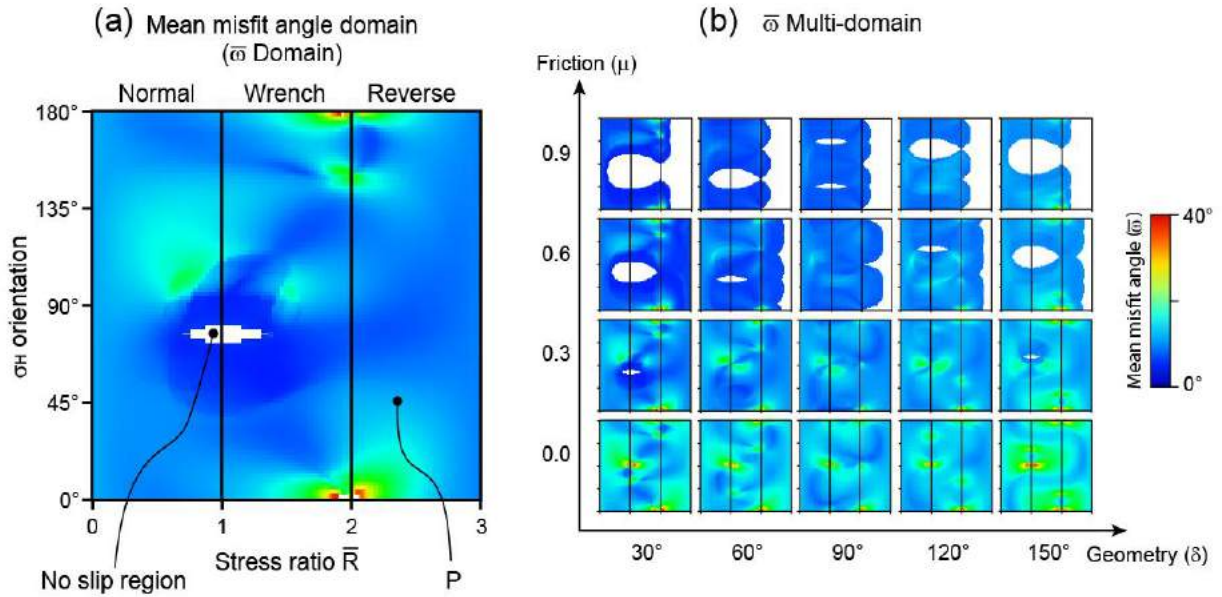


Figure 5. $\bar{\omega}$ domain and $\bar{\omega}$ multi-domain representation. (a) The $\bar{\omega}$ domain covers both the full tectonic stress regimes (\bar{R}) in the x-axis and the orientation of the maximum principal horizontal stress σ_H on the y-axis for a specific model ($\delta = 30^\circ$, $\mu = 0.3$). (b) The $\bar{\omega}$ multi-domain displays $\bar{\omega}$ domains (a) for specific parameters. Here intersecting fault geometries (δ) in the x-axis and friction coefficient (μ) in the y-axis.

The $\bar{\omega}$ domain in Figure 5a highlights for which model configurations the highest $\bar{\omega}$ (hot colors) and the lowest $\bar{\omega}$ (cold colors) can be found. White regions in the domain are defined as models configurations where no slip is computed, therefore no misfit angle can be estimated.

We further define the mean misfit angle multi-domain ($\bar{\omega}$ multi-domain), as the evolution of $\bar{\omega}$ with respect to the variation of other parameters such as the friction, the fault geometry or the material properties (see Figure 5b). In this example, friction evolution is reported on the main Y-axis, while fault geometry (fault strike angle δ) is reported on the main X-axis. This type of representation allows a quick and efficient analysis of 5 different parameters on the misfit angle.

3. Results

3.1. Effect of fault geometry

3.1.1. Single planar fault

Analyzing the pattern of the $\bar{\omega}$ domain for complex fault geometries can be a difficult task. We therefore need to understand the pattern observed for a single planar elliptical fault. In Figure 6, the main X-axis represents the tested fault dip angles ($\beta = 0^\circ$ to 90°), while the main Y-axis represents the fault strike ($\alpha = 0^\circ$ and 60°). For a single planar elliptical fault, it is important to note that the maximum misfit angle for such geometric fault configuration is low (maximum $\omega = 2.7^\circ$). For a NS-striking fault ($\alpha = 0^\circ$) and fault dipping 60° E ($\beta = 60^\circ$), three regions for which $\bar{\omega}$ is very low are highlighted in blue (see Figure 6). These regions are interpreted as pure normal, pure wrench and pure reverse regimes as illustrated on graph of Figure 7, which shows similarities with the graph presented by Célerier and Seranne (2001, Figure 2). $\bar{\omega}$ is also very low for σ_H orientations orthogonal or parallel to the fault plane ($\theta = 0^\circ$ or 180° and $\theta = 90^\circ$). White regions in the domain represent model configurations where no slip is computed, therefore no misfit angle can be estimated. This is the case when the fault is horizontal ($\beta=0^\circ$), where the entire domain is white and when the fault is vertical ($\beta=90^\circ$), where the domain is white only for 4 stress configurations: $\bar{R} = 1$, $\bar{R} = 3$, $\theta = 0^\circ$ or 180° and $\theta = 90^\circ$). This is represented by straight white lines in the stress domain, while $\bar{\omega}$ is constant for the rest of the domain ($\bar{\omega}=1.2$, light blue color). Otherwise, $\bar{\omega}$ is higher and is displayed as colored pattern in the remaining domain (Figure 6 and Figure 7). When fault dip increases, the low $\bar{\omega}$ regions around the 'pure wrench' area expand, while the high $\bar{\omega}$ regions become thinner. For a given dip angle of a single elliptical fault (i.e. $\beta = 60^\circ$ in Figure 6), when fault strike changes (α), the same $\bar{\omega}$ pattern is observed except that it is shifted by the amount of fault strike angle, α .

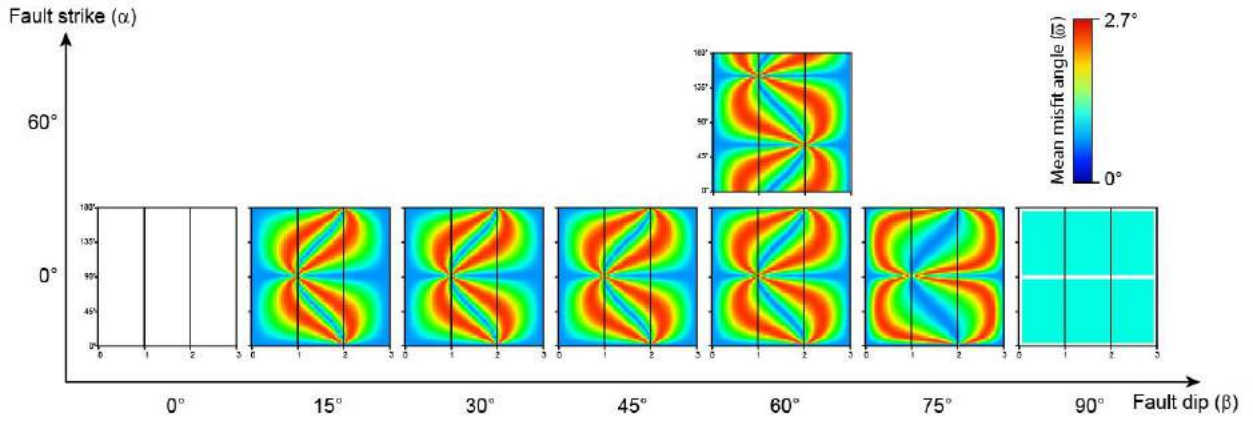


Figure 6. $\bar{\omega}$ multi-domain for a planar elliptical fault, where fault strike (α) and fault dip angle (β) are the tested parameters.

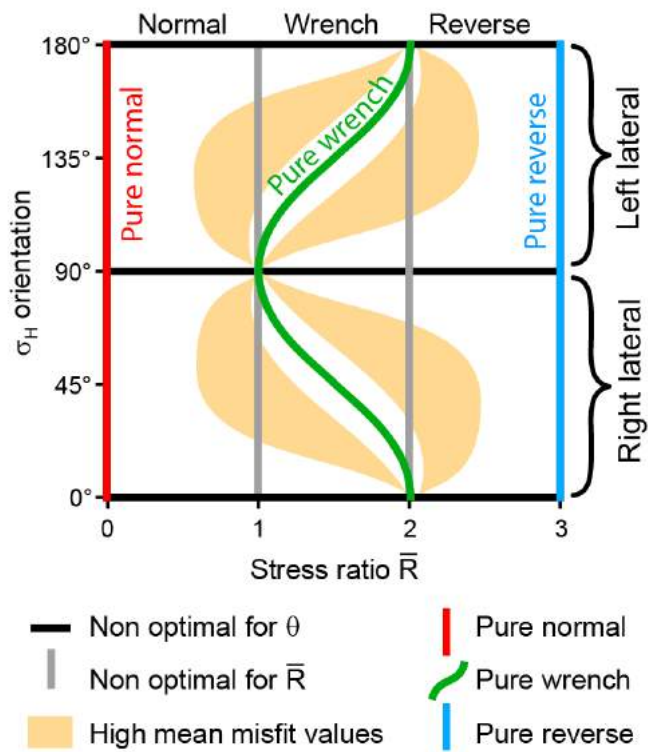


Figure 7. Standard $\bar{\omega}$ domain for a planar elliptical fault with $\alpha = 0^\circ$, $\beta = 60^\circ$. It shows main features of $\bar{\omega}$ distribution.

3.1.2. Intersecting faults

Understanding the $\bar{\omega}$ domain pattern for two intersecting faults is easier if described as the result of the combination of two single planar faults. Analysis of Figure 8 shows that $\bar{\omega}$ is notably increased around

specific tectonic stress as illustrated in Figure 8.c at location A ($\bar{R} = 1, \theta = 90^\circ\text{N}$), A' ($\bar{R} = 1, \theta = 60^\circ\text{N}$), B ($\bar{R}=2, \theta = 0^\circ\text{N}$) and B' ($\bar{R}=2, \theta = 150^\circ\text{N}$). The distance between pair of points A-A' and B-B' corresponds to the difference between the principal and secondary fault strike δ (Figure 8.c). When friction ($\mu = 0.3$) is added (see Figure 8b), the misfit $\bar{\omega}$ is slightly reduced in the entire domain except in a large area where points A and A' were located. Here, slip along the faults reaches zero as shown with the white area at (point C).

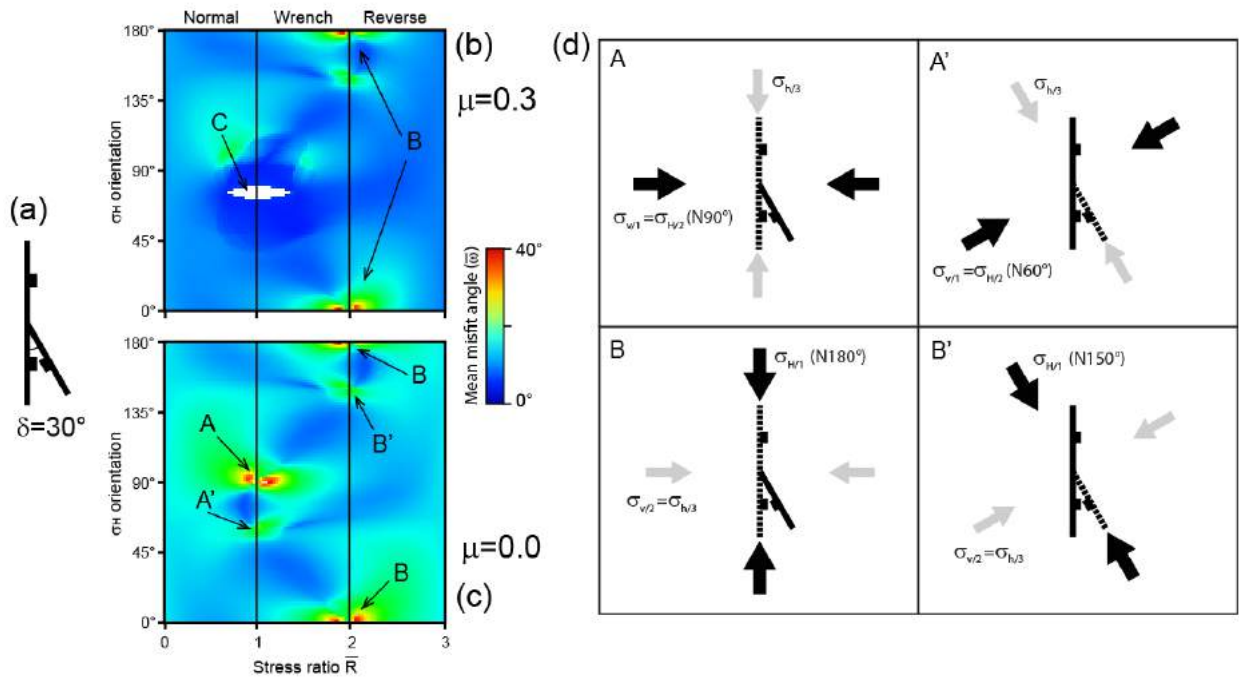


Figure 8. Example of complex $\bar{\omega}$ domain for (a) an intersecting fault geometry ($\delta = 30^\circ$) and varying friction coefficient, (b) $\mu = 0.3$ and (c) $\mu = 0$. (d) Model configurations for points A, A', B and B'.

$\bar{\omega}$ is shown in the $\bar{\omega}$ multi-domain of Figure 9. The horizontal axis of this $\bar{\omega}$ multi-domain is the strike angle between the two intersecting faults (δ) described in section 2.2 while the vertical axis is the sliding friction (μ). The global trend of the observed $\bar{\omega}$, for frictionless faults ($\mu = 0$), is higher for acute angle ($\delta = 30^\circ$ or 150°) between fault strikes and lower for faults with orthogonal intersection ($\delta = 90^\circ$). We also observe that $\bar{\omega}$ is globally higher when the two intersecting faults have an opposite dip azimuth (as for $\delta = 30^\circ$).

In Figure 10, the dip angles of the intersecting faults have been changed ($\beta = 30^\circ$ and $\beta = 90^\circ$) while the acute angle between the fault strike has been kept constant ($\delta = 30^\circ$). We observe that white region of the tectonic stress domain are concentrated in the normal and wrench stress regimes when friction increases. Similarly, when fault dip angle is $\beta = 90^\circ$, the white regions of the tectonic stress domain are concentrated in the normal and reverse stress regimes when friction increases.

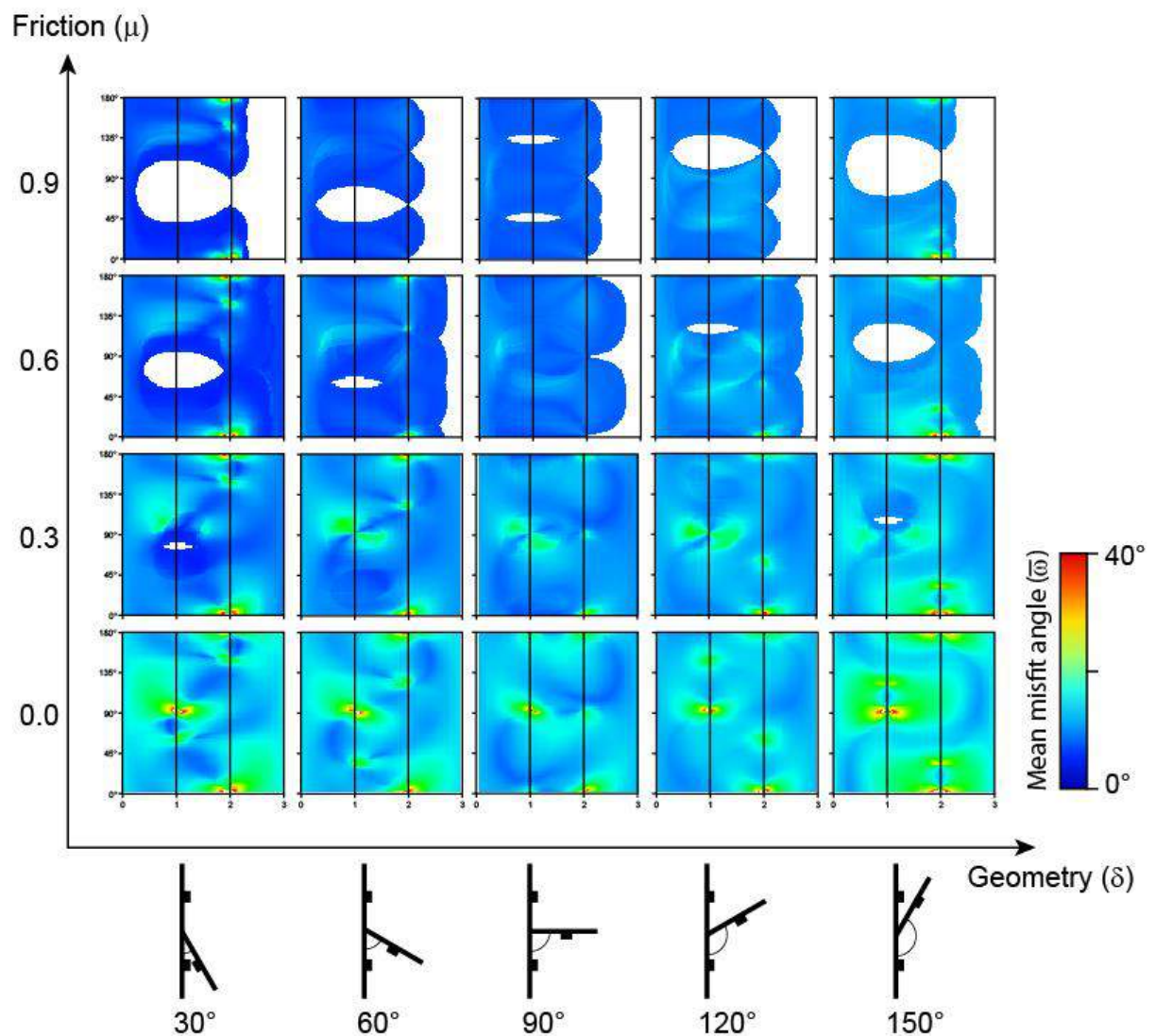


Figure 9. $\bar{\omega}$ multi-domain for the intersecting fault geometry variation (δ). For each intersecting fault geometry (x-axis) and friction coefficient (μ -axis), a $\bar{\omega}$ domain is computed and $\bar{\omega}$ is displayed.

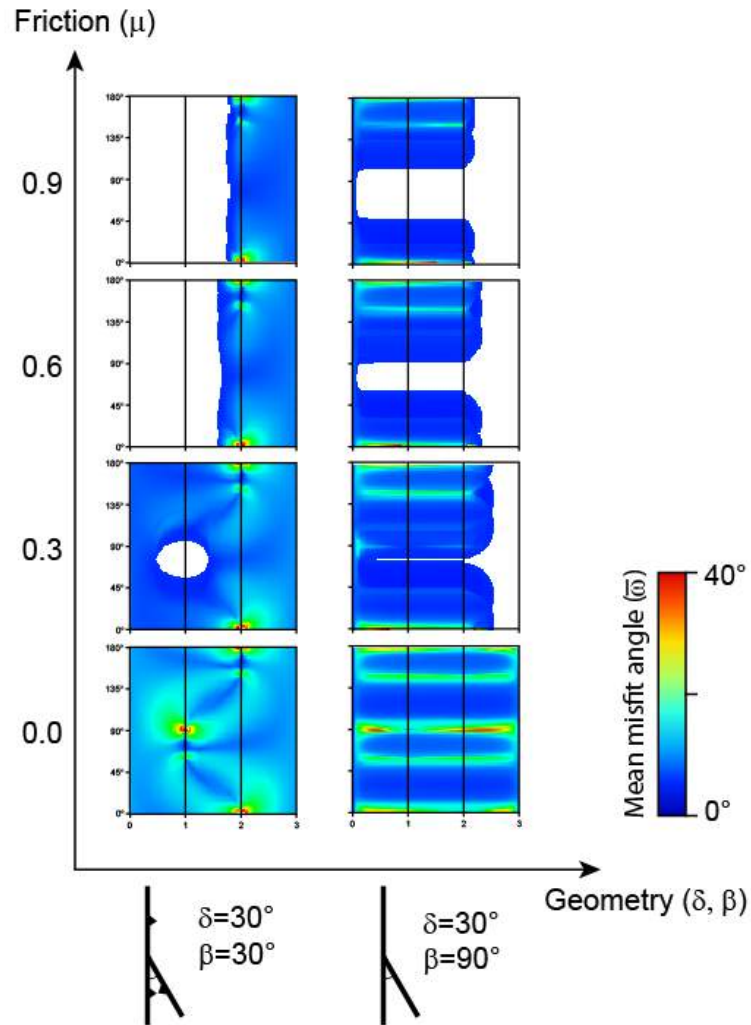


Figure 10. $\bar{\omega}$ multi-domain for the intersecting fault geometry ($\delta = 30^\circ$) and varying dip angle, $\beta = 30^\circ$ for reverse faults and $\beta = 90^\circ$ for wrench faults. For each fault pattern (x-axis) and friction coefficient (y-axis), a $\bar{\omega}$ domain is computed and $\bar{\omega}$ is displayed.

3.1.3. Sinusoidal faults

The mean difference between predicted WB slip vectors and mechanically computed slip vectors is shown in the $\bar{\omega}$ multi-domain of Figure 11. The horizontal axis of this $\bar{\omega}$ multi-domain is the amplitude Am of the corrugated fault, while the vertical axis is the sliding friction angle. A 35° maximum $\bar{\omega}$ is observed for $\mu = 0$, while the average $\bar{\omega}$ is higher for the high amplitude geometry (see Figure 11).

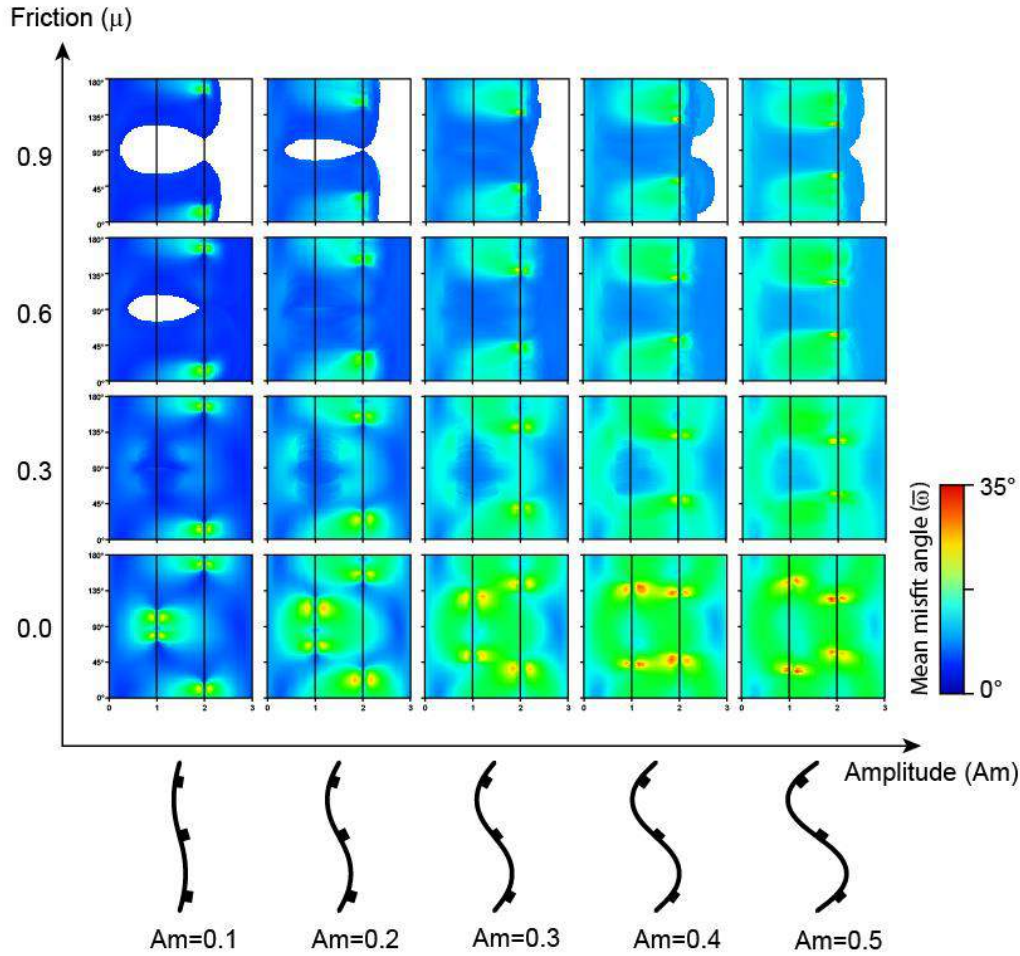


Figure 11. $\bar{\omega}$ multi-domain for the corrugated fault geometry variation (A_m). For each fault geometry (x-axis) and friction coefficient (y-axis), a $\bar{\omega}$ domain is computed and $\bar{\omega}$ is displayed.

3.2. Effect of the traction free surface of the Earth

The effect of the traction free surface of the Earth on ω has been tested using a single semi-elliptical fault touching the Earth surface with a dip angle $\beta = 60^\circ$ as shown in Figure 3. The computed $\bar{\omega}$ is shown in the $\bar{\omega}$ multi-domain of Figure 12. The horizontal axis of this $\bar{\omega}$ multi-domain is both the whole and half space option (see Figure 3), while the vertical axis is the sliding friction angle. Although this frictionless semi-elliptical planar fault in whole space yields a maximum $\bar{\omega}$ of 6° , in half space (Figure 12), the maximum $\bar{\omega}$ will be decreased by 1° to 3° in average for all tested sliding frictions.

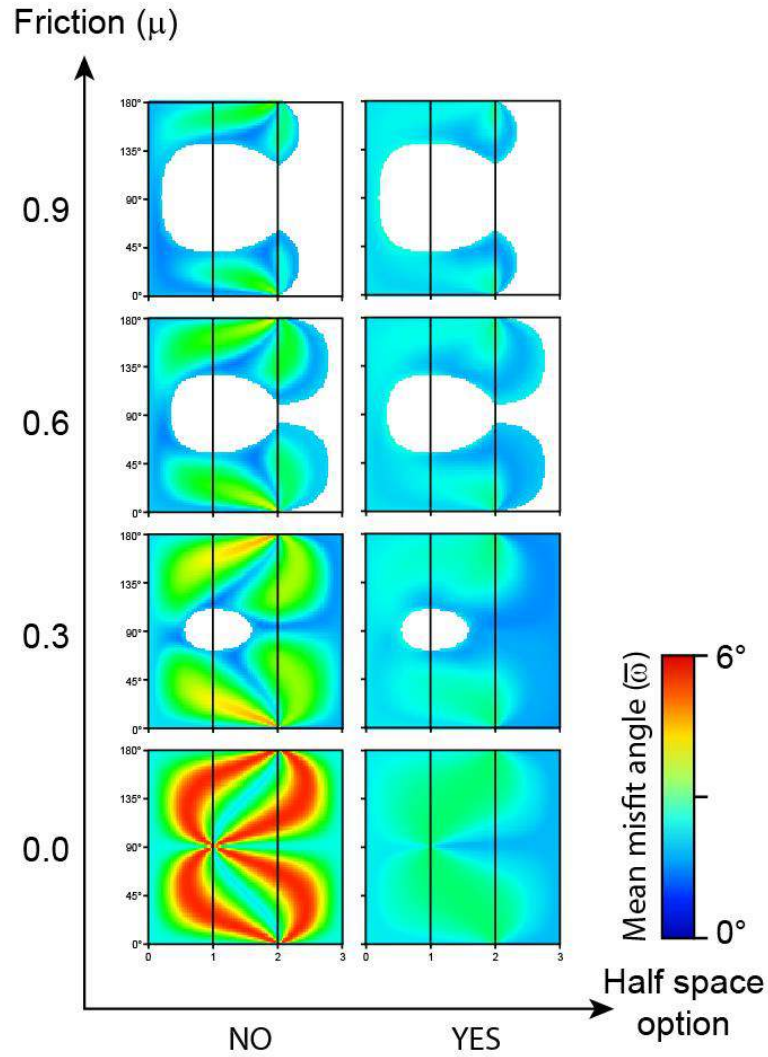


Figure 12. $\bar{\omega}$ multi-domain for the semi-elliptical planar fault geometry in half or whole space. For all tested friction coefficients (y-axis), two model configurations have been tested in the x-axis (activation or not of the traction free surface of the Earth option: half space option). A $\bar{\omega}$ domain is computed and $\bar{\omega}$ is displayed for all given parameters.

3.3. Effect of Poisson's ratio

The effect of Poisson's ratio (ν) on $\bar{\omega}$ has been tested on the intersecting fault geometry as described earlier ($\beta = 60^\circ$ and $\delta = 30^\circ$). We found that $\bar{\omega}$ for the frictionless model is 6.6° for $\nu = 0.01$, 8° for $\nu = 0.25$ and 10.7° for $\nu = 0.499$. $\bar{\omega}$ is lower for an elastic medium behaving such that very little lateral

expansion is observed ($\nu \approx 0$). $\bar{\omega}$ is higher for a medium closer to real rock behavior ($\nu \approx 0.25$) and much higher for an incompressible medium where $\nu \approx 0.5$.

3.4. Effect of fault friction

We have shown in the previous simulations that adding friction along sliding faults will systematically reduce both the mean and maximum $\bar{\omega}$ until there is no slip along the faults (white regions). Subsequently, in order to better understand and evaluate the effect of the sliding friction on $\bar{\omega}$, we have used the intersecting fault geometry as described earlier ($\beta = 60^\circ$ and $\delta = 60^\circ$). We apply a vertical compressive load which will produce, in the absence of faults, a horizontal radial extension and a uniform vertical shortening. Such tectonic stress condition is representative of a normal fault regime for which the stress ratio $\bar{R} = 0$. In our simulation we are testing the friction along the faults for values ranging from 0 to 0.9 with an increment of 0.1.

Figure 13.a shows, for a frictionless model, the computed slip vectors (continuous grey curves) along the intersecting fault as well as the resolved shear stress orientation (dashed dark lines). It illustrates that most of discrepancy is located near the intersection line as described by Maerten (2000). When friction is increased, slip magnitude is reduced and slip vectors tends to become parallel to the resolved shear stress (dashed line in Figure 13.b). To quantitatively evaluate the effect of sliding friction we analyze the evolution of both the normalized displacement and ω in two areas along the intersecting fault (see Figure 13.a): point A, located near the intersection line, where large ω are expected due to greater mechanical interaction and point B, located far from the intersection line, where low ω are expected due to lesser mechanical interaction. Figure 13.c and d represent the evolution of both the normalized displacement and ω for the two point A and B respectively. They clearly show that close to the intersection line (point A) the misfit angle (ω) is very high and decreases with increasing friction. The same trend is observed when far from the

intersection line (point B) even if the misfit angle (ω) is lower for no friction. In both cases slip magnitude decreases with increasing friction.

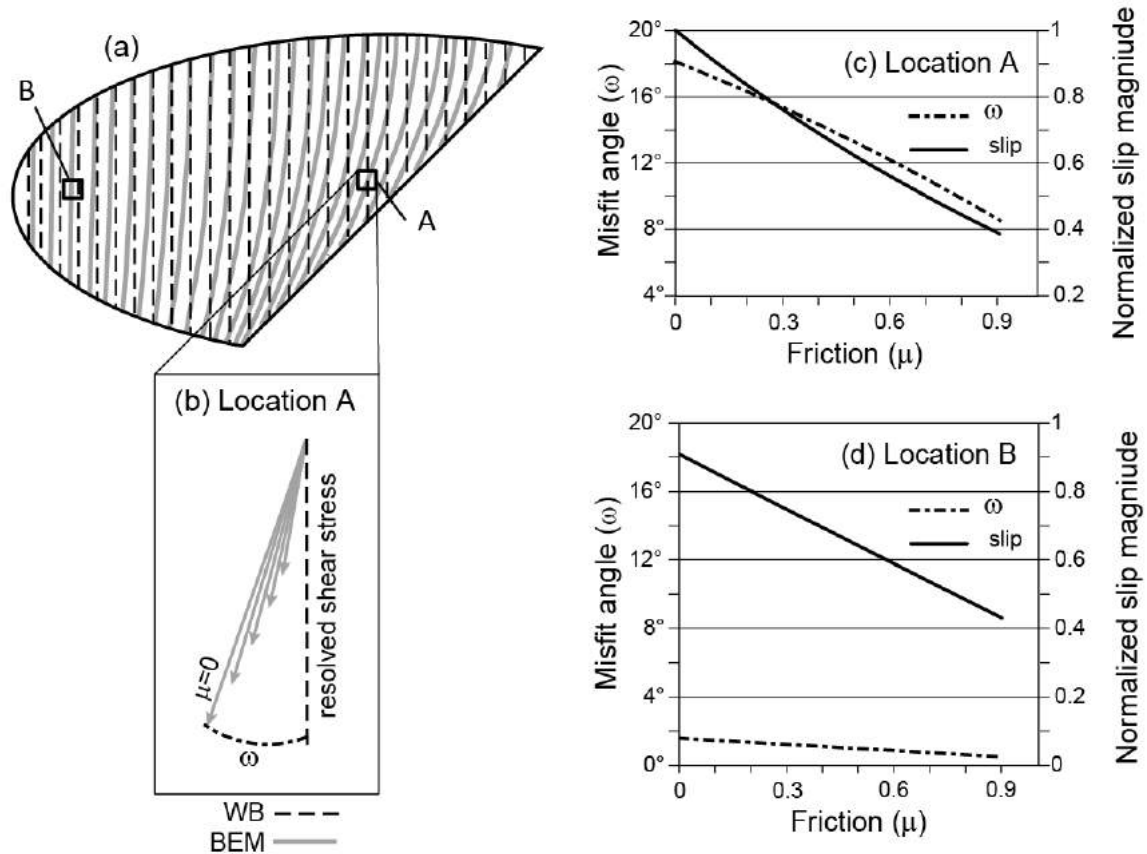


Figure 13. Effect of coefficient of friction on ω . (a) Resolved shear stress vectors from WB (dashed black lines) and computed slip vectors from BEM (gray curves) on the intersecting fault of Figure 1 for $\mu = 0$ and $\bar{R} = 0$. (b) Effect of increasing friction (every 0.2) on the computed slip vector. As friction increases ω decreases. (c) Graph showing the relationship between normalized slip magnitude and ω as friction increases for point A located near the fault intersection line where mechanical interaction is high. (d) Graph showing the relationship between normalized slip magnitude and ω as friction increases for point B located far from the fault intersection line where mechanical interaction is low.

3.5. Effect of fault fluid pressure

Figure 14 illustrates that, as opposed to increasing fault friction, adding fluid pressure along the faults increases $\bar{\omega}$, which can reach values as high as 80° when $P = 0.9$ and $\sigma_3 = 0$. The mean $\bar{\omega}$, when $\sigma_3 = 0$, is 11.9° for $P = 0.3$, 22.5° for $P = 0.6$ and 40.2° for $P = 0.9$. When $\sigma_3 = 0.3$, the mean $\bar{\omega}$ is 15.4° for $P = 0.6$ and 37.4° for $P = 0.9$. Finally, for $\sigma_3 = 0.6$, $\bar{\omega}$ is 30.6° for $P = 0.9$. It is interesting to note that adding fault fluid pressure tends to increase $\bar{\omega}$ when the maximum horizontal compressive stress σ_H orientation (θ) is aligned with the faults strike (here \sim NS), and decreases for σ_H orthogonal to the fault strike. Furthermore, adding fault fluid pressure tends to increase $\bar{\omega}$ when $\bar{R}=0$ and $\bar{R}=2$ and to decrease $\bar{\omega}$ when $\bar{R}=1$ and $\bar{R}=3$.

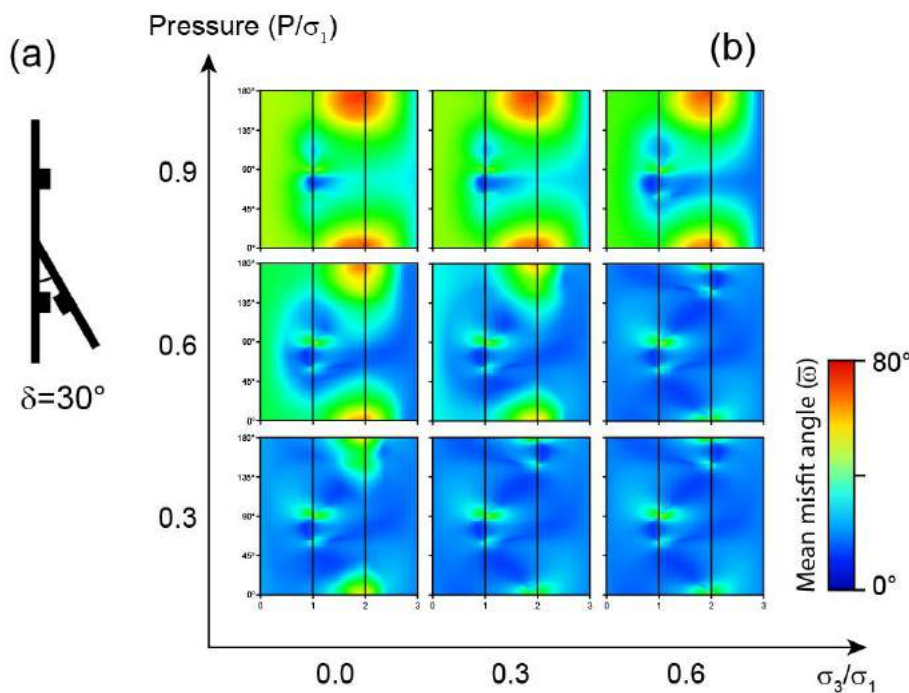


Figure 14. $\bar{\omega}$ multi-domain showing the effect of fault fluid pressure. (a) Model geometry of the intersecting fault geometry ($\delta = 30^\circ$, $\beta = 60^\circ$). (b) For each normalized least principal compressive stress σ_3/σ_1 tested (x-axis) and normalized fault fluid pressure P/σ_1 (y-axis), a $\bar{\omega}$ domain is computed and $\bar{\omega}$ is displayed.

4. Discussion

4.1. Fault geometry

The single planar elliptical fault results (Figure 6) clearly demonstrate that, even though the maximum mean misfit angle $\bar{\omega}$ is low ($\sim 2.7^\circ$), the strike and dip angle relative to stress axes of a planar fault have an influence on the pattern of $\bar{\omega}$. We attribute this misfit to the mechanical interaction that the fault has with itself. We call it self-mechanical interaction.

In order to better understand the notion of self-mechanical interaction, one needs, as in numerical simulations, to represent a fault surface as being discretized by many elementary flat surfaces that perfectly fit with each other (i.e. with no overlaps and no gaps). Each elementary flat surface can be viewed as a single sliding discontinuity that will mechanically interact with its neighbors. As an idealized fault can be viewed as a planar surface with a finite geometry with various length-to-width ratio and delimited by a tipline that can be rectangular, elliptical or irregular, one can acknowledge that the mechanical interaction between all elementary flat surfaces will strongly depend on their respective position with respect to the fault geometry. Pollard et al. (1993) and Willemse et al. (1996) have shown that both the geometry of the periphery (rectangular or elliptical) and the length-to-width ratio of an isolated fault have an influence on the slip distribution and magnitude. Similarly, Kaven et al. (2011) have shown that a single isolated corrugated fault can also have highly perturbed slip distribution and magnitude. This is attributed to what we call the self-mechanical interaction.

Higher self-mechanical interactions are expected for specific configurations such as optimally oriented fault to slip. Indeed, an optimally oriented planar fault, with respect to the applied tectonic stress, will have the highest slip magnitude, hence increased self-mechanical interaction that will potentially deviate slip vector from the resolved shear stress vector. Similarly, a non-optimally oriented fault will have the lowest slip magnitude, hence decreased self-mechanical interaction that will in turn reduce the misfit angle. This

series of simulations shows that variations of $\bar{\omega}$ are not only related to the stress ratio but also to the orientation of the maximum horizontal principal stress. It also illustrates that the maximum $\bar{\omega}$ occurs when the fault is optimally oriented to enhance slip. The white regions of the domain, where no slip occurred along the fault, are explained by the fact that there is no resolved shear stress on the fault for specific stress configurations. When the fault is vertical ($\beta=90^\circ$), the stress domain shows a constant value of $\bar{\omega}$ for all stress regimes. This is explained by the fact that, while the vertical stress does not resolve any shear stress on the vertical fault, the ratio between the two horizontal stresses will not change the pattern (orientation and relative magnitude) of the resolved shear stress along the fault. This is equivalent to an uniaxial compressive horizontal stress (σ_H). In such condition $\bar{\omega}$ will be constant for all stress configurations.

Now that the misfit angle pattern is understood for a simple elliptical fault, it is relevant to analyze and understand the pattern of $\bar{\omega}$ for more complex fault configurations such as the intersecting fault geometry (Figure 8.a). The high $\bar{\omega}$ regions are related to the mechanical interaction between faults as described by Maerten (2000), specifically when one fault is not optimally oriented to slide. Indeed, in such a configuration, slip on the non-optimally oriented fault is only triggered by slip on the nearby more optimally oriented fault. This is analogous to stress transfer described by geophysicists studying earthquakes sequences (Stein, 1999; Muller et al., 2003). As a consequence, it is likely that slip on non-optimally oriented fault is driven by the local perturbed stress and not directly by the applied tectonic stress, hence of ω should be higher along this fault. This is illustrated in Figure 8d that shows in which specific conditions $\bar{\omega}$ is increased. For both point A and point B configurations, the largest NS-striking fault is non-optimally oriented for slip. Indeed, both the horizontal stress parallel to the fault as well as the two remaining equal stresses will induce no shear stress on the NS-striking fault hence no slip. On the other hand the smaller fault, which is more optimally oriented for slip, will be the main driver to trigger slip on the larger NS-striking fault as described above. Analogous explanation is applicable to both point A' and point B' configurations (see Figure 8d) except that here, it is the smaller fault that is less optimally oriented for slip. The magnitude of $\bar{\omega}$ is

greater for stress configurations at points A and B compared to points A' and B' because the area of the NS-striking fault is twice larger than the other fault. On the other hand, when the two faults are both non-optimally oriented, the mechanical interaction described earlier is less pronounced. Therefore $\bar{\omega}$ is reduced as illustrated by the blue regions in Figure 8.b.c. The main idea here is that strong mechanical interaction between faults, combined with geometrical complexity, increases $\bar{\omega}$.

When friction increases (i.e. $\mu = 0.3$) $\bar{\omega}$ will globally decrease (see Figure 8.b), while for specific boundary conditions the fault stops sliding. In such case, no slickenlines are created, which leads to a white region (see point C $\theta = 80^\circ$ and $\bar{R} = 1$ of Figure 8.b). Globally, increasing fault friction decreases displacement magnitude, hence mechanical interaction and $\bar{\omega}$. This phenomenon has already been described by Pascal (2002). It is interesting to note, in Figure 8b.c. that tectonic stress configurations giving high $\bar{\omega}$ (points A and B) for models with no friction, are often associated with tectonic stress configurations yielding white regions for models with friction. This is explained by the fact that at point C ($\theta = 75^\circ$ and $\bar{R} = 1$), the maximum horizontal stress σ_H makes the highest angle with the two modeled fault. Stress configuration at point C will be the intermediate configuration between case A and A'. Therefore, in such configuration we would expect the highest resolved normal stress along the faults, increasing the effect of the friction. This phenomenon is accentuated by the fact that friction will also more easily prevent fault slip on non-optimally oriented faults as the tectonic stress has less effect on such faults. In contrast, $\bar{\omega}$ is not reduced between the two points B and B' as much as at point C, because in such stress configuration the maximum horizontal stress σ_H makes the lowest angle with the two modeled faults. Hence, we expect the lowest resolved normal stress along the faults, inhibiting the effect of the friction.

Figure 9 also illustrates the general trend of $\bar{\omega}$ when friction is added. In this case, increased friction will globally decrease $\bar{\omega}$. White regions of the domain are produced when friction is high and faults are not optimally oriented for sliding. When the ratio between the shear and normal traction is low, the fault will stop sliding. It is interesting to note in Figure 9 that since faults are dipping 60° (average for normal faults),

they are not optimally oriented for a reverse stress regime. This explains why, while friction increases, the white regions become larger and concentrated in the reverse fault domain ($2 < \bar{R} < 3$). This is also illustrated in Figure 10, when fault dip angle is $\beta = 30^\circ$, the faults are optimally oriented for reverse faulting and therefore the white regions of the tectonic stress domain are concentrated in the normal and wrench stress regimes when friction increases. Similarly, when fault dip angle is $\beta = 90^\circ$, the faults are optimally oriented for wrench faulting and therefore the white regions of the tectonic stress domain are concentrated in the normal and reverse stress regimes when friction increases. Here, as predicted by mechanics (Maerten, 2000), slip is highly perturbed close to the intersection between two faults and when the angle between these faults is acute. In such a configuration, slip vectors greatly deviate from the resolved shear stress and tend to be parallel to the fault intersection.

The sinusoidal fault model can be viewed as an intersecting fault set with 2 principal equivalent faults A and B (see Figure 2) as suggested by Willemse et al., (1996) and Crider and Pollard (1998) for slip behavior along short wavelengths and high amplitude corrugated fault surfaces. It is interesting to note that this pattern exhibits similar slip behavior to that of an echelon fault array mechanically interacting (Marshall and Morris, 2012) when one equivalent fault strike is non-optimally oriented for slip. This geometrical analogy should help interpreting the corrugated faults as being a particular configuration of the intersecting faults geometry. Low amplitude geometries can be compared to the large angle between intersecting fault strikes, while high amplitude geometries can be compared to acute angle between intersecting fault strikes. The main difference between intersecting and sinusoidal fault models is that for the latter, the equivalent faults A and B (Figure 2) have a common edge (intersection line). This implies some small differences in the $\bar{\omega}$ patterns between both the sinusoidal and the intersecting fault models. The analogy should nevertheless be useful for the current interpretation of the sinusoidal fault model. Figure 11 shows that as the amplitudes increases, two separate tectonic stress (θ) with opposite orientations maximize fault mechanical interaction and in turn $\bar{\omega}$. Very low amplitude will be equivalent to an isolated dipping fault as shown in Figure 6. In

analogy to the intersecting fault model, the $\bar{\omega}$ multi-domain for sinusoidal fault geometry (Figure 11), shows that $\bar{\omega}$ increases as the amplitude increases, thus as the angle between intersecting fault geometries decreases (acute angle). On the other hand, it is less for low amplitude, thus as the angle between intersecting fault geometries increases. Non optimal tectonic stress orientation relative to fault surfaces and high sliding friction for low amplitude fault geometry lead to no slip along faults, (white regions on Figure 11). Resor (2009) showed that the Arkitsa Fault had $\bar{\omega} = 4.8^\circ$. He suspected that near-fault stress perturbations due to slip on the irregular surface (Pollard et al. 1993) was the main mechanism responsible for this misfit. This value seems small compared to the maximum values given in our study. However, tectonic stresses involved in the reactivation of this fault and implication of a high friction angle may have had a strong effect on this fault, reducing the stress perturbations, hence $\bar{\omega}$.

4.2. Traction free surface

The decrease in $\bar{\omega}$, when the single planar dipping fault is touching the Earth surface, can be explained by the fact that the fault is intersecting a traction free surface where no confinement is applied. Therefore, the propensity for a fault to slip is increased and slip gradients are greater than an isolated fault at depth. Increasing slip magnitude and slip gradient will decrease the effect of the fault tip-line (fault self-mechanical interaction), hence $\bar{\omega}$. Therefore, we could assume that the traction free surface of the Earth will have little effect on paleostress inversion using the WB assumptions.

4.3. Poisson's ratio

Taking the observations on Poisson's ratio $\bar{\omega}$ multi-domain into account, increasing Poisson's ratio by 0.1 will increase $\bar{\omega}$ to about 1° . Since Poisson's ratio for rock ranges from 0.1 to 0.45 with a mean at $\nu = 0.25$, we expect a small implication of this parameter in the invalidation of the WB assumptions. As for the other tested geometry parameters, friction has the same global reduction effect on $\bar{\omega}$.

4.4. Fault friction

Observations from Figure 13 show that increasing friction will decrease slip magnitude as well as ω until slip vector becomes parallel to resolved shear stress. This effect is more pronounced for point A located in a highly perturbed area near the intersection line, where ω decreases from 18° to 0° for friction increasing from 0 to 0.9. In summary, friction globally lowers slip magnitude and therefore reduces ω . As a result, in such a configuration, if we require having valid WB assumptions for ω less than 5° , it would imply having a sliding friction superior to 1. This friction would be too high with regards to known values of measured friction (Byerlee, 1978) and it would generate slip magnitudes so low that no slickenlines could be observed and measured in outcrop.

4.5. Fault fluid pressure

The results shown in Figure 14 clearly demonstrate that fault fluid pressure, P , has a stronger impact on increasing $\bar{\omega}$ than the other parameters described in this study, assuming that $P \geq \sigma_3$. The results observed in Figure 14 can be explained by the fact that fault fluid pressure has a stronger effect on the fault propensity to slide when the resistance to open the pressurized fault is less, which means when the least applied compressive stress (σ_3) becomes normal to the fault surfaces. For 60° dipping and \sim NS striking faults, as in the example of Figure 14, it is particularly evident when θ is close to NS and when $R=0$, thus when σ_3 is normal to the main fault strike as observed for $\theta=0^\circ$ or $\theta=180^\circ$, $\bar{R}=0$ and $\bar{R}=2$.

4.6. Complementary study

Here, we want to complement the study that Pascal (2002) has done, which lead to the conclusion "*in favor of the validity of the simplified WB model*". We want to evaluate whether the selection of model configurations used to reach such conclusion is representative.

Pascal (2002) has tested two fault geometries (a conjugate pair of non-intersecting faults and two intersecting faults with perpendicular strikes), assigning one coefficient of friction ($\mu = 0.58$) for both fault

geometries, one fixed stress orientation per model (σ_h oblique to the faults) and 3 stress ratios ($\bar{R} = 0.3, 0.5$ and 0.7) in a normal fault regime. Here we will concentrate on Pascal's second fault geometry, which consists of a pair of perpendicular intersecting faults subjected to oblique extension. One fault F1 strikes N180° with a 55° dip angle towards the east and the second fault F2 strikes N90° with a 65° dip angle towards the south (see Figure 15). In Pascal's model, applied σ_h (σ_3) makes angles of 30° and 60° with F1 and F2 respectively.

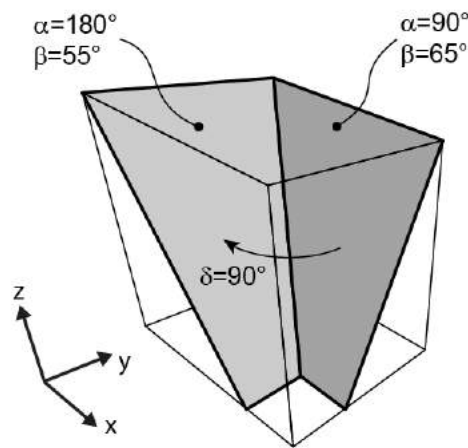


Figure 15. 3D BEM fault geometry from Pascal (2002) showing a pair of perpendicular and intersecting faults.

According to Pascal (2002), $\bar{\omega}$ given by this model is less than 10° and decreases when \bar{R} increases. We used the same model geometry and, to complete Pascal's analysis, we applied the full set of Andersonian tectonic stresses. In addition, five friction angles have been investigated ($\mu = 0.0, 0.3, 0.58$ and 0.9).

The $\bar{\omega}$ multi-domain displayed in Figure 16a.b shows, for a given tectonic stress, the influence that the pair of intersecting faults has on $\bar{\omega}$. As for the previous model of this present work, $\bar{\omega}$ decreases as friction increases. For the frictionless model, $\bar{\omega}$ is around 22° with a maximum of 45°. When $\mu = 0.3$, $\bar{\omega}$ is around 17°, 7° for $\mu = 0.58$ and 5° for $\mu = 0.9$.

Figure 16.b shows $\bar{\omega}$ for $\mu = 0.58$ used in Pascal (2002) simulations. It is interesting to note that $\bar{\omega}$, does not necessarily follow a linear relationship with the stress ratio \bar{R} as described by Pascal (2002). Indeed, in Pascal's experiments (white dots in Figure 16.b) this relationship is only valid for the tested normal fault regime and when the maximum horizontal stress orientations are greater than 90° . When the full set of Andersonian tectonic stress regimes is covered, we notice that $\bar{\omega}$ variation is not only related to the stress ratio \bar{R} , but also to the orientation of σ_H (θ). It is clear by analyzing Figure 16 that other tectonic stress model configurations would have generated larger $\bar{\omega}$ than the specific configurations used by Pascal (2002). On the other hand, there are tectonic stress configurations that would have generated much smaller $\bar{\omega}$.

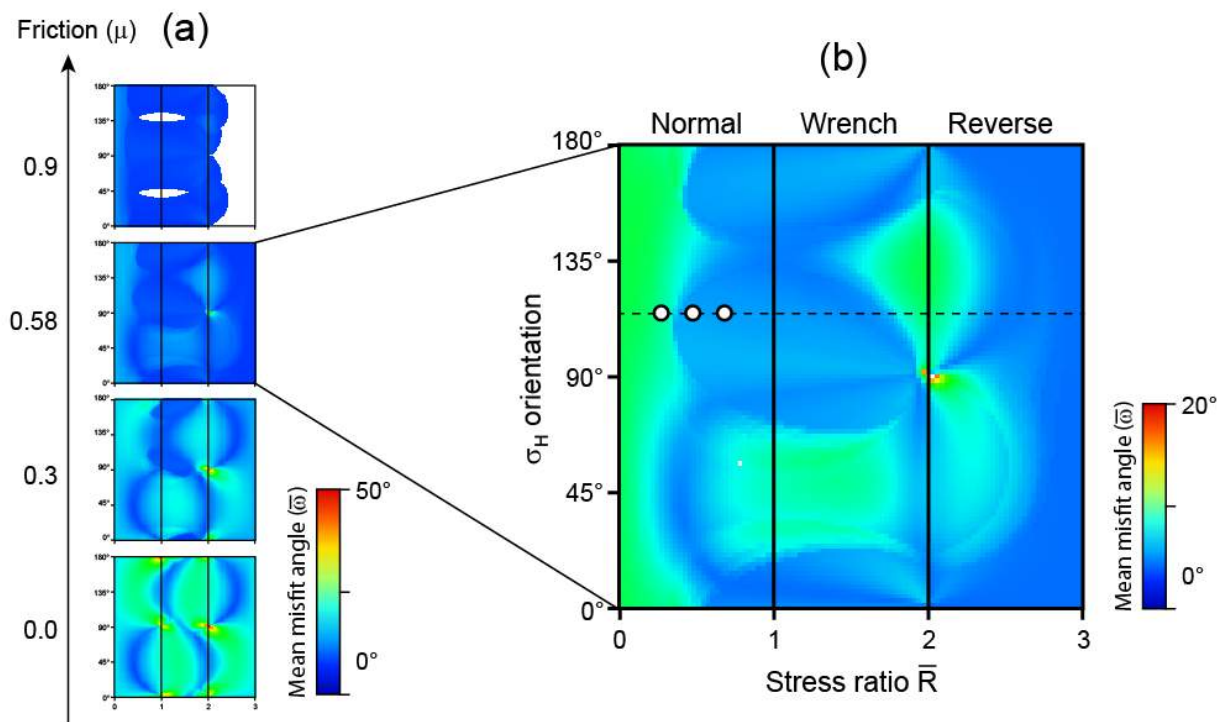


Figure 16. $\bar{\omega}$ domain of the Pascal (2002) model. (a) For varying friction coefficient (y-axis), a $\bar{\omega}$ domain is computed and $\bar{\omega}$ is displayed. (b) $\bar{\omega}$ domain for the same model geometry and friction ($\mu = 0.58$). The white dots represent the 3 model configurations investigated by Pascal (2002).

Finally, following our previous analysis of intersecting fault geometries, it appears that the two intersecting faults with perpendicular strikes used by Pascal (2002) are not the optimum geometric choice to

highlight the highest ω that intersecting faults could produce. Indeed, the orthogonal pair of intersecting faults has the lowest $\bar{\omega}$ compared to acute intersecting faults ($\delta = 30^\circ$ and $\delta = 150^\circ$) as shown in Figure 9. Therefore, we expect higher $\bar{\omega}$ for two intersecting faults with non-perpendicular strike configurations.

5. Conclusions

Since paleostress inversion methods using fault slip data are all based on the WB assumptions, it is fundamental to check the fundamental assumption that fault slip occurs more or less parallel to the greatest resolved shear stress. Previous studies suggested that slip discrepancies between geomechanical models and WB analytical models should remain modest, while other studies and observations invalidate the WB assumptions for faults with strong mechanical interactions.

In this present study, although we show that Poisson's ratio has a very small effect on the mean misfit angle $\bar{\omega}$, we highlight that specific tectonic stress conditions applied to corrugated faults and intersected fault geometries could generate high stress perturbations and increase $\bar{\omega}$, invalidating the WB model. This effect is slightly reduced when faults touch the traction free surface of the Earth. In all studied configurations, we also show that increasing friction decreases $\bar{\omega}$. However, as many authors emphasize that fault reactivation occurs for low friction (around $\mu=0.3$) (Zoback and Beroza, 1993; Marone, 2004; Colletini et al. 2009; Reches and Lockner, 2010; Di Toro et al. 2011), much lower than historical values ($\mu = 0.6$ and $\mu = 0.85$) reported in the literature (Byerlee, 1978), one can conclude that friction should not have a significant effect in reducing $\bar{\omega}$. Indeed, in our simulations when $\bar{\omega}$ can reach up to 40° for frictionless faults, it nonetheless reaches 20° for $\mu = 0.3$. Furthermore, it is important to acknowledge that high friction reduces the propensity of a fault to slip for some given tectonic stresses, meaning that these high friction faults should exhibit very few slickenlines, hence reducing available data necessary to perform the paleostress inversion.

Many authors suggested that, in spite of the lack of microstructural indicators, fault fluid pressure might overcome friction and have a strong mechanical effect, reorienting the local stress (Sibson, 2000; Faulkner et al., 2010). Here we showed that increasing fault fluid pressure will generate slickenlines highly incompatible with the WB assumptions.

Using a right angle intersected fault model, Pascal (2002) concluded in favor of the validity of the simplified WB assumptions. However, our study shows that this conclusion is only true for specific tectonic stress configurations as well as for specific fault geometry (two intersecting orthogonal faults). Indeed, intersected faults with acute angle, or high amplitude sinusoidal faults, have a greater $\bar{\omega}$ than orthogonal pairs of faults or low amplitude sinusoidal faults. We also demonstrate that for a given fault geometry, $\bar{\omega}$ can be extremely variable and often high.

From our thorough parametric study we estimate that the average percentage of fault area showing ω higher than 10° is around 6.5%. Of course this number has been derived from limited and idealized fault geometries and parameters, it is therefore not entirely representative of all possible natural fault configurations. However, considering the complexity of fault pattern often observed in nature compared to the ones investigated in this work, we could assume that this would be a lower limit. Therefore, in this context, the collected fault slip data and sampling methods could be critical for the validity of the stress inversion results using classical methods based on the WB assumptions. This could be particularly true if most of the collected data are located along fault planes where large ω are mechanically anticipated. Further analyses should focus on estimating the real impact of the recognized ω between resolved maximum shear stress and the actual slip vector, on the fault slip data inversion methods based on the WB assumptions.

Acknowledgements

This study is part of M. Lejri's PhD thesis, granted by both the French Ministry of Research and Schlumberger. These are deeply acknowledged. We also thank Romain Plateaux, Scott Marshall and Tom Blenkinshop for helpful review of the early version of the manuscript.

References

- Amonton G., 1699. Histoire de l'Académie Royale des Sciences avec les Mémoires de Mathématique et de Physique, p.206.
- Anderson, E.M., 1951. The Dynamics of Faulting and Dyke Formation with Applications to Britain, 2nd Edition. Oliver and Boyd, Edinburgh.
- Angelier J., Mechler P., 1977. Sur une méthode graphique de recherche des contraintes principales également utilisable en tectonique et en séismologie: la méthode des dièdres droits. – Bull. Soc. géol. Fr. XIX (6), 1309-1318.
- Angelier, J., 1975 a. Sur l'analyse de mesures recueillies dans des sites faillés: l'utilité d'une confrontation entre les méthodes dynamiques et cinématiques. C. R. Acad. Sci. Série D 281, 1805–1808.
- Angelier, J., 1979. Determination of the mean principal directions of stresses for a given fault population. Tectonophysics 56, T17–T26.
- Angelier, J., Colletta, B., Anderson, R.E., 1985. Neogene paleostress changes in the Basin and Range: a case study at Hoover Dam, Nevada-Arizona. Geol. Soc. Amer. Bull. 96, 347– 361.
- Angelier, J., 1990. Inversion of field data in fault tectonics to obtain the regional stress — III. A new rapid direct inversion method by analytical means. Geophysical Journal International 103 (2), 363–376.
- Angelier, J., 1994a. Failles, non-failles et structures de pression/tension dans l'inversion des données de tectonique cassante en termes de tenseurs des contraintes. Bull. Soc. géol. de France. 165 (3), 211–220.
- Angelier, J., 1994b. Fault slip analysis and palaeostress reconstruction. In: Hancock, P.L. (Ed.), Continental Deformation. Pergamon Press, Oxford, pp. 53–100.
- Arthaud, F., 1969. Méthode de détermination graphique des directions de raccourcissement, d'allongement et intermédiaire d'une population de failles. Bull. Soc. géol. De France 7 (XI), 729–737.

- Barnet. J. A. M., Mortimer, J., Rippon. J. H., Walsh. J. J. & Watterson. J., 1987. Displacement geometry in the volume containing a single normal fault. *The American Association of Petroleum Geologists Bulletin*. 71. 925-937.
- Barrier E., Angelier J., 1986. Active collision in eastern Taiwan: The Coastal Range. *Tectonophysics* 125, 39-72.
- Barton, N.R., 1973. Review of a new shear strength criterion for rock joints. *Eng. Geol.* 7,287-332.
- Bergerat, F., 1987. Stress fields in the European platform at the time of Africa-Eurasia collision. *Tectonics* 6, 99-132.
- Bott, M.H.P., 1959. The mechanics of oblique slip faulting. *Geological Magazine* 96, 109–117.
- Bourne S.J., Willemse E.J.M., 2001. Elastic stress control on the pattern of tensile fracturing around a small fault network at Nash Point, UK. *J. Struct. Geol.* 23:1753-1770
- Byerlee, James D., 1978. "Friction of Rocks". *Pure and Applied Geophysics* 116 (4-5): 615–626.
- Carey, E., Brunier, B., 1974. Analyse théorique et numérique d'un modèle mécanique élémentaire appliqué à l'étude d'une population de failles. – *C. R. Acad. Sci., D*, 279, 891-894.
- Celerier B., 1988. How much does slip on a reactivated fault plane constrain the stress tensor? *Tectonics* 7, 1257-1278.
- Célérier, B., Seranne, M., 2001. Breddin's graph for tectonic regimes. *J. Struct. Geol.* 23, 789-801
- Celerier, B., 2006. FSA version 28.8: Fault & stress analysis software, in: Editor (Eds.), <http://www.pages-perso-bernard-celerier.univ-montp2.fr/software/dcmt/fsa/fsa.html>.
- Celerier, B., Etchecopar, A., Bergerat, F., Vergely, P., Arthaud, F., Laurent, P., 2012. Inferring stress from faulting: from early concepts to inverse methods. *Tectonophysics*, Volume 581, 18 December 2012, Pages 206-219
- Chester, F.M., Chester, J.S., 2000. Stress and deformation along wavy frictional faults. *J. Geophys. Res.-Solid Earth* 105, 23421–23430.

- Colletini, C., Niemeijer, A., Viti, C., and Marone, C., 2009. Fault zone fabric and fault weakness. *Nature* 462, 907-910, doi: 10.1038/nature 08585.
- Crider, J.G., and Pollard, D.D., 1998, Fault linkage: 3D mechanical interaction between overlapping normal faults. *Journal of Geophysical Research, Special Section on Stress Triggers, Stress Shadows, and Implications for Seismic Hazard*, v. 103, p. 24,373-24,391.
- Cundall, P.A., 1971. A computer model for simulating progressive large scale movement in blocky rock systems. *International Symposium on Rock Mechanics. International Society of Rock Mechanics, Nancy*, p. II-8.
- Cundall, P.A., 1988. Formulation of a three dimensional distinct element model: Part I. A scheme to detect and represent contacts in a system composed of many polyhedral blocks. *Int. J. Rock Mech. Min. Sci. Geomech. Abstr.* 25, 107-116.
- Delvaux, D., Sperner, B., 2003. Stress tensor inversion from fault kinematic indicators and focal mechanism data: the TENSOR program. In: Nieuwland, D. (Ed.), *New Insights into Structural Interpretation and Modelling*, 212. Geological Society, London, Special Publication, pp. 75-100.
- Di Toro G., Han R., Hirose T., De Paola N., Nielsen S., Mizoguchi K., Ferri F., Cocco M., Shimamoto T. 2011. Fault lubrication during earthquakes. *Nature*, 471(7339): 494–498.
- Dupin, J.M., Sassi, W., Angelier, J., 1993. Homogeneous stress hypothesis and actual fault slip: a distinct element analysis. *J. Struct. Geol.* 15, 1033-1043.
- Etchecopar, A., Vasseur, G., Daignieres, M., 1981. An inverse problem in microtectonics for the determination of stress tensors from fault striation analysis. *J. Struct. Geol.* 3, 51-65.
- Etchecopar, A., 1984. Étude des états de contrainte en tectonique cassante et simulations de déformations plastiques (approche mathématique). Thèse d'État. Ph.D. thesis, Université des Sciences et Techniques du Languedoc.

- Faulkner, D., R., Jackson, C. A. L., Lun, R.J., Schlische, R.W., Shipton, Z. K., Wibberley, C.A.J., Withjack, M.O., 2010. A review of recent developments concerning the structure, mechanics and fluid flow properties of fault zones. *J. Struct. Geol.*, 32, 1557-1575.
- Gapais, D., Cobbold, P.R., Bourgeois, O., Rouby, D., de Urreiztieta, M., 2000. Tectonic significance of fault slip data. *J. Struct. Geol.* v22,7:881-888.
- Gephart, J. W., Forsyth, D. W., 1984. An improved method for determining the regional stress tensor using earthquake focal mechanisms data: Application to the San Fernando earthquake sequence, *J. Geophys. Res.*, 89, 9305-9320.
- Griffith, W. A., Di Toro, Pennacchioni G., Pollard, D.D., Nielsen S., 2009. Static stress drop associated with brittle slip events on exhumed faults, *J. Geophys. Res.*, 114, B02402.
- Hancock, P.L., 1985. Brittle microtectonics: principles and practice *J. Struct. Geol.* V7,3:347-457.
- Hansen, J.-A., 2013. Direct inversion of stress, strain or strain rate including vorticity: A linear method of homogenous fault-slip data inversion independent of adopted hypothesis. *J. Struct. Geol.*, 51, 3-13.
- Hardcastle, K.C., Hills, L.S., 1991. BRUTE3 and SELECT: Quick Basic 4 programs for determination of stress tensor configuration and separation of heterogeneous populations of fault-slip data. *Computers & Geosciences*, 17, 23-43.
- Hoek, E. and Bray, J.W. (1981). *Rock Slope Engineering*, Revised 3rd edition, The Institution of Mining and Metallurgy, London, pp 341 - 351.
- Huchon, P., Jestin, F., Cantagrel, J.-M., Gaulier, J.M., Al Khirbash S., Gafaneh, A., 1991. Extensional deformations in Yemen since Oligocene and the Africa-Arabia-Somalia triple junction. *Ann.*
- Kaven J.O., Maerten F., Pollard, D.D., 2011. Mechanical analysis of fault slip data: Implications for paleostress analysis. *J. Struct. Geol.* 33, 78-91.
- Kocabas, I., 2004. Geothermal reservoir characterization via thermal injection backflow and interwell tracer testing. *Geothermics*, 34(1), 27-46.

- Lacombe O., Angelier J., Laurent O., Bergerat F. Tournieret C., 1990. Joint analyses of calcite twins and fault slips as a key for deciphering polyphase tectonics: Burgundy as a case study. *Tectonophysics*, 182, 279-300.
- Lacombe O., Mouthereau, F., Angelier, J., Deffontaines, B., 2001. Structural, geodetic and seismological evidence of tectonic escape in SW Taiwan. *Tectonophysics* 333, 323-345.
- Lacombe, O., 2012. Do fault slip data inversions actually yield paleostresses that can be compared with contemporary stresses? A critical discussion. *C. R. Geoscience*, 344:159-173.
- Lee, J. J. and Bruhn R. L., 1996. Structural anisotropy of normal fault surfaces. *J. Struct. Geol.* 18, 1043-1059.
- Letouzey J. and Tremolieres P., 1980. Paleo-stress fields around the Mediterranean since the Mesozoic from microtectonic comparison with plate tectonic data. *Rock Mech., Suppl.* 9, 173-192.
- Letouzey, J., 1986. Cenozoic paleo-stress pattern in the Alpine foreland and structural interpretation in a platform basin. *Tectonophysics* 132, 215–231.
- Liesa C.L. and Simon J.L., 2009. Evolution of intra-plate stress fields under multiple remote compressions: The case of the Iberian chain (NE Spain). *Tectonophysics* ,474, 144-159.
- Lisle, R.J., 1992. New method of estimating regional stress orientations: applications to focal mechanism data of recent British earthquakes. *Geophys. J. Internat.*, 110, 276-282.
- Lisle, R.J., 1998. Simple graphical constructions for the direction of shear. *J. Struct. Geol.*, 20, 969-973.
- Lisle, R.J., and Srivastava, D.C., 2004. Test of the frictional reactivation theory for faults and validity of fault-slip analysis *Geology*, 32 (7). pp. 569-572.
- Lisle, R.J., Orife, T.O., Arlegui, L., Liesa, C., Srivastava, D.C., 2006. Favoured states of palaeostress in the earth's crust: evidence from fault-slip data. *J. Struct. Geol.* 28 (6), 1051–1066.
- Lisle, R.J., 2013. A critical look at the Wallace-Bott hypothesis in fault-slip analysis. *Bull. Soc. géol. Fr.*, 184,4-5, 299-306.
- Lohr, T., Krawczyk, C., Oncken, O., Tanner, D., 2008. Evolution of a fault surface from 3D attribute analysis and displacement measurements. *J. Struct. Geol.* 30 (6), 690-700.

- Maerten, F., 2010a. Adaptive cross-approximation applied to the solution of system of equations and post-processing for 3D elastostatic problems using the boundary element method. *Engineering Analysis with Boundary Elements* 34 (5), 483-491.
- Maerten, L., 2000. Variations in slip on intersecting normal faults: implications for paleostress inversion. *J. Geophys. Res.* 270, 197– 206.
- Maerten F., Maerten L., Cooke M., 2010b. Solving 3D boundary element problems using constrained iterative approach. *Computational Geosciences*. 14, 551-564.
- Maerten F., Maerten L., Pollard D.D., 2014. iBem3D, a three-dimensional iterative boundary element method using angular dislocations for modeling geologic structures. *Computers & Geosciences* 72, 1-17.
- Marone C., 2004. Earthquake science: faults greased at high speed. *Nature*, 427(6973):405-6.
- Marshall, S. T., and Morris A.C., 2012. Mechanics, slip behavior, and seismic potential of corrugated dip slip faults. *J. Geophys. Res.*, 117, B3.
- Mattauer, M., Mercier, J.L., 1980. Microtectonique et grande tectonique. *Mém. h. ser. Soc. géol. de France* 10, 141–161.
- Mercier et al. 1989 Extensional tectonic regimes in the Aegean basin during the Cenozoic. *Basin Research*, 2,1, 49-71.
- Michael, A., 1985. The determination of stress from slip data, faults and folds. *Journal of Geophysical Research* 89, 11517-11526.
- Muller, J. R., Aydin, A. and Maerten F., 2003, Investigating the transition between the 1967 Mudurnu Valley and 1999 Izmit earthquakes along the North Anatolian fault with static stress changes. *Geophysical Journal International* 154, 471-482.
- Nemcok, M., Lisle, R.J., 1995. A stress inversion procedure for polyphase fault/slip data sets. *J. Struct. Geol.*, 17, 1445-1457.

- Nicol, A., Watterson, J., Walsh, J.J., Childs, C., 1996. The shapes, major axis orientations and displacement patterns of fault surfaces. *J. Struct. Geol.* 18 (2/3), 235-248.
- Nieto-Samaniego, A. F., and Alaniz-Alvarez, S. A., 1997, Origin and tectonic interpretation of multiple fault patterns: *Tectonophysics*, v. 270, p. 197-206.
- Pascal, C., 1998. Etude mécanique et modélisation de la fracturation en extension, application au domaine de la Mer du Nord. Unpublished PhD thesis, Sciences de la Terre, Univ. P. M. Curie, Paris, 410pp.
- Pascal C., 2002. Interaction of faults and perturbation of slip: influence of anisotropic stress states in the presence of fault friction and comparison between Wallace–Bott and 3D Distinct Element models. *Tectonophysics* 356, 307–322.
- Petit, J.-P., 1987. Criteria for the sense of movement on fault surfaces in brittle rocks. *J. Struct. Geol.*, 9, 597-608.
- Pollard, D.D., Saltzer, S.D., Rubin, A.M., 1993. Stress inversion methods: are they based on faulty assumptions. *J. Struct. Geol.*, 15, 1045-1054.
- Power, W.L., Tullis, T.E., Brown, S.R., Boitnott, G.N., Scholz C.H., 1987. Roughness of natural fault surfaces. *Geophys. Res. Lett.*,14, 29-32.
- Reches, Z., 1987. Determination of the tectonic stress tensor from slip along faults that obey the Coulomb yield condition. *Tectonics* 6, 849–861.
- Reches Z., Lockner D. A., 2010. Fault weakening and earthquake instability by powder lubrication *Nature* 467, 452–455.
- Resor, P.G., Meer, V.E., 2009. Slip heterogeneity on a corrugated fault. *Earth and Planetary Science Letters* 288 483–491.
- Rippon, J.H., 1985. Contoured patterns of throw and hade of normal faults in the coal measures (Westphalian) of northeast Derbyshire, *Proc. Yorks. Geol. Soc.*, 45, 147-161.
- Ritz E. and Pollard D.D., 2012. Stick, slip, and opening of wavy frictional faults: A numerical approach in two dimensions. *Journal of Geophysical Research*, vol. 117, B03405.

- Sagy, A., Brodsky, E.E., Axen, G.J., 2007. Evolution of fault-surface roughness with slip. *Geology* 35, 283–286.
- Sagy, A., Brodsky, E.E., 2009. Geometric and rheological asperities in an exposed fault zone. *J. Geophys. Res.* 114.
- Saucier, F., Humphreys, E., Weldon, R., 1992. Stress near geometrically complex strikeslip faults — application to the San-Andreas fault at Cajon Pass, Southern California. *J. Geophys. Res.-Solid Earth* 97, 5081–5094.
- Sibson, R.H., 2000. Fluid involvement in normal faulting. *Journal of Geodynamics*, 29, 469-499.
- Simon-Gomez 1986 Analysis of a gradual change in stress regime (example from the eastern Iberian Chain, Spain). *Tectonophysics*, 124, 37-53.
- Soliva, R., Maerten, F., Petit, J.-P., and Auzias, V., 2010. Field evidences for the role of static friction on fracture orientation in extensional relays along strike-slip faults ; comparison with photoelasticity and 3D numerical modelling. *J. Struct. Geol.* 32, 1721–1731, doi:10.1016/j.jsg.2010.01.008.
- Stein, R. S., 1999, The role of stress transfer in earthquake occurrence. *Nature* 402, 605-609.
- Thomas, A.L., 1993. Poly3D: a three-dimensional, polygonal-element, displacement discontinuity boundary element computer program with applications to fractures, faults, and cavities in the Earth's crust. M.S. thesis, Stanford University, California.
- Tibaldi, A., 1998. Effects of topography on surface fault geometry and kinematics: examples from the Alps, Italy and Tien Shan, Kazakstan. *Geomorphology* 24, 225– 243.
- Twiss, R.J., Geffel, M.J., 1990. Curved slickenfibers: a new brittle shear sense indicator with application to a sheared serpentinite. *J. Struct. Geol.*, 12, 173-183.
- Twiss, R.J., Protzman, G.M., Hurst, S.D., 1991. Theory of slickenline patterns based on the velocity gradient tensor and microrotation. *Tectonophysics* 186 (3–4), 215–239.
- Vandycke, S., Bergerat, F., Dupuis, Ch., 1991. Meso-Cenozoic faulting and inferred palaeostresses in the Mons basin, Belgium. *Tectonophysics*, 192, 261-271.
- Wallace, R.E., 1951. Geometry of shearing stress and relation to faulting. *J. Geol.*, 59, 118-130.

- Wallace, R.E., Morris, H.T., 1986. Characteristics of faults and shear zones in deep mines. *Pure Appl. Geophys.* 124. 107-126.
- Wallbrecher, E.H., Fritz, H., Unzog, W., 1996. Estimation of the shape factor of a palaeostress ellipsoid by comparison with theoretical slickenline patterns and application of an eigenvalue method, *Tectonophysics*, v. 255, p. 177-187.
- Walsh, J.J., Watterson, J., Bailey, W.R., Childs, C., 1999. Fault relays, bends and branch-lines. *J. Struct. Geol.* 21, 1019-1026.
- Willemse, J.M., Pollard, D.D., Aydin, A., 1996. Three-dimensional analyses of slip distribution on normal fault arrays with consequences for fault scaling. *J. Struct. Geol.* 18, 295-309.
- Xu S., Nieto-Samaniego A.F., Alaniz-Álvarez. S.A., 2013. Origin of superimposed and curved slickenlines in San Miguelito range, Central México. *GeologicaActa*, 11(1), 103-112.
- Yamaji, A., 2000. The multiple inverse method: a new technique to separate stresses from heterogeneous fault-slip data. *J. Struct. Geol.*, 22, 441-452.
- Zoback, M. D., Beroza, G. C., 1993. Evidence for near-frictionless faulting in the 1989 (m-6.9) loma-prieta, california, earthquake and its aftershocks. *Geology* ; 21, 181-185.
- Zoback, M.D., Moos, D., Mastin, L., Anderson, R.N., 1985. Well Bore Breakouts and in Situ Stress. *Journal of Geophysical Research*; 90, 5523-5530.
- Zoback, M.L., Anderson, R.E., Thompson, G.A., 1981. Cainozoic evolution of the state of stress and style of tectonism of the Basin and Range Province of the Western United States. In: Vine, F.J., Smith, A.G. (Eds.), *Extensional Tectonics Associated with Convergent Plate Boundaries*. *Philos. Trans. R. Soc. Lond. Ser. A: Math. Phys. Sci.*, vol. 300. Royal Society of London, London, UK, p. 1454.
- Žalohar, J., Vrabec, M., 2007. Paleostress analysis of heterogeneous fault-slip data: The Gauss method. *J. Struct. Geol.*, 29, 1798–1810.

Table 1: Variable definitions.

Symbol	Comments
<i>Fault geometry</i>	
α	Fault strike defined clockwise from the North
β	Fault dip angle
δ	Angle between the strike of 2 intersecting faults
Am	Amplitude of corrugated fault surface
\vec{n}	Fault plane normal
<i>Fault properties</i>	
μ	Friction coefficient
C_0	Cohesion
P	Fluid pressure
ω	Misfit angle between resolved shear stress and slip vector
$\bar{\omega}$	Mean misfit angle
<i>Rock properties</i>	
ν	Poisson's ratio
E	Young's modulus
ρ	Density
<i>Stress</i>	
$\sigma_1 \geq \sigma_2 \geq \sigma_3$	Principal effective stress magnitudes (positive compression)
σ_v	Magnitude of the vertical stress
σ_H	Magnitude of the maximum horizontal stress
θ	Orientation of σ_H defined clockwise from the North
σ_n	Normal stress magnitude
τ	Shear stress magnitude
R	Stress ratio $R = (\sigma_2 - \sigma_3) / (\sigma_1 - \sigma_3)$
\bar{R}	Stress ratio defined by Maerten 2014 for Andersonian regimes
<i>Acronyms</i>	
WB	Wallace-Bott
DEM	Distinct Element Method
BEM	Boundary Element Method
$\bar{\omega}$ Domain	Mean misfit angle tectonic domain
$\bar{\omega}$ Multi-domain	Mean misfit angle tectonic multi-domain

Table 2. List of parameters used in the simulations.

Symbol	Default values
ν	0.25
E	1
ρ	Constant
μ	[0, 0.3, 0.6, 0.9]
C_0	0
Half-space	No
P	0
σ_1	1
σ_3	0

CHAPTER II: Accuracy evaluation of both Wallace-Bott and BEM-based paleostress inversion methods

Mostfa Lejri^{1,2}, Frantz Maerten¹, Laurent Maerten¹, Roger Soliva²

¹Schlumberger – MpTC, Parc Euromédecine, 340 rue Louis Pasteur, 34790 Grabels, France

²Géosciences Montpellier, Université Montpellier 2, Place E. Bataillon, 34095 Montpellier cedex 5, France

To be submitted to Tectonophysics.

Key words: stress inversion, Geomechanics, Wallace & Bott, Friction, Fault geometry, stress state, slickenlines, angular misfit, stress distance,

Abstract

Three decades after their introduction, the validity of fault slip inversion methods based on Wallace (1951) and Bott (1959) hypothesis, which states that the slip on each fault surface has the same direction and sense as the maximum resolved shear stress, is still the subject of debate. According to some authors, this hypothesis is questionable as fault mechanical interactions induce slip reorientations as confirmed by geomechanical models. This leads us to ask as to what extent the Wallace and Bott simplifications are reliable as a basis hypothesis for stress inversion from fault slip data we compare two inversion methods. The first is based on the Wallace & Bott hypothesis, and the second relies on geomechanics and mechanical effects on fault heterogeneous slip distribution. In that context, a multi-parametric stress inversion study covering (i) the friction coefficients (μ), (ii) the full range of Andersonian state of stress and (iii) slip data sampling along the faults is performed. For each tested parameter, the results of the mechanical stress inversion and the Wallace-Bott (WB) based stress inversion for slip are compared in order to understand their respective effects. The predicted discrepancy between the solutions of both stress inversion methods (based on WB and mechanics) will then be used to explain the stress inversions results for the chimney Rock case study. It is shown that a high solution discrepancy is not always correlated with the misfit angle (ω) and

can be found under specific configurations (\bar{R} , θ , μ , geometry) invalidating the WB solutions even though fault friction tends to minimize the discrepancy. We conclude that in most cases the mechanical stress inversion and the WB based stress inversion are both valid and complementary depending on the fault friction. Some exceptions (i.e. low fault friction, simple fault geometry and pure regimes) that may lead to wrong WB based stress inversion solutions are highlighted.

1. Introduction

Understanding the tectonic stress history that drives the reactivation of faults in the brittle crust is necessary to a good appraisal of seismic hazard, earthquake physics and a better assessment of natural reserves. For this reason, during the last three decades, estimation for the state of stress using stress inversion methods from focal mechanisms and fault slip measurements has widespread among scientists and engineers in the oil, gas and mining industries. Most of the stress inversion methods are based on the Wallace (1951) and Bott (1959) (WB) assumptions assuming that: (1) the fault slip vector, during reactivation, is parallel to the resolved shear stress, (2) Faults are planar, (3) stress field is homogeneous (no perturbations and no block rotations), and (4) all the measured slickenlines are synchronous.

Fault-slip analysis discipline generalization was then encouraged by the emergence of the earliest methods based on the WB hypothesis (Arthaud, 1969; Carey and Brunier, 1974; Angelier, 1975) and the development of many stress inversion algorithms (Carey and Brunier, 1974; Angelier, 1975, 1979; Etchecopar et al., 1981; Gephart and Forsyth, 1984; Michael 1985; Celerier, 1988; Lisle, 1992, 1998; Yamaji, 2000; Delvaux and Sperner, 2003; Žalohar and Vrabec, 2007; Hansen, 2013). These techniques, which have been successfully applied to regional studies, strengthened the confidence in the validity of these WB assumptions (e.g. Mattauer and Mercier, 1980; Letouzey and Tremolière, 1980; Zoback et al., 1981; Angelier et al., 1985; Barrier and Angelier, 1986; Letouzey, 1986; Bergerat, 1987; Mercier et al., 1989; Huchon et al., 1991; Lacombe et al., 1990; Vandycke et al., 1991; Lacombe et al., 2001; Liesa and Simon, 2009). It became

then evident, despite the constant caution that some researchers have had about the WB hypothesis reliability, that the use of striations measured of along fault planes was the most efficient way to invert paleostresses.

However, the natural complexity of fault networks (Wallace and Morris, 1986; Tibaldi, 1998, Resor and Meer, 2009), the evidences of local stress perturbations derived from microstructures observation (Hancock, 1985; and Petit, 1987), the fault block rotations (Twiss and Geffel, 1990; Twiss et al., 1991; Pascal, 1998), and the spatial variability of fault-slip data due to local fault complex geometry (Gapais et al., 2000), lead to ask as to what extent the WB assumptions are reliable when used for stress inversion.

Pollard et al. (1993) and Dupin et al. (1993) were the first to check the validity of the WB assumptions by using mechanical numerical methods, taking internal deformation of faulted blocks and local stress perturbations into account. Dupin et al. (1993) predicted high misfit angles (reaching 37° to 47° for intersecting faults). Later, Nieto-Samaniego and Alaniz-Alvarez (1997) observed that the slip on intersected fault surfaces could deviate from resolved shear stress orientation and should be parallel to the intersection line. Maerten (2000) confirmed these predictions by field observations along the Chimney Rock fault array in Utah, USA and found that the majority of slickenlines is not parallel to the resolved shear stress but is consistent with stress perturbations caused by fault mechanical interaction. Kaven et al. (2011) used simple fault planes to show that even if stress inversion results are similar, WB type inversions yields more uncertainty for limited ranges of slickenlines orientations. Lisle (2013) showed from simple models, that any stress field anisotropy such as that arising from 3D fault geometry, can lead to a significant angular difference between the directions of maximum shear stress and the slip direction predicted by the WB assumptions. Later, Pascal (2002) used the 3D distinct element method (Cundall, 1971 and 1988) and demonstrated that friction attenuates slip perturbations and thus the misfit angle between resolved shear stress and slip vector. More recently, Lejri et al. (2015) conducted a multi-parametric study to estimate this misfit angle. They have tested all possible Andersonian stress regimes, the effect of sliding friction, fault fluid

pressure and Poisson's ratio and have tested various idealized fault geometries. They showed that high misfit angles are to be expected, invalidating the WB assumptions under specific fault configurations such as intersecting faults or highly corrugated fault surfaces, regardless of high fault sliding friction. However, although high misfit angle are expected, no stress inversion techniques based on the debatable WB assumptions have been tested on these specific configurations. Indeed, is a low mean misfit angle correlates to a fair stress inversion result? And inversely, is a high misfit angle correlates to an incorrect stress inversion result using the WB assumptions?

In this contribution we have used the intersecting fault geometry (Maerten, 2000) that yields one of the highest misfit values (Lejri et al., 2015), to test both a WB based stress inversion technique and a BEM-based inversion technique (Maerten et al., 2014) and inverted stress results are compared to the mean misfit angle along the tested fault models. A multi-parametric study covering the most influential parameters such as sliding friction coefficients (μ), the full range of Andersonian state of stress and slip data sampling methodology, as suggested by Lejri et al, (2015), is conducted in order to understand the effect of each parameter on the reliability of the tested stress inversion techniques. For that purpose, we have developed and used a new criterion that measures and compares the 'distance' between the imposed state of stress and the inverted state of stress. It is shown that the 'distance' strongly depends on the fault sliding friction and the special diversity of the slickenline data set used to constrain to inversion. Both stress inversion techniques have also been tested on real data set from Chimney Rock, Utah (USA) (Maerten, 2000) highlighting that the WB-based stress inversions results should be interpreted and used with care.

2. Method

2.1. Stress inversion methods

To evaluate each methods, we compared the results from both methods using synthetic examples for which we know the imposed stress tensor characteristic and the associated computed mechanical slip vector computed.

In order to test the influence of friction coefficient, tectonic stress conditions and sampling methodology, iBem3D, a boundary element method (BEM) for elastic isotropic and heterogeneous half-space (Maerten et al., 2014), formerly called Poly3D (Thomas, 1993), is used through a scripting language. For our purpose, this code is fast enough (Maerten, 2010a) and allows the use of fault friction, which has been implemented using a Gauss-Seidel iterative solver with inequality constraints (Maerten et al., 2010b). This method for implementing friction appears to be stable and less subject to round off errors compared to other techniques (Lagrange multipliers, Penalty methods, or complementary problem). Although heterogeneous and anisotropic sliding friction distribution can be used, we employ a constant friction for the whole sliding fault surface, making the results easier to analyze and comprehend. Another advantage of this numerical method is that fault surfaces are discretized using three dimensional triangulated meshes, allowing complex fault geometries and fast model construction. In such simulation faults will mechanically interact and slide in response to the applied 3D tectonic stress, rock properties and fault friction. The result of the simulation, which is of interest to us, is the heterogeneous slip orientation along the fault planes.

The heterogeneous slip orientations are hereafter used as a slip data for testing stress inversion methods.

Here we test the parameters that may influence the stress inversion solutions accuracy. The tested WB-based stress inversion technique is based on the Ethecopar (1981, 1984) stress inversion method, which uses

a Monte Carlo simulation to find the best fitting resolved shear stress as to the slip data in order to define the paleostress tensor. We expect that other codes and methods based on the same principles would yield similar results.

The tested BEM-based stress inversion technique uses iBem3D technology and is an extension of Maerten et al. (2014) for focal mechanisms. The steps to recover paleo tectonic stress are to run thousands of simulations covering the range of all possible tectonic stress configurations. Then, for each simulation we compare attributes of the modeled slip vectors with the observed slip vector. Finally, we analyze, sort and select the simulations that give the best fit with observed fracture data. The key idea of the technology is to reduce the computation time using the principle of superposition (Brillouin, 1946), a well-known principle in linear elasticity. It allows recovering the displacement, strain and stress at any observation point P using pre-computed specific values from three linearly independent simulations. This principle stipulates that a given value can be entirely determined by a linear combination of independent solutions. One main advantage of this method is that it takes both fault mechanical interactions and heterogeneous stress field into account.

In both methods, we look only for the reduced tensor that can be expressed by the stress ratio \bar{R} (Lejri et al., 2015) and the principal horizontal stress orientation θ .

For both stress inversion methods, a simple cost function (1), taking the sense of slip into account, is used:

$$C = \frac{1 - (\vec{\tau} \cdot \vec{a})}{2} \quad (1)$$

where $\vec{\tau}$ is the shear stress vector and \vec{a} the slip vector. Using this cost function, $C = 0$ if the vectors are collinear, $C = 0.5$ when orthogonal and $C = 1$ when opposed in sense.

For all simulations done in the coming sections, when a parameter is not tested, its default value is given in Table 2. Furthermore, to facilitate the reading of this paper we have listed and defined all variables and parameters in Table 1.

2.2. Fault geometry

As suggested in Dupin et al. (1993), Pollard et al. (1993), Maerten (2000), Pascal (2002), Lisle (2013) and Lejri et al. (2015), we assume that the accuracy of the stress inversion depends on the discrepancy between resolved shear stress orientations (WB assumptions) and computed slip vectors caused by the mechanical interactions between faults. As tested by Dupin et al. (1993), Pollard et al. (1993), and Maerten (2000), fault geometry is a critical controlling factor for mechanical interactions. In that context, Maerten (2000) tested the effect of intersecting idealized normal faults and reported that the misfit angle between the resolved shear stress and the computed slip vector can reach 50° close to the fault intersection line. Xu et al. (2013) observed the same discrepancy on similar pair of intersecting normal faults.

Following these evidences, Lejri et al, (2015) investigated the influence of fault geometry on the misfit angle between slip vectors and the resolved shear traction using : planar faults, intersected faults and sinusoidal faults. It was found that the interactions were maximized for intersecting geometries and corrugated fault geometries. We expect that, since sinusoidal and intersecting faults can be considered as equivalent geometries and yield comparable misfit patterns (Lejri et al., 2015), so that only the intersecting fault geometry is used in this study.

We therefore adopt the idealized fault model with intersecting geometry (Figure 1), consisting of two normal faults, (A) the main fault and (B) the secondary fault, dipping at $\beta = 60^\circ$ with an elliptical tip line and an aspect ratio of 2, defined by the ratio of the major axis (along the strike) length, over the minor axis length (along the dip direction). This average aspect ratio is commonly observed for isolated normal fault (Rippon, 1985; Barnett et al, 1987; Walsh et al., 1989; Nicol et al., 1996). Fault A truncates fault B, and both

faults are linked at their centers with an oblique intersection line. λ is defined by the angle between the strike lines of the faults (**Figure 1**). Here we consider an acute angles $\lambda = 30^\circ$ between the intersecting faults strikes, and opposite dip azimuths. This fault geometry is used for all the following multi-parametric study.

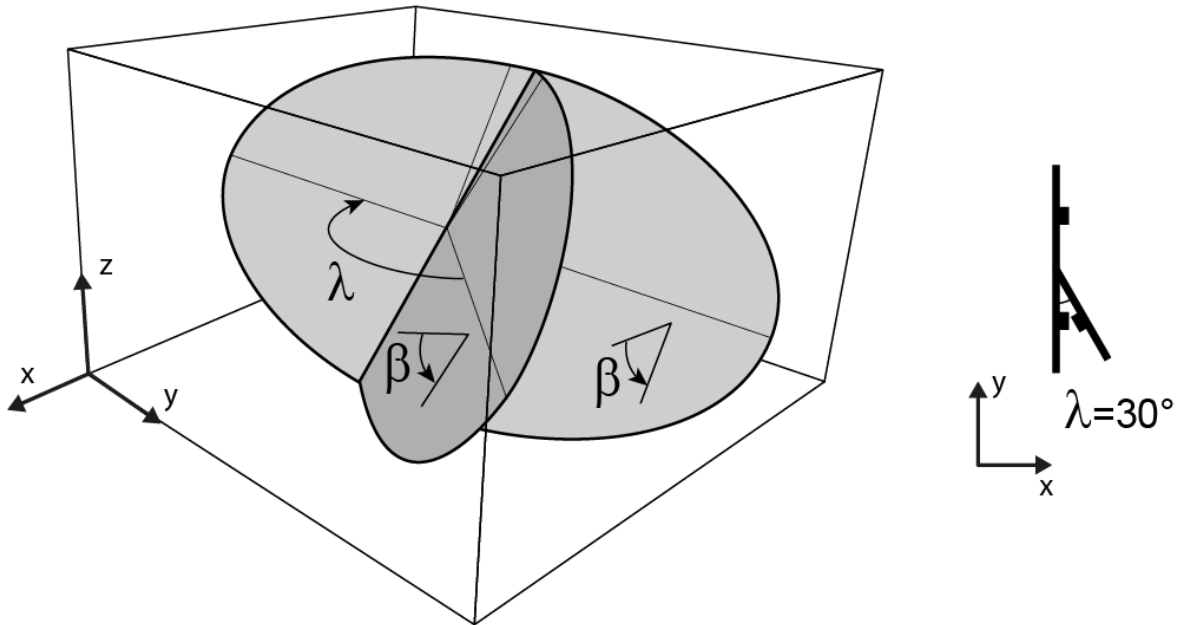


Figure 1. 3D BEM geometry model of intersecting faults. 3D view of one fault model with the intersecting fault pattern used in the simulations where the angle between the strike of 2 intersecting faults, λ , is 30° . The dip angle, β , of the two faults, defined by the dip line and the horizontal line, is 60° .

2.3. Tectonic stress

As it was shown in Lejri et al. (2015), stress has a strong control over faults mechanical interactions. We chose to use only Andersonian tectonic stresses as it is a good approximation of the stress state in the earth crust (Anderson, 1951; Lisle et al. 2006). As shown in Lejri et al. (2015), the full range of possible Andersonian stresses and orientations is necessary in order to investigate stress inversion accuracy. For that purpose, the stress ratio \bar{R} , defined in (2), is used:

$$\left\{ \begin{array}{l} \text{Normal } \bar{R} = R \in [0,1] \\ \text{Wrench } \bar{R} = 2 - R \in [1,2] \\ \text{Reverse } \bar{R} = 2 + R \in [2,3] \end{array} \right\} \quad (2)$$

$$\text{with } R = \frac{(\sigma_2 - \sigma_3)}{(\sigma_1 - \sigma_3)}, \quad (3)$$

Here, depending on which of the principal stresses is vertical, we can cover the normal, wrench and reverse regimes with $\sigma_v = \sigma_1$, $\sigma_v = \sigma_2$ and $\sigma_v = \sigma_3$ respectively, with only one parameter that varies from 0 to 3 continuously. The azimuth θ of the maximum principal horizontal stress defined clockwise from the North is also tested.

2.4. Sliding friction

Lejri et al. (2015) demonstrated that increasing the sliding friction reduces the degree of fault mechanical interactions, hence reducing heterogeneous slip vector distribution, confirming Pascal (2002) prediction that even for intersecting fault geometry, the WB assumption should still be valid when friction is high. However, this is true only for specific tectonic stress configurations (Lejri et al., 2015).

In order to test the effect of sliding friction on the two inversion techniques, we define two types of friction: (1) The imposed sliding friction along faults for the forward mechanical simulations (μ_{imp}) that are used to generate synthetic slip orientations and (2), the inversion friction (μ_{inv}), which is used in the BEM based stress inversion method. We therefore compare computed slip that occurred for μ_{imp} to the slip vectors predicted using μ_{inv} . We thus expect that inverting the stress field using a sliding friction (μ_{inv}) different than the imposed sliding friction (μ_{imp}) should induce inversion solution mismatches. To better understand the effect these sliding friction parameters on stress inversion accuracy, we explore friction coefficients from 0 to 1 with a 0.1 increment (see Table 2). We then study the accuracy of the mechanical frictionless stress inversion method to the WB-based stress inversion method for imposed sliding friction coefficients (μ_{imp}) varying from 0 to 1.

However, when fault friction is added during the inversion process, the principle of superposition does not hold anymore and computation time is highly increased (between 2 to 6 hours for one frictional Δ_{wb} domain depending on the fault model).

2.5. Data sampling

It is generally accepted (Delvaux and Sperner, 2003; Sperner et al., 2003; Lacombe, 2012) that the spatial distribution and variety of collected fault slip data is critical for the accuracy of the inverted paleostress solutions based on the WB assumptions. Particularly, we anticipate that sampling fault slip data along corrugated fault planes or near fault intersections could have a strong impact on these inverted paleostress solutions as several authors (Pollard et al., 1993; Dupin et al., 1993; Maerten, 2000; Lejri et al., 2015) have demonstrated that, for these fault configurations, a strong angular misfit between resolved shear stress and actual slip vector can be found.

Following the results from Lejri et al. (2015), we consider that local angular misfits above 10° could be sufficiently large to impact the accuracy of the inverted paleostress solutions based on the WB assumptions. In order to quantify the stress inversion sensitivity to data sampling, we therefore set the angular misfits of 10° as a threshold value for data sampling methodology. For that purpose we compute the misfit angle, for given far field stress, as the angle between the resolved shear stress (WB assumption) and the mechanically perturbed slip vector. When the local misfit angle is higher than 10°, the fault slip data is classified in the DS+ data category. To study the data sampling effect, we compare the retrieved stress solution using the full dataset and a using DS+ data solely. The main goal here is to quantify as to what extent the DS+ data will deviate the inverted paleostress solution from the expected solution.

2.6. Analysis procedure

In order to test the two stress inversion methods, we define Δ as the ‘distance’ between two Andersonian tectonic stresses (Figure 2a). Since θ (the y-axis of the stress domain in Figure 2) has a symmetry of revolution around the x-axis (i.e. \bar{R}), the distance is defined as:

$$\Delta = \frac{(R_2 - R_1)^2}{18} + \frac{1}{2} \sin^2(\theta_2 - \theta_1) \quad (4)$$

where Δ is the 'distance' between two states of stress in the stress domain, R_1 is the first solutions stress ratio and R_2 is the second solutions stress ratio, θ_1 is the first solution principal horizontal stress orientation according to the north and θ_2 is the second solution principal horizontal stress orientation. A 'distance' Δ of 1 is equivalent to a solution distance of 90° along θ axis and 3 along \bar{R} axis. Using the normalized distance (Δ) instead of θ and \bar{R} distances, which do not have the same units, provides a better way to measure and comprehend the solution uncertainty.

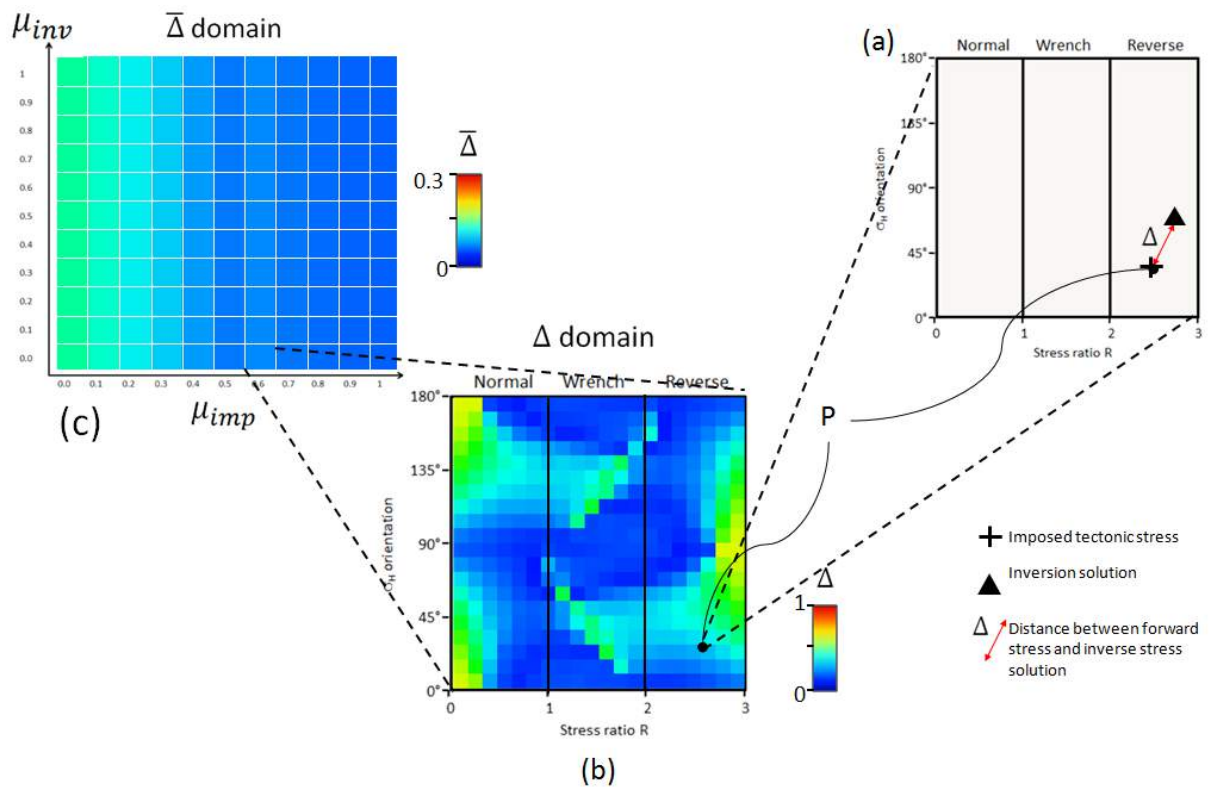


Figure 2. Δ domain and $\bar{\Delta}$ graph. (a) shows the distance between the forward simulation and the recovered tectonic stresses. (b) shows the Δ domain wherein the distance is plotted for each simulation covering the entire tectonic stress domain by a 20x20 resolution. (c) shows the $\bar{\Delta}$ domain, where mean value of each Δ domain is plotted for different μ_{imp} and μ_{inv} (from 0 to 1 by with an increment of 0.1).

The distance domain (Δ domain) (see Figure 2b), used to analyze the multi-parametric simulations, is a 2D parameter space, similar to the domains shown in Lejri et al. (2015), that covers the full Andersonian tectonic stress configurations. We define Δ_m and Δ_{wb} as the BEM-based stress inversion distance to the

imposed reference far field stress and the WB-based stress inversion solutions distance to the imposed reference far field stress respectively. The x-axis represents the stress ratio \bar{R} , whereas the y-axis is the orientation θ of the maximum principal horizontal stress defined clockwise according to the North. For a given stress $\sigma(\bar{R}, \theta)$, represented by point P in Figure 2b, Δ is computed and reported in the 2D domain as a color coded point. The same procedure is repeated for each point of the Δ domain until the entire parameter space is covered. Δ domain is covered with a resolution of 20*20, which makes a total of 400 stress inversions per domain. The Δ domain in Figure 2ab highlights for which model configurations the highest Δ (hot colors) and the lowest Δ (cold colors) can be found. White regions in the domain are defined as model configurations where no slip is computed in the forward simulation; therefore no stress inversion can be performed.

We also define the mean distance graph ($\bar{\Delta}$ domain), as the evolution of mean 'distance' (Δ), written $\bar{\Delta}$, with respect to the variation of other parameters. In this study, it is limited to the sliding friction coefficient (Figure 2c, Figure 5a, Figure 5b). In Figure 2c, the imposed sliding friction along the faults for the forward mechanical simulations (μ_{imp}) that are used to generate synthetic slip orientations, is reported on the X-axis, while the inversion friction (μ_{inv}), which is used in the BEM stress inversion method, is reported on the Y-axis. This type of representation allows a better understanding of the general trends of $\bar{\Delta}$ according to both imposed and inversion friction parameters. As an example, the Δ domain highlighted in Figure 2b has been computed for a μ_{imp} of 0.6 and a μ_{inv} of 0 and shows a $\bar{\Delta}$ of 0.35 (see Figure 2c).

We have seen in the introduction that many authors have questioned the validity of the WB-based stress inversion methods exclusively analyzing the misfit angle (ω) between the resolved shear stress and the mechanically derived slip vector (Dupin et al., 1993; Pollard et al., 1993 ; Maerten, 2000; Pascal, 2002; Lejri et al., 2015). Kaven et al. (2011) pushed the analysis a little further as they discussed the accuracy of WB-based stress inversion method by comparing the stress inversion results to the known stress solutions. However, their analysis, which concluded that the WB-based inversion method does not perform well, has

been performed on too simplified fault configurations. Indeed, stress inversion on isolated faults or on fault systems with limited strike ranges, which yield restraining slip vector orientations, are likely to produce inaccurate stress inversion results as the method will be under-constrained (Sperner et al., 2003; Lacombe, 2012). Therefore, the correlation between the misfit angle (ω) and the accuracy of the inversion solution has never really been established. To fill this gap, we propose to compare the Δ domain with the domain of the mean misfit angle ($\bar{\omega}$ domain), which is the mean of all constitutive element misfit angles on the considered fault network display on a (\bar{R}, θ) domain, as shown in Figure 3 that will be analyzed later. To quickly assess the correlation and anti-correlation patterns between the two domains, we create a correlation domain (see Figure 4) in which to most significant correlation between the normalized two domains is highlighted. For each point of the domain we define D as being the difference between the normalized Δ and the normalized $\bar{\omega}$ such that $D = \Delta - \bar{\omega}$. When $-0.33 < D < +0.33$ we said that there is correlation. When $D > +0.33$ and $D < -0.33$ we said that there is positive (red color) and negative (blue color) anti-correlation respectively.

Similarly, in Figure 5 we compare the $\bar{\Delta}$ domain with the $\bar{\omega}$ graph, $\bar{\omega}$ being the average of $\bar{\omega}$. For the BEM-based stress inversion, 2D domains can be established ($\bar{\Delta}_m$ domain and $\bar{\omega}_m$ domain) since we cover both the full range of μ_{imp} and μ_{inv} . The x-axis represents the imposed friction (μ_{imp}), while the y-axis represents the inversion friction (μ_{inv}). However, for the WB-based stress inversion, only 1D domains can be established ($\bar{\Delta}_{wb}$ domain and $\bar{\omega}_{wb}$ domain) since we only cover the full range of μ_{imp} . So here, the x-axis also represents the imposed friction (μ_{imp}), while there is no y-axis.

3. Analyses

3.1. Relationship between $\bar{\omega}$ and Δ

Understanding the relationship between $\bar{\omega}$ and Δ is necessary in order understand whether a low $\bar{\omega}$ is related to reliable stress inversion result or not. The idea that $\bar{\omega}$ is a good criterion for validating a stress

inversion has been mentioned and used in some published work (Pollard et al, 1993; Dupin et al., 1993; Maerten, 2000; Lejri et al., 2015). We therefore need to investigate the relationship between the $\bar{\omega}$ and Δ patterns for the selected fault geometry (Figure 1).

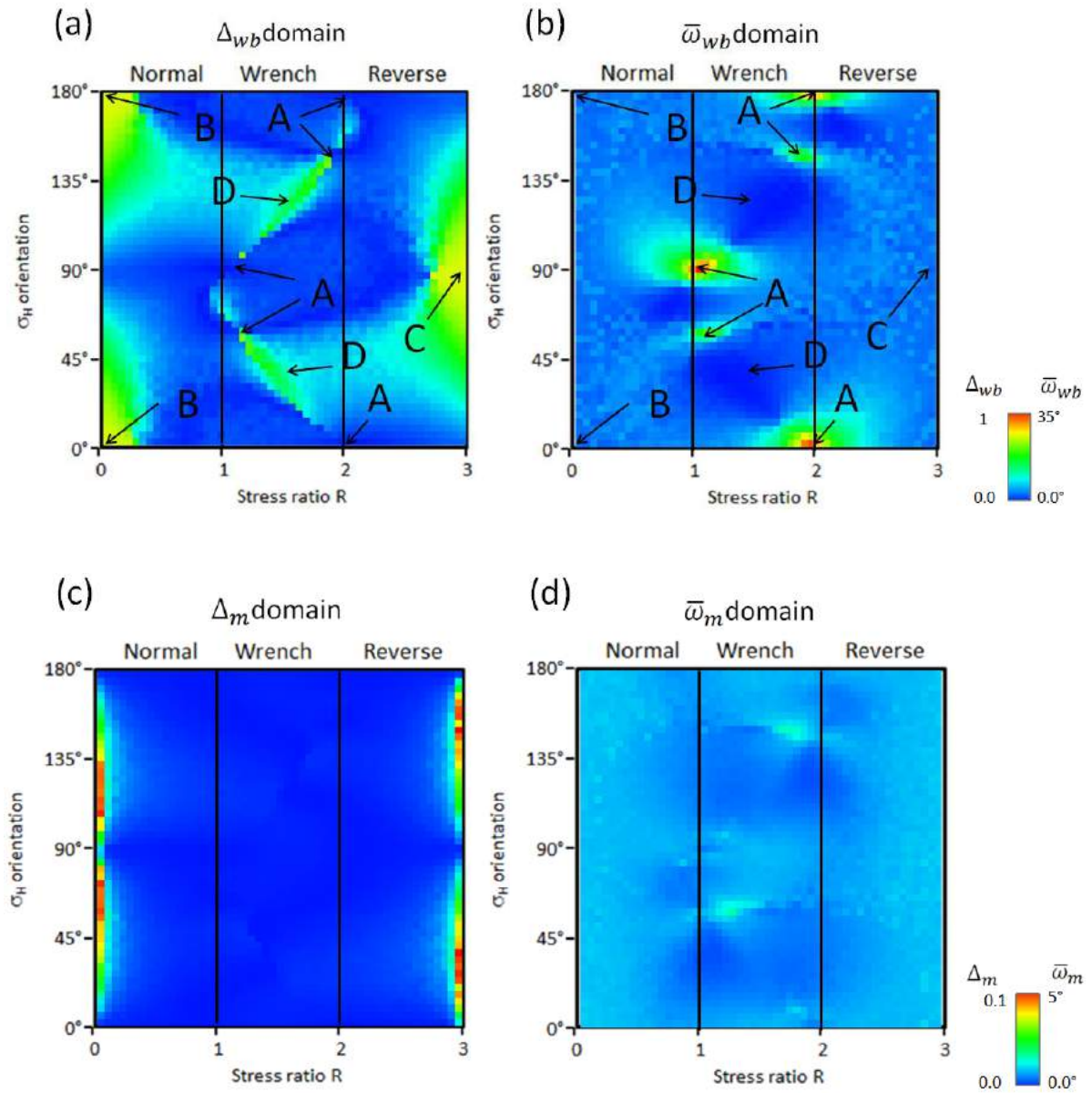


Figure 3. Δ vs $\bar{\omega}$ patterns for the studied synthetic case with frictionless fault ($\mu_{imp} = 0$) and ($\mu_{inv} = 0$) for (a,b) the WB-based stress inversion and (c,d) the BEM-based stress inversion.

$\bar{\omega}_{wb}$ domain and Δ_{wb} domain are shown in Figure 3ab. An imposed sliding friction $\mu_{imp} = 0$ is used for the reference model. $\bar{\omega}_{wb}$ patterns are explained in Lejri et al. (2015). High $\bar{\omega}_{wb}$ matches higher mechanical interaction between faults, specifically when one fault is not optimally oriented to slide. In Figure 3b, the highest values of $\bar{\omega}_{wb}$ are observed along the pure wrench band near A regions (Lejri et al., 2015), while in Figure 3a, the highest values of Δ_{wb} are observed along the pure normal regime and along the pure reverse regime, near B and C regions and along the pure wrench band, near D regions. It is important to note that near these bands of pure tectonic regimes (normal, wrench and reverse), $\bar{\omega}_{wb}$ and Δ_{wb} seem to be anti-correlated. This anti-correlation is mostly noticeable around regions A and D (see Figure 3ab) of the domain following the pure wrench band. Other anti-correlation examples are seen following both the pure normal and reverse bands near regions B and C respectively.

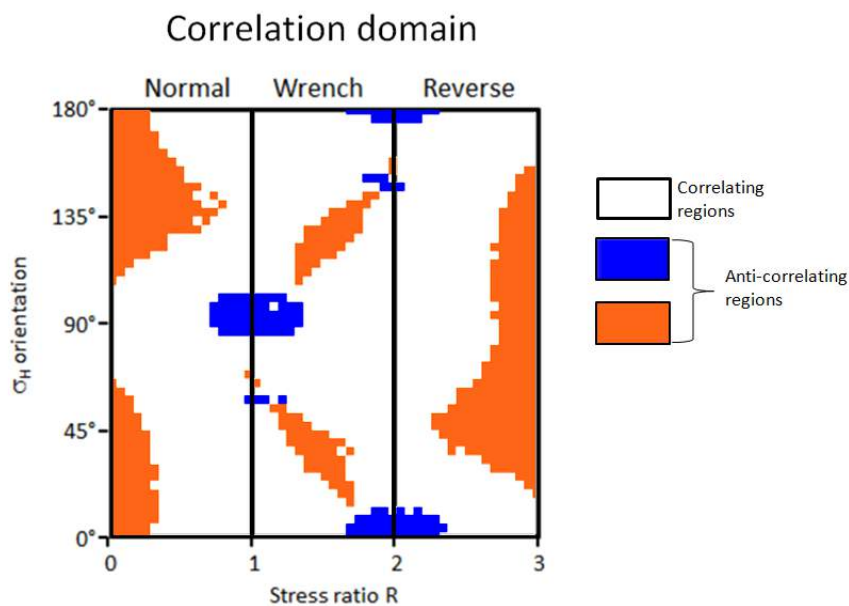


Figure 4. Correlation domain. Blue color is for high $\bar{\omega}$ and low Δ , Red is for low $\bar{\omega}$ and high Δ (taking 0.33 as a threshold value) the total area of these anticorrelation regions is 26.6% of the domain. The white domain is for correlating regions between $\bar{\omega}$ and Δ .

In order to better simplify the analysis of these observations, the correlation domain of Figure 4 is used to highlight that about 30% of the domain shows an anti-correlation (red and blue colors) between $\bar{\omega}_{wb}$ and Δ_{wb} . Therefore, $\bar{\omega}_{wb}$ and Δ_{wb} are correlated for 70% of the domain area (white color). In other words, a low $\bar{\omega}_{wb}$ is not necessarily correlated to a strong stress inversion result and inversely, a high $\bar{\omega}_{wb}$ is not always correlated to a weak stress inversion result using the WB assumptions. The anti-correlation between $\bar{\omega}_{wb}$ and Δ_{wb} is preserved when sliding friction is added along the faults (not shown here), even though the maximum values of both $\bar{\omega}_{wb}$ and Δ_{wb} tend to be attenuated with increasing friction.

Figure 3c illustrates that there is a perfect match between the imposed far field stress used as reference and the inverted stress as the entire Δ_m domain is blue ($\Delta_m=0$) except along the $\bar{R}=0$ and $\bar{R}=3$, where the θ cannot be determine. The $\bar{\omega}_m$ domain shown in Figure 3d displays a pattern similar to the $\bar{\omega}_{wb}$ domain of Figure 3b but with a much lower maximum mean misfit angle $\bar{\omega}_m=2^\circ$. No correlation domain has been generated for the BEM-based stress inversion models as there is a perfect match between the imposed far field stress used as reference and the inverted stress.

3.2. Sliding friction effect

In order to understand how the sliding friction affects the stress inversion accuracy, we need to study its effect using both the imposed sliding (μ_{imp}) friction on the reference model and the sliding friction used for the inversion (μ_{inv}). The latter will be used only for the BEM-based inversion method. The effect of the imposed sliding friction (μ_{imp}) and the inversion friction (μ_{inv}) on $\bar{\Delta}_m$ and $\bar{\omega}_m$ as well as on $\bar{\Delta}_{wb}$ and $\bar{\omega}_{wb}$ are explored using the intersecting fault model shown in Figure 1 and the results are shown in Figure 5.

The $\bar{\Delta}_m$ domain (Figure 5a) shows that $\bar{\Delta}_m$ is 0 when μ_{inv} and μ_{imp} are equal, and that $\bar{\Delta}_m$ increases when μ_{inv} is different from μ_{imp} . The $\bar{\omega}_m$ domain (see Figure 5a) shows a similar trend where $\bar{\omega}_m$ is 0 when μ_{inv} and μ_{imp} are equal and where $\bar{\omega}_m$ increases when μ_{inv} is different from μ_{imp} . In addition, $\bar{\Delta}_m$ and $\bar{\omega}_m$

are globally lower when $\mu_{inv} \leq \mu_{imp}$ than for $\mu_{inv} > \mu_{imp}$. The $\bar{\Delta}_m$ and $\bar{\omega}_m$ patterns have the same trends and seem to be correlated.

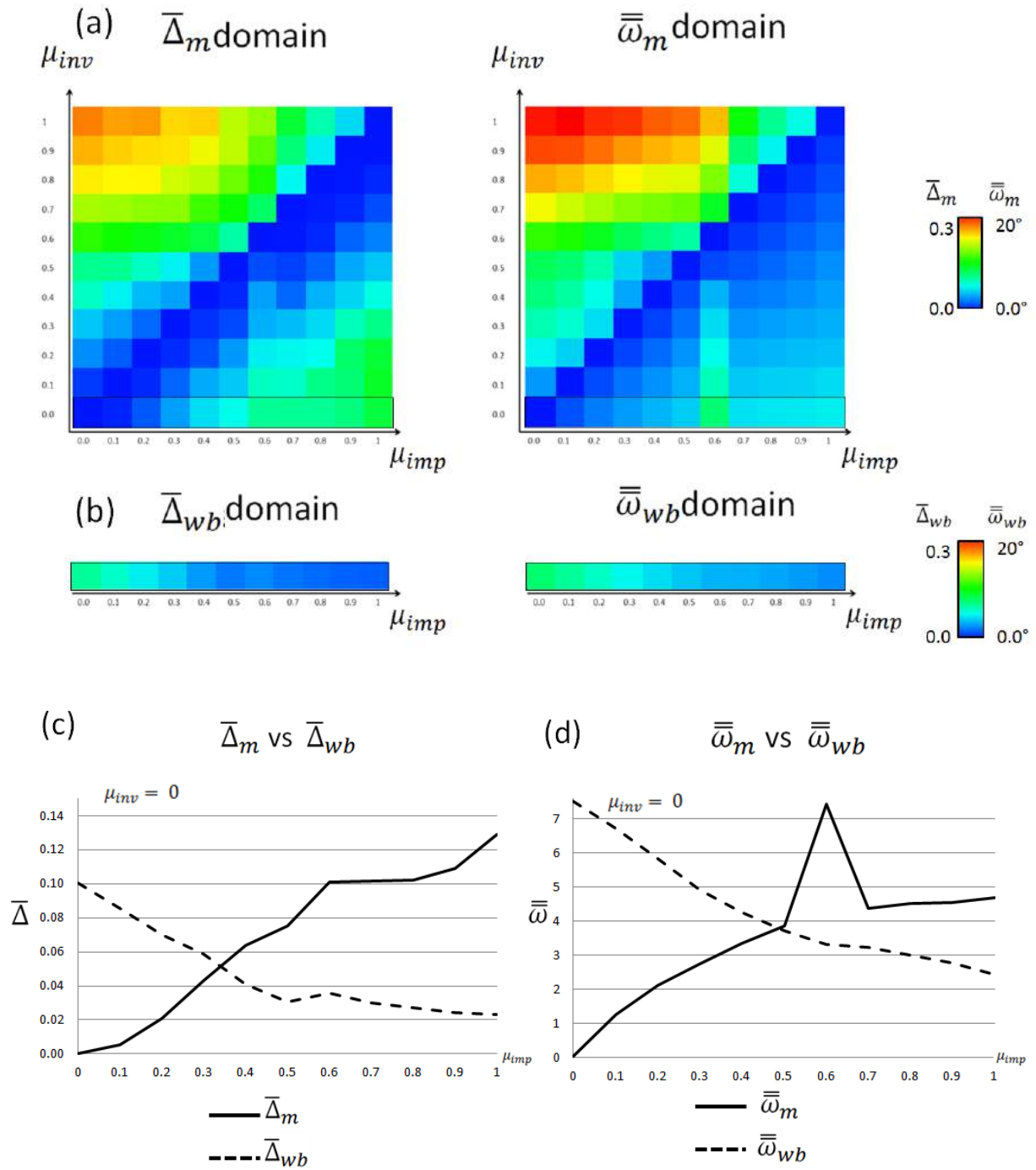


Figure 5. (a) $\bar{\Delta}_m$ and $\bar{\omega}_m$, (b) $\bar{\Delta}_{wb}$ and $\bar{\omega}_{wb}$ (c) $\bar{\Delta}$ comparison for frictionless inversion (d) $\bar{\omega}$ comparison for frictionless inversion.

As seen earlier, since inversion friction cannot be used for the WB-based stress inversion, the $\bar{\Delta}_{wb}$ and $\bar{\omega}_{wb}$ domains (Figure 5b) are 1D domains, where only the x-axis (μ_{imp}) is exposed. A direct comparison between $\bar{\Delta}_m$ and $\bar{\Delta}_{wb}$, as well as between $\bar{\omega}_m$ and $\bar{\omega}_{wb}$ is therefore performed for a BEM-based stress inversion using a fixed μ_{inv} . Here we use $\mu_{inv} = 0$ for the graphs shown in Figure 5cd as computation time is much lower when no sliding friction is used.

Figure 5cd, which represent the 2D graphs of the 1D domains described earlier, show that $\bar{\Delta}_{wb} = 0.1$ for $\mu_{imp} = 0$ and decreases when μ_{imp} increases to reach $\bar{\Delta}_{wb} = 0.02$ for $\mu_{imp} = 1$. The $\bar{\omega}_{wb}$ graph shows the same trend as $\bar{\omega}_{wb}$ varies from 7.4° to 2.4° when μ_{imp} increases from 0 to 1. $\bar{\Delta}_{wb}$ and $\bar{\omega}_{wb}$ are therefore correlated. Similarly, that $\bar{\Delta}_m = 0$ for $\mu_{imp} = 0$ and increases when μ_{imp} increases to reach $\bar{\Delta}_m = 0.13$ for $\mu_{imp} = 1$. The $\bar{\omega}_m$ graph shows the same trend as $\bar{\omega}_m$ varies from 0° to 4.8° when μ_{imp} increases from 0 to 1. $\bar{\Delta}_m$ and $\bar{\omega}_m$ are therefore correlated. The picks observed along the $\bar{\Delta}$ and $\bar{\omega}$ curves for $\mu_{imp} = 0.6$ are explained in annex.

Figure 5b also show, for an inversion sliding friction $\mu_{inv} = 0$, that $\bar{\Delta}_m$ and $\bar{\Delta}_{wb}$ as well as $\bar{\omega}_m$ and $\bar{\omega}_{wb}$ are anti-correlated. The $\bar{\Delta}$ curves cross cut each other for $\mu_{imp} = 0.34$ while $\bar{\omega}$ curves cross cut each other for $\mu_{imp} = 0.48$.

3.3. Sampling effect

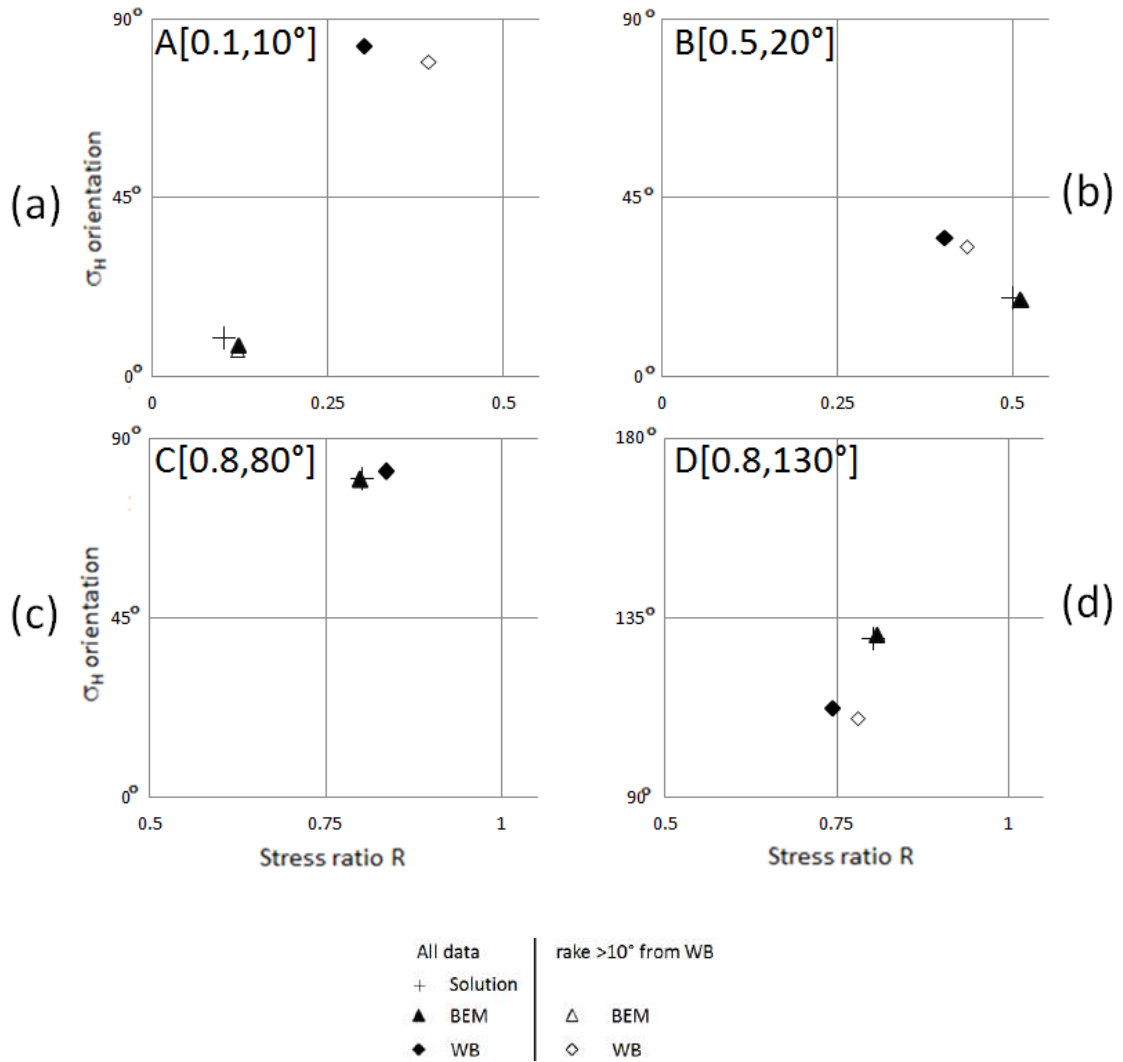


Figure 6. Tectonic Domains for the synthetic model solutions. The domains show the stress inversions solution discrepancy when using all data and only perturbed data for different imposed tectonic stresses (a,b,c,d)

In order to study the sampling effect (see Figure 6) we compare the stress inversion solutions using the full slip vectors generated mechanically in a forward sense (black symbols in Figure 6), and the solution using DS+ slip vectors only (empty symbols in Figure 6), to the imposed far field stress for a frictionless fault model (crosses in Figure 6). The main goal is to evaluate the uncertainty of the stress inversion solutions when

using sampled data. We always make sure that slip vector orientations are heterogeneous enough to avoid under-constrained model incompatible with methods based on the WB assumptions. The x-axis represents the stress ratio (\bar{R}), while the y-axis represents the maximum horizontal stress orientation (θ). Four tectonic stress fields (a, b, c and d in Figure 6) have been tested, all in the normal regime ($0 \leq \bar{R} \leq 1$). Far field stresses too close to the special case of $\bar{R} = 0$, where there is a strong uncertainty in θ , have been avoided.

On one hand, Figure 6 shows that the BEM-based stress inversion solutions (triangles in Figure 6) are always very close to the imposed far field stress, where Δ is always lower than 0.028, whatever the data sampling. On the other hand, WB-based stress inversion solutions have higher distance to the solution. The worst case is for model A, where Δ reaches 0.68 (see Figure 6a). This is equivalent to an uncertainty of 73° in θ and 0.2 in \bar{R} . As explained in the previous sections (see Figure 3 and 4), Δ is higher when the tested far field stress that needs to be inverted is close to the pure normal regime band ($\bar{R} = 0$) and ever more when the orientation of the maximum horizontal stress is parallel to the main fault ($\theta=0^\circ$ or 180°) as demonstrated by Lejri et al. (2015). Using the sampled data set (DS+ slip vectors), the WB-based stress inversion systematically gives different solutions than with the full dataset. The maximum distance found between DS+ solutions and the full dataset solutions using WB-based stress inversion is $\Delta = 0.053$ for model A (Figure 6a). This distance is reduced when the imposed far field stress is far from pure stress regime bands ($\bar{R}=0$ and $\bar{R}=3$).

4. *Chimney Rock case study*

In this section we intend to apply our findings to a real case study that should associate the knowledge of both the 3D fault pattern and the slip vectors observed along most of the fault traces. It appeared then obvious that the Chimney Rock fault array, central Utah (USA), would be a perfect candidate for such exercise.

4.1. Geologic setting and previous models

The Chimney Rock normal fault system is located in a 6° dipping strata (Krantz, 1988) on the northern anticlinal hinge of the San Rafael swell (Figure 7a). The swell is a dome-like structure part of the Colorado plateau region, composed of a Phanerozoic sedimentary sequence (Kelley, 1955; Dickinson and Snyder, 1978). The normal fault system was formed during the Paleocene Laramide Orogeny 60-40 million years ago. It offsets Jurassic Navajo sandstone, covered by thinly bedded limestones, siltstones, and mudstones of the basal Carmel Formation and has been exposed to erosion by flash floods ever since (Figure 9). Chimney rock system is composed of thirteen major faults (Figure 8a,b). It was first mapped by Gilluly (1928) as part of the analysis of the San Rafael Swell.

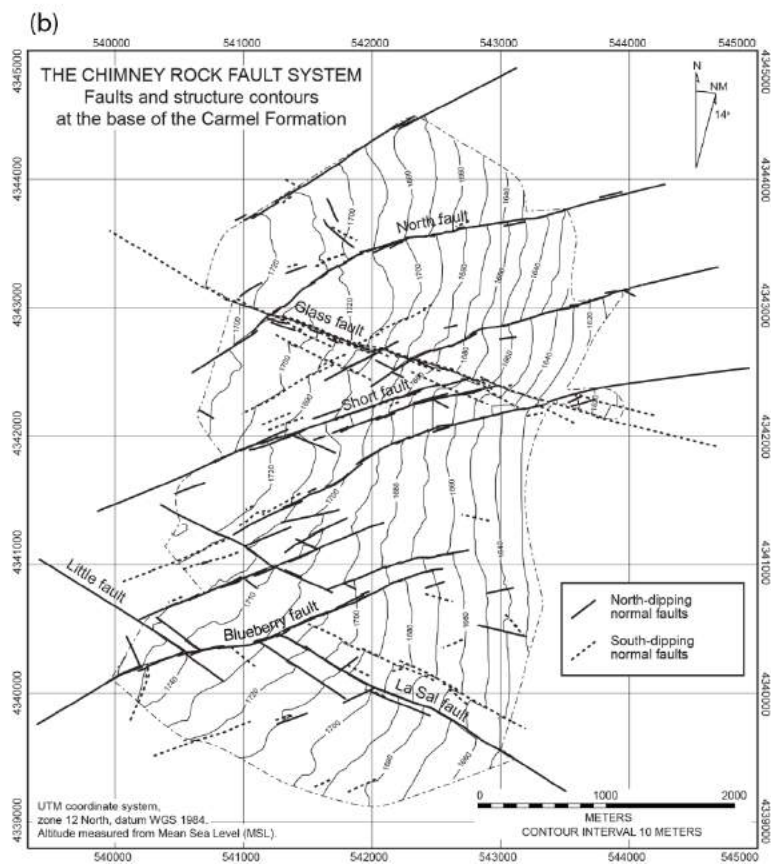
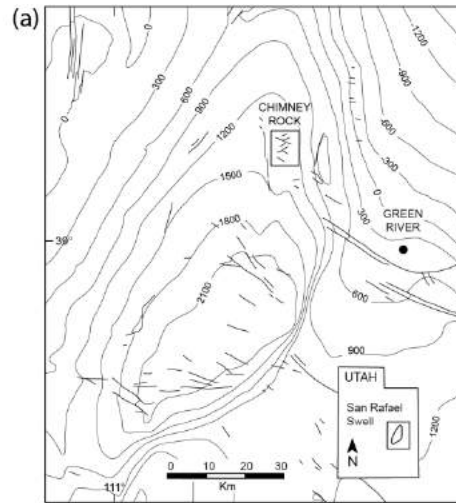


Figure 7. Maps of the (a) San Rafael swell and the (b) Chimney Rock fault system, UTAH, USA. (After Maerten, 2000).

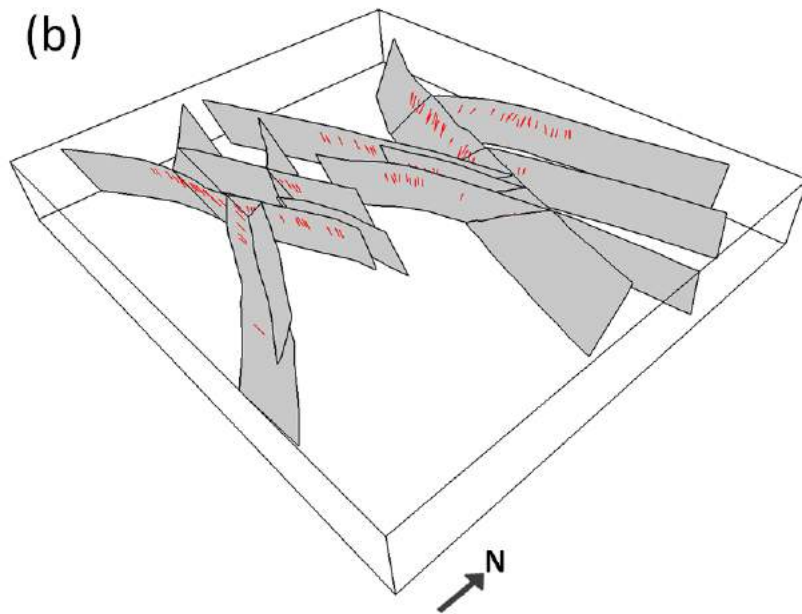
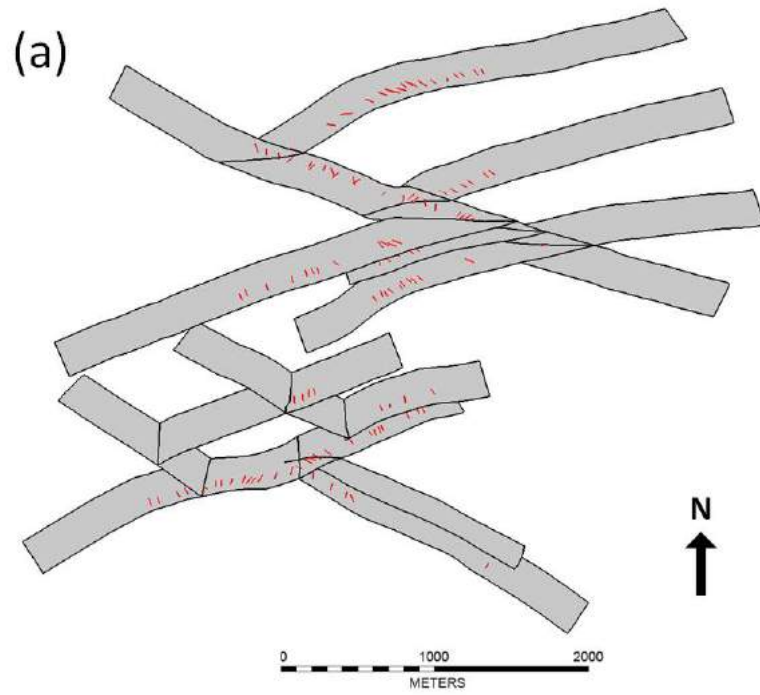


Figure 8. Chimney rock fault system geometry. (a) top view and (b) perspective view. Red lines are for the measured slickenline orientations (slickenline size is exaggerated for better visibility).

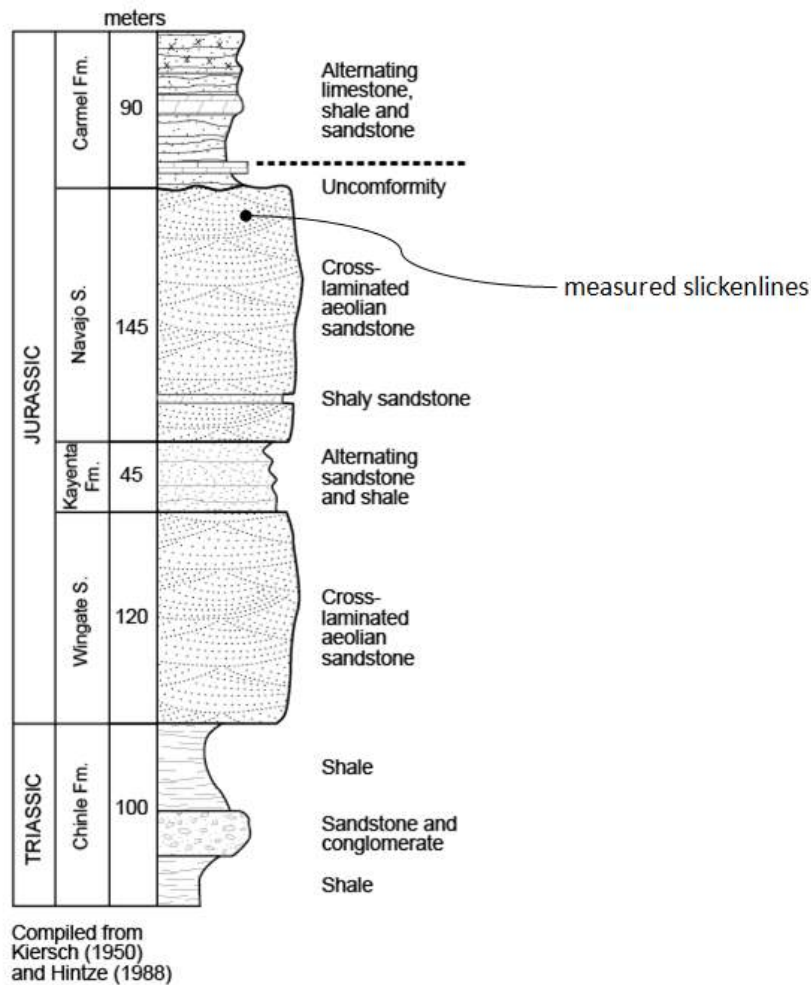


FIGURE 9. Stratigraphic log of the Rafael swell. The position of the measured slickenlines is indicated (at the top of the Navajo formation). (After Maerten, 2000).

The fault system has been interpreted to have formed simultaneously in response to general three-dimensional strain (Oertel, 1965; Aydin and Reches, 1982). Thus, in 1986, Krantz used the orthorhombic nature of the fault system and the direction of fault poles to predict the principal paleostrain orientations and ratios (Krantz, 1986, 1989). Krantz (1988) analysis is based on the fault geometry, spacing, and offset distributions. His analysis assumed coeval fault formation and uniform slip rate on all fault sets resulting in coaxial strain.

Davatzes (2003) suggested that the development of the Chimney Rock faults took place after two faulting phases characterized by the two deformation mechanisms described by Aydin (2000) that can take place in sandstones. The first phase of faulting was characterized by deformation bands produced principally ENE-striking faults. After the first phase of faulting, the formation of WNW-striking regional joint sets marked a change in deformation mechanism. The joints provided discontinuities that localized shearing leading to the formation of WNW-striking faults. Davatzes (2003) suggested that during the second phase, all the faults sets could have slipped simultaneously, explaining the reorientation of slickenlines in proximity to fault intersections as observed by Maerten (2000), indicating mechanical interaction among sets of faults (Maerten, 2000).

Maerten (2000) did an extensive measurement of the slip vectors along the faults. It striations rake from 50°E to 50° W with a peak at 90° (pure dip slip) while the maximum vertical offset across a single fault in the entire study area is 38 m (Maerten, 2000; Maerten et al., 2001). Maerten, (2000) compared the observed slip directions to the simplified elastic model. He showed that the computed heterogeneous slip has similar directions and magnitude to the observed slip distributions, especially close to the intersection lines. His study confirmed the evaluations done by Dupin et al. (1993) and Pollard et al. (1993), on the validity of the WB assumptions.

4.2. Fault model configuration

Using the map of the fault array produced by Krantz (1988) and later improved by Maerten et al. (2000) using GPS measurements, the 3D fault model comprising 13 major faults surfaces was reconstructed (Figure 8a,b) The dip of the faults at Chimney Rock faults varies from 57° to 81° (Krantz, 1988; Maerten, 2000) with an average around 70°, we use a constant fault dip of 70°. The vertical position of the faults has been centered on the Kayenta Formation, which is approximately the center of the competent mechanical units of the stratigraphic column comprising the Navajo Sandstone and the Wingate Sandstone (see Figure 9). In order to approach the average fault aspect ratio between 2 to 3, which is defined by the ratio of the

horizontal length over the fault dip dimension (Rippon, 1985; Barnett et al, 1987; Walsh et al. 1989; Nicol et al., 1996) and commonly observed for normal faults, a total of 750 m was chosen for the vertical dimension of the faults. This fault height takes into consideration the portion of the faults in the less competent units above and below the more competent units.

208 high confidence striation rakes measured along six of the major faults (Maerten, 2000) within the first 10 meters of the top Navajo Sandstone, were considered for this study (see Figure 9) . Maerten (2000) gives a detailed description of the striation rake perturbations observed along the major faults, especially near fault intersections.

A homogeneous triangular mesh size of 50m was used for the fault model. At each triangular element a combination of traction and displacement boundary conditions was prescribed. A displacement component normal to the fault plane was initially set to 0 in order to prevent any opening or interpenetration of the fault walls. The two other components parallel to the fault plane, which may represent the local slip along a dip-slip or strike-slip fault, were set to have initial tractions (or stress drop) equal to 0 in order to let the faults freely slip in response to the remote load. These local boundary conditions allow for mechanical interaction between the faults. This fault boundary condition is essential if we want to use the reduced tensor for the paleostress inversion.

4.3. Stress inversions and sampling methodology

In order to test the stress inversion methods accuracy, a stress inversion using, firstly, the full dataset (208 high confidence slickenline dip, strike and rakes from Maerten 2000) and secondly, selected data following the DS+ sampling process, is conducted using both the WB-based and the BEM-based stress inversion methods. As opposed to the previous synthetic examples, the exact far field paleostress is not known, only the paleostrain has been estimated (Krantz, 1986, 1988, 1989), so we do not have a direct way to evaluate the paleostress inversion results. We therefore adopted the following procedure: (i) we first

perform paleostress inversion using both techniques, (ii) we use both paleostress solutions to constrain forward simulations and compute associated slip vectors along the faults and (iii), we perform paleostress inversion using both techniques constrained by synthetic slip vectors and compare the results.

Stress inversion solutions for Chimney Rock

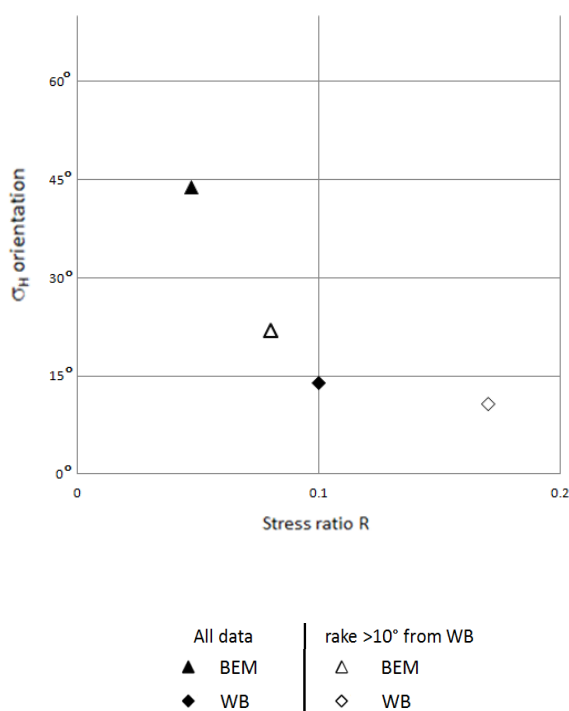


Figure 10. Stress inversion solutions using BEM inversion and WB inversion, using the full slickenlines data set, and the DS+ slip orientations dataset.

Using the entire observed slip vectors dataset, the BEM-based stress inversion method yields a normal stress regime with the orientation of the maximum horizontal stress $\theta = 43.5^\circ\text{N}$ and a stress ratio $\bar{R} = 0.047$ (black triangle in Figure 10). Using the same dataset, the WB-based stress inversion method also gives a normal stress regime but with $\theta = 13.9^\circ\text{N}$ and $\bar{R} = 0.1$ (black diamond in Figure 10). The computed distance (Δ) between these two solutions is $\Delta = 0.35$. When using the DS+ data only, the BEM-based stress inversion method gives $\theta = 22^\circ\text{N}$ and $\bar{R} = 0.08$ (white triangle in Figure 9) and $\theta = 11^\circ\text{N}$ and $\bar{R} = 0.17$ (white diamond in Figure 9) for the the WB-based stress inversion method. The computed distance (Δ) between these two solutions is $\Delta = 0.14$. In both cases, the paleostress inversion solutions using the full data set or the sample

data set (DS+) do not give the same results. Most of the uncertainty is on θ for the BEM-based stress inversion method and on \bar{R} for the WB-based stress inversion method.

Thereafter, both paleostress solutions (black symbols in Figure 10 and crosses in Figure 11ab) using the two techniques and the full slip data set are used in a forward sense in order to generate a synthetic data set based on computed slip vectors along the Chimney Rock faults. We then use this new synthetic dataset to constrain the paleostress inversions using the two techniques. Both the full dataset and the sampled data set (DS+) have been investigated.

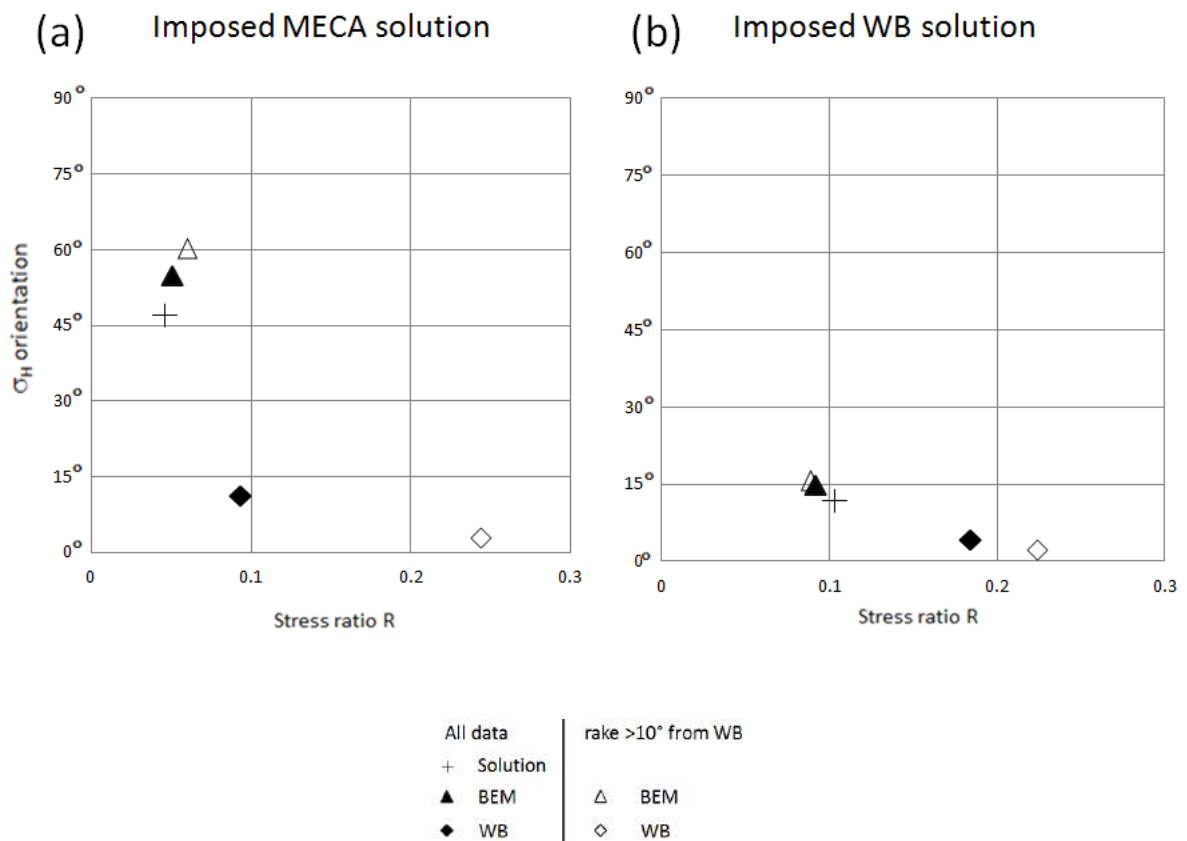


Figure 11. Tectonic domain for (a) the imposed mechanical solution and (b) the imposed WB solution. Using the full generated slip orientations and the DS+ only generated slip orientations.

In Figure 11a we compare the stress inversion solutions of both techniques using the slip vectors generated from the previous BEM-based stress inversion solution ($\theta = 43.5^\circ\text{N}$, $\bar{R} = 0.047$, black triangle in Figure 10 and cross in Figure 11a). Here, the BEM-based stress inversion method gives a solution close to the reference with $\theta = 55^\circ\text{N}$ and $\bar{R} = 0.05$ using the full dataset and $\theta = 63^\circ\text{N}$ and $\bar{R} = 0.06$ using the sampled data set (DS+). The computed distances (Δ) between the two solutions using the full and sampled data set (triangles in Figure 11a) and the far field stress reference (cross in Figure 11a) are $\Delta = 0.14$ and $\Delta = 0.23$ respectively with a bigger uncertainty on θ than on \bar{R} . However, the WB-based stress inversion method gives a solution far from the reference with $\theta = 11.25^\circ\text{N}$ and $\bar{R} = 0.09$ using the full dataset and $\theta = 2.7^\circ\text{N}$ and $\bar{R} = 0.24$ using the sampled data set (DS+). The computed distances (Δ) between the two solutions using the full and sampled data set (diamonds in Figure 11a) and the far field stress reference (cross in Figure 11a) are $\Delta = 0.39$ and $\Delta = 0.47$ respectively with a bigger uncertainty on \bar{R} than on θ .

Similarly, in Figure 11b we compare the stress inversion solutions of both techniques using the slip vectors generated from the previous WB-based stress inversion solution ($\theta = 13.1^\circ\text{N}$, $\bar{R} = 0.1$, black diamond in Figure 10 and cross in Figure 11b). With this configuration, the BEM-based stress inversion method gives a solution close to the reference with $\theta = 14.6^\circ\text{N}$ and $\bar{R} = 0.09$ using the full dataset and $\theta = 15.6^\circ\text{N}$ and $\bar{R} = 0.088$ using the sampled data set (DS+). The computed distances (Δ) between the two solutions using the full and sampled data set (triangles in Figure 11b) and the far field stress reference (cross in Figure 11b) are $\Delta = 0.008$ and $\Delta = 0.02$ respectively. On the other hand, the WB-based stress inversion method gives a solution away from the reference with $\theta = 4^\circ\text{N}$ and $\bar{R} = 0.18$ using the full dataset and $\theta = 2.1^\circ\text{N}$ and $\bar{R} = 0.22$ using the sampled data set (DS+). The computed distances (Δ) between the two solutions using the full and sampled data set (diamonds in Figure 10b) and the far field stress reference (cross in Figure 11b) are $\Delta = 0.123$ and $\Delta = 0.147$ respectively, with a bigger uncertainty on \bar{R} than on θ .

4.4. Stress inversions accuracy prediction domain

As for the synthetic model (see Figure 1), it is possible to compute Δ_{wb} domain for the Chimney Rock fault system. The analysis of this Δ_{wb} domain together with the results of the previous paleostress inversion solutions should give an idea as to what extent the WB-based stress inversion method is reliable compared to the BEM-based stress inversion method.

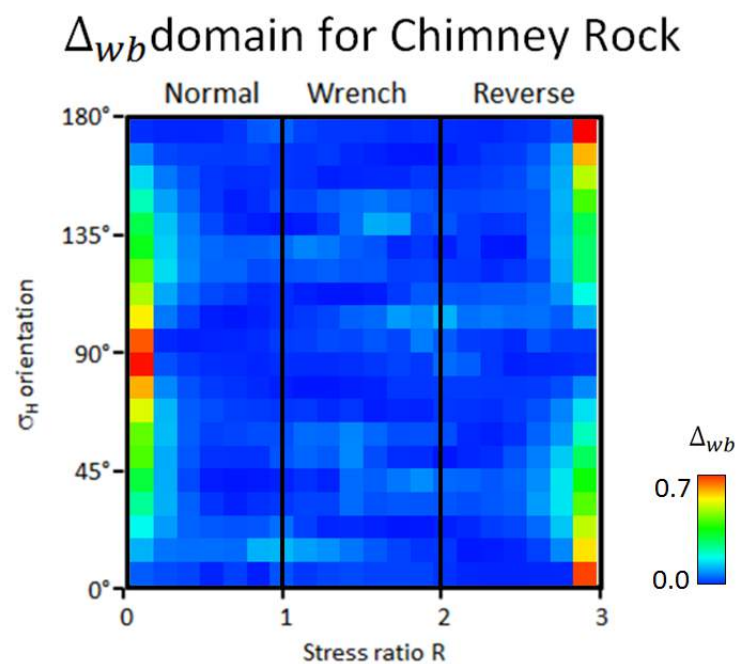


Figure 12. Uncertainty domain for the WB based stress inversion method using the chimney rock model.

Figure 12 shows the Δ_{wb} domain for the Chimney Rock faults generated using imposed friction $\mu_{imp}=0$. Maximum Δ_{wb} ($\Delta_{wb} \approx 0.68$) are observed near both the pure normal (extensional) and the pure reverse (compressive) regimes, while lower heterogeneous values ($\Delta_{wb} \approx 0.1$) are observed elsewhere.

Note that, while Δ_{wb} it is still high for the pure normal and reverse regime bands, it is globally lower for the Chimney Rock model than the intersecting synthetic fault model (see Figure 1). Also, the anticorrelation area (18%) is reduced (Figure 13) compared to the synthetic model (Figure 3).

Correlation domain for Chimney Rock

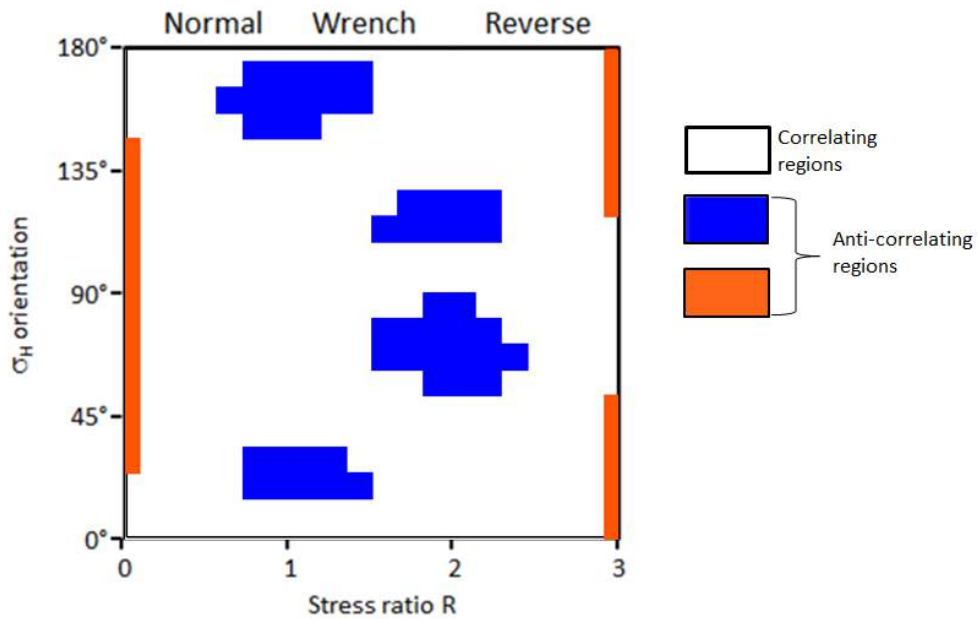


Figure 13. Correlation domain for Chimney Rock fault model. Green color is for high $\bar{\omega}_{wb}$ and low Δ_{wb} , Red is for low $\bar{\omega}_{wb}$ and high Δ_{wb} (taking 0.33 as a threshold value) the total area of these anticorrelation regions is 18.5% of the domain. The white domain is for correlating regions between $\bar{\omega}_{wb}$ and Δ_{wb} .

5. Discussion

5.1. Relationship between $\bar{\omega}$ and Δ

The observations on both $\bar{\omega}_{wb}$ and Δ_{wb} domains counter-intuitively suggest that, when WB assumptions are invalid with high mean misfit ($\bar{\omega}$), the WB-based stress inversion yields a good solution

(blue color Figure 4). Similarly, when the WB assumptions are valid with low mean misfit ($\bar{\omega}$), the WB-based stress inversion yields bad solutions (orange color Figure 4). However, these conditions are specifically located near pure stress regime regions (normal, wrench and reverse). Far from these regions, $\bar{\omega}_{wb}$ and Δ_{wb} are correlated and the WB-based stress inversion seems to give correct solutions when $\bar{\omega}_{wb}$ is low and vice versa.

Two phenomena can be put forward to explain such observations:

1) Figure 3ac highlight that both stress inversion techniques perform badly near pure normal and reverse regimes, where $\bar{R}=0$ and $\bar{R}=3$ respectively. This can be explained by the fact that, in these extreme cases, we have both a radial extension ($\bar{R}=0$ and $\sigma_2 = \sigma_3$) and a radial compression ($\bar{R}=3$ and $\sigma_2 = \sigma_1$). In both cases, only the vertical stress is well defined while the two horizontal stresses will have no effects on the slip vectors whatever their orientation (θ) (Delvaux and Sperner, 2003). Therefore, when approaching such extreme stress configurations, the stress inversion techniques provide highly uncertain results (see points B and D in Figure 3a).

2) Figure 3ab show that there is strong anti-correlation near pure strike-slip regime (dashed sinusoid in Figure 3), which could either produce good or bad stress inversion results. This is explained by the fact that slip on the non-optimally oriented fault is only triggered by slip on the nearby more optimally oriented fault. This has been described in details in Lejri et al. 2015. They show that the high values in the $\bar{\omega}$ domains (see Figure 3b) are related to the mechanical interaction between faults, specifically when one fault is not optimally oriented to slide. Indeed, in such a configuration, slip on the non-optimally oriented fault is only triggered by slip on the nearby more optimally oriented fault. As a consequence, it is likely that slip on non-optimally oriented fault is driven by the local perturbed stress and not directly by the applied tectonic stress, hence slip vectors should be highly perturbed along this fault and ω should increase accordingly. This phenomenon, associated to the fact that WB-based stress inversion techniques perform better with a wide

variety of slip vector orientations (Sperner et al., 2003; Lacombe, 2012), produces the counter-intuitive anti-correlated pattern observed in the Δ_{wb} domain (see Figure 3a). Heterogeneous slip orientation is therefore a condition that better constrain WB-based stress inversion methods. Thus, near pure strike-slip regimes region, the WB-based stress inversion performs relatively well if $\bar{\omega}$ is high.

The anti-correlation patterns (Figure 3 and 4) demonstrate that for a specific model, $\bar{\omega}$ is not always a good criteria to evaluate the consistency of the WB-based stress inversion. High $\bar{\omega}$ values do not systematically invalidate WB assumptions, while low $\bar{\omega}$ values do not always guaranty a consistent inverted stress solution. This leads us to consider Δ as a better candidate for evaluating the validity of the WB-based stress inversion.

Figure 3 also highlights that in general the BEM-based stress inversion method performs better over a greater ranger of tectonic stresses than the WB-based stress inversion methods. Indeed, Δ_m and ω_m domains, which are related to the BEM-based stress inversion method, are much less perturbed than the Δ_{wb} and ω_{wb} domains, which are related to the WB-based stress inversion methods.

5.2. Sliding friction

Pascal C. (2002) and Lejri et al. (2015) have demonstrated that increasing friction will tend to reduce the misfit between the resolved shear stress and slip vector. This is highlighted in Figure 5cd where increasing the imposed friction (μ_{imp}) decreases both the $\bar{\Delta}$ and the $\bar{\omega}$. The opposite tendency is observed for the BEM-based stress inversion method when the inversion friction used is zero ($\mu_{inv}=0$). In such case, both the $\bar{\Delta}$ and the $\bar{\omega}$ increase as the imposed friction (μ_{imp}) increases.

However, it is important to highlight that using both inversion techniques and whatever the imposed friction (ranging from 0 to 1), the stress inversion solutions are relatively good with the $\bar{\Delta}$ and the $\bar{\omega}$ values very low. This is less true for the BEM-based stress inversion method when high inversion friction (μ_{inv}) is

high compare to the imposed friction (μ_{imp}). On the other hand, when the inversion and imposed friction are the same, there is no mechanical stress inversion uncertainty. This is explained by the fact that the numerically modeled slip vectors derived from the stress inversion will perfectly match the slip vectors generated using the imposed friction in the forward sense.

Is it shown in Figure 5c that the BEM-based stress inversion method performs better than the WB-based stress inversion methods until the imposed friction reaches 0.34, whereas for imposed friction higher than 0.34, the WB-based stress inversion becomes more accurate but never reaches the expected result perfectly.

It must be noted that the computed average distance, $\bar{\Delta}$, for both stress inversion methods never exceeds 0.14 (or 8°). This is equivalent to a discrepancy of 0.6 along \bar{R} or 11° along θ , or 0.4 along \bar{R} and 8° along θ , which is, as a worst case where fault friction is close to 0 or 1, a tolerable uncertainty. The average distance $\bar{\Delta}$ for the case where $\mu_{imp}=0.3$, as reported for low frictional faults (Zoback and Beroza, 1993; Marone, 2004; Colletini et al., 2009; Reches and lockner, 2010; Di Toro et al., 2011), is close to 0.05. This corresponds to a discrepancy of 0.21 along \bar{R} or 4° along θ , or 0.15 along \bar{R} and 3° along θ , which is a good accuracy. This points out to the fact that even if both methods have different efficiency according to the fault friction coefficient, both globally yield acceptable results. As shown in Figure 3 and Figure 4 it is only true when the WB-based stress inversion is performed far from pure stress regime region of the domain.

An unexpected observation is that, for this model, the average Δ_{wb} evolution along $\mu_{imp} = 0.5$ can be compared to Δ_m evolution when $\mu_{inv} = 0.5$. This means that the WB assumptions seem to implicitly include a friction inversion of 0.5, which contributes to a better approximation of the results since authors generally report frictions along reactivated faults, must be low, around $\mu < 0.4$ (Zoback and Beroza, 1993; Marone, 2004; Colletini et al. 2009; Reches and lockner, 2010; Di Toro et al. 2011).

The peak values at $\mu_{imp} = 0.6$ is due to the averaging methodology. As a matter of fact, when friction increases, non-optimally oriented fault models for specific stress states, will not slip, and thus decreases the

number of points in the domain, which mathematically increases the calculated mean values (see Annex). This effect is greater for the mechanical model since for $\mu_{imp} = 0.6$, non-optimally oriented fault is reactivated by the perturbed stress field of the adjacent fault, which yields higher $\bar{\Delta}_m$ and $\bar{\omega}_m$. Further friction increase, decreases the slip magnitude on the adjacent fault, reducing the perturbed stress field and leading the non-optimally oriented fault to completely stop slipping, hence removing the peak value.

5.3. Data sampling

The analysis of the distance between the imposed far field stress and the retrieved BEM-based and WB-based stress inversions solutions using DS+ data, clearly demonstrates that, for the synthetic model used, BEM-based stress inversion method performs better. On the other hand, WB-based stress inversion solutions have higher distance to the solution and never retrieve the imposed far field stress correctly, especially when using the DS+ data (as shown in Kaven et al, 2011). In other words, using WB-based stress inversion methods might yield poor results depending not only on the proximity to pure stress regime regions but also on where data has been collected along the faults with respect to the fault configuration such as near zones of fault intersections.

5.4. Chimney rock

Stress inversion and sampling

The distance Δ between the two stress inversion solutions using the observed data on Chimney Rock faults (see Figure 1) is relatively high ($\Delta = 0.7$) as predicted by the distance results on the synthetic model near pure normal stress regime region (Figure 3, Figure 4).

The distance Δ computed between the imposed far field stresses (see Figure 11) and the solutions of the two stress inversion methods confirm that the WB-based stress inversion methods are not as accurate as the

BEM-based stress inversion method for this stress configuration. Indeed, the distance is systematically small for the BEM-based stress inversion method than for the WB-based stress inversion methods, whatever the data sampling used.

The distance Δ between the two BEM-based stress inversion solutions, using full data and sampled data of Figure 11a, is smaller than the solutions shown in Figure 10. This could be explained by measurements errors, simplified fault geometries, mechanically interacting fault along omitted segments or a combination of some or all of these factors. However, this altering effect cannot explain the high distance Δ between the solutions of both stress inversion methods (Figure 10).

The small discrepancy between the imposed far field stress and the BEM-based solutions (Figure 11a) is induced by the proximity to pure normal stress regime region as predicted in Figure 3 and Figure 4. However, this precision loss is low compared to the WB-based stress inversion solution inaccuracy, showing that even if both methods loose accuracy near pure normal stress regime region, the BEM-based stress inversion method gives better results. This is probably due to the fact that BEM-based stress inversion method takes stress perturbations into account explicitly while the WB-based stress inversion methods take stress perturbations in an implicit manner as described by Lisle, 2013. Indeed, the WB assumptions are not pertinent to the small-scale, where specific local conditions invalidate the assumption yet delivering regional (large scale) consistent results. In other words, while the radial distribution of two principal stress orientations near pure stress regime regions (normal and reverse) leads to highly inaccurate WB-based stress inversion results, it is expected that very small reorientations of few number of slickenline rakes may help to better constrain the BEM-based stress inversion. These observations tend to validate the BEM-based stress inversion results and show the inaccuracy of the WB-based stress inversion methods for the tested stress configurations.

Chimney rock fault array evolution

Previously, Oertel (1965), Aydin and Reches (1982) and Krantz (1988, 1989) proposed the hypothesis that this four sets of faults with the orthorhombic geometry, as observed at Chimney Rock, have formed simultaneously in response to a far field three-dimensional strains, thereby, Krantz (1988) assumed fault initiation undergone simultaneous and uniform slip rate on all fault sets during a N-S extension, resulting in coaxial strain. However, Krantz (1988) predicted slip vector rakes of 90° on the average fault plane and excluded highly deviating angles from the dataset to reduce the average deviation to 6.3° .

Davatzes (2003) who demonstrated that the four sets of faults at Chimney Rock could probably be the result of two successive tectonic phases, suggested that the development of the observed Chimney Rock faults slickenlines could have taken place during a second NNE extension tectonic phase, where all the faults sets were activated.

This study shows that the ESE-WNW extension solution of the WB-based stress inversion using the full data set, is not consistent with any of the Krantz (1988) or Davatzes (2003) predictions. The NW-SE extension solution, retrieved by the BEM-based stress inversion, also strongly deviates from the previous studies.

We propose, since the measured slickenlines correspond to a phases were all sets of faults slipped simultaneously as demonstrated by Maerten, (2002), that the faults were reactivated near the end of a second phase of deformation (Davatzes, 2003)or during a third phase. The NW-SE extension reactivated optimally oriented ENE-striking faults which in turn, reactivated some portion of the non-optimally oriented WNW-striking faults (Lejri et al., 2015).

Predition domain

Analysis of the consistency of the distance between BEM and WB-based stress inversion solutions (Figure 10) and the Δ_{wb} domain (Figure 12), demonstrate that, for the Chimney Rock case study, the BEM solution seems to be more accurate than the WB solution.

The average Δ_{wb} for Chimney Rock faults (Figure 12) is lower compared to the synthetic intersecting fault model (Figure 3). This can be explained by a higher diversity of slickenline orientations (Sperner et al. 2003) induced by irregular fault plane orientations, fault segments and mechanical interactions near fault intersections. However, despite this optimal condition, the WB-based stress inversion performs rarely perfectly for the entire domain.

High Δ_{wb} near the pure normal (\bar{R} near 0) and reverse (\bar{R} near 3) stress regime regions is to be related to the uncertainty for the WB-based stress inversion to constrain the orientation θ , as the two horizontal principal stresses are very close (σ_2 and σ_3 for normal stress regime and σ_1 and σ_2 for reverse stress regime). Presence of reoriented slip vectors induced by stress perturbations near intersection lines helps the stress inversion to perform slightly better (example at $\theta=90^\circ$ Figure 3 and $\theta=0^\circ$ in Figure 12). This shows that the WB-based stress inversion takes perturbations into account in an implicit manner that gives an approximation of the solution while the exact solution is not achievable for some stress conditions.

6. Conclusions

Since Paleostress inversion methods using fault slip data being all based on the Wallace and Bott assumptions, which predicts that fault slip occurs parallel to the resolved shear stress on the fault plane, it was essential to study their validity. Lejri et al. (2015) study showed that the misfit between resolved shear stress and slip vector could invalidate the WB assumptions for complex faults geometries with strong mechanical interactions under specific stress conditions. Parameters such as fault geometry, fault fluid pressure, Poisson's ratio, traction free of the Earth surface, were proven to be responsible for large misfit (ω), while it was shown that increasing sliding friction would tend to reduce the misfit.

In the present study, it is shown, unlike the previous intuitive conclusions (Lejri et al. 2015), that the stress inversion solution accuracy can be inversely correlated to ω for specific tectonic stress conditions

(covering 26.6% of the tectonic domain). In fact, models that invalidate the WB assumptions seem to yield good results, especially for low sliding frictions ($\mu_{imp} < 0.4$). This clearly demonstrates that the misfit angle can be a good indicator of WB assumptions validity but not always a good criterion to evaluate the WB stress inversion solution accuracy. This leads to the counterintuitive result that WB-based stress inversions with a high misfit (ω) can lead to a good solution, and inversely, that a low misfit (ω) can yield an inaccurate solution. This goes against the idea that suggests filtering the data with high misfit prior to performing stress inversion.

Additionally, it was shown that the WB and BEM-based stress inversion methods are globally good and complementary depending on the sliding fault friction. Using imposed sliding friction (μ_{imp}) in our models, we show that frictional inversion (μ_{inv}) performs perfectly when the sliding friction is well evaluated ($\mu_{imp} = \mu_{inv}$), and performs well when $\mu_{imp} > \mu_{inv}$. This means that BEM-based frictionless stress inversion performs well for faults with sliding friction and even better when sliding friction is low ($\mu \leq 0.4$), which seems to be the general case as described by some authors emphasizing that fault reactivation occurs for low friction ($0 \leq \mu \leq 0.4$) (Zoback and Beroza, 1993; Marone, 2004; Colletini et al. 2009; Reches and Lockner, 2010; Di Toro et al. 2011).

While the lack of diversely oriented slickenlines, and stress ratios near pure stress regime regions, affects both stress inversion methods solution accuracy, explicit integration of locally perturbed slickenline orientations leads the BEM-based stress inversion to perform better than the WB-based stress inversion. The solutions inaccuracy should be negligible for a macro-scale analysis, yet it might yield discrepancies for micro-scale applications.

We show that WB-based stress inversions, using diverse data orientations (including stress perturbation), implicitly implements an average friction inversion of 0.5, which contributes to better approximation of the solution for low sliding frictions.

We also show that BEM-based stress inversion method is less sensitive to data sampling along the faults, than the WB-based stress inversion methods. Therefore, large datasets covering diverse fault plane locations is necessary for the WB-based stress inversion methods in order to obtain a good approximation of the paleostress. This has been demonstrated using the data set along the Chimney Rock faults.

This field case study also allowed to better understand and refine how faults developed and were reactivated at Chimney Rock with respect to variation of the local stress field. Based on previous study by Krantz (1988), Maerten (2000), Davatzes (2003) and this study we propose the hypothesis that the two fault sets at Chimney Rock are not contemporaneous as proposed by Krantz (1988) but rather formed under two successive events (Davatzes, 2003). However, field observations and geomechanical models (Maerten, 2000; and this study) suggest that the main faults of the area were all reactivated during a third stress state allowed mechanical interaction inducing slip vector perturbation near fault intersections. This last stress state is believed to be a normal stress regime with low stress ratio ($R = 0.047$) and an extension direction of 133°N .

Table 3 and Table 4 show the Pros and cons of both BEM and WB methods. It is worth noting that the BEM-based stress inversion, despite being more accurate for low sliding friction, performs as well as WB-based stress inversion for higher sliding frictions. However, the BEM-based stress inversion method requires a good knowledge of the fault model geometry, while the WB-based stress inversion gives good and fast approximations of the stress inversion solution without any fault model construction. We therefore advise to use WB-based stress inversion methods to retrieve the paleostress for a macro-scale analysis, for frictional faults ($\mu > 0.5$), and to use BEM-based stress inversion method as a complementary micro-scale solution, for doubtful tectonic stress conditions (near pure regime bands) and low sliding frictions ($\mu < 0.5$) under the necessary condition that a 3D fault model can be built.

Another concern is the fact that in our study, we only use static homogeneous isotropic friction on fault surfaces. Using anisotropic, heterogeneous and dynamic friction into account should be considered as it could lower WB-based stress inversion accuracy.

Plastic behavior on materials should also be considered since plastic deformation might not be directly related to the stress state especially near fault zone and non isochore deformation regions, especially for carbonates. In such cases, the geologist expertise is the only reliable data filter to decide which data is reliable and which data is to be neglected.

Finally, Figure 14 summarizes the relationship between the model complexity and the stress inversion solutions accuracy. It shows how the linear elastic approach, including sliding friction, tested in this study, performs fast and better than WB-based stress inversion. More complex models (frictional inversion, plastic behavior, dynamic friction, temperature ...) should tend to give slightly more accurate results at the cost of tedious model construction and time consuming calculations. While the simple WB assumptions tend to give approximate results for specific conditions, but do not require any model construction which make it faster and suitable for field cases study, provided that the slickenlines are sufficient in number and diversely oriented. We advise that, for suspected near pure regimes or low frictions for fault reactivation, a Δ_{wb} domain should be investigated before running WB-based stress inversion method.

One of the main challenges of the oil industry is the exploration and production of resources in structurally complex areas such as naturally fractured reservoirs. While understanding the macro-scale paleostress is useful for regional structural geology analysis, knowing the heterogeneous distribution of the paleostress around complex fault systems is critical to optimize the modeling of natural fractures in fractured reservoirs. Since the slip on faults is difficult to observe in the subsurface, we anticipate that fracture orientation data (joints, faults, stylolites) could naturally be taken into account during the stress inversion.

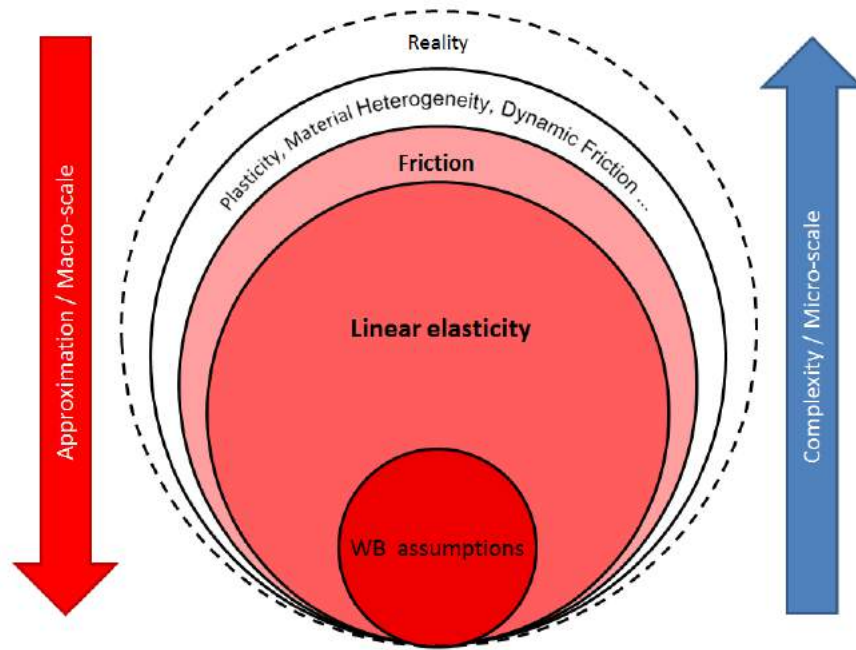


Figure 14. Degrees of complexity of the geomechanical stress inversion compared to the WB assumptions based stress inversion as part of the complete physical behavior problem. The more complex is the model, the better the result, and inversely for simple assumptions. Here the Linear elasticity with friction is a good compromise of result approximation and complexity (time consumption)

Acknowledgements:

This study is part of M. Lejri's PhD thesis, granted by both the French Ministry of Research and Schlumberger. These are deeply acknowledged.

Tables

Table 1: Variable definitions.

Symbol	Comments
<i>Fault geometry</i>	
α	Fault strike defined clockwise from the North
β	Fault dip angle
λ	Angle between the strike of 2 intersecting faults
Am	Amplitude of corrugated fault surface
<i>Fault properties</i>	
μ	Friction coefficient
C_0	Cohesion
P	Fluid pressure
ω	Misfit angle between resolved shear stress and slip vector
$\bar{\omega}$	Mean misfit angle
Δ	Distance
$\bar{\Delta}$	Mean distance
<i>Rock properties</i>	
ν	Poisson's ratio
E	Young's modulus
ρ	Density
<i>Stress</i>	
$\sigma_1 \geq \sigma_2 \geq \sigma_3$	Principal effective stress magnitudes (positive compression)
σ_v	Magnitude of the vertical stress
σ_H	Magnitude of the maximum horizontal stress
θ	Orientation of σ_H defined clockwise from the North
σ_n	Normal stress magnitude
τ	Shear stress magnitude
R	Stress ratio $R = (\sigma_2 - \sigma_3) / (\sigma_1 - \sigma_3)$
\bar{R}	Stress ratio defined by Maerten 2014 for Andersonian regimes
<i>Acronyms</i>	
WB	Wallace-Bott
DEM	Distinct Element Method
BEM	Boundary Element Method
DS+	Data sampling when misfit angle is $>10^\circ$
Δ Domain	Distance domain
$\bar{\Delta}$ Graph	Mean distance domain
$\bar{\omega}$ Domain	Mean misfit angle tectonic domain
$\bar{\omega}$ Multi-domain	Mean misfit angle tectonic multi-domain

Table 2. List of parameters used in the simulations.

Symbol	Default values
ν	0.25
E	1
ρ	Constant
μ	[0, 0.1, 0.2, 0.3, 0.4, 0.5, 0.6, 0.7, 0.8, 0.9, 1]
C_0	0
Half-space	No
P	0
σ_1	1
σ_3	0

Table 3. List of parameters used in the simulations.

		Pros	Cons
BEM	Accuracy	Very good results	Time consuming in frictional
	Model construction	- None	- Needs faults geometry and exact location of slickenlines on each fault as well as the mechanical properties of the material.
	data	- Can take any deformation type into account (list) - Low Sensitivity to lack of diversity of orientations. - Good correlation to the misfit angle.	- Monophasic tectonic event related data.

Table 4. List of parameters used in the simulations.

		Pros	Cons
WB	Accuracy	- Fast	- Approximative results for some conditions - Works better for higher frictions.
	Model construction	- Very fast and easy (doesn't include fault geometry)	Doesn't take rock mechanics into account
	data	- Slickenlines, focal mechanisms, calcite twinnings, joints, shear faults, stylolites.	- Very sensitive to lack of diversity of orientations. - Results anti-correlation with the misfit angle in some cases

Annex

In Figures 15 and 16, the evolution of $\bar{\omega}_{wb}$ and Δ_{wb} is studied for an increasing imposed siding friction coefficient. The average value of the $\bar{\omega}_{wb}$ and Δ_{wb} domains is used to create the $\bar{\bar{\omega}}_{wb}$ and $\bar{\bar{\Delta}}_{wb}$ domains (Figure 5b).

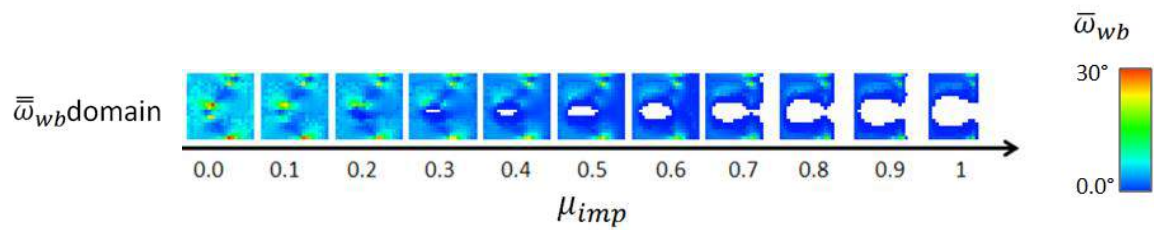


Figure 15. Evolution of the $\bar{\omega}_{wb}$ vs μ_{imp}

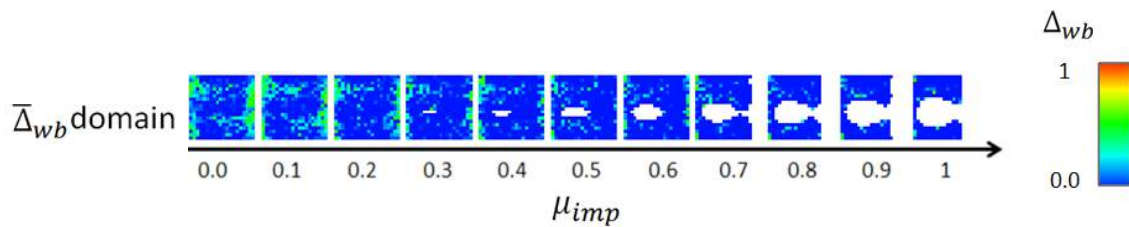


Figure 16 Evolution of the $\bar{\Delta}_{wb}$ vs μ_{imp}

In Figures 17 and 18, the evolution of $\bar{\omega}_m$ and Δ_m is studied for different imposed siding friction and inversion friction coefficients. The average value of the $\bar{\omega}_m$ and Δ_m domains is used to create the $\bar{\bar{\omega}}_m$ and $\bar{\bar{\Delta}}_m$ domains (Figure 5a).

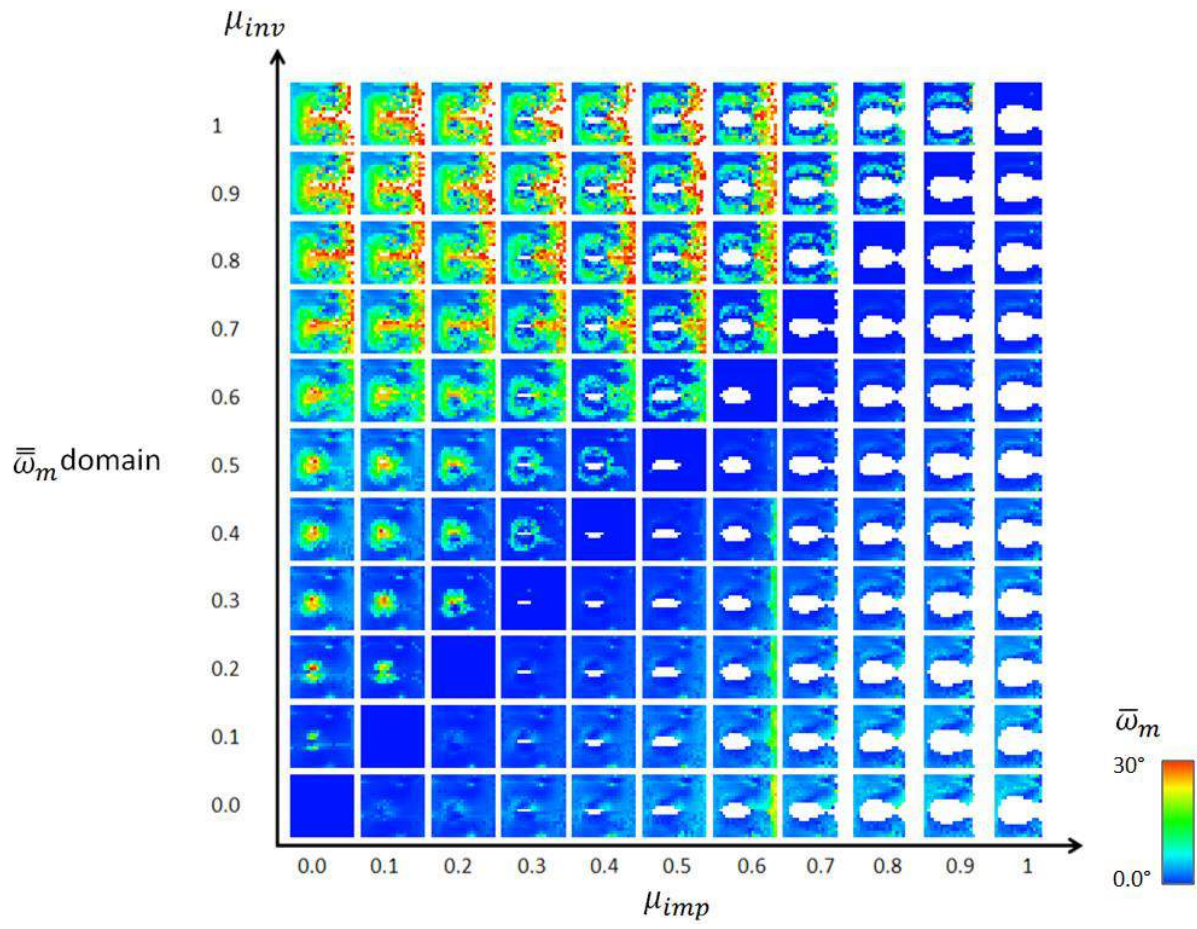


Figure 17. Evolution of the $\bar{\omega}_m$ vs μ_{imp} and μ_{inv}

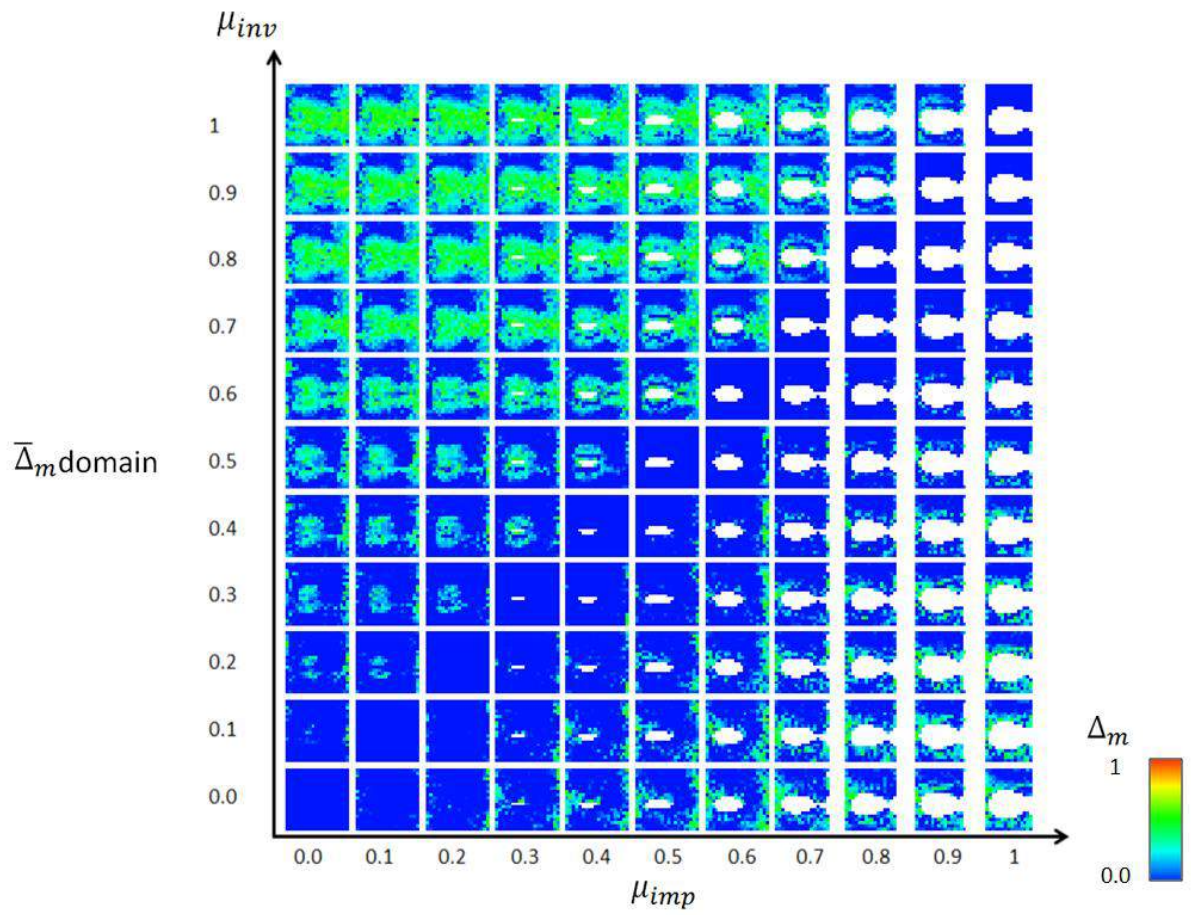


Figure 18. Evolution of the Δ_m vs μ_{imp} and μ_{inv}

References

- Anderson, E.M., 1951. *The Dynamics of Faulting and Dyke Formation with Applications to Britain*, 2nd Edition. Oliver and Boyd, Edinburgh.
- Angelier, J., 1985. Neogene paleo-stress changes in the Basin and Range : a case study at Hoover Dam, Nevada-Arizona., *Bulletin Geological Society of America*, 96, 347–361.
- Angelier, J., 1975. Sur l'analyse de mesures recueillies dans des sites faillés : l'utilité d'une confrontation entre les méthodes dynamiques et cinématiques, *Comptes Rendus de l'Académie des Sciences - Series IIA - Earth and Planetary Science*, D281, 1805–1808.
- Angelier, J., 1979. Determination of the mean principal directions of stresses for a given fault population, *Tectonophysics*, 56, T17–T26.
- Arthaud, F., 1969. Méthode de détermination graphique des directions de raccourcissement, d'allongement et intermédiaire d'une population de failles, *Bulletin de la Société Géologique de France*, 7 (XI), 729–737.
- Aydin, A., 2000. Fractures, faults, and hydrocarbon entrapment, migration and flow. *Mar. Pet. Geol.* 17, 797–814.
- Aydin, A., Reches, Z., 1982. Number and orientation of fault sets in the field and in experiments. *Geology* 10, 107-112.
- Barnet. J. A. M., Mortimer, J., Rippon. J. H., Walsh. J. J. & Watterson. J., 1987. Displacement geometry in the volume containing a single normal fault. *The American Association of Petroleum Geologists Bulletin*. 71. 925-937.
- Barrier E. and Angelier J., 1986. Active collision in eastern Taiwan: The Coastal Range. *Tectonophysics*, 125, 39-72.

- Bergerat, F., Stress fields in the European platform at the time of Africa-Eurasia collision, *Tectonics*, 6(2), 99–132, 1987.
- Bott, M.H.P., 1959. The mechanics of oblique slip faulting. *Geological Magazine* 96, 109–117.
- Brillouin, L., 1946, *Wave propagation in Periodic Structures: Electric Filters and Crystal lattices*, McGraw Hill, New York, 255
- Carey, E., Brunier, B., 1974. Analyse théorique et numérique d'un modèle mécanique élémentaire appliqué à l'étude d'une population de failles. – *C. R. Acad. Sci., D*, 279, 891-894.
- Celerier B., 1988. How much does slip on a reactivated fault plane constrain the stress tensor? *Tectonics* 7, 1257-1278.
- Colletini, C., Niemeijer, A., Viti, C., and Marone, C., 2009. Fault zone fabric and fault weakness. *Nature* 462, 907-910, doi: 10.1038/nature 08585.
- Cundall, P.A., 1971. A computer model for simulating progressive large scale movement in blocky rock systems. *International Symposium on Rock Mechanics*. International Society of Rock Mechanics, Nancy, p. II-8.
- Cundall, P.A., 1988. Formulation of a three dimensional distinct element model: Part I. A scheme to detect and represent contacts in a system composed of many polyhedral blocks. *Int. J. Rock Mech. Min. Sci. Geomech. Abstr.* 25, 107-116.
- Davatzes, N.C., Aydin, A., 2003. The formation of conjugate normal fault systems in folded sandstone by sequential jointing and shearing. In *J. Geophys. Res.* 108.
- Delvaux, D., Sperner, B., 2003. Stress tensor inversion from fault kinematic indicators and focal mechanism data: the TENSOR program. In: Nieuwland, D. (Ed.), *New Insights into Structural Interpretation and Modelling*, 212. Geological Society, London, Special Publication, pp. 75-100.
- Di Toro G., Han R., Hirose T., De Paola N., Nielsen S., Mizoguchi K., Ferri F., Cocco M., Shimamoto T. 2011. Fault lubrication during earthquakes. *Nature*, 471(7339): 494–498.

- Dickinson, W. R., and W. S. Snyder, 1978. Plate tectonics of the Laramide orogeny, Mem. Geol. Soc. Am., 151, 355-366,
- Dupin, J.M., Sassi, W., Angelier, J., 1993. Homogeneous stress hypothesis and actual fault slip: a distinct element analysis. *J. Struct. Geol.* 15, 1033-1043.
- Etchecopar, A., 1984. Étude des états de contrainte en tectonique cassante et simulations de déformations plastiques (approche mathématique). Thèse d'État. Ph.D. thesis, Université des Sciences et Techniques du Languedoc.
- Etchecopar, A., Vasseur, G., Daignieres, M., 1981. An inverse problem in microtectonics for the determination of stress tensors from fault striation analysis. *J. Struct. Geol.* 3, 51-65.
- Gapais, D., Cobbold, P.R., Bourgeois, O., Rouby, D., de Urreiztieta, M., 2000. Tectonic significance of fault slip data. *J. Struct. Geol.* v22,7:881-888.
- Gephart, J.W., Forsyth, D.W., 1984. An improved method for determining the regional stress tensor using earthquake focal mechanism data: application to the San Fernando earthquake sequence. *Journal of Geophysical Research* 89 (B11), 9305–9320.
- Gilluly, J., 1928. United States geology and oil and gas prospects of parts of the San Rafael Swell, Utah. U.S. Geol. Surv. Bull. 806-C, 69– 130.
- Hancock, P.L., 1985. Brittle microtectonics: principles and practice *J. Struct. Geol.* V7,3:347-457.
- Hansen, J.-A., 2013. Direct inversion of stress, strain or strain rate including vorticity: A linear method of homogenous fault–slip data inversion independent of adopted hypothesis. *J. Struct. Geol.*, 51, 3–13
- Huchon, P., Jestin, F., Cantagrel, J.-M., Gaulier, J.M., Al Khirbash S., Gafaneh, A., 1991. Extensional deformations in Yemen since Oligocene and the Africa– Arabia– Somalia triple junction. *Ann.*
- Kaven, J. O., F. Maerten, and D. D. Pollard (2011), Mechanical analysis of fault slip data: Implications for paleostress analysis, *J. Struct. Geol.*, 33(2), 78–91.
- Kelley, V. C., 1955. Regional tectonics of the Colorado Plateau and relationship to origin and distribution of uranium, N .M. Univ. Publ. Geol., 5, 120 pp.

- Krantz, R. W., 1986. The odd-axis model: orthorhombic fault patterns and three-dimensional strain fields, Ph.D. thesis, Univ. of Ariz., Tucson.
- Krantz, R. W., Multiple fault sets and three-dimensional strain: Theory and application, *J. Struct. Geol.*, 10, 225-237, 1988.
- Krantz, R. W., 1989. Orthorhombic fault patterns: The odd axis model and slip vector orientations, *Tectonics*, 8, 483-495.
- Lacombe, O., 2012. Do fault slip data inversions actually yield paleostresses that can be compared with contemporary stresses? A critical discussion. *C. R. Geoscience*, 344:159-173.
- Lacombe O., Mouthereau, F., Angelier, J., Deffontaines, B., 2001. Structural, geodetic and seismological evidence of tectonic escape in SW Taiwan. *Tectonophysics* 333, 323-345.
- Lacombe O., Angelier J., Laurent O., Bergerat F. Tournet C., 1990. Joint analyses of calcite twins and fault slips as a key for deciphering polyphase tectonics: Burgundy as a case study. *Tectonophysics*, 182, 279-300.
- Lejri, M., Maerten, F., Maerten, L., Soliva, R., 2015. Paleostress inversion: A multi-parametric geomechanical evaluation of the Wallace-Bott assumptions. Accepted in *Tectonophysics* (Chapter 1)
- Letouzey, J., 1986. Cenozoic paleo-stress pattern in the Alpine foreland and structural interpretation in a platform basin. *Tectonophysics* 132, 215–231.
- Letouzey J. and Tremolieres P., 1980. Paleo-stress fields around the Mediterranean since the Mesozoic from microtectonic comparison with plate tectonic data. *Rock Mech., Suppl.* 9, 173-192.
- Liesa C.L. and Simon J.L., 2009. Evolution of intra-plate stress fields under multiple remote compressions: The case of the Iberian chain (NE Spain). *Tectonophysics*, 474, 144-159.
- Lisle, R.J., 2013. A critical look at the Wallace-Bott hypothesis in fault-slip analysis. *Bull. Soc. géol. Fr.*, 184, 4-5, 299-306.
- Lisle, R.J., Orife, T.O., Arlegui, L., Liesa, C., Srivastava, D.C., 2006. Favoured states of palaeostress in the earth's crust: evidence from fault-slip data. *J. Struct. Geol.* 28 (6), 1051–1066.

- Lisle, R.J., 1992. New method of estimating regional stress orientations: applications to focal mechanism data of recent British earthquakes. *Geophys. J. Internat.*, 110, 276-282.
- Lisle, R.J., 1998. Simple graphical constructions for the direction of shear. *J. Struct. Geol.*, 20, 969-973.
- Maerten, L., 2000. Variations in slip on intersecting normal faults: implications for paleostress inversion. *J. Geophys. Res.* 270, 197– 206.
- Maerten, M., Pollard, D., Maerten, F., 2001. Digital mapping of three-dimensional structures of the Chimney Rock fault system, central Utah. *Journal of Structural Geology*, 23,585-592
- Maerten F., Maerten L., Cooke M., 2010b. Solving 3D boundary element problems using constrained iterative approach. *Computational Geosciences*. 14, 551-564.
- Maerten F., Maerten L., Pollard D.D., 2014. iBem3D, a three-dimensional iterative boundary element method using angular dislocations for modeling geologic structures. *Computers & Geosciences* 72, 1-17.
- Maerten, F., 2010a. Adaptive cross-approximation applied to the solution of system of equations and post-processing for 3D elastostatic problems using the boundary element method. *Engineering Analysis with Boundary Elements* 34 (5), 483-491.
- Marone C., 2004. Earthquake science: faults greased at high speed. *Nature*, 427(6973):405-406.
- Mattauer, M., Mercier, J.L., 1980. Microtectonique et grande tectonique. *Mém. h. ser. Soc. géol. De France* 10, 141–161.
- McKenzie, D.P., 1969. The relation between fault plane solutions for earthquakes and the directions of the principal stresses. *Bull. Seismol. Soc. Am.* 59, 591–601.
- Mercier J.L., Sorel D. and Vergely P. 1989. Extensional tectonic regimes in the Aegean basin during the Cenozoic. *Basin Research*, 2,1, 49-71.
- Michael, A., 1985. The determination of stress from slip data, faults and folds. *Journal of Geophysical Research* 89, 11517-11526.

- Nicol, A., Watterson, J., Walsh, J.J., Childs, C., 1996. The shapes, major axis orientations and displacement patterns of fault surfaces. *J. Struct. Geol.* 18 (2/3), 235-248.
- Nieto-Samaniego, A. F., and Alaniz-Alvarez, S. A., 1997, Origin and tectonic interpretation of multiple fault patterns: *Tectonophysics*, v. 270, p. 197-206.
- Oertel, G., 1965. The mechanism of faulting in clay experiments. *Tectonophysics* 2, 343–393
- Pascal C., 2002. Interaction of faults and perturbation of slip: influence of anisotropic stress states in the presence of fault friction and comparison between Wallace–Bott and 3D Distinct Element models. *Tectonophysics* 356, 307–322.
- Pascal, C., 1998. Etude mécanique et modélisation de la fracturation en extension, application au domaine de la Mer du Nord. Unpublished PhD thesis, Sciences de la Terre, Univ. P. M. Curie, Paris, 410pp.
- Petit, J.-P., 1987. Criteria for the sense of movement on fault surfaces in brittle rocks. *J. Struct. Geol.*, 9, 597-608.
- Pollard, D.D., Saltzer, S.D., Rubin, A.M., 1993. Stress inversion methods: are they based on faulty assumptions. *J. Struct. Geol.*, 15, 1045-1054.
- Reches, Z., Lockner D. A., 2010. Fault weakening and earthquake instability by powder lubrication *Nature* 467, 452–455.
- Resor, P.G., Meer, V.E., 2009. Slip heterogeneity on a corrugated fault. *Earth and Planetary Science Letters* 288 483–491.
- Rippon, J.H., 1985. Contoured patterns of throw and hade of normal faults in the coal measures (Westphalian) of northeast Derbyshire, *Proc. Yorks. Geol. Soc.*, 45, 147-161.
- Sperner, B., Muller, B., Heidbach, O., Delvaux, D., Reinecker, J. & Fuchs, K. 2003. Tectonic stress in the Earth's crust: advances in the World Stress Map project. In: Nieuwland, D. A. (ed.) *New Insights into Structural Interpretation and Modelling*. Geological Society, London, Special Publications, 212, 101-116.

- Thomas, A.L., 1993. Poly3D: a three-dimensional, polygonal-element, displacement discontinuity boundary element computer program with applications to fractures, faults, and cavities in the Earth's crust. M.S. thesis, Stanford University, California.
- Tibaldi, A., 1998. Effects of topography on surface fault geometry and kinematics: examples from the Alps, Italy and Tien Shan, Kazakstan. *Geomorphology* 24, 225–243.
- Twiss, R.J., Geffel, M.J., 1990. Curved slickenfibers: a new brittle shear sense indicator with application to a sheared serpentinite. *J. Struct. Geol.*, 12, 173-183.
- Twiss, R.J., Protzman, G.M., Hurst, S.D., 1991. Theory of slickenline patterns based on the velocity gradient tensor and microrotation. *Tectonophysics* 186 (3–4), 215–239.
- Vandycke, S., Bergerat, F., Dupuis, Ch., 1991. Meso-Cenozoic faulting and inferred palaeostresses in the Mons basin, Belgium. *Tectonophysics*, 192, 261-271.
- Wallace, R.E., 1951. Geometry of shearing stress and relation to faulting. *J. Geol.*, 59, 118-130.
- Wallace, R.E., Morris, H.T., 1986. Characteristics of faults and shear zones in deep mines. *Pure Appl. Geophys.* 124. 107-126.
- Walsh, J. J., and J. Watterson, 1989. Displacement gradients on fault surfaces, *J. Struct. Geol.*, 11, 307-316.
- Xu S., Nieto-Samaniego A.F., Alaniz-Álvarez. S.A., 2013. Origin of superimposed and curved slickenlines in San Miguelito range, Central México. *GeologicaActa*, 11(1), 103-112.
- Yamaji, A., 2000. The multiple inverse method: a new technique to separate stresses from heterogeneous fault-slip data. *J. Struct. Geol.*, 22, 441-452. Žalohar and Vrabc, 2007
- Zoback, M. D., Beroza, G. C., 1993. Evidence for near-frictionless faulting in the 1989 (m-6.9) loma-prieta, california, earthquake and its aftershocks. *Geology* ; 21, 181-185.
- Zoback, M.L., Anderson, R.E., Thompson, G.A., 1981. Cainozoic evolution of the state of stress and style of tectonism of the Basin and Range Province of the Western United States. In: Vine, F.J., Smith, A.G. (Eds.), *Extensional Tectonics Associated with Convergent Plate Boundaries*. *Philos. Trans. R. Soc. Lond. Ser. A: Math. Phys. Sci.*, vol. 300. Royal Society of London, London, UK, p. 1454.

CHAPTER III: Geomechanical paleostress inversion using fracture data: Application to modeling natural fractures in reservoirs

Mostfa Lejri^{1,2}, Laurent Maerten¹, Frantz Maerten¹, Jean-Pierre Joonnekindt¹, Paul Gillespie³

¹Schlumberger – MpTC, Parc Euromédecine, 340 rue Louis Pasteur, 34790 Grabels, France

²Géosciences Montpellier, Université Montpellier 2, Place E. Bataillon, 34095 Montpellier cedex 5, France

³ Statoil, Stavanger, Norway

To be submitted to the Journal of Structural Geology.

Key words: stress inversion, phase separation, fracture mechanical type inversion, geomechanics.

Abstract

It is today widely accepted that major petroleum companies are greatly dependent on producing oil and gas from fractured reservoirs. Therefore, characterizing and managing natural fractures is becoming the most challenging topic in the oil and gas industry. Among the technologies available for modeling natural fractures, geomechanical simulation seems to be the most promising despite its apparent complexity and use restricted to experts. In this contribution we demonstrate how we can improve the geomechanical modeling of natural fractures in reservoirs in terms of simplicity, speed and use. We describe a fast paleostress inversion technique that uses observed fracture data along well bore to constrain the geomechanical simulations. The method is then tested against well exposed faults and fractures in outcrops and applied to a fractured reservoir in the North Sea.

1. Introduction

Natural fractures alter the flow of hydrocarbons, either during the migration from the source to the reservoir rock or during exploitation of natural reserves. Therefore, understanding and quantifying the spatial and temporal development of these fractures as well as their properties (e.g. geometry, throw, aperture, permeability, etc.) can have great economic impact in the context of hydrocarbon exploration and production and thus significantly improve decision making and reduce production risks. Furthermore, as it has been estimated that more than 60% of the world's proven hydrocarbon reserves lie in naturally fractured carbonate reservoirs (Schlumberger Market Analysis, 2007), these considerations become crucial. Hence, to address these economic issues, methods have been developed to model and/or detect natural fractures in reservoirs.

The curvature analysis methods, intensively utilized in the industry, are used to predict fracture orientations and clustering of bent or folded strata (Murray, 1968; Thomas et al., 1974, Lisle, 1994; Fisher and Wilkerson, 2000; Hennings et al., 2000). However, some authors have raised some strong doubts about the predictive capability of such analyses (Schultz-Ela and Yeh, 1992; Gibbs et al., 1997; Jamison, 1997). Indeed, the effect of faulting and layer thickness is ignored and the technique is too sensitive to seismic reflection data acquisition and processing. The statistic methods, based on the fault power-law size distribution (Childs et al., 1990; Walsh and Watterson, 1991; Schlische et al., 1996; Sassi et al., 1992; Yielding et al., 1992), on the stochastic clustering process (Munthe et al., 1993; Damsleth, 1998) or on the hypothetical fractal nature of faulting (Gauthier and Lake, 1993), are also used to model fractures in reservoirs. However, although the size distributions are predictable, fracture mechanics is not considered with these techniques and therefore it is more difficult to predict the orientations and location of the fractures. Pioneer work by Hudson (1981) has shown that it could be possible to detect fracture networks through seismic attribute processing (Schoenberg and Sayers, 1995; Neves et al., 2004), which illuminates features within the original seismic data that correlate with faulting and fracture corridors. Pedersen et al.

(2005) introduced a method known as ant-tracking, based on artificial swarm intelligence to detect lineament associated to natural fractures. However, despite the tremendous detail now available from 3D seismic reflection techniques and the recent advance in seismic attribute processing, most of the natural fractures cannot be detected at the current resolution of the seismic reflection data. Recently structure restoration methods, used by structural geologists to check the consistency of the subsurface structural interpretations, have been extended to predict areas that have undergone large strains and to relate the strains to structural heterogeneities such as faults and joints (Hennings et al., 2000; Sanders et al., 2002; Kloppenburg et al., 2003; Sanders et al., 2004). However, as for the previous techniques to model fractures, geometric restoration does not include mechanical consideration. Maerten and Maerten (2006) have demonstrated that adding mechanics to structural restoration could help model natural fractures in reservoirs for some configurations only as these new techniques are too dependent on unphysical boundary conditions (Lovely et al., 2012).

Today, numerical models of rock deformation based on continuum mechanics are becoming industry standard in providing efficient means for modeling natural fractures in reservoirs. Over the past decade, pioneer studies (Maerten, 1999; Bourne et al., 2000) have proven that adding a geomechanical rationale to stochastic techniques improves their predictive capability and leads to more realistic fractured reservoir models. The basic idea is to assume that fractures might develop, whatever the fracturing mechanism, in a heterogeneous stress field that can be perturbed by faulting, folding or by any other geological processes that would locally perturb the stress field. This could result in heterogeneous fracture orientation and density. Therefore, geomechanical methods consist on calculating the stress distribution at the time of fracturing using the available reservoir structure data such as faults, fractures and folds, the rock type and the tectonic setting that can be characterized by stress or strain magnitude and orientation. Then, the calculated stress fields, perturbed by the main structures, combined with rock failure criteria are used to model natural fracture networks (i.e. orientation, location, and spatial density trends). An instructive 2D

illustration of the geomechanically-based methods is exposed in Figure 1. It shows a preexisting discontinuity subjected to a far field stress that is sheared to create a fault. The stress is perturbed around the fault showing both tensile (light grey) and compressive areas (dark grey). Both the orientation of σ_1 (the most compressive principal stress) and the σ_2 (the least compressive principal stress) are close to the fault. This stress pattern can be compared to outcrop example such as reactivated preexisting fracture showing branch crack in least compressive areas and stylolites in most compressive areas (Rispoli, 1981), both following the orientation of σ_1 and σ_2 respectively.

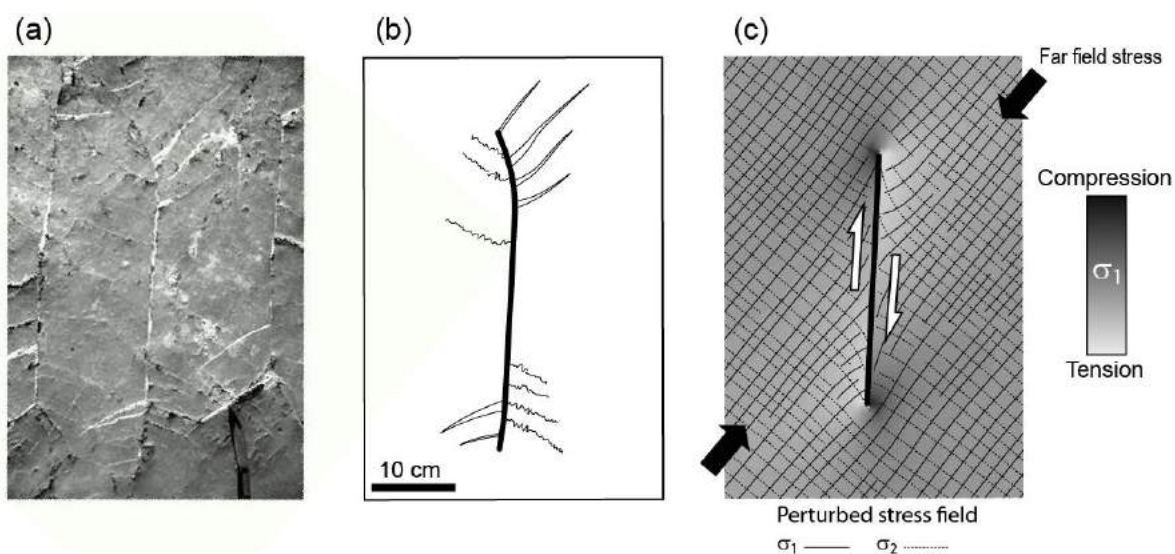


Figure 1: Comparison between (a) photo of secondary features such as tensile cracks and stylolites observed around a reactivated fracture in limestone at Les Matelles, southern France (Rispoli, 1981; Petit and Mattauer, 1995) and (b) its interpretation of observed fractures with (c) stress perturbation computed around a single fault showing σ_1 intensity and orientation.

The geomechanical method has been successfully applied to both outcrops and reservoirs demonstrating how geomechanics can provide a high degree of predictability of natural fracture networks. For instance, the 3D boundary element method (BEM) has been successfully applied to model subseismic faults (Maerten, 1999; Maerten et al., 2006) in Northern North Sea highly faulted reservoirs as well as undetected joints in naturally fractured carbonate reservoirs (Bourne et al., 2000). Similarly elastic

dislocation modeling have been applied for small-scale fault and fracture network characteristics in normal and reverse fault regimes (Dee et al., 2007).

Three key elements are essential for a complete geomechanical modeling. The first element is the geological model, which is referred as the geometry of the subsurface geology. Although this element is the most important element in geomechanical modeling, it is recurrently simplified. This includes sedimentary layers, faults, salt diapirs, cavities, folds, or any geological objects. The second element is the stress, which is referred as the type (normal, wrench or reverse), orientation and magnitude of the regional or local tectonic stresses through time. This important element of the geomechanical modeling is the most difficult to evaluate and corresponds to the boundary conditions of the geomechanical modeling. While there are techniques for measuring some components of the present day tectonic stress, it is difficult to constrain past tectonic stresses. There are poorly estimated introducing very high uncertainties in the stress modeling. Finally, the third element is the mechanical rock properties, which is referred as the rock properties and mechanical behavior. This element of the geomechanical modeling is the least uncertain to estimate. Thanks to laboratory testing we have a fair understanding of the rock properties and behavior. These can be extrapolated using known rules on how the rock was in the past (i.e. compaction, porosity, etc.).

In this contribution we focus on the major unknown, which is the far field stress that we also call the far field boundary conditions in geomechanical simulation. We show how such far field tectonic stress can be recovered through mechanical stress inversion technique using knowledge of the geological structure of the subsurface (i.e. 3D seismically observable fault network) and the observed natural fractures characteristics (i.e. kinematic, orientation and location). While the basic principles of such technique have been used in the past (Muller and Pollard, 1977; Baer and Reches, 1991; Maerten, 1999; Bourne and Willemse, 2001; Maerten et al., 2002; Homberg et al., 2004), to our knowledge, it has never been used on complex fault systems nor fully automatized. So, after describing the automatized method and the associated theory, we test it against outcrop analogues of fractured carbonates from both Nash Point, U.K., which contains well exposed faults

and joints and the Matelles, France, which contains well exposed faults, veins and stylolites. We demonstrate, through these case studies, how the method is efficiently applied to natural examples and we highlight both its advantages and limitations. We then successfully apply it to the North Sea Oseberg reservoir that has previously been studied by Maerten et al. (2002). Finally, we discuss how such method could provide complementary constraints for discrete fracture models and help characterizing fractured reservoir.

2. Method

The proposed method concentrates solely on the case where faulting is the main driver for stress perturbation that would affect secondary fracture development. We then make the assumption that in a growing and active fault system, the orientation of new fractures will be influenced by the regional tectonic stress as well as by the perturbation of that stress state around nearby pre-existing larger faults. Consequently, we propose to use geomechanical modeling to compute the stress field around active faults through time and thereby model the orientation and density of the natural fractures.

Since the main unknown in such modeling is the boundary conditions applied to the geomechanical model under the form of 3 principal stress orientations and magnitudes, we have set up a theoretical workflow that should help recover, or at least better constrain, this state of stress. We first create a 3D geomechanical model of the subsurface fault networks. The model should honor as much as possible the interpreted 3D fault model. We then run thousands of geomechanical simulations covering the range of all possible remote stresses in terms of orientation and magnitude. For each simulation, we compare the modeled local heterogeneous stress field with the observed natural fractures and check whether such fractures could have been developed within the modeled stress field. Finally, we analyze all the simulation results in order to find the one that gives the best fit between modeled stresses and observed fractures. The

optimum stress regime configuration can then be used to produce maps of fracture strike and density trends that in turns are used to constrain discrete fracture network simulations.

This idealized workflow, which is meant to find the paleo tectonic stress, needs however to be optimized using a proper 3D numerical method associated with appropriate techniques both to reduce the computation time, as thousands of simulations should take days, and to automatically analyze and to find the optimum solutions. The foundation of the proposed stress inversion technique, meant to optimize the idealized workflow and detailed in the next sections, is based on the principle of superposition (see Brillouin (1946) for the history of the principle of superposition) to compute the stress at any location in the model using pre-computed specific values from three linearly independent simulations. This principle, combined with the 3D boundary element method (BEM) and a Monte Carlo procedure, is used to reduce the number of simulations needed for the inversion, and hence time.

2.1. Numerical tool

Geomechanical modeling of natural fractures rely on the finite element method (FEM), distinct element method (DEM) or BEM. We have chosen to develop and use the BEM for four main reasons: (i) complex and realistic models can easily be constructed as it uses frictional surfaces as 3D discontinuities (i.e. faults, joints, salt diapirs, bedding interfaces or cavities) in a homogeneous elastic medium that does not need to be discretized as with the FEM, (ii) discontinuity surfaces are made of triangular elements, which are particularly well suited to model complex surfaces such as a curving fault with irregular tip-line, (iii) computation is fast (i.e. several seconds to few minutes) and (iv), as opposed to FEM, it is more convenient to impose a far field tectonic stress as it is independent of the orientation and geometry of the model edges (outer boundaries).

With that regards iBem3D have been developed (an evolution from Poly3D initially developed by Thomas (1993)), a numerical tool based on innovative iterative 3D BEM method (Maerten et al., 2010;

Maerten, 2010; Maerten et al., 2014). It is founded on the analytical solution for the elastic boundary value problem of an angular dislocation in an infinite "whole" space or semi-infinite "half" space composed of a homogeneous and isotropic linear-elastic material. One approximates rock mass of the upper crust as a linear elastic material. This elastic rock mass is cut by discontinuities (3D surfaces), which for instance, represent the geometry of the faults that have been interpreted from the seismic reflection survey. Only the boundary surfaces themselves are modelled, whereas the surrounding material need not be modelled explicitly. Modelled faults are discretized as triangular elements with specified constant displacement and/or traction boundary conditions. Fault friction, cohesion and fluid pressure can also be set as boundary conditions on discontinuities. Maerten et al. (2014) gives a summary of iBem3D technology as well as a list of published applications in the field of structural geology, fracture mechanics, geophysics and oil and gas industry.

When modeling faults in the following paleostress inversion technique, the displacement component normal to the element plane is prescribed to be zero, to avoid opening and interpenetration of the fault walls. The initial two in-plane shear tractions on each element are set to be zero but will be automatically determined and prescribed by remotely applied stresses. This fault boundary condition is essential if we want to use the reduced tensor for the paleostress inversion. Therefore, fault friction, cohesion and fluid pressure cannot be used during the inversion process. Nevertheless, the underlying assumption is that this approximation captures the first-order relationship between fault geometry, fault displacement distributions, and perturbed stress fields.

2.2. Fault Paleo-Geometry

To reduce geomechanical uncertainties associated with the geometry we must preserve the model structural integrity and complexity. Therefore, a realistic 3D geological model has to be built. In geomechanical simulation, a model of the present day observed geological structures is often used as proxy for past geometry. This is particularly true in normal faulting areas, where the local extension does not

exceed 10 to 20%. However, for highly deformed areas such as fold and thrust belt, present day geometry cannot be used. In such cases, a 3D restoration of the geological structure has to be achieved in order to obtain the structure geometry through geological time.

2.3. Paleo tectonic stresses

The main unknown for geomechanical simulations is the remote paleo stresses that need to be applied to the model as boundary conditions. It is always difficult to estimate in terms of both the orientation and the relative magnitude. In addition, calibration with available fracture data measured along wellbore for instance, is often time consuming as the process is not automatized. We are thus often tempted to neglect that part of the process by guessing the paleo tectonic stresses and not fully using on available data.

To fill this important gap we have developed a new generation of paleostress analysis using iBem3D software, which is an extension of Maerten et al. (2015) for focal mechanisms but using fracture data. The theoretical steps to recover paleo tectonic stress are to run thousands of simulations covering the range of all possible stress configurations. Then, for each simulation we compare attributes of the modeled stresses with the observed fracture geometry. Finally, we analyze, sort and select the simulations that give the best fit with observed fracture data. However, three main problems need to be solved in order to make the technique valuable: (i) The dimension of parameter space for covering the range of all possible tectonic stress configurations needs to be decreased, (ii) the computation time must be optimized as running thousands of geomechanical simulations would take days and (iii), the analysis of the results must be efficient and automatized.

2.3.1. Parameter Space

The full range of stresses is described by a 6 dimensions (6D) parameter space, which is related to the full symmetric stress tensor defined by:

$$\sigma = \begin{pmatrix} \sigma_{xx} & \sigma_{xy} & \sigma_{xz} \\ & \sigma_{yy} & \sigma_{yz} \\ & & \sigma_{zz} \end{pmatrix} \quad (1)$$

However, covering a 6D parameter space would take hours of computation. We have therefore decided to reduce it to a 2 dimensional (2D) parameter space.

According to Lisle et al. (2006) and as predicted by Anderson (1905), one of the principal stress directions must be vertical for a flat Earth (Celerier, 2008). Therefore, assuming that one principal stress is vertical the 2D parameter space can be defined by:

$$\sigma = \sigma(\theta, \bar{R}), \quad (3)$$

where θ is the orientation of the maximum principal horizontal stress σ_H defined clockwise according to the north from 0° to 180° and \bar{R} the stress ratio for the three possible tectonic regimes, extensional (normal), strike slip (wrench) and reverse (compressive) fault regimes (Lejri et al., 2015). The stress ratio \bar{R} , is defined such as:

$$\left\{ \begin{array}{l} \text{Normal } \bar{R} = R \in [0,1] \\ \text{Wrench } \bar{R} = 2 - R \in [1,2] \\ \text{Reverse } \bar{R} = 2 + R \in [2,3] \end{array} \right\} \quad (4)$$

$$\text{with } R = \frac{(\sigma_2 - \sigma_3)}{(\sigma_1 - \sigma_3)}, \quad (5)$$

Here, depending on which of the principal stresses is vertical, we can cover the normal, wrench and reverse regimes with $\sigma_v = \sigma_1$, $\sigma_v = \sigma_2$ and $\sigma_v = \sigma_3$ respectively, with only one parameter that varies from 0 to 3 continuously.

2.3.2. Computation Time

The computation time is reduced by using the principle of superposition (Brillouin, 1946), a well-known principle in linear elasticity. It allows recovering the displacement, strain and stress at any observation point P using pre-computed specific values from three linearly independent simulations. This principle stipulates that a given value σ^t can be entirely determined by a linear combination of independent solutions such that:

$$\sigma^t = \sum_{i=1}^3 \alpha_i(\theta, \bar{R}) \cdot \sigma_i^t, \quad (5)$$

where σ^t is the tectonic stress, $\alpha_i(\theta, \bar{R})$ are scalar coefficients and σ_i^t are the linearly independent pre-computed tectonic stresses.

Here, the 3 scalars ($\alpha_1, \alpha_2, \alpha_3$) are enough to cover the full range of tectonic stresses. Suppose that for each linearly independent tectonic stress $\sigma_R^{(i)} \in [1,3]$, applied to a model, we compute and store the corresponding total stress tensor, $\sigma_P^{(i)}$, at a fracture location, P . Then, the total stress tensor at P due to the tectonic stress defined by $\sigma_R(\alpha) = \sum_i \alpha_i \sigma_R^{(i)}$ ($\alpha_i \in \mathbb{R}$) will be $\sigma_P = \sum_i \alpha_i \sigma_P^{(i)}$, involving only 18 multiplications. The total stress is defined as the imposed tectonic stress plus the perturbations caused by the slipping faults (Crouch and Starfield, 1983). As shown previously, any reduced Andersonian tectonic stress is entirely defined by only two parameters, θ and \bar{R} . Although we are inverting for these two parameters, we need to perform three simulations at initialization. This is because we have to use the components of the tectonic stress in the global coordinate system, i.e., σ_{xx} , σ_{xy} and σ_{yy} , in order to use the principle of superposition from linearly independent simulations. Using θ and \bar{R} does not provide any linear relationship.

Using the principle of superposition does not require re-computing the unknown displacement discontinuities on triangular elements, making possible to perform many simulations in few seconds (i.e.

50,000 in a couple of minutes). Therefore, if measurements of geological features are known at some given locations such as displacement, strain and/or stress, fractures orientation or secondary fault planes, which formed in the vicinity of major active faults, then it is possible to recover the triple components ($\alpha_1, \alpha_2, \alpha_3$) and therefore the tectonic stress σ^t and the corresponding tectonic regime (Maerten et al., 2015).

2.3.3. Fracture data and cost functions

We then use a Monte Carlo method to find the parameters ($\alpha_1, \alpha_2, \alpha_3$), which minimize some cost functions given three independent far field stresses. The cost functions must be as simple as possible as we do not want add extra computation time to the overall process. In the present study we constrain the paleostress inversion with observed fracture data exclusively.

Fracture data

We defined 3 natural structures types (fractures, faults and stylolites...) based on their development mechanism and their relationship with the orientations of the 3 principal stresses as described in Figure 2.

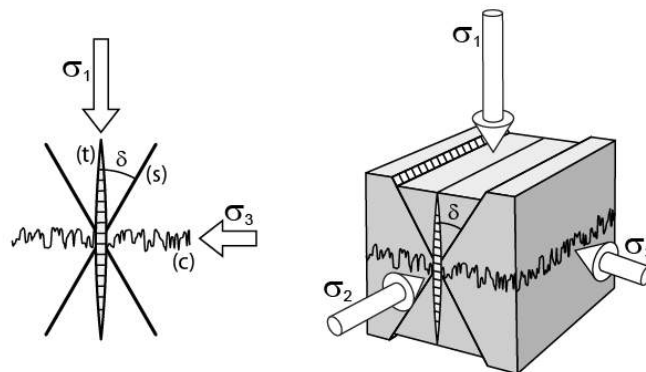


Figure 2: Mechanical fracture types and relationship with principal stresses. (t) Tension fracture (i.e. joint), (c) Compressive fracture (i.e. stylolite) and, (s) Shear fracture (i.e. fault).

Tension fractures form in a direction perpendicular to the potential fracture plane reaches the tensile strength of the rock. Tension fractures show an extension perpendicular to the fracture walls. The most

common tensile fractures are the joints but it also includes veins (tension gashes) and dikes. Tension fractures will form in a plane perpendicular to the least compressive principal stress σ_3 .

Stylolites peaks form with a compressive stress in a direction parallel to the potential stylolite peaks. Stylolites are common in carbonates but compressive stress can also lead to the formation of compaction bands (perpendicular to the most compressive principal stress σ_1) and stylolites in clastic rocks. Here we only consider stylolites with perpendicular peaks.

Shear fractures are generated by shear stress. Shear fractures is a fracture along which the relative movement is parallel to the fracture walls. The most common shear fractures are the faults but it also includes deformation bands. A shear fracture is one of the two conjugate planes, oriented at acute angles δ on either side of the most compressive principal stress, σ_1 , and with opposite sense of shear direction (see Figure 2). δ is such that:

$$\delta = \frac{\pi}{4} - \frac{\phi}{2}, \quad (6)$$

where ϕ is the angle of rock internal friction.

Cost functions

For a given tectonic stress defined by θ and \bar{R} , the minimum cost for tension fractures, $C_{tension}$, is such that the computed local minimum principal stress, σ_3 , is aligned with the normal \vec{n} of the observed tension fracture plane:

$$C_{tension} = 1 - (\vec{\sigma}_3 \cdot \vec{n})^2 \quad (7)$$

For stylolites, the minimum cost, $C_{stylolites}$, is such that the computed local maximum principal stress, σ_1 , is aligned with the normal \vec{n} of the observed stylolites:

$$C_{stylolites} = 1 - (\vec{\sigma}_1 \cdot \vec{n})^2 \quad (8)$$

For shear fractures, the minimum cost C_{shear} , is such that the computed local minimum principal stress, σ_3 , is at angle ϕ (friction angle) from the normal \vec{n} of the observed shear fracture plane:

$$C_{shear} = \left| (\vec{\sigma}_3 \cdot \vec{n})^2 - \frac{1}{2}(1 + \sin \phi) \right| \quad (9)$$

The cost is normalized for the 3 fracture types and varies from 0 and 1. A cost of 0 means a perfect match between observed fractures orientation and local computed stresses, while a cost of 1 means the worst match. The 3 types of fractures can be combined and the total cost for one simulation will be the average cost of all observed fractures used to constrain the inversion. Each fracture data or data type can be weighted according to a user defined confidence criterion.

2.3.4. Tectonic stress domain

To better visualize and analyze the results of one paleostress inversion, which consists of thousands of simulations, we introduce the tectonic stress domain (Lejri et al., 2015), a 2D graph (see Figure 3) for which the x-axis is the stress ratio \bar{R} , and the y-axis is the orientation (θ) of the maximum horizontal stress according to the North. A point in the domain represents one simulation that is color coded with respect to the computed cost which goes from 0 to 1. As we can have numerous observed fractures, the color symbolizes the mean cost of all the fractures. For a given model, the inversion procedure will try to find the best solutions (\bar{R}, θ) by minimizing the cost functions.

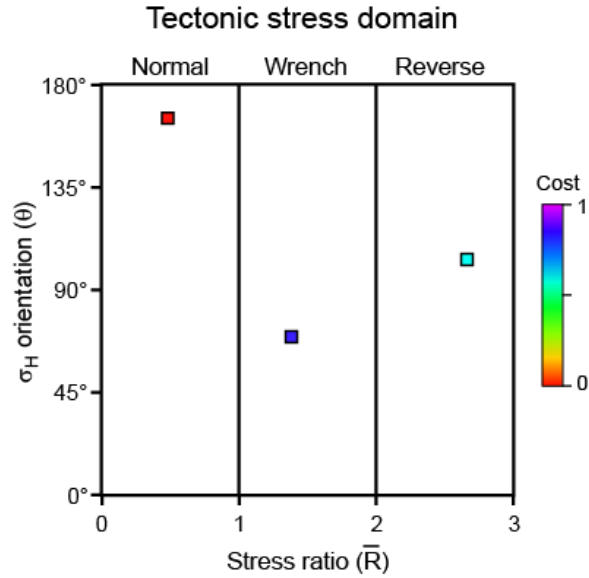


Figure 3: Example of a tectonic stress domain. The x-axis is the stress ratio, \bar{R} , and the y-axis is the orientation, θ , of the maximum horizontal stress according to the North. A point in the domain represents one simulation that is color coded with respect to the computed cost which goes from 0 to 1.

These will be highlighted in the tectonic stress domain with warm colors (see Figure 3). The optimum simulation (lowest cost), which will be the result of paleostress inversion, includes the orientation and relative magnitude of the paleo-tectonic regime as well as the style (normal, wrench or reverse fault regime).

2.3.5. Under-constrained model

Depending on the model configuration and available fracture data, the paleostress inversion could be under-constrained. It is not necessarily related to the number or quality of the available data but rather to the type of tectonic stress to be inverted or the data used (fault model and fracture data).

The first main under-constrained configuration is for stress ratio $\bar{R}=0$ and $\bar{R}=3$, which correspond to radial extension (normal fault regime) and radial compression (reverse fault regime) respectively. Indeed, in

such horizontal radial stress configurations, where $\sigma_h = \sigma_H$, the orientation of the maximum horizontal stress, θ , cannot be determined as all possible orientations are valid. This produces uncertainty in finding θ .

The second main under-constrained configuration is for a vertical fault model under an Andersonian state of stress, where displacement normal to the fault plane is not allowed and where only frictionless slip is induced by the two horizontal stresses σ_h and σ_H . Such configuration produces uncertainty in finding \bar{R} and it can be easily demonstrated (see Annex 1) that variation of the stress ratio \bar{R} or, in other words the ratio between the two horizontal stresses, will produce a pattern of stress trajectories around the sliding faults not different than for the same fault model under uniaxial compressive horizontal stress (σ_H). This has previously been described by Bourne and Willemse (2001). However, the opposite conclusion has been misleadingly presented by de Jossineau et al. (2003). Indeed, in their 2D physical experiments using PMMA (polymethyl methacrylate), which could be comparable to modeling vertical faults in 3D, the only driver for stress trajectory variation around active fault with changing biaxial load ($Hr = \sigma_h / \sigma_H$) is the simple fact that the faults are open defects (PMMA plates cut using a 0.3-mm-diameter micro-saw) being partly closed and sheared in response to the imposed compressive loading conditions. Without the normal displacement component necessary to close the open defects during loading, the horizontal stress ratio $Hr = \sigma_h / \sigma_H$ (i.e. biaxial compressive loading conditions) has no effect on the stress trajectories. Therefore, in both physical and numerical simulations, the assumption of displacement normal to the fault plane has to be used and applied with care. Indeed, in nature, the pure shear displacement assumption along faults must be the general rule. However, it is only in few circumstances that the normal displacement should occur either dilating the fault zone by increasing porosity or by fluid pressure or, contracting the fault zone by closing the fault gaps created by previous sliding along irregular fault surfaces, by grain crushing (i.e. deformation bands) or by dissolution. In such circumstances, the stress trajectories will be locally influenced by the horizontal stress ratio $Hr = \sigma_h / \sigma_H$. In geomechanical simulations allowing normal displacement along the faults and/or adding fault sliding friction, which is a nonlinear process, will make the modeled stress

trajectories dependent on the horizontal stress ratio H_r . This will be investigated and discussed in the next sections.

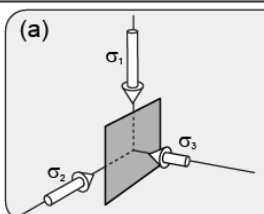
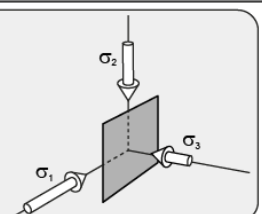
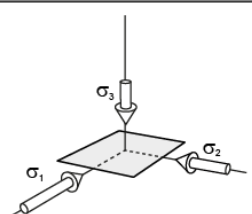
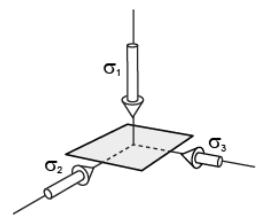
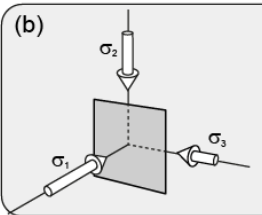
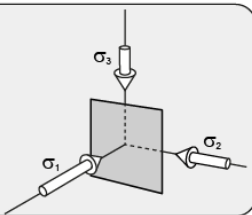
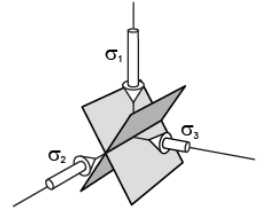
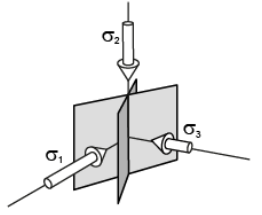
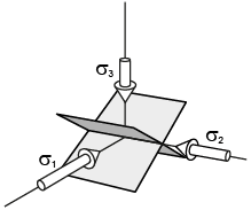
		Tectonic regimes		
		Normal	Wrench	Reverse
Mechanical fracture types	Tension	(a) 		
	Compression		(b) 	
	Shear			

Figure 4: Table showing the relationship between tectonic stress regimes and associated fracture types. (a) Under constrained configuration in the case of sub-vertical 3D fault model and sub-vertical tension fractures. Here the uncertainty will be in \bar{R} between normal and wrench fault regimes. (b) Under constrained configuration in the case of sub-vertical 3D fault model and sub-vertical stylolite planes. Here the uncertainty will be in \bar{R} between wrench and reverse fault regimes.

In our paleostress inversion simulations, for both normal and wrench fault regimes, the tension fractures will be vertical (see Figure 4a), so a model with sub-vertical faults and only observed vertical tension fractures will be under-constrained as it will be difficult to discriminate between σ_1 being vertical (normal fault regime) or σ_2 (wrench fault regime). In such case there will be an uncertainty in \bar{R} in both normal and wrench fault regimes as shown in the outcrop case study of the next section. A combination of vertical tension fractures and vertical stylolite planes should restrain the inversion to the wrench fault regime (see Figure 4ab), but \bar{R} will still be under-constrained in that tectonic regime. Similarly, for both wrench and

reverse fault regimes, the stylolite planes will be vertical (see Figure 4b), so a model with sub-vertical faults and only observed vertical stylolite planes will be under-constrained as it will be difficult to discriminate between σ_2 being vertical (wrench fault regime) or σ_3 (reverse fault regime). In such case there will be an uncertainty in \bar{R} in both wrench and reverse fault regimes.

3. Nash Point outcrop case study

The study area occurs in east of Nash Point, UK, on the northern margin of the Bristol Channel (longitude $3^{\circ}33'W$, latitude $51^{\circ}24'N$). Along this section, large coastal outcrops of the sub-horizontal Lower Jurassic (Liassic) sedimentary succession provide outstanding examples of strike slip faults and tension fractures (joints), making it among the best known structural localities in Europe for tension structures (Figure 5).

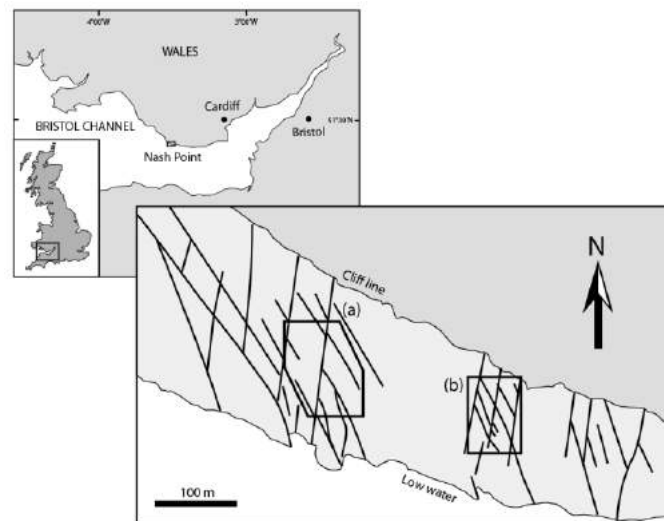


Figure 5: Location map and mapped fault pattern of the Nash Point outcrop (modified from Petit et al., 2000). (a) Location of the studied faults and joints. (b) Location of outcrop studied by Petit et al. (2000) and Bourne and Willemse (2001).

3.1. Geological Setting

Exposures along the beach at Nash Point consist of inter-bedded Liassic shallow marine pale grey limestone and shale. Individual layers, rarely greater than 1 m thick, are laterally continuous for up to 2 km

except where faulted, and dip consistently to the south at less than 5°. Based upon regional geological knowledge (Peacock and Sanderson, 1992; Rawnsley et al., 1992), the faults are conjugate strike-slip faults related to late Cretaceous to early Tertiary Alpine shortening. Faults display sub-horizontal striations with very small vertical offsets. Analyses of regional unperturbed joint pattern consisting of parallel joints yields an azimuth of maximum horizontal compression around $170^{\circ} \pm 10^{\circ}$ (Petit et al., 2000).

The joint patterns exposed in the area have been described and partly mapped by Rawnsley et al. (1992), Rawnsley et al. (1998) and Petit et al. (2000). Here we concentrate on area (a) of Figure 5 that we have carefully mapped from high quality air photos. The air photos are approximately true vertical photos that have been scaled, oriented and geo-referenced. In the vicinity of the faults, joints tend to be perturbed and are often sinuous with quite regular spacing. Figure 6 shows the fault network of the studied area and associated complex pattern of joints (tension fractures). Next to the faults, joints become either parallel or at high angle to the fault traces. This is particularly true around fault extremities (point A in Figure 6), where observed joints and stylolites pattern follow the pattern described on Figure 1. At fault intersection showing acute angle ($\sim 35^{\circ}$), their general orientation tendency is to converge towards the fault intersection points (point B in Figure 6). Locally, joints undoubtedly converge to points along some of the fault traces (point C in Figure 6 and Figure 7). To our knowledge Rawnsley et al. (1992) were the first to describe such points of joint convergence.

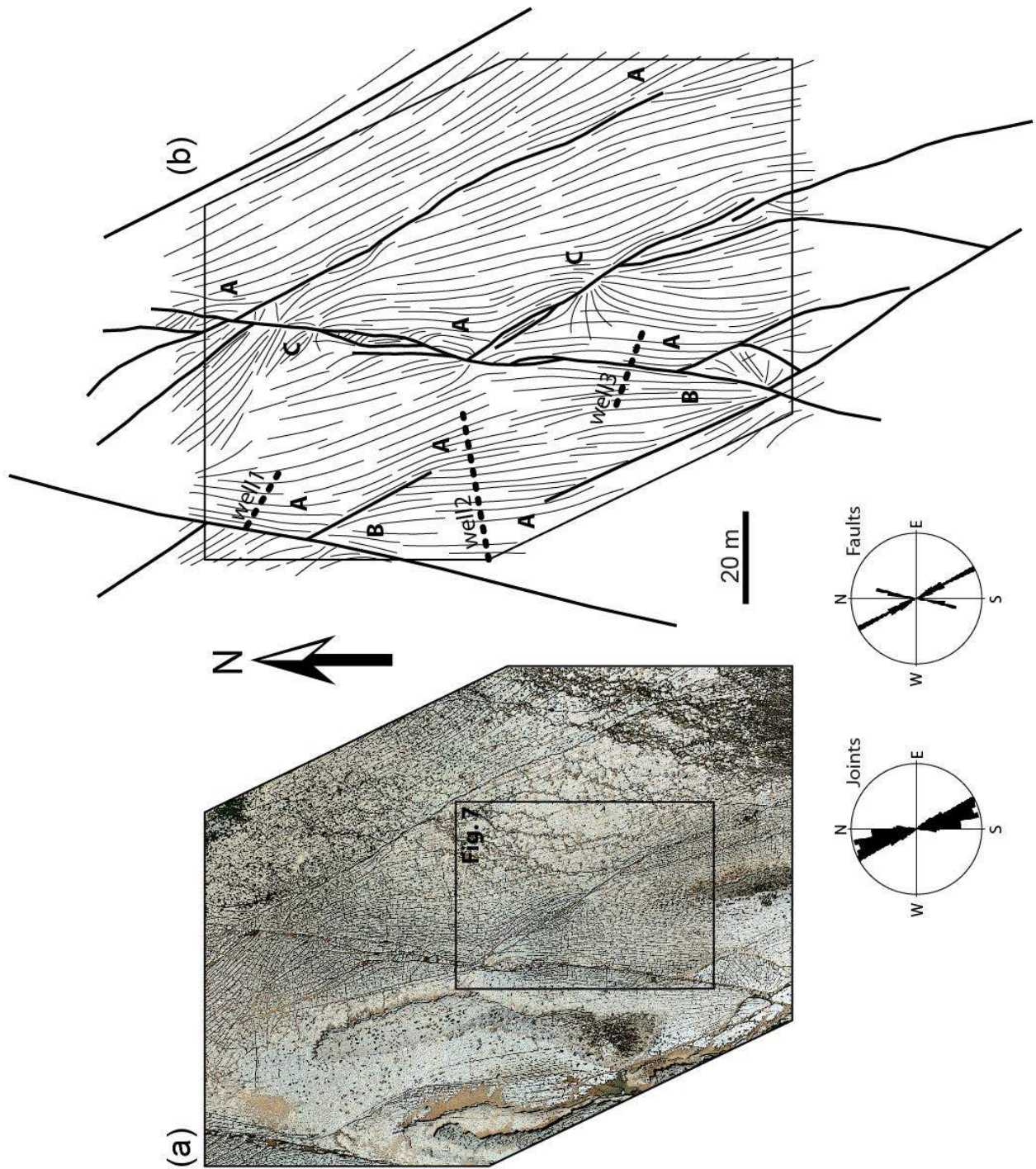


Figure 6: Nash Point outcrop example. (a) Air photo of the area (photo courtesy of the Fault Analysis Group) and (b) detailed air photo interpretation the showing joint pattern (thin black curves) and fault traces (thick black curves).

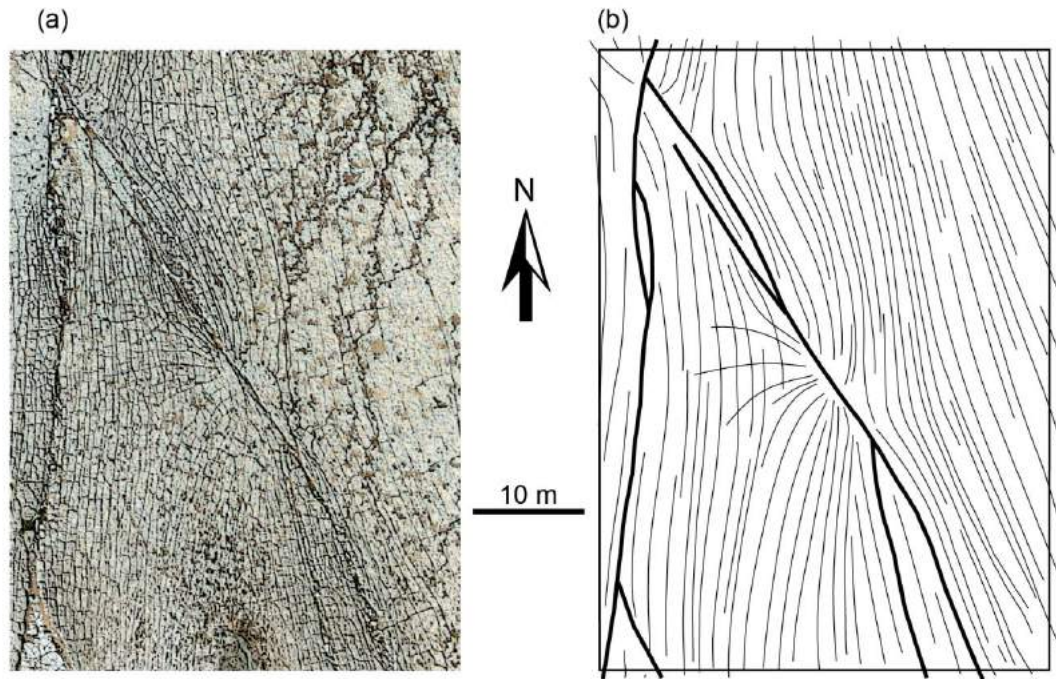


Figure 7: Close-up of convergent joint pattern at Nash Point. (a) Air photograph used for the interpretation of the faults and joints. (b) Line drawing of the faults and joints.

The variability of the joints pattern at Nash Point clearly highlights the relationship between the strike slip faults and the development of the joints. While joints do not seem to be genetically linked to the faulting they nonetheless appear to have developed within the perturbed stress field caused by slip along faults. The joint patterns at Nash Point, area (b) of Figure 5, have been previously modelled using photo-elastic models (Auzias, 1995; Rawnsley et al., 1997; Petit et al., 2000) as well as using 3D elastic dislocation model (Bourne and Willemse, 2001). These previous studies nicely corroborate the mechanical relationship between the faults and the development of the joints.

3.2. Paleostress inversion

The first set of experiment is a paleostress inversions using a 3D model of the faults mapped in the area constrained with all the interpreted joints.

3.2.1. Model configuration

The 3D fault model (Figure 8) has been built from the detailed interpretation of the fault traces of Figure 6. The fault traces have been vertically extruded in order to build sub-vertical fault model with a height of 40 m (Rawnsley et al., 1998; Bourne and Willemse, 2001). A combination of traction and displacement boundary conditions was prescribed along each fault. A displacement component normal to the fault plane was initially set to 0 in order to prevent any opening or interpenetration of the fault walls.

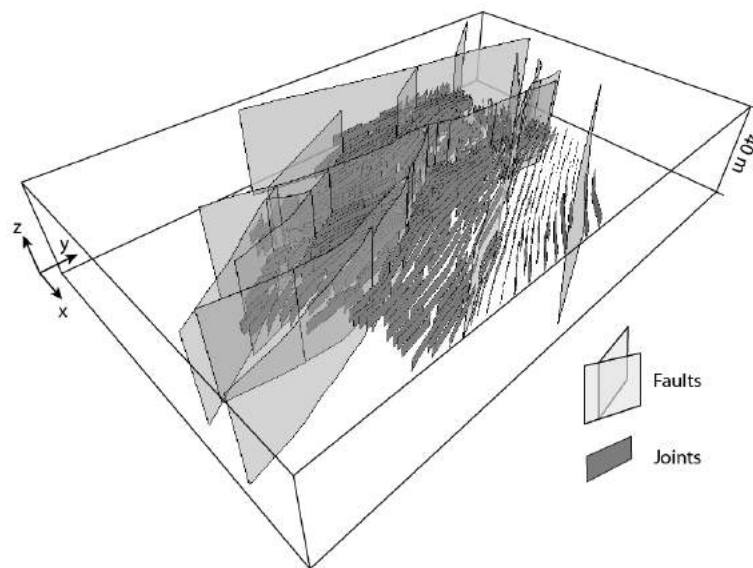


Figure 8: Nash Point model configuration. 3D model made of sub-vertical faults and interpreted joints. Y-axis points to the North.

The two other components parallel to the fault plane, which may represent the local slip along a dip-slip or strike-slip fault, were set to have initial tractions equal to 0 in order to let the faults freely slip in response to the remote load. These local boundary conditions allow for mechanical interaction between the faults.

In the following mechanical models, we used a homogeneous whole elastic space with a linear elastic and isotropic behavior characterized by two constants, Poisson's ratio and Young's Modulus. We used a

value of 0.25 for Poisson's ratio (ν), 50 GPa for Young's Modulus (E), which are the mean values representative for limestone (Clark, 1966). The paleostress inversion is constrained by the mapped joint traces (see Figure 6a and 8) along which the dip angle (90°) and dip azimuth are known. The cost function used for the simulation that is described earlier for tension fractures described earlier and each data has the same weight. A layer parallel observation grid, covering the entire studied area, has been used and placed at mid height of the faults, which could represent the sub-horizontal exposed limestone layer. These observation points, at which we compute the resulting perturbed stress field, are used to compare with the observed joint patterns.

3.2.2. Model results

The paleostress inversion, which consists of 50,000 geomechanical simulations, has been run in less than 2mn. The optimum paleo tectonic stress found is oriented N163° (σ_H) for a mean cost $\bar{C} = 0.0646$. As anticipated, the corresponding tectonic stress domain displayed in Figure 9 shows that the model is under-constrained. Indeed, there is a strong uncertainty in \bar{R} that covers both the normal and wrench fault domain, which means that any values of \bar{R} in the yellow zone (see Figure 9) would give similar results.

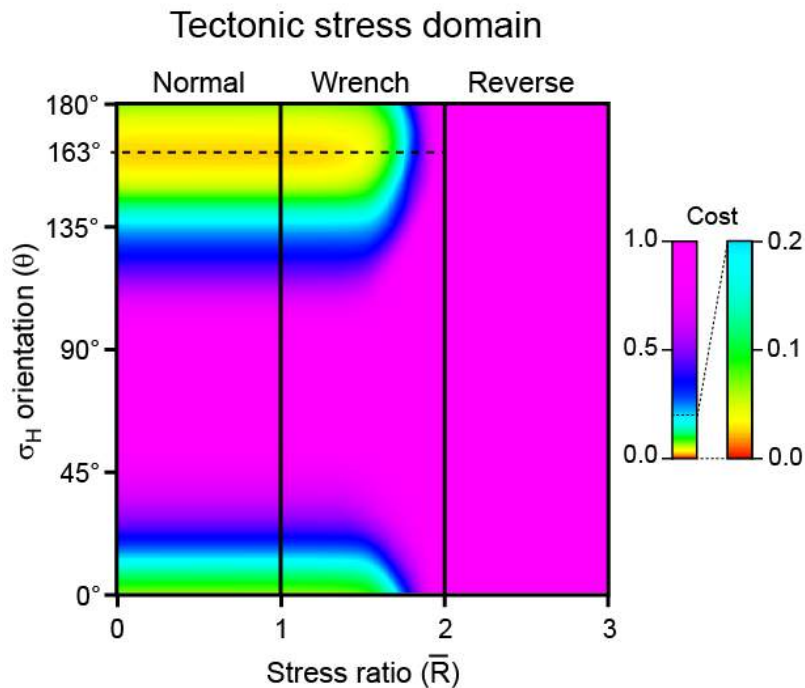


Figure 9: Nash Point paleostress inversion results. Tectonic stress domain of the Nash Point inversion showing that the best maximum horizontal stress (σ_H) is oriented 163°. It also highlights that the model is under-constrained resulting in a strong uncertainty in \bar{R} .

Figure 10ab shows a qualitative comparison between the observed joint pattern and the model joint trajectories. Since joints (i.e. tension fractures) propagate in a surface normal to the local direction of the least compressive stress (i.e. σ_3), the streamlines shown in figure 10bc represent the strike of the plane made σ_1 and σ_2 , which is mostly sub vertical in this case as σ_3 is horizontal for both normal and strike slip regimes. The modeled joint trajectories of Figure 10b show a good correspondence with the observed joint pattern of Figure 10a. Near the faults, the modelled trajectories become either parallel or at high angle to the fault traces as observed at points A in Figure 10ab around fault extremities and at fault intersections with an obtuse angle ($\sim 145^\circ$). At fault intersections showing acute angle ($\sim 35^\circ$), the modelled trajectories tend to converge towards the fault intersection points (points B in Figure 10ab). However, joints trajectory converging to points along some of the fault traces (points C in Figure 6 and Figure 7) cannot be reproduced

using the actual boundary conditions suggesting that other stress perturbation mechanisms are involved. These possible mechanisms will be discussed in the following sections.

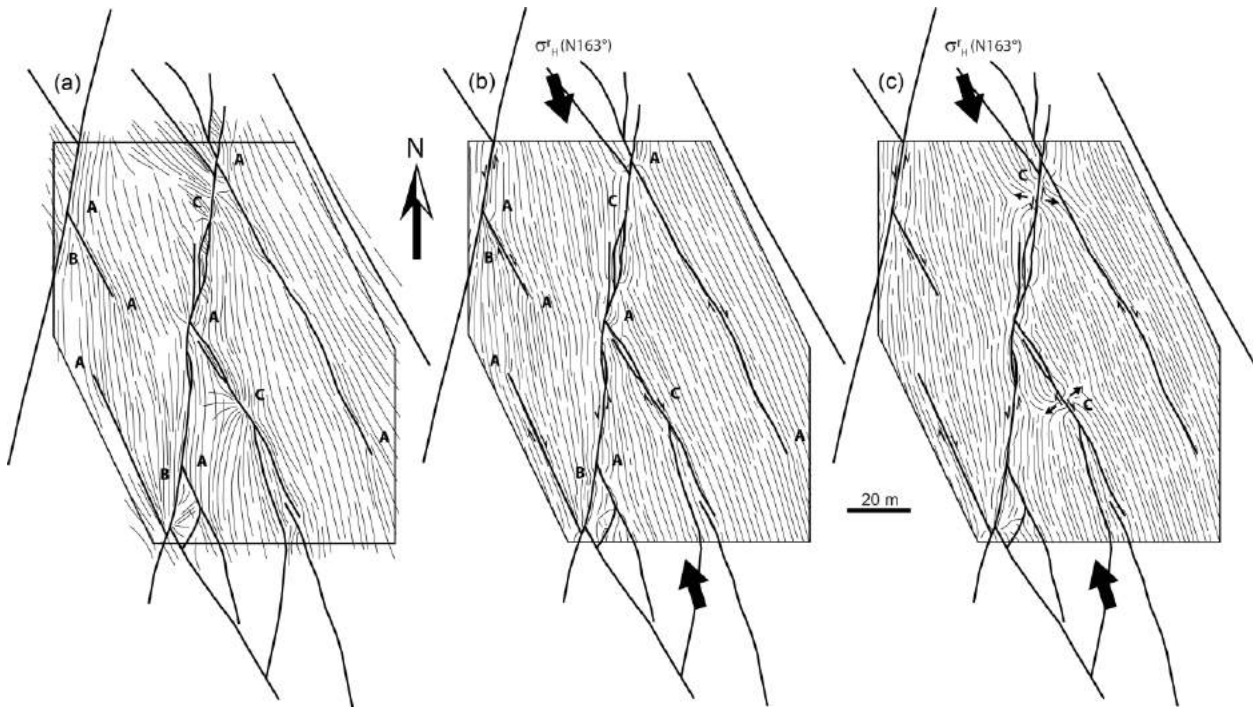


Figure 10: Result of the Nash Point model. (a) Map of the observed joint pattern. (b) Map illustrating the modeled trajectories of the perturbed maximum horizontal stress, σ_H around faults (thick lines) and (c) same as (b) with added local fluid pressure. Black arrows represent the orientation of the inverted regional σ_H . Points A, B and C, are described in the text.

3.2.3. Sensitivity to fracture data location

This section aims at evaluating to what extent the paleostress inversion is sensible to the spatial distribution of fracture data used to constrain the inversion. The following paleostress inversion tests are summarized in Table 2 and include as constraining fracture data, (i) all the interpreted joints, (ii) all the interpreted joints minus those associated to local perturbations (joint trajectory convergence around points C), (iii) the joints from 3 wells taken individually, these 3 synthetic horizontal wells being located where the joints orientation are the most perturbed but away from local perturbations at points C (see Figure 6b) and

(iv), the joints from selected combinations of the 3 wells (well1+well2, well2+well3 and well1+well2+well3).

Figure 11 and Table 1 show the results of these paleostress inversions.

The highest cost is for the inversion constrained by all the joints. The orientation of σ_H found is N163° and is similar to the mean joint strike or the inversion without any faults perturbing the stress. When the joint data used has been cleaned from all the joints associated to local perturbations around points C, the orientation of σ_H found is still N163° but the cost is sensibly reduced (divided by 3.5), emphasizing the confidence in the inversion results. We therefore consider that N163° is the best candidate for σ_H orientation and use it as a reference.

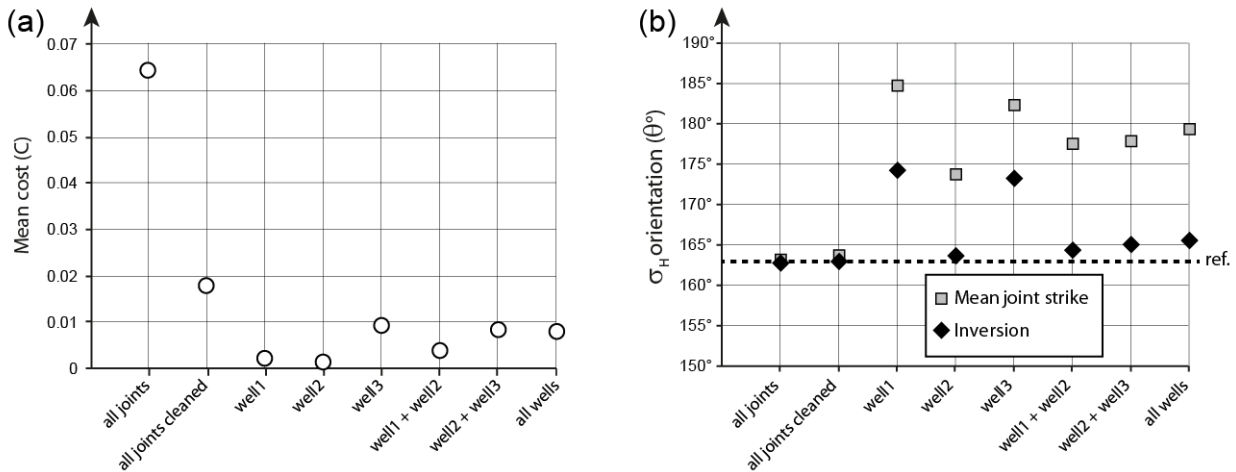


Figure 11: Effect of fracture data location at Nash Point model. (a) Graph showing the mean cost (C) with respect to data location along wells and well combinations. (b) Graph showing both the inverted maximum horizontal stress (σ_H) orientation (grey squares) and the mean joint strike (black diamond) with respect to data location along wells and well combinations. Dashed line represents the reference σ_H when using all fracture data.

When the joint data taken from individual wells are used to constrain the inversion there is a discrepancy of $10^\circ \pm 1^\circ$ in σ_H orientation with the mean joint strike. Furthermore, σ_H orientation derived from the mean joint strike is 11° to 20° away from the reference N163°. Among the 3 wells, Well 2 located between two mechanically interacting overlapping faults, gives a σ_H orientation similar to the reference. All

the selected combinations of the 3 wells show that the inversion results always gives a σ_H orientation similar to or greater than the reference to a maximum of 2.5° , while the σ_H orientation derived from the mean joint strike is always greater than the reference to about 15° .

These results clearly illustrate that taking into account the stress perturbation around the faults is essential if we want to estimate the far field tectonic stress responsible for the joint development at Nash Point. It also highlights that, for paleostress inversion, it is important to use fracture data scattered throughout the area of interest rather than a spatially concentrated high number of fracture data.

3.3. Joint trajectory convergence investigation

In this section we intend to explain and model the local joint perturbation described in Figure 7. Two mechanisms are investigated: (i) the contact point mechanism proposed by Hyett and Hudson (1990), Rawnsley et al. (1992), Auzias (1995) and Petit et al. (2000) and (ii) the fluid pressure point mechanism as suggested by Gillespie et al. (2011).

3.3.1. Contact point model

The contact point model was first proposed by Rawnsley et al. (1992) to explain joint trajectory convergences observed near some of the faults at Nash Point and at Lilstock, UK (Rawnsley et al., 1998). The model is based on the fact that the behavior of the two surfaces in contact is best described by the existence of distinct points of contact, rather than an even contact along the interface. Therefore, this model assumes, in addition to the shear displacement, that displacement normal to the two surfaces of the discontinuities must occur, except at contact points. The stress is then transmitted and concentrated across the surfaces at these contact points causing local perturbation in the stress field. Auzias (1995), Rawnsley et al. (1997) and Petit et al. (2000) have shown from photo-elastic studies that the stress trajectories are found to converge towards distinct points of contact. As joints follow the stress trajectories they should converge towards each point of contact.

To model this behavior using iBem3D, we have used different combinations of traction and displacement boundary conditions prescribed along the faults. To simulate the contact point (dashed line of Figure 12a), a displacement component normal to the fault plane was initially set to 0 in order to prevent any interpenetration of the fault walls. Along all the other faults a traction component normal to the fault plane was initially set to 0 in order to authorize interpenetration of the fault walls in response to the remote load. Since we are modeling faults, the two other components parallel to the fault plane, which may represent the local slip along a dip-slip or strike-slip fault, were set to have initial tractions equal to 0 in order to let the faults freely slip in response to the remote load. These local boundary conditions allow for mechanical interaction between the faults.

A series of models have been run to test the horizontal stress ratio $Hr = \sigma_h / \sigma_H$ effect on the mean fit between the observed joint pattern and the modeled joint trajectories derived from computed heterogeneous stress tensor. The graph of Figure 12b illustrates that the best fit is for a horizontal stress ratio $Hr=0.7$ with a mean cost $\bar{C}=0.0667$. Figure 12a represents the modeled joint trajectories for this optimum model configuration. The figure is to be compared to the observed joint trajectories of Figure 7. The joint convergence pattern is reproduced where no normal displacement is allowed along local fault segment (dashed line).

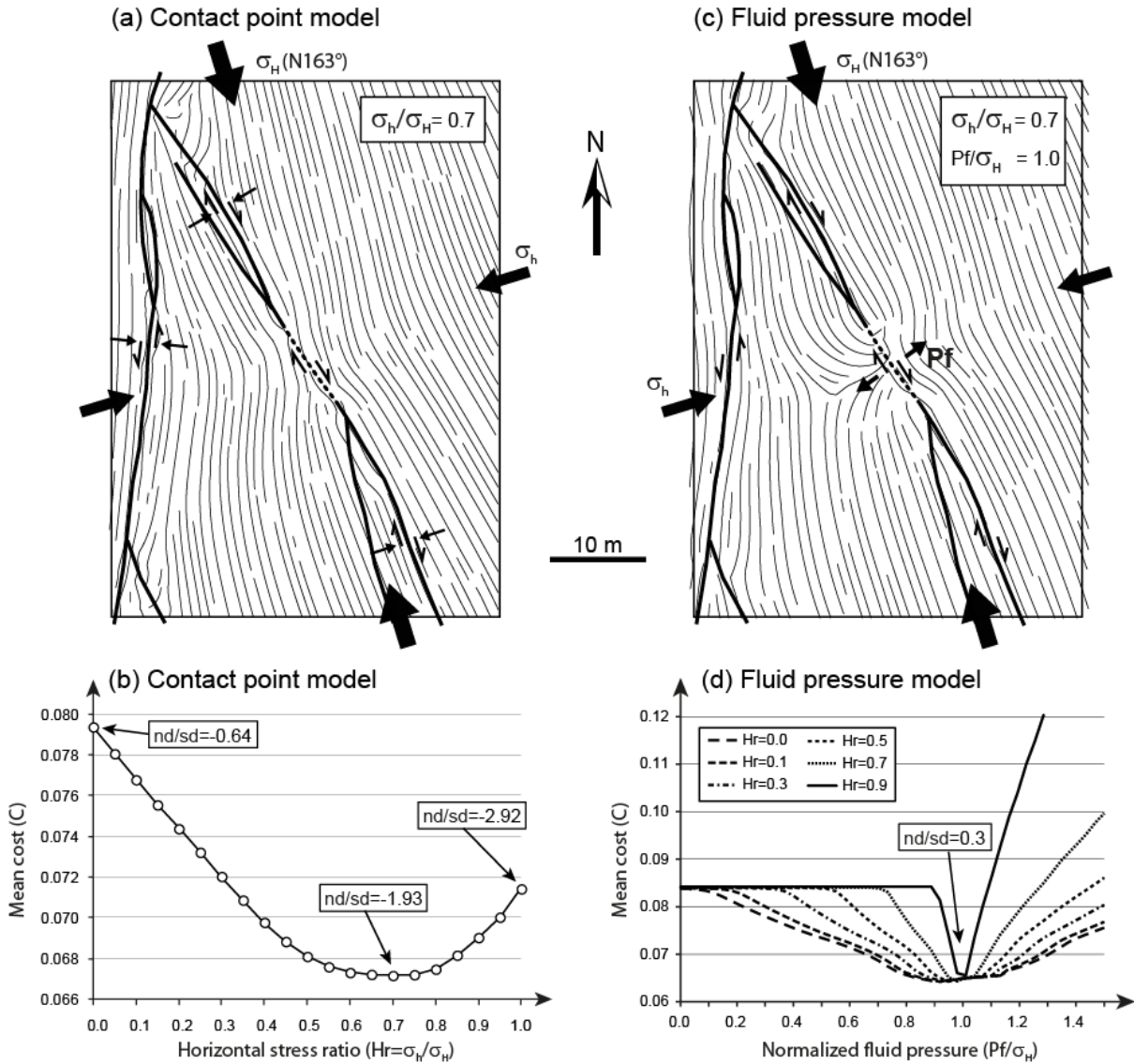


Figure 12: Joint trajectory convergence at Nash Point. (a) Modeled joint trajectories convergence using localized contact point model and a horizontal stress ratio $\sigma_h / \sigma_H = 0.7$. (b) Graph of mean cost (C) versus the horizontal stress ratio σ_h / σ_H . nd/sd is the ratio of the maximum interpenetration displacement over the maximum shear displacement. (c) Modeled joint trajectories convergence using localized fluid pressure model such that $Pf/\sigma_H = 1.0 \pm 0.5$ and a horizontal stress ratio $\sigma_h / \sigma_H = 0.7$. (d) Graph of mean cost (C) versus the normalized fluid pressure (Pf/σ_H) applied at the observed convergence point.

3.3.2. Fluid pressure model

Another way to explain joint trajectory convergence is to have localized fluid pressure along the faults causing local perturbation in the stress field. This has been suggested by Gillespie et al. (2011) to explain the

observed points of joint convergence at Lilstock, UK. The points of localized fluid pressure represent regions of the otherwise cemented fault zone that were open and that contained high-pressure fluid at the time of jointing.

To model this behavior, we have used different combinations of traction and displacement boundary conditions prescribed along the faults. To simulate the fluid pressure point (dashed line of Figure 12c), a traction component normal to the fault plane was initially set to the fluid pressure (Pf) in order to authorize opening or interpenetration of the fault walls in response to both the imposed pressure Pf and the remote load. Along all the other faults a displacement component normal to the fault plane was initially set to 0 in order to prevent any interpenetration of the fault walls. As for the previous model, the two other components parallel to the fault plane were set to have initial tractions equal to 0 in order to let the faults freely slip in response to the remote load.

A series of models have been run varying both the fluid pressure Pf , normalized against the maximum horizontal stress σ_H , and the horizontal stress ratio $Hr = \sigma_h / \sigma_H$, which should have a local effect around the pressurized fault segment. The graph of Figure 12d illustrates that the best fit between the observed joints and the modeled joint trajectories is for a normalized fluid pressure of $Pf/\sigma_H = 1.0 \pm 0.5$ with a mean cost $\bar{C} = 0.0645$, and this regardless of the horizontal stress ratio value. The range of optimum normalized fluid pressure, Pf/σ_H , increases as the horizontal stress ratio decreases. In contrast, the optimum normalized fluid pressure converges towards 1.0 as the horizontal stress ratio increases to reach 1.0. Figure 12c represents the modeled joint trajectories for a normalized fluid pressure of $Pf/\sigma_H = 1.0$ and a horizontal stress ratio of $Hr = 0.7$. The figure is to be compared to the observed joint trajectories of Figure 7. The joint convergence pattern is reproduced where fault segment has been pressurized (dashed line).

A simulation (see Figure 10c) using the entire fault model, a horizontal stress ratio $Hr = 0.0$, and a normalized fluid pressure ($Pf/\sigma_H = 1.0$) also imposed to the northernmost interpreted joint convergence

(points C), gives a mean fit of $\bar{C}=0.0609$. This computed mean fit is lower than a similar simulation without any fluid pressure as well as lower than a model using contact points.

4. *Les Matelles outcrop case study*

This second study area is located 15 km North of Montpellier, France, close to the village called Les Matelles. The exposure, located in a dry flat-bottomed valley (longitude 3°48'E, latitude 43°43'N), is well suited for the study of brittle tectonics in limestones and stress perturbations around meso-scale faults (Rispoli, 1981; Petit & Mattauer, 1995; Soliva et al., 2010). Indeed, the exposure displays a large number of features such as faults, stylolites, joints and veins filled with calcites.

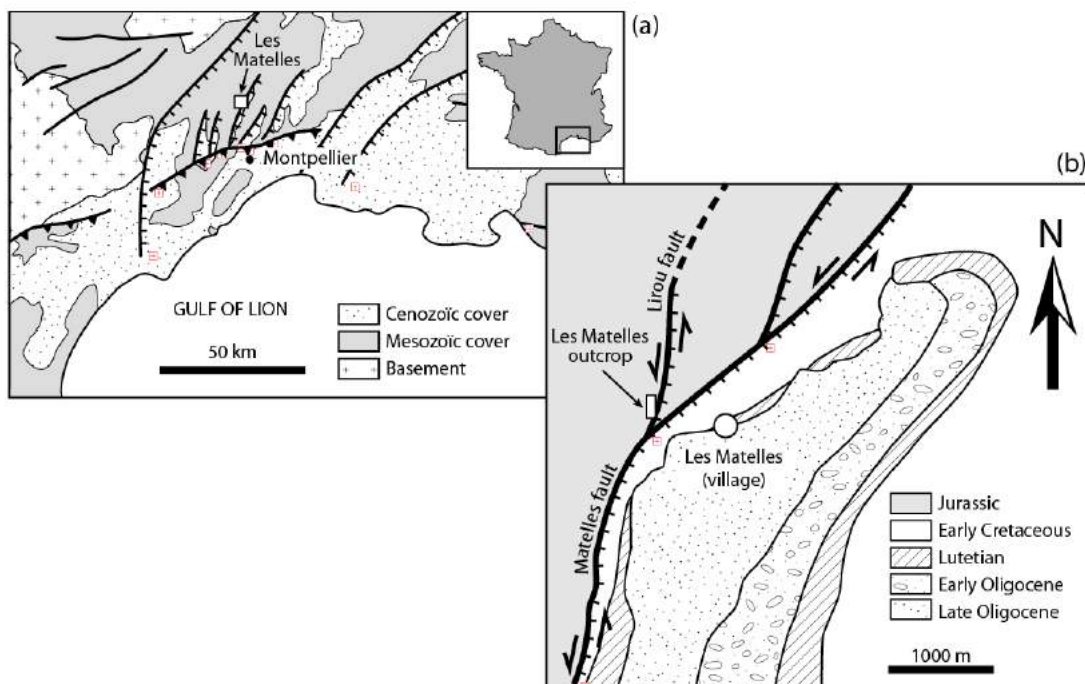


Figure 13: Location and geological context of the Matelles study area. (a) Regional structural scheme of the study area. (b) Structural sketch map showing the geological setting of the Matelles Fault and the Lirou fault branch (from the 1:50,000-scale geological maps of Montpellier and Saint Martin de Londres), with location of the presented outcrop.

4.1. Geological Setting

The exposure, situated along the Lirou fault, one of the branch faults of the Matelles fault, consists of very gently tilted ($<10^\circ$) Jurassic micritic limestone layers. Individual layers, 20-30 cm thick, are laterally continuous along the Lirou valley for up to 200 m. Like most of the NE-trending faults bounding half-grabens north of Montpellier (see Figure 13), the Matelles fault has been affected by two successive tectonic events: (i) a NS-trending contraction during the Pyrenean orogeny of Eocene age creating a left-lateral strike-slip movement and (ii), a SE-trending extension during the rifting of the Gulf of Lion continental passive margin of late Oligocene - early Miocene age creating a normal dip-slip movement. Along the Lirou fault, these two successive contractional and extensional events are visible through the presence of both sub-horizontal slickenlines (Petit and Mattauer, 1995). Three types of structures are observed on the exposure and have been fully described in a number of previous studies (e.g. Rispoli, 1981; Taha, 1986; Petit and Mattauer, 1995; Petit et al., 1999; Watkinson and Ward, 2006; Soliva et al., 2010); long and straight faults attributed to reactivated joints, shorter and sinuous veins filled with calcite and stylolites. The most detailed map and interpretation of these structures have been proposed by Petit and Mattauer (1995). We therefore base our analysis on their work in addition to our own field observations.

The fault pattern consists of two conjugate sets, a $N20^\circ \pm 10^\circ$ trending left-lateral set and a $N140^\circ \pm 10^\circ$ trending right lateral set (see Figure 14ab). According to Petit and Mattauer (1995) these two sets are former joint sets being reactivated during the latest compressive event. A maximum horizontal offset of 60 cm has been observed on one of the $N20^\circ$ trending left-lateral faults. Horizontal offsets are generally smaller along the $N140^\circ$ set than on the $N20^\circ$ set.

The extensional fractures observed in the exposure are veins because they are more sinuous than joints and are often wide opened and filled with calcite. Their mean strike is $N170^\circ \pm 10^\circ$ throughout the exposure with local variation and they are almost systematically located (i) around fault extremities (points A in Figure 14a), where they follow the wing crack or horse tail pattern (Pollard and Segall, 1987; Granier, 1985), (ii) at

fault intersection showing acute angle, where their trend converges towards the fault intersection points (point E in Figure 14a) and (iii), at extensional jogs where they tend to be perpendicular to the overlapping fault traces (points C in Figure 14a). These veins have a clear genetic link with the faulting.

Two different sets of stylolites can be observed in the exposure. A regular set occurring throughout the exposure and is oriented N55°-60°. A N100° ±15° trending set of stylolites, which is always superimposed on the earlier N55°-60° set, is observed locally especially at contractional jogs along the N20° faults (points B in Figure 14a), at fault intersection showing acute angle (point E in Figure 14a) and occasionally near the tip of faults (point D in Figure 14a). This set of stylolites seems to be genetically linked to the faulting. Similarly, the nearly N50° trending dense stylolites observed between the two parallel N140° fault in the northern part of the exposure could be attributed, at least part of it, to the stress reorientation guided by the reactivation of the N140° joints during the latest shortening event. All the stylolites present in the exposure have peaks sub-perpendicular to the stylolite surfaces and can therefore be interpreted as anti-cracks (Fletcher and Pollard, 1981) or stylolite planes perpendicular to the most compressive stress.

The brittle deformation sequence described by Petit and Mattauer (1995) begins by two successive jointing stages of the Jurassic limestone layers with two principal trends, N20° and N140°. The third stage is the first generation of stylolite oriented N55°-60° (not represented in figure 14a). The fourth stage, which is the one that we consider in the following simulations, is the reactivation of the previous structures as both left-lateral and right-lateral strike slips due to the latest shortening event creating wing cracks, en echelon veins and a second generation of stylolites around the reactivated joints.

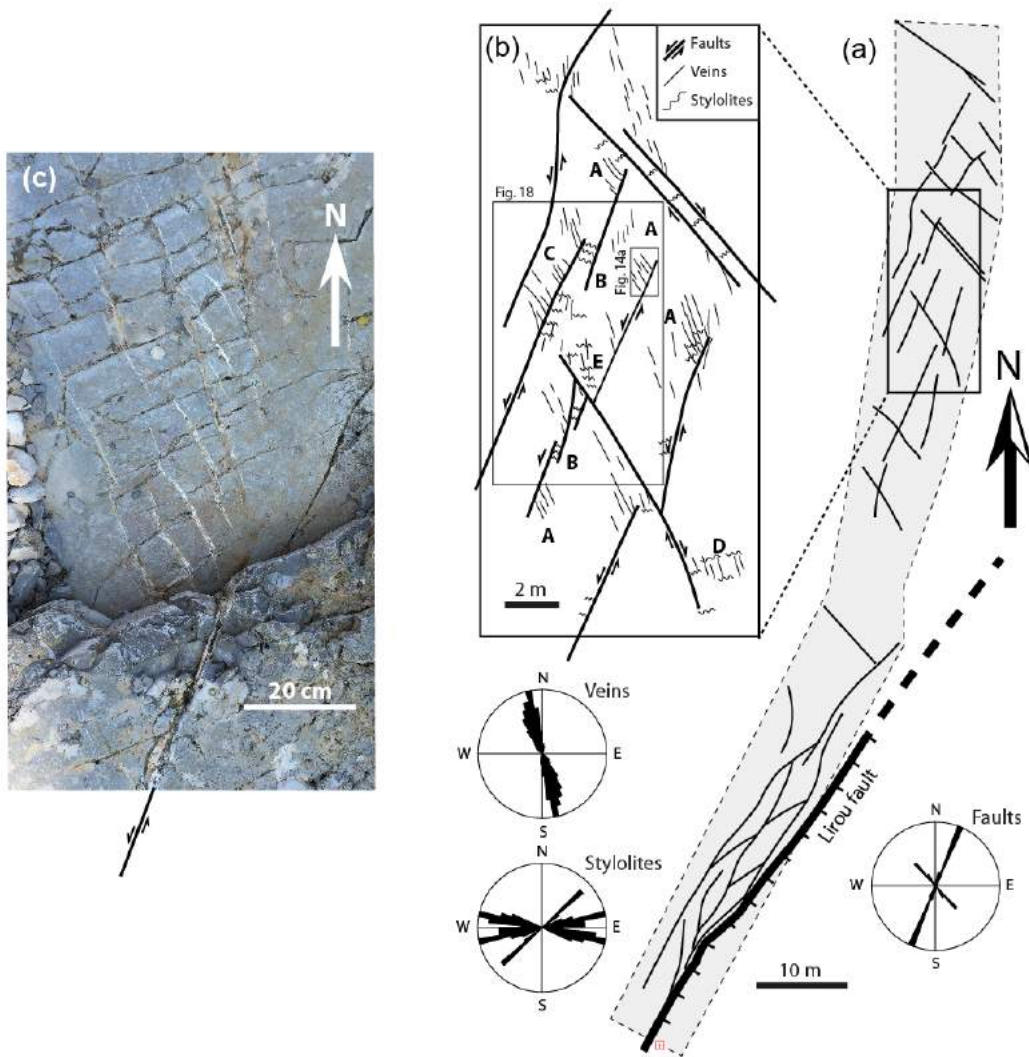


Figure 14: Interpreted fractures at the Matelles outcrop. (a) Map of the main fault pattern along the Lirou fault. (b) Detailed map of mesoscale structures used for the simulation. (c) Photograph of a strike-slip fault termination showing tail cracks (veins). The maps are modified from Petit and Mattauer (1995).

4.2. *Paleostress inversion*

4.2.1. *Model configuration*

The 3D fault model (see Figure 15) has been built from the interpretation of the fault traces of Figure 14a. The fault traces have been vertically extruded in order to build sub-vertical fault model with a height of 3 m, which is the greatest vertical size observed in the exposure. We use the same combination of traction

and displacement boundary conditions prescribed along each fault as in the Nash Point case study allowing for mechanical interaction between the faults.

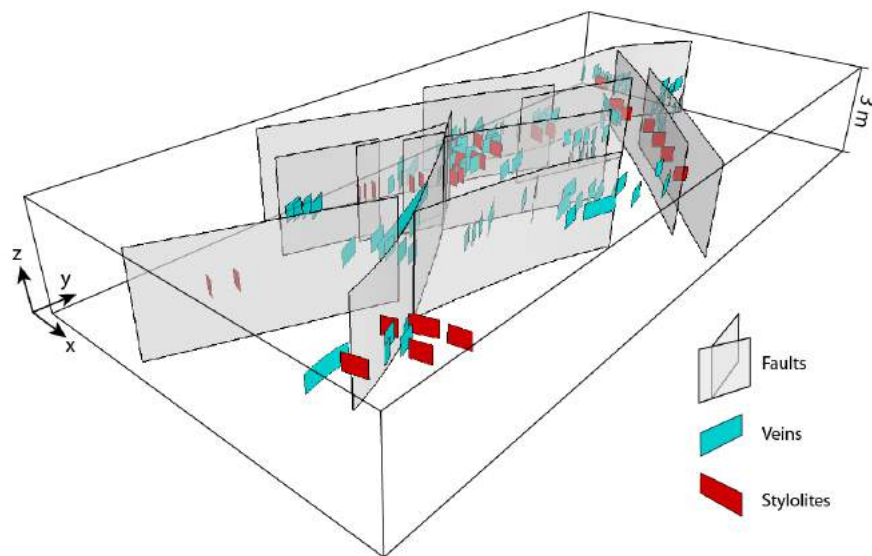


Figure 15: The Matelles model configuration. 3D model made of sub-vertical faults and interpreted veins and stylolites. Y-axis points to the North.

In the following mechanical models we used a homogeneous whole elastic space with a linear elastic and isotropic behavior characterized by two constants, Poisson's ratio and Young's Modulus with the same values as in the Nash Point case. The paleostress inversion is constrained by both the mapped vein and stylolite traces (see Figure 14) of known dip angle (90°) and dip azimuth. The cost functions used for the simulation are those for both the tension and the compression fractures described earlier. A layer parallel observation grid, covering the entire studied area, has been used and placed at the mid height of the faults, which could represent the sub-horizontal exposed limestone layer. The resulting perturbed stress field, computed at observation points along the observation grid, is compared with the observed joint patterns.

4.2.2. Model results

The paleostress inversion, which results from 50,000 geomechanical simulations, has been run in less than 30s (intel Xeon E5 QuadCore processor (2014)). The optimum found paleo tectonic maximum horizontal

stress is also oriented N163° (σ_H) for a mean cost $\bar{C}=0.0361$. The corresponding tectonic stress domain is displayed in Figure 16. We have seen in the previous section that performing paleostress inversion on Nash Point data set was a special under-constrained case with sub-vertical faults and sub-vertical joints exclusively to constrain the inversion (see Figure 4a). In such case we found a strong uncertainty in \bar{R} that covers both the normal and wrench fault domain, meaning that any values of \bar{R} would give similar results (see Figure 9). Even though the Matelles model is very similar to the Nash Point example with sub-vertical faults, it is better constrained. Indeed, as described in Figure 4, we illustrate through that example that adding a second type of mechanical fracture, such as the sub-vertical stylolites (compression fractures), reduces the uncertainty in the paleostress inversion in the \bar{R} domain. The corresponding tectonic stress domain displayed in Figure 16 shows that the model better constrained than for the Nash Point simulation using vertical tension fractures only and that now the uncertainty in \bar{R} is restricted to the wrench fault domain.

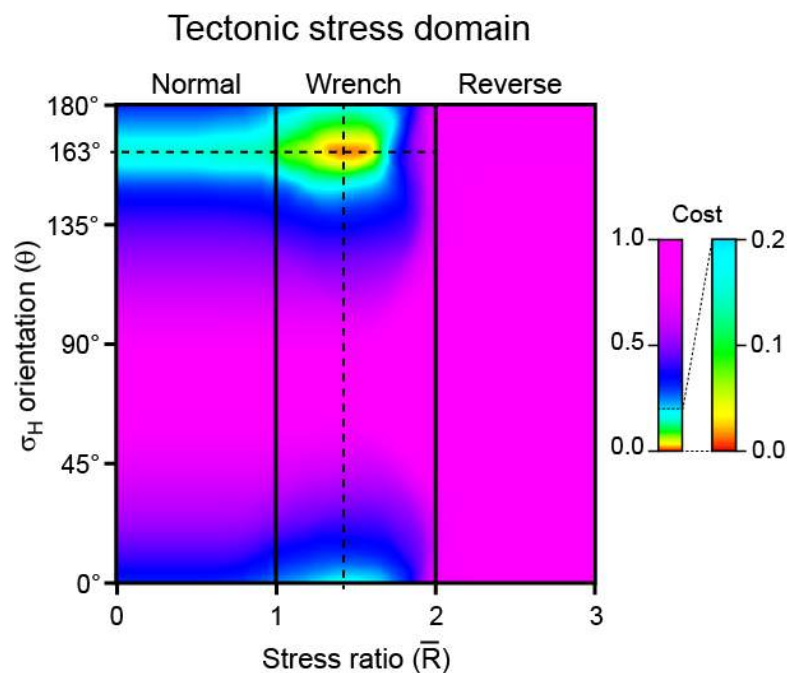


Figure 16: The Matelles paleostress inversion results. Tectonic stress domain of the Matelles inversion showing that the best maximum horizontal stress (σ_H) is oriented 163°.

Figure 17 shows a qualitative comparison between the observed fractures and the modeled trajectories of the same fractures based on the computed stress tensor. Since veins (i.e. tension fractures) propagate in a surface normal to the local direction of the least compressive stress (i.e. σ_3), the streamlines shown in figure 17a represent the strike of the plane made by σ_1 and σ_2 , which is mostly sub-vertical in this case as σ_3 is horizontal for strike slip regime. Similarly, as stylolites (i.e. compression fractures) propagate in a surface normal to the local direction of the most compressive stress (i.e. σ_1), the streamlines shown in figure 17b represent the strike of the plane made by σ_2 and σ_3 , which is also mostly sub-vertical in this case. Figure 17c represents the mean stress used here to illustrate the zones that underwent more or less compression and that can be related to the location/density of observed stylolites and veins respectively. The modeled fracture trajectories show a good correlation with the observed fracture patterns. Observed veins are located in areas of computed low compressive stress as shown in the extensional jogs (point C see Figure 17ac), where veins become perpendicular to the overlapping fault traces, and around fault extremities (points A in Figure 17ac), where veins tend to be at high angle to the fault traces with a horse tail pattern. Similarly, stylolites are concentrated in areas of computed higher compressive stress as shown in the contractional jogs (point B see Figure 17bc), where stylolites become perpendicular to the overlapping fault traces, and at fault intersection showing acute angle, where their general orientation tendency is to be perpendicular to the bisector of the said angle (point E in Figure 17bc). The modeled veins trajectories of Figure 17a, analogous to the σ_1 trajectories as σ_2 is mostly vertical everywhere (strike slip fault regime), can be compared to figure 10 of Petit and Mattauer (1995), which is an interpretative map synthesizing the σ_1 stress trajectories derived from all local meso-scale fracture interpretations.

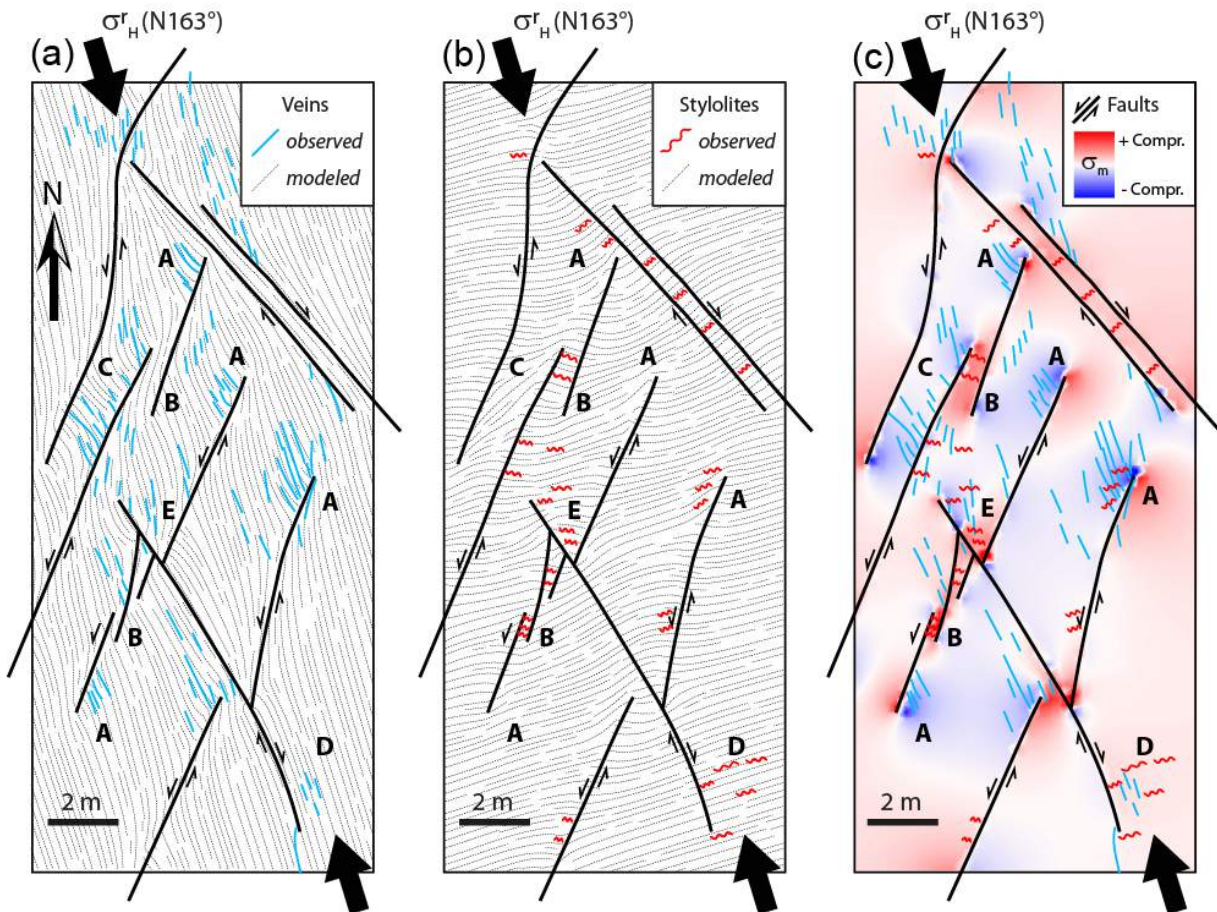


Figure 17: Result of the Matelles model. (a) Map illustrating the modeled trajectories of the veins around faults. (b) Map illustrating the modeled trajectories of the stylolites around faults. (c) Map of the modeled mean stress illustrating areas of more or less compression that can be linked the observed mesoscale fractures.

The geomechanical simulation shows that the maximum horizontal offset along the faults is on the N20° trending fault set. The N140° fault set presents a computed average maximum slip magnitude about 25% less than for the N20° fault set. This is in agreement with the observation made by Petit and Mattauer (1995). For a frictionless model, the N140° trending faults are indeed less optimally oriented for slip with respect to the N163° direction of σ_H than the N20° set. This also highlights that the two sets of faults are not likely to be coeval conjugate sets, as suggested by Rispoli (1986), but rather two set of pre-existing fractures being reactivated as proposed by Petit & Mattauer (1995).

4.2.3. Sensitivity to 3D fault model geometry

Here we want to evaluate the effect of the 3D fault model geometry, which perturbs the stress field, on the paleostress inversion results. The following test is not an exhaustive analysis but rather serves as a representative example. For this test we concentrate on the area described in Figure 14 and we changed the 3D fault model geometry by removing the two overlapping faults (see Figure 18b), which create both extensional and contractional jogs with associated veins and stylolites. The same model parameters are used for the paleostress inversion except that we exclusively use the fractures (veins and stylolites) observed in this local area of interest to constrain the inversion. The first results displayed on Figure 18a are for a complete fault model. As the previous model, we obtain the same N163° orientation of σ_H but with a slightly higher mean cost $\bar{C}=0.038$. This demonstrates the consistency of the paleostress inversion when less fracture data are used for the same 3D fault model. The second results displayed on Figure 18b are for the altered 3D fault model, where the two faults have been removed. As opposed to the previous test, we do not obtain the same orientation of σ_H (N161°) and the mean cost is much higher ($\bar{C}=0.088$) meaning that in such conditions it is more difficult to find a good solution. This is qualitatively highlighted in Figure 18b, where we can see that most of the observed meso-scale fractures (i.e. veins and stylolites) near the two missing faults cannot be matched with the modeled trajectories.

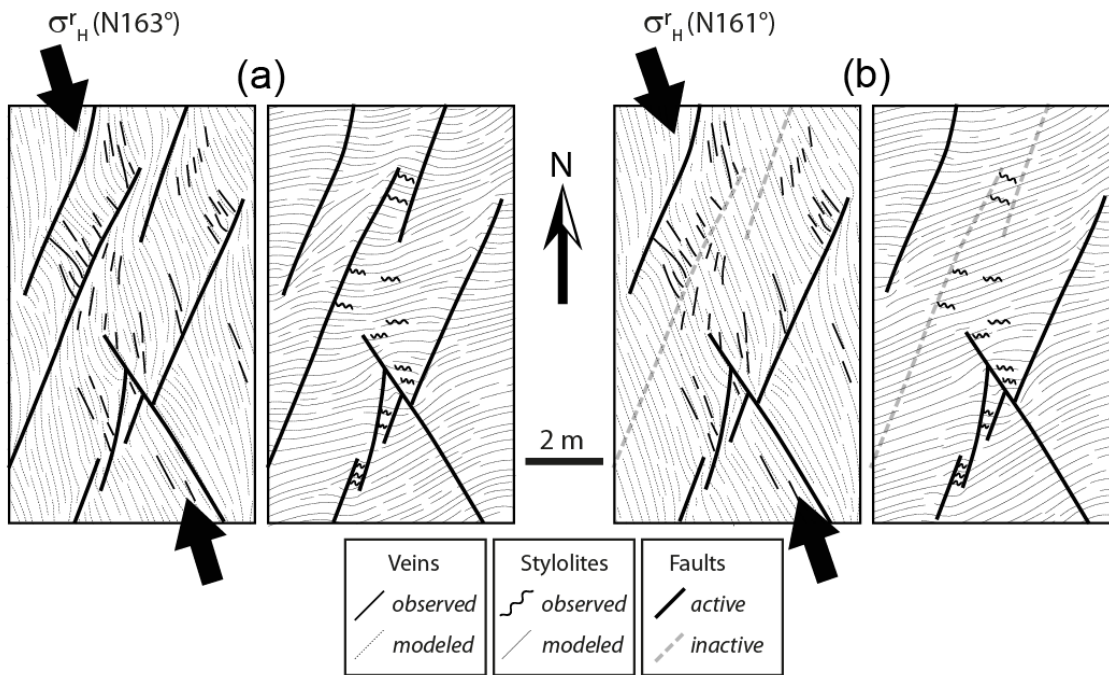


Figure 18: Sensitivity to fault model geometry. (a) Model results using all the interpreted faults. (b) Model results using incomplete fault model. In both cases modeled veins are on the left and modeled stylolites on the right.

4.3. Influence of fault friction

In their comprehensive geomechanical sensitivity analysis, Bourne and Willemsse (2001) commented that adding fault friction would tend to render the calculated fracture pattern less consistent with the joint pattern observed at Nash Point. They stated that zero fault friction (i.e. weak fault) is the simplest but realistic assumption that should correspond to the Nash Point case given that most of the observed joints are either parallel or normal to the fault traces as frictionless faults would produce. So, in this section we intend to evaluate how the fault friction parameter would affect the modeled fracture trajectories at the Matelles exposure and hence attempt to estimate what could have been the average friction along the faults during faulting (i.e. joint reactivation).

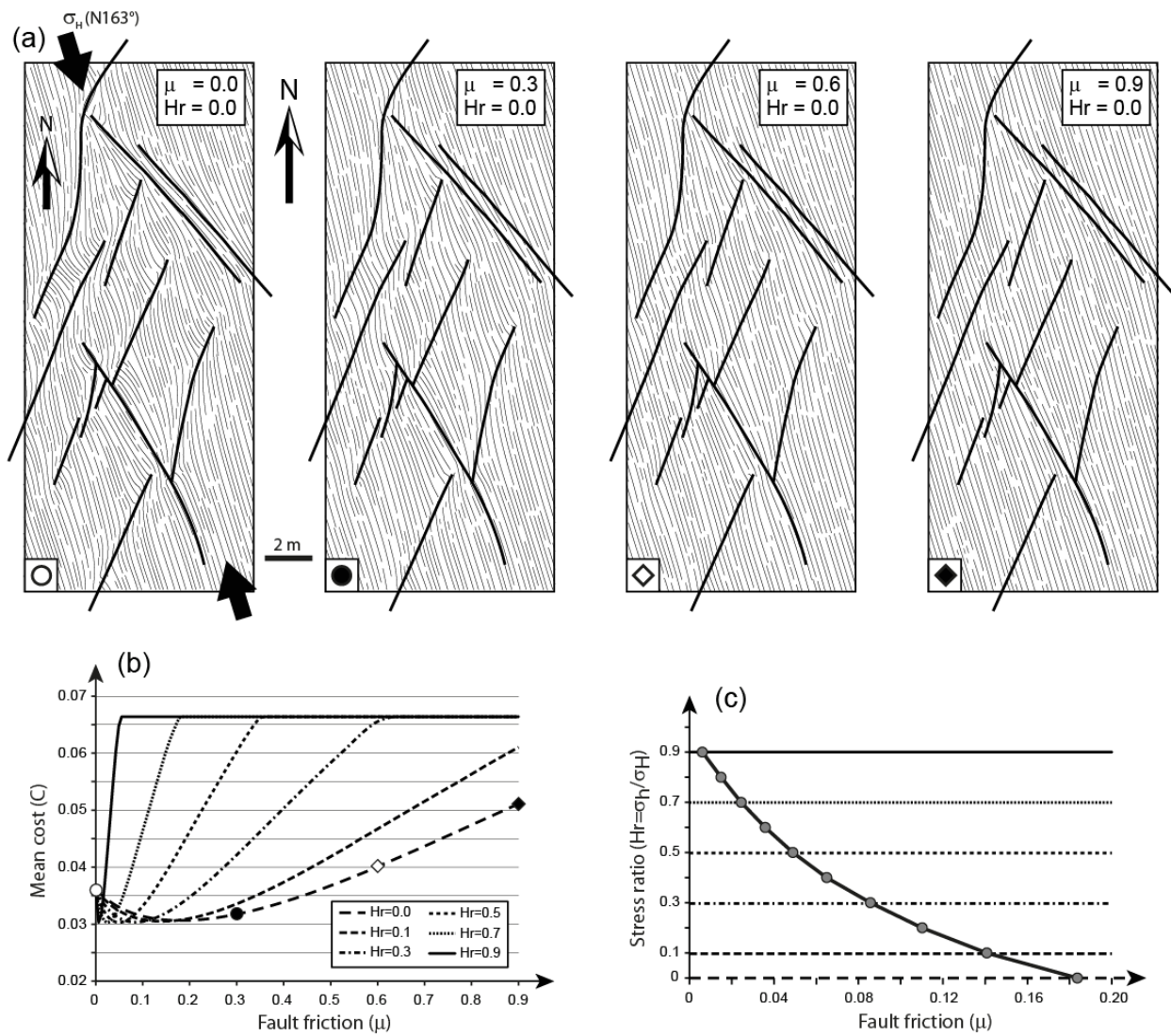


Figure 19: Effect of fault friction on stress trajectories at the Matelles. (a) Modeled joint trajectories using fault sliding friction ranging from 0 to 0.9 and a horizontal stress ratio $\sigma_h / \sigma_H = 0$. (b) Graph of mean cost (C) versus sliding friction for different horizontal stress ratio σ_h / σ_H . (c) Graph of the horizontal stress ratio σ_h / σ_H versus the sliding friction for the lowest mean cost (C).

A first series of forward geomechanical simulations have been run using the same parameters as the previous models but imposing a uniaxial horizontal far field stress ($Hr=0$), σ_H oriented N163°, and varying the fault sliding friction, μ , from 0 to 0.9. In order to have a frictional behavior, the iBem3D has been extended to support inequality constraints on traction and displacement. Specifically, the static Coulomb friction has been implemented as a traction inequality constraint and validated against analytical and numerical

solutions (Maerten et al., 2010). As anticipated by Bourne and Willemsse (2001), Figure 19a shows that increasing fault friction reduces the stress perturbation, hence the fracture trajectory perturbations. The higher the friction the closer the local stress trajectories are to the imposed remote state of stress.

A second series of forward geomechanical simulations have been run using the same configuration but with varying both the fault friction μ (from 0 to 0.9) and the horizontal stress ratio $Hr=\sigma_h/\sigma_H$ (from 0 to 0.9). The graph of Figure 19b illustrates how, for an imposed σ_H oriented N163°, the mean cost (\bar{C}) varies with respect to increasing fault friction and the horizontal stress ratio σ_h/σ_H . Fault model loaded with a high stress ratio $Hr=\sigma_h/\sigma_H$ will only slip if the friction is low. The smaller the stress ratio the larger the friction is necessary to lock the system. The mean cost plateau at $\bar{C}=0.0664$ is for a model where no faults is perturbing the stress field. For all stress ratio $Hr=\sigma_h/\sigma_H$ the best fit between the observed meso-scale fractures and the modeled fracture trajectories is for a mean cost $\bar{C}=0.0303$. However, graph of Figure 19c illustrates how much friction is needed to obtain this best fit (mean cost $\bar{C}=0.0303$) for a given stress ratio $Hr=\sigma_h/\sigma_H$. It shows that for uniaxial horizontal stress, $Hr=0$, a sliding friction of 0.182 is needed, while for biaxial horizontal stress when $Hr=0.9$, a sliding friction of 0.0061 is needed.

5. Oseberg Sør field case study

In this example, we would like to illustrate, using a known subsurface case study from the oil and gas industry (Maerten et al., 2006), that it is possible to recover the paleo tectonic stress responsible for the development of the small scale faults. We use the interpreted secondary fault surfaces from the Oseberg Sør field, Northern North Sea, to recover the paleo tectonic stress responsible for the development of these faults.

5.1. Geological Setting

The faulted Oseberg Sør reservoir (longitude 2°45'E, latitude 60°25'N) is located on the Norwegian Continental Shelf and forms part of the eastern flank of the Northern Viking Graben (Figure 20a). Most of the largest faults in the study area (maximum displacements) are ~N-S striking. On the basis of sedimentary thickness variations, we have concluded that these faults were active from Lower to Upper Jurassic. Smaller faults (grey color in Figure 20b), with displacements of between 30 and 250 m have a much more variable orientation than the larger faults and initiated later, predominantly in the Upper Jurassic, while the major faults (black color in Figure 20b) were still active. Examination of the fault pattern (see Figure 20b) shows that the orientations of the smaller faults is not consistent across major fault blocks, suggesting that the orientations of the smaller faults could have been controlled by stress perturbations around the larger faults and not necessarily explained by a series of successive tectonic events with different stress orientations (Maerten et al., 2002). Geomechanical analysis of the area has also been previously done by Maerten et al. (2006) to yield an extension direction of about N80°.

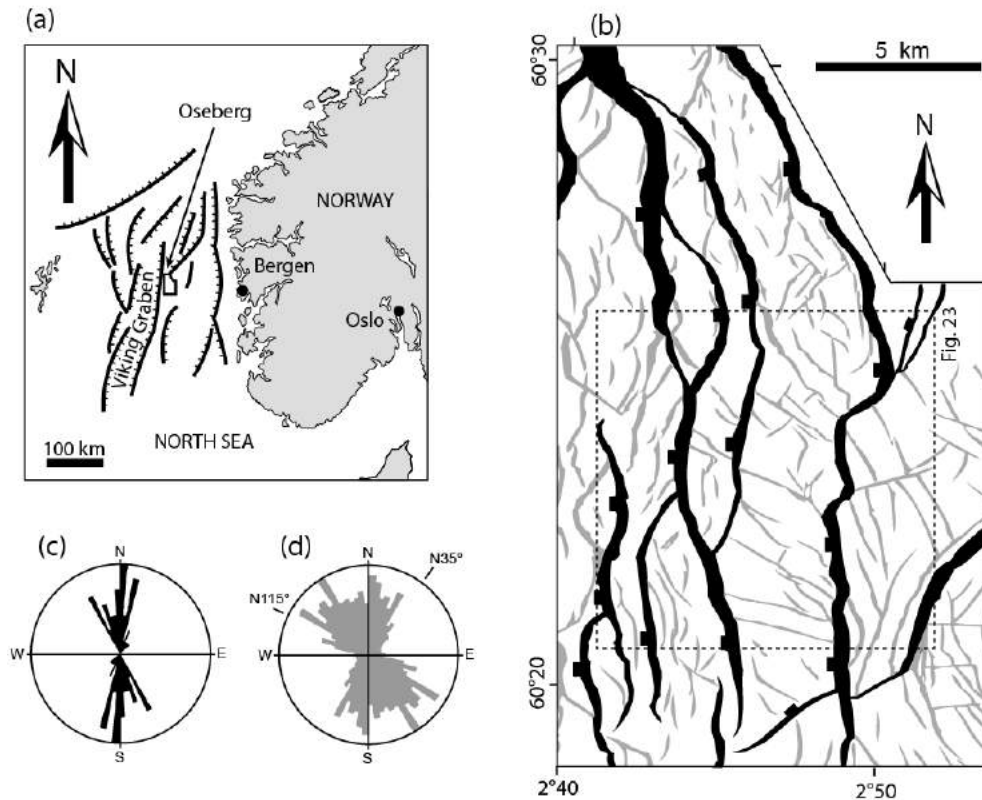


Figure 20: The Oseberg Sør area. (a) Localization of the Oseberg Sør reservoir in the Northern North Sea. (b) Fault map of the Base Brent horizon. Black faults are the major west-dipping, ~N-S striking normal faults (Lower to Upper Jurassic age). Gray smaller faults have much more variable orientation and are later, being predominantly Upper Jurassic. (c) and (d) Rose diagrams of the major ~N-S striking normal faults (black) and of the smaller Upper Jurassic normal faults (gray).

5.2. Paleostress inversion

5.2.1. Model configuration

The ten major normal faults of the area (black fault in Figure 20b), interpreted from 3D seismic data and believed to be early faults, were imported into the mechanical models (Figure 21). The same combination of traction and displacement boundary conditions as the previous case studies was prescribed along each fault. In the following mechanical model of the Oseberg Sør reservoir, we used a homogeneous elastic whole space with a linear elastic and isotropic behavior characterized by two constants, Poisson's ratio and Young's Modulus. We used a value of 0.15 for Poisson's ratio and 30 GPa for Young's Modulus, which are typical

values for partially consolidated sand. We believe that these values adequately represent the reservoir lithology at the time of deformation.

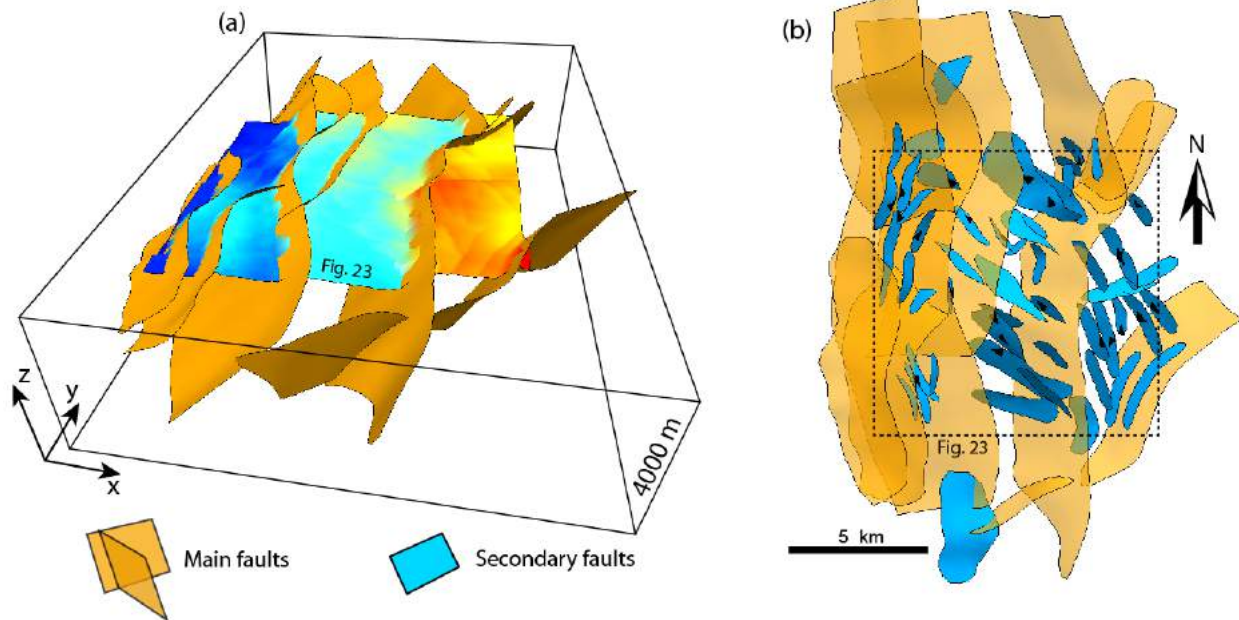


Figure 21: Oseberg model configuration. (a) 3D model of 10 intersecting normal faults (orange) and base Brent horizon. (b) Top view showing secondary faults (blue) and location of 23 fault information (black triangles) used to constrain the paleostress inversion.

The paleostress inversion is constrained by only 23 data points (see figure 21b) taken randomly amongst 3D surfaces of the observed smaller scale faults (blue faults in Figure 21b), along which the dip angle and dip azimuth are known. The cost function used for the simulation is the one for shear fractures described earlier with an imposed internal friction angle $\phi=30^\circ$. Each shear fracture data has the same weight. The resulting perturbed stress field, used to compare with the observed secondary faults, is computed along an observation grid defined by a regular grid with 200 m spacing in x and y, which corresponds to the Base Brent horizon (see figure 21).

5.2.2. Model Results

After less than 2mn and 50,000 simulations, the optimum paleo tectonic stress found, for a mean cost $\bar{C}=0.0635$, shows that (i) there is a single tectonic even, (ii) the tectonic event is a normal fault regime with a stress ratio $\bar{R}=0.51$, (iii) σ_H is oriented N167° thus the extension direction is oriented N77°. As opposed to the two previous case studies, the corresponding tectonic stress domain displayed in Figure 22 is not under-constrained as the fault model is not limited to subvertical faults and the fracture data used to constrain the inversion are shear fractures (see Figure 4).

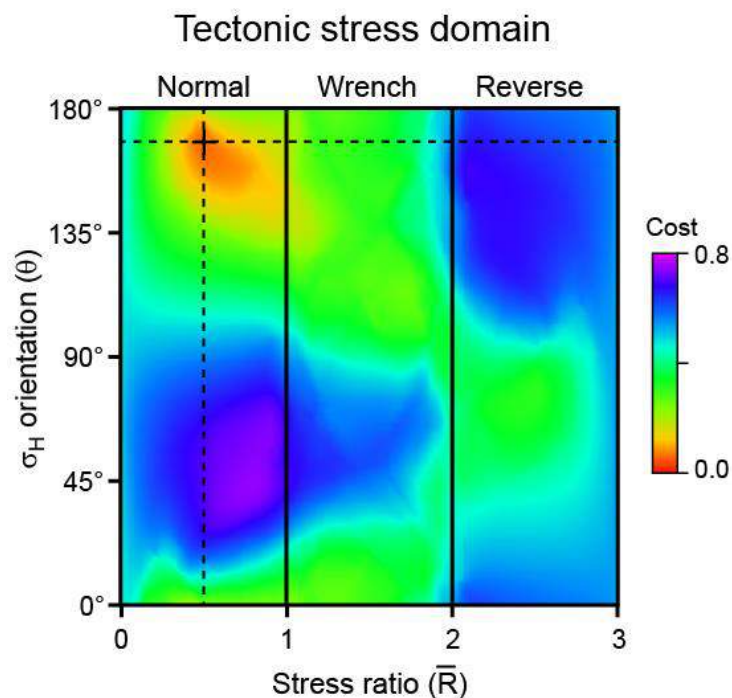


Figure 22: The Oseberg paleostress inversion results. Tectonic stress domain of Oseberg inversion showing that the best maximum horizontal stress (σ_H) is oriented 167° for a normal fault regime and a stress ratio $\bar{R}=0.51$.

Figure 23 shows the comparison between the observed secondary fault pattern and the computed fault orientation. The streamlines shown in figure 23b represent the strike of one of the two conjugate shear fractures derived from the computed stress tensor and the angle of rock internal friction (ϕ). As σ_1 is everywhere nearly vertical in the model results, except very close to some of the main faults, the strike of

the modeled two conjugate shear fractures is approximately identical and given by the direction of σ_2 . Over most of the area there is a fair correlation between the computed strikes and the observed strikes of the smaller faults. Local variations in strike close to large faults are well represented. Secondary faults curve where close to bends along the major faults and close to fault intersections where the stress perturbations are the greatest.

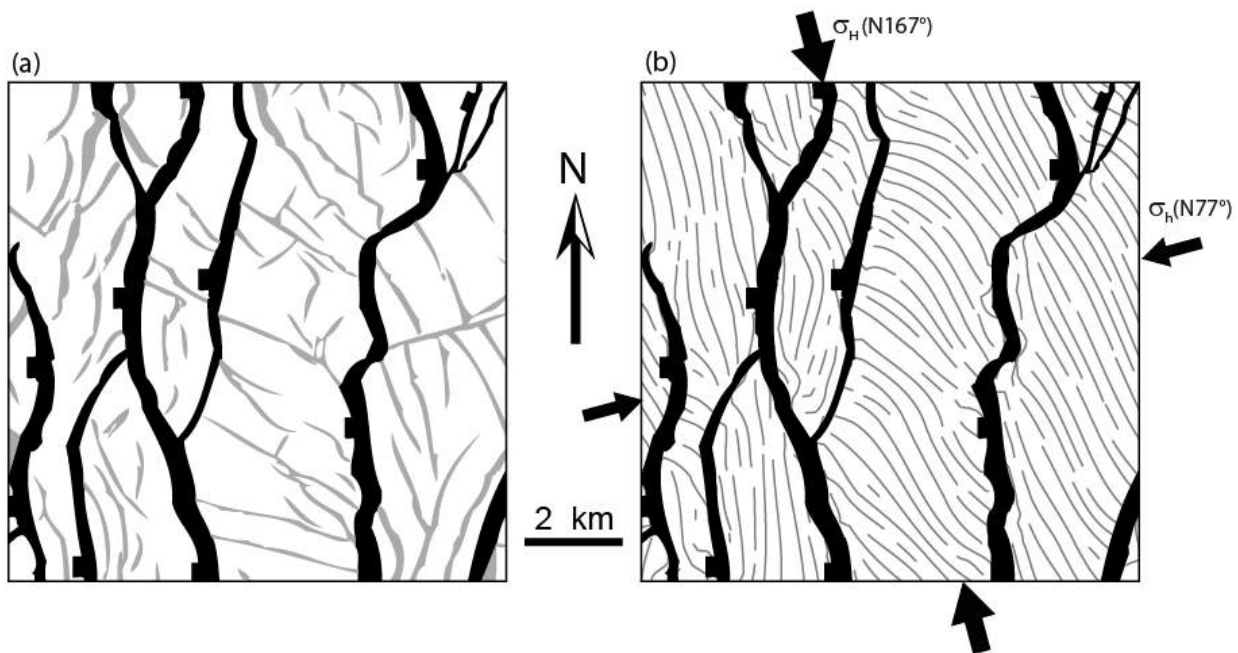


Figure 23: Comparison between observed and computed fault strike. (a) Interpreted fault map. (b) Computed fault strike.

6. Discussion and conclusions

6.1. The method

We have demonstrated that it is possible to reduce uncertainty in the paleo-tectonic stress characteristics (style, orientation and relative magnitude) needed to efficiently constrain geomechanical simulations used for modeling natural fractures in the subsurface. This is done using the new generation of mechanically-based paleostress inversion developed by Maerten (2010). The method is based on the physical fact that any large scale rock discontinuities such as faults, salt bodies, décollement layers or

cavities, subjected to far field stresses, generate local stress perturbations that in turns can be the drivers for the development of secondary structures such as smaller scale fractures. Knowing the location and characteristics of these natural fractures as well as the kind and geometry of the large scale discontinuities, should be sufficient to recover the far field stress responsible for the development of the smaller scale fractures. Therefore, the method depends upon the assumption that, for instance, in a growing and active fault system, the orientation of natural fractures will be influenced by the regional tectonic stress as well as by the perturbation of that stress state by nearby active larger faults (Maerten et al., 2014).

As opposed to most paleostress inversion techniques, which are mainly based on measured fault slip data, our method takes into account any type of observed and measured deformation that can be associated to a local state of stress. We have demonstrated that the three mechanical fracture types, extension, compression and shear fractures, can be efficiently used to constrain the paleostress inversion. This is a major advantage over existing methods based on measured fault slip data, especially in the oil and gas industry as fault planes with slickenlines are not observed in well log images and seldom observed in cores. In addition, the proposed method takes into account the heterogeneous state of stress that can be found around active faults, which is not the case of the commonly used paleostress inversion techniques.

The linear elastic assumption used in the proposed method might seem restrictive. Indeed, non linear behavior such as plasticity is not considered here. However, this linear elastic assumption appears nonetheless appropriate to explain most of the observed brittle natural deformations as shown in the three natural examples of the work. In addition, it provides a substantially useful advantage to the proposed paleostress inversion method. Indeed, the principle of superposition, only relevant to linear systems like ours, allows very fast and efficient computation time. In the selected case studies, 50,000 geomechanical simulations can be run in less than 2 minutes whatever the fault model geometry complexity.

However, we have shown that such geomechanically-based paleostress inversion method is highly dependent on the knowledge of the 3D fault pattern. As this information is not always available from outcrop observations, the use of the method seems to be better suited to subsurface observation such as in the oil and gas industry, where seismic reflection data often leads to a realistic 3D model of the geological structure. Additionally, we have found configurations where the model (3D fault pattern and fracture data) used to constrain the paleostress inversion is under-constrained. For instance a sub-vertical fault model associated to vertical fractures can lead to uncertainty in finding the tectonic regime and the stress ratio \bar{R} (Celerier, 1995). Another under-constrain model is when fracture data is not enough spatially distributed around the active faults. In such cases, the paleostress result can present a strong uncertainty in both \bar{R} and θ as there will be more chance to find several stress regimes that could explain the observed localized fracture data.

Another drawback of the method is in case of fracture data developed from multiple tectonic phases and when fracture mechanical type is not known, as it frequently happens when analyzing well log images from the oil and gas industry. In both cases a tedious manual typing and sorting of the fracture data is necessary to test several tectonic phase hypotheses. Further development should focus on both inverting the mechanical fracture data type, when not known, and on estimating the different tectonic phases in case of a poly-phase tectonic history.

6.2. *The Nash Point example*

The Nash Point case study is a very good example of fracture (i.e. joints) that is not genetically linked to the initial faulting but which development and propagation was constrained by the state of stress perturbed by slip on nearby faults at the time of jointing. The joint density is almost constant while the joint trajectories clearly follow stress pattern. Performing paleostress inversion on Nash Point data set is a special under-constrained case as the faults are strike-slip sub-vertical. This leads to an uncertainty in finding the stress ratio \bar{R} as well as the tectonic regime. However, we have demonstrated in annex 1, for a vertical fault

model under an Andersonian state of stress (i.e. one principal stress is vertical) where displacement normal to the fault plane is not allowed and where only shear is induced by the two horizontal stresses σ_h and σ_H without friction, that any stress ratio \bar{R} will produce a pattern of stress trajectories around the sliding faults not different than for the same fault model under uniaxial compressive horizontal stress (σ_H). In other words, the uncertainty in \bar{R} will not impact the modeled stress trajectories. The optimum paleo tectonic stress found is oriented N163° (orientation of σ_H) which is in agreement with previous field observations (Rawnsley et al., 1998; Petit et al., 2000) and modeling studies (Auzias, 1995; Bourne and Willemse, 2001). This far field stress orientation imposed to the interpreted 3D sliding fault model creates a heterogeneous perturbed stress field that nicely matches most of the joint trajectories observed at Nash Point except locally where joint trajectories converge to points along the faults.

The joint convergence shown in Figure 7 and first described by Rawnsley et al. (1992) has been explained by some authors (Rawnsley et al., 1997; Rawnsley et al., 1998; Petit et al., 2000; Bourne and Willemse, 2001) as being a compressional kink along the strike slip fault trace creating a contact point that concentrates the stresses. This hypothesis is supported by PMMA experiments (Auzias, 1995; Rawnsley et al., 1997) that clearly reproduce such stress trajectory convergence around contact points.

However, an older published picture of the close up of Figure 7, which has been used in the literature by the same authors to support the compressional kink hypothesis, presents a significant distortion probably caused by the photograph view point. A correction of the picture, presented in Annex 2, together with the analysis of the air photo show that the fault kink is not as pronounced as previously described, suggesting that the compressional kink hypothesis might not be sufficient to explain the joint trajectory convergence. In addition, the PMMA experiments used to support the contact point hypothesis present an important boundary effect that significantly enhances the stress perturbation at contact points. This boundary effect concerns the PMMA saw cuts used to model the faults that are open defects being closed and sheared during loading. De Jossineau et al (2003) have indirectly shown that such fault defect closure (fault normal

displacement) is very sensible to biaxial loading and greatly enhances stress perturbations. This has been modeled in our numerical experiments using the same boundary conditions and while we can reproduce the stress convergence at contact points (see Figure 12a) we also highlight that a significant fault normal displacement (fault closure) is needed. Our model results (see Figure 12b) tell us that for the optimum simulation with a horizontal stress ratio of 0.7 ± 0.5 , the ratio of the maximum interpenetration displacement (normal to the fault plane) over the maximum shear displacement (along the strike of the fault) is $nd/sd=1.93$. This means that for a 1 meter strike slip value, an unrealistic 1.93 meter normal displacement (closing gap or lost of material through pore reduction or dissolution) is necessary along all the fault planes except at the contact points where normal displacement has been constrained to be zero.

An alternative explanation for joint trajectory convergences and presented in this contribution is the presence of high fluid pressure circulating within the fault zone. In such model, normal displacement along the fault is only allowed locally where fluid pressure increase is suspected. Our numerical model results show that the joint trajectory convergence can be reproduced (see Figure 12c) using a local fluid pressure equals to the maximum horizontal stress whatever the horizontal stress ratio used. Such model also tells us that the ratio of the maximum opening displacement (normal to the fault plane) over the maximum shear displacement (along the strike of the fault) is $nd/sd=0.3$. This means that for a 1 meter strike slip value, a more realistic 0.3 meter, but still high, normal displacement (fault opening) is necessary at convergence points. However, we do not have independent field evidences that localized high fluid pressure occurred at these particular locations even though it seems systematic that the convergence points are located near or at fault intersections where fluid circulation, hence fluid pressure, is suspected to be more important than in other places along the fault planes.

6.3. *The Matelles example*

As opposed to Nash Point, the Matelles case study is a nice example of fractures (i.e. veins and stylolites) that are genetically linked to the faulting. The fracture density is heterogeneous and always located near

fault extremities or at contractional or extensional relays, suggesting that their development was controlled by the faulting. Even though the Matelles faults are sub-vertical, the model is less under-constrained than the Nash Point model because we have combined two types of fractures (i.e. extension and compression fractures). The optimum paleo tectonic stress found is strike-slip stress regime also oriented N163° (orientation of σ_H), which is in agreement with previous field observations (Petit and Mattauer, 1995). This far field stress orientation imposed to the interpreted 3D sliding fault model creates a heterogeneous perturbed stress field that matches most of the observed fractures trajectories and locations observed at the Matelles outcrop.

We have shown that adding sliding friction along the faults could produce a stress pattern that would better match the observed fractures. However, the optimum friction coefficients are much lower than the commonly used values of friction (Byerlee, 1978) but in agreement with Soliva et al. (2010) who also found that, at the Matelles exposure, friction along reactivated joints must have been very low. This also corroborates the fact that reactivated joints must have been weak at the Matelles exposure perhaps because of the presence of circulating pressurized fluids during faulting as proposed by Petit et al. (1999).

6.4. *The Oseberg Sør example*

The Oseberg field case study was meant to illustrate how such paleostress inversion technique could be applied to subsurface data coming from the oil and gas industry. Since the field has been studied in the past (Maerten et al., 2006) to model natural fractures, our goal here was not to redo the entire fracture modeling workflow but rather to evaluate how the proposed paleostress inversion technique would behave with limited but spatially distributed shear fractures.

Here we show that, using inclined fault geometry, the model is not under-constrained albeit the number of fracture data used to constrain the inversion is very low (23 data points). The optimum paleo tectonic stress found is a normal stress regime with a stress ratio $\bar{R}=0.51$ and a maximal horizontal stress (σ_H)

oriented N167°. This is equivalent to an extension direction oriented N77° as found by Maerten et al. (2002), with an extension direction oriented N80°, using a similar numerical simulation but with an imposed 3D far field strain. This far field stress orientation imposed to the interpreted 3D sliding fault model creates a heterogeneous perturbed stress field that matches most of the observed shear fractures characteristics interpreted in the Oseberg field.

6.5. *Further applications*

Paleostress information derived from the proposed technique is not exclusively used for constraining the far field tectonic stress used in the BEM. It could for instance be used to constrain the boundary conditions of any numerical program based on Finite Element Method (FEM) that would more easily integrate the effect of plasticity or any other rock behaviors.

As we have seen earlier in the method section, we must preserve the model structural integrity and complexity. Therefore, a realistic 3D geological model has to be built. This also applies to paleo geometry of the subsurface and, when it is necessary, a thorough and well constrained 3D restoration of the geological structure has to be achieved in order to have a good estimate of the structure geometry through geological time. The proposed paleostress inversion technique could then be applied to the restored fault and fracture model.

The method is not entirely bound to using fracture data such as tension, compression and shear fractures. The paleostress inversion can be constrained by any data that would record the deformation and/or the stress state around active faults. Therefore, we could define cost functions for a large variety of dataset used to constrain the inversion such as in-situ stress (breakout, Leak Off Test, induced fractures, well bore ovalization), fault throw, slickenline, GPS, InSAR, tiltmeter, focal mechanism, calcite twins, micro-seismicity and deformed horizons. These data, if appropriate, could of course be combined during the inversion.

Finally, this technology also applies to model present day 3D heterogeneous stress field caused by many other type of objects (discontinuities) that would perturbed the stresses such as salt, décollement layers, cavities and well bore. Knowing the present day in-situ stress distribution in the subsurface is a key parameter for optimum well planning, stability and integrity.

Acknowledgments

We would like to thanks Alvaro Gonzalez, Patxi Lahetjuzan, Emmanuel Malvesin and Fabrice Levassor for their support during this work. We thank the reviewers for their diligent review of the manuscript. Simmons Aerofilms are thanked for producing aerial survey of the Nash Point area as well as the Fault Analysis Group for letting us exploit the air photos. Finally, Jean-Pierre Petit is thanks for providing us with his detailed fracture maps of the Matelles outcrop and Roger Soliva for guidance in the field. This study is part of M. Lejri's PhD thesis, granted by both the French Ministry of Research and Schlumberger.

References

- Anderson, E.M., 1951. *The Dynamics of Faulting and Dyke Formation with Applications to Britain*, 2nd Edition. Oliver and Boyd, Edinburgh.
- Auzias, V., 1995. *Contribution à la caractérisation tectonique des réservoirs fracturés*. PhD thesis, Université Montpellier II.
- Bourne, S. J., Rijkels, L., Stephenson, B. J., Willemse, E. J. M., 2000, Predictive modeling of naturally fractured reservoirs using geomechanics and flow simulation: *GeoArabia*, v. 6, p. 27-42.
- Bourne, S. J., and E. J. M. Willemse, 2001, Elastic stress control on the pattern of tensile fracturing around a small fault network at Nash Point, UK: *Journal of Structural Geology*, v. 23, p. 1753-1770.
- Brillouin, L., 1946, *Wave propagation in Periodic Structures: Electric Filters and Crystal Lattices*, McGraw-Hill, New York, 255 p.
- Byerlee, J.D., 1978. Friction of rocks. *Pure and Applied Geophysics* 116, 615–626.
- Childs, C., J. J. Walsh, and J. Watterson, 1990, A method for estimation of the density of fault displacements below the limits of seismic resolution in reservoir formations, in G. Trotman, eds., *North Sea oil and gas reservoirs: The Norwegian Institute of Technology, Liverpool*, v. 2.
- Clark, S. P. Jr., ed., 1966, *Handbook of physical constants (revised edition)*, Geological Society of America Memoirs, v. 97, 587 p.
- Damsleth, E., V. Sangolt, and G. Aamodt, 1998, Subseismic faults can seriously affect fluid flow - a stochastic modelling case study: *SPE 49024*, p. 1-11.
- Dee, S.J., Yielding, G., Freeman, B., Healy, D., Kuszniir, N.J., Grant, N., Andellis, P., 2007, Elastic dislocation modelling for prediction of small-scale fault and fracture network characteristics, in Lonergan, L., Jolly, R. H., Rawnsley, K., and Sanderson, D.J. eds., *Fractured Reservoirs: Geological Society of London, Special Publication 270*, p. 139–155.

- de Jossineau, G., Petit, J.-P., Gauthier, B. D. M., 2003, Photoelastic and numerical investigation of stress distributions around fault models under biaxial compressive loading conditions, *tectonophysics*, v. 363, p. 19-43.
- Fischer, M. P., and M. S. Wilkerson, 2000, Predicting the orientation of joints from fold shape: Results of pseudo-three-dimensional modeling and curvature analysis: *Geology*, v. 28, p. 15-18.
- Fletcher, R. C. and Pollard, D. D., 1981, Anticrack model for pressure solution surfaces. *Geology*, v. 9, p. 419-424.
- Gauthier, B. D. M., and S. D. Lake, 1993, Probabilistic modeling of faults below the limit of seismic resolution in Pelican Field, North Sea, offshore United Kingdom: *AAPG Bulletin*, v. 77, p. 761-776.
- Gibbs, A. D., F. Jaffri, and T. Murray, 1997, New techniques for fracture distribution and prediction from kinematic modelling of 3D strain fields: *American Association of Petroleum Geologists Annual Convention Abstracts*, p. 40.
- Gillespie, P., Monsen, E., Maerten, L., Hunt, D., Thurmond, J., and Tuck, D., 2011, Fractures in carbonates: From digital outcrops to mechanical models, *Society for Sedimentary Geology*, v. 10, p. 137-147.
- Granier, T., 1985, Origin, damping and pattern of development of faults in granite, *Tectonics*, v. 4, p. 721-737.
- Hennings, P. H., J. E. Olson, and L. B. Thompson, 2000, Combining outcrop data and threedimensional structural models to characterize fractured reservoirs: an example from Wyoming: *American Association of Petroleum Geologists Bulletin*, v. 84, p. 830-849.
- Hudson, J.A., 1981, Wave speeds and attenuation of elastic material containing cracks: *Geophysics journal of the Royal Astronomical Society* 64, 133-150.
- Hyett, A.J., Hudson, J.A., 1990. A photoelastic investigation of the stress state close to rock joints. In: Barton, N.R., Stephansson, O. (Eds.), *Rocks joints*. Balkema, Rotterdam, pp. 227 – 233.

- Jamison, W. R., 1997, Quantitative evaluation of fractures on Monkshood anticline, a detachment fold in the foothills of Western Canada: *American Association of Petroleum Geologists Bulletin*, v. 81, p. 1110-1132.
- Kloppenburg, A., J. C. Alzate, and G. R. Charry, 2003, Building a discrete fracture network based on the deformation history: A case study from the Guaduas Field, Colombia: Extended abstract for the VIII Simposio Bolivariano, Cartagena, Colombia.
- Lejri, M., Maerten, F., Maerten, L., Soliva, R., 2015, Paleostress inversion: A multi-parametric geomechanical evaluation of the Wallace-Bott assumptions, Accepted to *Tectonophysics*.
- Lisle, R., 1994, Detection of zones of abnormal strains in structures using Gaussian curvature analysis; *AAPG bulletin*, v. 78 (12), p. 1811-1819.
- Lisle, R.J., Orife, T.O., Arlegui, L., Liesa, C., Srivastava, D.C., 2006. Favoured states of palaeostress in the earth's crust: evidence from fault-slip data. *J. Struct. Geol.* 28 (6), 1051–1066.
- Lovely, P., Flodin, E., Guzofski, C., Maerten, F., and Pollard, D. D., 2012, Pitfalls among the promises of mechanics-based restoration: Addressing implications of unphysical boundary conditions: *Journal of Structural Geology*, v. 41, p. 47-63.
- Maerten, L., 1999, Mechanical interaction of intersecting normal faults: theory, field examples and applications: Ph.D. thesis, Stanford University, Stanford, California, U.S.A., p. 167.
- Maerten, L., Pollard, D. D., Gillespie, P., 2002, Effects of local stress perturbation on secondary fault development: *Journal of Structural Geology*, v. 24, p. 145-153.
- Maerten, L., Maerten, F., 2006, Chronologique modeling of faulted and fractured reservoirs using geomechanically based restoration: Technique and industry applications: *American Association of Petroleum Geologist Bulletin*, v. 90, p. 1201-1226.
- Maerten, L., Gillespie, P., Daniel, J.-M., 2006, 3-D geomechanical modeling for constraint of subseismic fault simulation: *American Association of Petroleum Geologists*, v. 90, p. 1337-1358.

- Maerten, F., Maerten, L., Cooke, M. L., 2010, Solving 3D boundary element problems using constrained iterative approach: *Computational Geosciences*, v. 14, p. 551-564.
- Maerten, F., 2010, Adaptive cross-approximation applied to the solution of system of equations and post-processing for 3D elastostatic problems using the boundary element method: *Engineering Analysis with Boundary Elements*, v. 34, p. 483-491.
- Maerten, F., and L. Maerten, 2011, Stress and fracture modeling using the principle of superposition, *Slb Patent declaration and assignment for docket no. 94.0276*.
- Maerten, F., Maerten, L., and Pollard, D. D., 2014, iBem3D, a three-dimensional iterative boundary element method using angular dislocations for modeling geologic structures: *Computers and Geosciences*, v. 72, p. 1-17.
- Maerten F., Madden, B., Pollard, D. D., Maerten, L., 2015, Accounting for fault mechanics in the inversion of geophysical data for the tectonic driving stress: Application to the 1992 Landers, California earthquake, Submitted to JGR.
- Munthe, K.L., H. Omre, L. Holden, E. Damsleth, K. Heffer, T. S. Olsen, and J. Watterson, 1993, Subseismic faults in reservoir description and simulation: *SPE 26500*, p. 843-850.
- Murray, G. H., 1968, Quantitative fracture study-Sanish Pool, McKenzie County, North Dakota: *American Association of Petroleum Geologists Bulletin*, v. 52, p. 57-65.
- Neves, F.A., Zahrani, M.S., Bremkamp, S.W., 2004, Detection of potential fractures and small faults using seismic attributes: *The Leading Edge*, Society of Exploration Geophysicists, September, p. 903-906.
- Peacock, D. C. P. and Sanderson, D. J., 1992, Effect of layering and anisotropy on fault geometry. *J.Geol. Soc. Lond.*, v. 149, p. 793-802.
- Pedersen, S. I., T. Skov, T. Randen and L., Sonneland, 2005, Automatic Fault Extraction Using Artificial Ants, in Armin Iske and Trygve Randen (eds.), *Mathematical Methods and Modelling in Hydrocarbon Exploration and Production*, Springer Verlag, Berlin/Heidelberg, DE, pp. 107-116.

- Petit, J.-P., Mattauer, M., 1995. Palaeostress superimposition deduced from mesoscale structures in limestone: the Matelles exposure, Languedoc, France. *Journal of Structural Geology* 17, 245–256.
- Petit, J.P., Wibberley, C.A. J., Ruiz, G., 1999. 'Crack-seal, slip': a new fault valve mechanism? *Journal of Structural Geology* 21, 1199–1207.
- Petit, J.-P., Auzias, V., Rawnsley, K.D., and Rives, T., 2000, Development of joint sets in association with faults, in Lehner F.K. and Urai, J.L. eds., *Aspects of Tectonic Faulting – in honour of Georg. Mandl*: Springer, Berlin, p. 167–183.
- Pollard, D. D. and Segall, P, 1987, Theoretical displacements and stress near fractures in rocks: with applications to faults, joints, veins, dikes, and solution surfaces. In: *Fracture Mechanics of Rock* (edited by Atkinson B. K.). Academic Press, London, 277-349.
- Rawnsley, K. D., Rives, T., Petit J.-P., Hencher, S. R., and Lumsden, A. C., 1992, Joint development in perturbed stress fields near faults, *Journal of Structural Geology*, v. 14, p. 939-951.
- Rawnsley, K., Auzias, V., Petit, J.P., Rives, T., 1997. Extrapolating fracture orientations from horizontal wells using stress trajectory models. *Petroleum Geoscience* 3, 145 – 152.
- Rawnsley, K. D., Peacock, D. C. P., Rives, T., and Petit J.-P., 1998, Joints in the Mesozoic sediments around the Bristol Channel Basin: *Journal of Structural Geology*, v. 20, p. 1641-1661.
- Rispoli, R., 1981, Stress fields about strike-slip faults inferred from stylolites and tension gashes: *Tectonophysics*, 75, p.29-36.
- Sassi, W., S. E. Livera, and B. P. R. Caline, 1992, Reservoir compartmentalization by faults in Cormorant Block IV, U.K, in R. M. Larsen, N.P.S., eds., *Structural and tectonic modeling and its application to petroleum geology*, v. 1, p. 147-156.
- Sanders, C., M. Bonora, E. Kozlowski, and C. Sylwan, 2002, From 2D to 4D fracture network model, structural modeling of a complex thrust trap: A case study from the Tarija Basin, Argentina: SPE, ISRM78184, p. 1-8.

- Sanders, C., M. Bonora, D. Richards, E. Kozlowski, C. Sylwan, and M. Cohen, 2004, Kinematic structural restorations and discrete fracture modeling of a thrust trap: a case study from the Tarija Basin, Argentina: *Marine and Petroleum Geology*, v. 21, p. 845-855.
- Schlische, R. W., S. S. Young, R. V. Ackermann, and A. Gupta, 1996, Geometry and scaling relations of a population of very small rift-related normal faults: *Geology*, v. 24, p. 683-686.
- Schoenberg, M., and Sayers, C.M., 1995, Seismic anisotropy of fractured rock: *Geophysics*, 60, pp. 204-211.
- Schultz-Ela, D. D., and J. Yeh, 1992, Predicting fracture permeability from bed curvature: 33rd U.S. symposium on rock mechanics, p. 579-589.
- Soliva, R., Maerten, F., Petit, J.-P., and Auzias, V., 2010, Field evidences for the role of static friction on fracture orientation in extensional relays along strike slip faults: Comparison with photoelasticity and 3-D numerical modeling, *Journal of Structural Geology*, v. 32, p. 1721–1731.
- Taha, M., 1986, Apport de la microtectonique cassante au problème des trajectoires de contraintes et de leurs perturbations. Exemples du Nord de Montpellier, thèse d'Etat, Université de Montpellier, pp. 155.
- Thomas, A., J.-L. Mallet, and F. De Beaucourt, 1974, Une Methode analytique de localisation des accidents structuraux dans un massif rocheux: *Proceedings of the Congress of the International Society for Rock Mechanics*, p. 625-630.
- Thomas, A. L., 1993, Poly3D, a three-dimensional, polygonal-element, displacement discontinuity boundary element computer program with applications to fractures, faults, and cavities in the Earth's crust: M.S. dissertation, Stanford University, Stanford, California, 71p.
- Walsh, J. J., and J. Watterson, 1991, Geometric and kinematic coherence and scale effects in normal fault systems, in A. M. Roberts, G. Yielding and B. Freeman, eds., *The geometry of normal faults: Special Publication of the Geological Society, London*, v. 56, p. 193-203.
- Watkinson, A. J. and Ward, E., M., G., 2006, Reactivation of pressure-solution seams by a strike-slip fault-sequential, dilational jog formation and fluid flow, *AAPG Bulletin*, v. 90, p. 1187-1200.

Yielding, G., J. J. Walsh, and J. Watterson, 1992, The prediction of small-scale faulting in reservoirs: First Break, v. 10, p. 449-460.

Annex 1:

For a *vertical* frictionless 3D fault constrained by an Andersonian state of stress and for which the normal displacement to the fault plane is not allowed, it can be easily shown that the induced stress trajectories around such slipping fault are independent of the horizontal stress ratio and are similar to the same model subjected to uniaxial compressive horizontal stress.

If the vertical planar fault is defined by its normal $\vec{n}(x, y, 0)$ with $x^2 + y^2 = 1$, then, for a given applied far

$$\text{field stress } \sigma = \begin{bmatrix} \sigma_h & & \\ & \sigma_H & \\ & & \sigma_v \end{bmatrix}, \text{ the resolved traction on the fault plane is } \vec{t} = \sigma \cdot \vec{n} = \begin{Bmatrix} x\sigma_h \\ y\sigma_H \\ 0 \end{Bmatrix}.$$

The shear traction is given by

$$\vec{t}_s = \vec{t} - \vec{t}_n = \begin{Bmatrix} x\sigma_h - x(x^2\sigma_h + y^2\sigma_H) \\ y\sigma_H - y(x^2\sigma_h + y^2\sigma_H) \\ 0 \end{Bmatrix} = \begin{Bmatrix} -xy^2(\sigma_H - \sigma_h) \\ yx^2(\sigma_H - \sigma_h) \\ 0 \end{Bmatrix} = (\sigma_H - \sigma_h) \begin{Bmatrix} -xy^2 \\ yx^2 \\ 0 \end{Bmatrix}.$$

Consequently, the components of the resolved shear traction vector are proportional to $(\sigma_H - \sigma_h)$. When changing the magnitude of the horizontal principal stresses, the resolved shear traction is uniformly scaled but the direction and sense do not change. As a consequence, in a homogeneous and isotropic elastic medium, the resulting slip vector on the fault plane will be scaled accordingly and the perturbed stress around the slipping fault will be scaled as well. That is to say, the magnitudes of the displacement and stress field will be scaled uniformly, but the orientations will be the same.

Annex 2:

Here we want to demonstrate that the joint trajectory convergence outcropping at Nash Point and displayed on Figure 7, can hardly be attributed to a constraining fault bend as described by some authors (Rawnsley et al., 1997; Rawnsley et al., 1998, Bourne and Willemse, 2001; Petit et al., 2000). Indeed, the field photograph (Figure 24b), which has been published by the same authors, presents a strong distortion that could have misleadingly lead to the interpretation of a fault bend. The published photograph (Petit et al., 2000) distortion, which is probably due to the obliquity of the view point when the picture was taken, have therefore been restored back to what should be its real geometry (Figure 24c) using true vertical air photo (Figure 24a) as a reference. After applying a perspective distortion correction to the original image, it becomes now apparent that the fault bend previously described is much less pronounced.

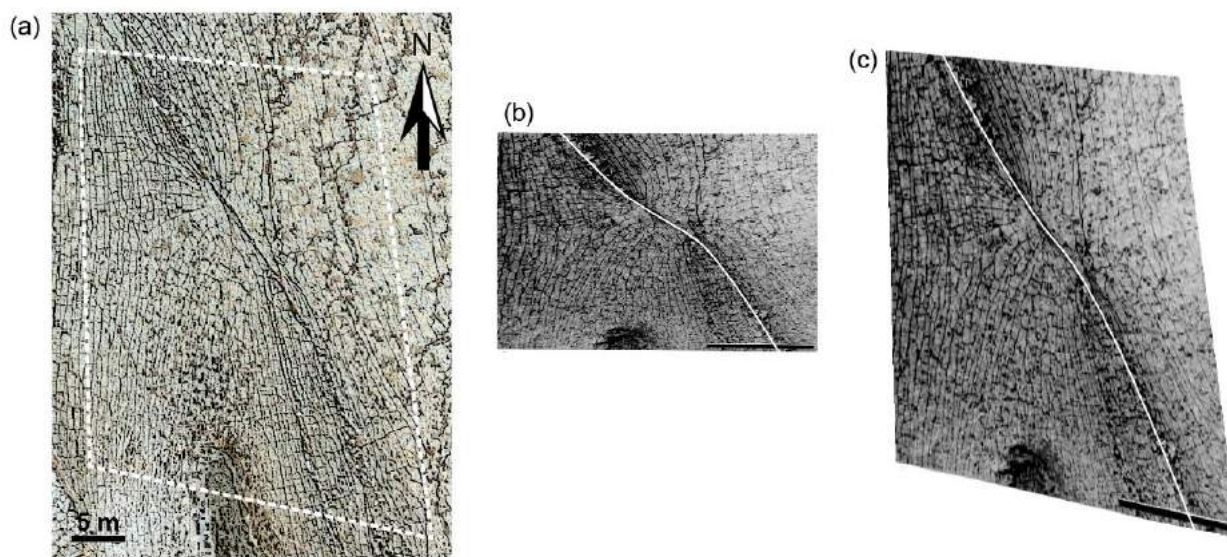


Figure 24: Correction of published outcrop photograph. (a) True vertical air photo. (b) Published distorted photograph from Petit et al. (2000). (c) Corrected photograph.

Table 1: Variable definitions.

Symbol	Comments
--------	----------

Fault properties

μ	Friction coefficient
P_f	Fluid pressure
δ	Angle between σ_1 and fault plane
\vec{n}	Fault plane normal

Rock properties

ν	Poisson's ratio
E	Young's modulus
ϕ	Friction angle

Stress

$\sigma_1 \geq \sigma_2 \geq \sigma_3$	Principal effective stress magnitudes (positive compression)
σ_v	Magnitude of the far field vertical stress
σ_H	Magnitude of the far field maximum horizontal stress
σ_h	Magnitude of the far field minimum horizontal stress
θ	Orientation of σ_H defined clockwise from the North
Hr	Horizontal stress ratio $Hr = \sigma_h / \sigma_H$
R	Stress ratio $R = (\sigma_2 - \sigma_3) / (\sigma_1 - \sigma_3)$
\bar{R}	Stress ratio defined by Maerten (2014) for Andersonian regimes

Acronyms

<i>BEM</i>	Boundary Element Method
<i>FEM</i>	Finite Element Method
<i>C</i>	Mean cost
<i>C_{tension}</i>	Cost for tension fracture
<i>C_{shear}</i>	Cost for shear fracture
<i>C_{stylolite}</i>	Cost for stylolites

Table 2:

	Fracture data	Fracture number	σ_H orientation (θ°) from mean joint strike	σ_H orientation (θ°) from inversion	Cost (\bar{C})
1	all joints	4516	163.1	162.7	0.0646
2	all joints cleaned	3812	163.6	162.9	0.0181
3	well1	7	184.7	174.2	0.0024
4	well2	13	173.7	163.6	0.0016
5	well3	12	182.3	173.2	0.0095
6	well1 + well2	20	177.5	164.3	0.0041
7	well3 + well2	25	177.8	165.0	0.0086
8	well1 + well2 + well3	32	179.3	165.5	0.0082

CHAPTER IV: Polyphasic geomechanical stress inversion using undefined fractures mechanical type

Mostfa Lejri^{1,2}, Frantz Maerten¹, Laurent Maerten¹, Jean-Pierre Joonnekindt¹

¹Schlumberger – MpTC, Parc Euromédecine, 340 rue Louis Pasteur, 34790 Grabels, France

²Géosciences Montpellier, Université Montpellier 2, Place E. Bataillon, 34095 Montpellier cedex 5, France

Key words: stress inversion, phase separation, fracture mechanical type inversion, geomechanics.

Abstract

Petroleum companies are greatly dependent on producing oil and gas from fractured reservoirs. Therefore, fracture modeling is becoming a significant challenge since fractures are known to significantly alter hydrocarbon flow. The stress condition at the time of formation of these fractures is a key element to understand their initiation and development. For several decades, paleostress inversion has been used to recover the regional stress field using slip along faults. However, in the oil and gas industry, slip along faults is rarely observed in wellbores, so we must rely on observed fracture characteristics to recover paleostress information. Performing stress inversion using fractures requires the knowledge of the mechanical type of each fracture. If the mechanical type is unknown, we need to find a way to recover it during paleostress inversion process. However, the problem becomes more complex if we take into account the inversion of multiple tectonic phases.

In this contribution we validate the paleostress inversion technique based on a boundary element method to recover multiple tectonic phases as well as the unknown fracture mechanical types. We show that if the fracture mechanical type is known, the proposed method allows to classifying fractures in their respective inverted tectonic phase. When the fracture mechanical type is unknown, the method inverts for both the tectonic phases and the fracture mechanical type, while classifying each fracture in its respective tectonic phase.

We successfully tested the method on both a synthetic model and the natural example taken from the Matelles outcrop, southern France.

1. Introduction

One of the main challenges of the oil industry is the exploitation of resource in structurally complex oil fields such as naturally fractured reservoirs. Fracture orientations are mechanically linked to the state of stress at the time of their formation. As structurally complex reservoir might have undergone multiple tectonic phases over time, each tectonic phase can be linked to a fracture set. It is therefore important to identify and separate paleo tectonic events in order to better predict fracture orientations.

For the last four decades, geologists have used stress inversion methods to recover the regional paleostress. All these stress inversion methods are based on the Wallace (1951) and Bott (1959) assumptions (WB), which stipulate that when faulting occurred, the shear stress resolved onto the fault plane is parallel to the slip vector and thus could be used to determine the stress tensor. In addition, these assumptions assume that faults are planar, that neither stress perturbations nor block rotations along fault surfaces occur and that the applied stress state is uniform.

The majority of these methods use fault slip (slickenlines) (e.g. Carey and Brunier, 1974; Angelier and Mechler, 1977; Angelier, 1979a, 1984; Etchecopar et al., 1981; Simon-Gomez, 1986; Lisle, 1987, 1988; Hardcastle and Hills, 1991) as input data to constrain the stress inversion, and assume, according to the WB hypothesis, that the faults slipped in a homogeneous stress field with no fault mechanical interaction.

Faults with heterogeneous orientations of slip (Hardcastle and Hills, 1991) are common in nature and is not compatible with a single tectonic event. Fault-slip data that can only be explained by more than one stress tensor have been commonly called “heterogeneous”. Traditional monopase techniques can easily lead to spurious solutions in the case of heterogeneous stress field. In most cases the inversion may yield to

a wrong stress tensor that is not compatible with any of the homogenous subsets, but is a compromise between many subsets (Carey, 1979; Delvaux and Sperner, 2003; Hardcastle, 1989; Nemcok and Lisle, 1995; Shan et al., 2003; Sperner and Zweigel, 2010).

The determination of multiple tectonic events

A numerical iterative method based on dynamic cluster analysis was developed by Diday (1971) in order to separate heterogeneous set of medical data into subsets. This method was used by Angelier and Manoussis (1980) to analyze the dynamics of faulting as it could separate fault slip data into subsets corresponding to different tectonic events. Since then, several methods have been developed for separating stresses from heterogeneous fault-slip data, (Angelier 1979a; Etchecopar et al. 1981; Armijo et al., 1982; Huang, 1989; Galindo-Zaldivar and Gonzalez-Lodeiro, 1988). A detailed analysis of most of these methods was presented by Angelier (1994). Recently, new methods, such as those based on cluster analysis (Nemcok and Lisle, 1995), the graphical procedure of Fry (1999), or the multiple inverse method (Yamaji, 2000), have been proposed for analyzing heterogeneous fault-slip data (Célérier, 2012).

Four methods have been investigated to deal with heterogeneous datasets (Célérier (2012) for a complete description): (1) Methods that clusterize slip data into datasets by analyzing the compatibility of the slip data before inversion, (2) methods that search for stress tensors that explain part of the dataset solely, (3) methods that use an altered misfit function so that it integrates the data clustering during the minimization process, (4) and methods that compute the stress tensor for each fault slip data and try to minimize the resulting variety of stress tensor variation.

The first category includes clustering of data that yield similar misfits with various trial stress tensors using the right-dihedral (Carey and Vergely, 1992; Mercier and Carey-Gailhardis, 1989; Nemcok et al., 1999). Another intuitive way to separate heterogeneous data into subsets is to represent the slip data in two dimensional graphical analyses. This representation requires that one of the principal stress directions is

assumed to be vertical (Anderson, 1951), simplifying the 4D problem into a 2D problem. Clustering can therefore be achieved using the γ -R method of Simón-Gómez (1986), the spherical plot version (Fry, 1992), or the superposition of a modified Breddin's graph to a rake versus strike plot of the data (Célérier and Séranne, 2001).

In the second category, one of the earliest and simplest approach is to compute the misfit function solely for the subsets of size N with the smallest misfits, with N usually chosen as a percentage of the data (Etchecopar, 1984; Etchecopar et al., 1981). A more recent approach is to clusterize the data into subsets of size N and systematically run stress inversion (Yamaji, 2000). A third approach is to look at the stress tensors that minimize the misfit below a chosen threshold for N data (Etchecopar, 1984; Etchecopar and Mattauer, 1988; Hardcastle, 1989; Hardcastle and Hills, 1991; Vasseur et al., 1983; Yamaji, 2003).

In the third category, a misfit function that reduces the influence of outliers is used (Gephart and Forsyth, 1984; Etchecopar and Mattauer, 1988; Gephart, 1990a,b; Yamaji, 2000; Angelier, 2002a,b; Will and Powell, 1991; Delvaux and Sperner, 2003; Yamaji, 2003; Burg et al., 2005). A similar, yet radical approach to reduce the influence of a large subset of outliers that are related to secondary phases, is to modulate the misfit criteria by a function that cuts it when it becomes large (Angelier, 1979, 1984, 1991a; Angelier and Manoussis, 1980; Yamaji, 2003), a triangular function (Yamaji et al., 2006), a Gaussian Function (Zalohar and Vrabec, 2007), or in the hard division scheme of Shan et al. (2003, 2004).

The fourth category is similar to the γ -R method (Simón Gómez, 1986). It consists on exploring stress tensor orientations for each slip data and to compute the stress ratio R so that it matches the observed slip directions. Therefore, the solution tensors are those with the least variation on a subset of the data (Armijo and Cisternas, 1978; Armijo et al., 1982; Galindo-Zaldívar and González-Lodeiro, 1988; Phan-Trong, 1993).

Liesa and Lisle (2004) and Lisle and Vandycke (1996) compared multiple polyphase methods (Angelier and Goguel, 1979; Sperner et al., 1993; Etchecopar et al., 1981; Nemcok and Lisle, 1995; Yamaji, 2000) on

the polyphase Ogmore data set. They showed that these methods may lead to spurious solutions as well as artifact stress tensors. Following Angelier's (1984), Delvaux and Sperner's (2003), and Sperner and Zweigel's (2010) opinion, they suggest that the geologist expertise is critical and that relying on automatic polyphase methods only is likely to be unsuccessful.

Although several numerical methods have been used for clustering fractures orientations (Shanley and Mahtab, 1976; Pecher, 1989; Hammah and Curran, 1998; Peel et al., 2001) and paleostress for dikes and veins using a Bingham distribution (Yamaji and Sato., 2011) or calcite twins using the right-dihedra clustering method (Nemcok and Lisle., 1995) they have not yet been used with heterogeneous data with multiple mechanical fracture types especially when the latter is undefined.

The oil industry problem: multiple phases and unknown fracture types.

Knowing the heterogeneous paleostress field is important to model and predict natural fractures. As slip along fault planes is rarely observed along wellbores, natural fractures (joints, faults, stylolites) are taken into account during the inversion of stresses (Maerten F., 2010).

It is admitted that natural fractures orientation is highly affected by the stress perturbation around complex fault systems (Martel and Boger, 1998; Kattenhorn et al., 2000; Bourne and Willemse, 2001; Soliva et al., 2010). In such conditions, using the simple Wallace (1951) and Bott (1959) assumptions is not recommended (Pollard et al., 1993; Kaven et al., 2011; Lejri et al., 2015) and, in some conditions, geomechanical models may yield better results (Kaven et al., 2011). In fact, numerical models based on continuum mechanics are becoming industry standard in providing efficient means for modeling natural fractures in reservoirs (see Chapter III). Over the past decade, pioneer studies (Maerten, 1999; Bourne et al.,

2000) have proven that adding a geomechanical rationale to stochastic techniques improves the prediction and leads to more realistic fractured reservoir models.

Furthermore, Maerten and Maerten, (2011) and Maerten et al., (2015) have developed a new generation of paleostress analysis using Boundary Element Method (BEM) technology which allows to use any kind of deformation data (slickenlines, joints and veins, conjugate fractures, deformation bands and faults, stylolites and compaction bands, focal mechanisms, inSAR data, GPS data, fold hinges,...)

Two main problems remain challenging for stress inversion using fracture orientation: (i) detecting multiple tectonic phases and classify fractures in their respective event, and (ii) determine the fracture mechanical type when unknown.

Our approach

In this paper we present an innovative polyphase stress inversion method that uses fracture data, similar to the Nemcok and Lisle, (1995) and Nemcok et al. (1999) data clustering method on slip data and calcite twins data, at the exception that we rely on linear elasticity to analyze the compatibility of fracture mechanical type when unknown and clusterize them before running any stress inversion on each subset.

The method allows to separate fracture types during the inversion process which will help reservoir engineers not only to predict fractures distribution and orientation but also fractures permeability through the rock mass for reservoir fluid flow simulations.

For validation purpose, the method is tested against a synthetic model composed of joints, conjugate fractures and stylolites. It is then applied to the outcrop of The Matelles, near Montpellier, southern France.

2. Methods and synthetic models validation

Numerical methods

2.1.1. BEM

iBem3D (formerly called Poly3D), a boundary element method for elastic isotropic and heterogeneous half-space (Thomas, 1993; Maerten et al., 2014), is used. Thus, complex and realistic faults can easily be constructed as 3D discontinuities in a homogeneous elastic medium that does not need to be discretized (see General introduction section 5).

2.1.2. Paleostress using Fractures

Paleostress inversion using iBem3D uses the principle of superposition that applies to linear elasticity for heterogeneous, isotropic whole- or half-space media (Maerten, 2010b; Maerten et al., 2014). Given some measures of the fault throw, dip-slip, slickenline directions, stress measurements as well as fault geometry, GPS data, InSAR data, fractures (joints, veins, dikes, pressure solution seams with stylolites), micro-seismicity, breakout orientations or secondary fault plane orientations, we invert for the remote stress state for multiple tectonic events efficiently using a complete mechanical scenario.

Though the present methodology is not restricted to this case, here we assume one principal stress is vertical (Anderson, 1905).

2.1.3. Tectonic stress domain

The tectonic stress domain (Figure 3a), can be used to analyze stress inversion results. This domain is a 2D parameter space that covers the full Andersonian tectonic configurations. The x-axis represents the extended stress ratio \bar{R} (between 0 and 3) (see General introduction, section 5.2), whereas the y-axis is the azimuth (θ between 0° and 180°) of the maximum principal horizontal stress defined clockwise with respect

to the North. As an example, the tectonic stress domain in Figure 1 illustrates two results of stress inversion simulations A ($\theta = 90^\circ N, \bar{R} = 0.5$) and B ($\theta = 145^\circ N, \bar{R} = 1.5$).

Polyphase stress inversion and type separation

The method to invert for the unknown fracture mechanical type is based on the cluster analysis, a statistical technique for identifying groups of from within a sample. The analysis is performed in 5 or 6 steps depending on the knowledge of the fracture mechanical types along the well. These steps are described as follow, and where we assume for simplicity that initially, all the fractures have unknown mechanical type:

- 1- If fracture type is unknown, a random type is assigned according to a fixed proportion that is guessed by the user. (e.g., 33% Joints, 33% stylolites and 33% conjugate fractures). If the fracture data type is known, this first step can be skipped.
- 2- A random fracture (described in term of spatial coordinates, dip-azimuth, dip angle and type) is selected and a mechanical stress inversion is performed using only this fracture as a constraint.
- 3- The tectonic stress solution from the inversion is then applied in forward sense to the model and each predicted fracture orientation is compared to the observed fracture. This gives the cost of the remaining fractures: the lower the cost, the higher the similarity to the randomly selected fracture. A threshold value set by the user (generally 0.05) is used in order to classify similar fractures into a subset.
- 4- Steps 2-3 are repeated until all the data (or a large part of the data) is clusterized into subsets. Once a large part of the data size is clusterized, step 1 to step 4 are repeated until a sufficient number of subsets are available.
- 5- Subsets are analyzed separately using the mechanical stress inversion method. Each stress inversion solution is plotted in the tectonic stress domain as a dot with variable size. The dot size is proportional to a confidence criterion based on the fracture subset size and data type

diversity (see Section 2.3 for the description of the criterion). A big dot should correspond to a well identified tectonic phase.

- 6- Using this domain representation, two solutions for data type separation are possible:
 - a. If the plotted solutions are considered correct by the geologist (compared to literature results and field observations): each plotted tectonic phase solution is used in a forward simulation and the locally perturbed stress field is compared to all the fractures from the original data. A modified cost function is used for each fracture in order to determine its type. When the cost is lower than a threshold value set by the user (generally between 0 and 0.1) all the identified fractures are removed from the original data and are associated to the selected tectonic phase solution. The threshold value here is critical as a large value will include fractures for wrong phases, and small value will decrease the number of identified fractures for each tectonic phase.
 - b. Once all possible solutions are plotted with the corresponding confidence criterion, a tectonic stress solution (corresponding to a tectonic phase) is selected and is applied in a forward sense. A modified cost function is used on each fracture plane in order to determine its fracture type. When the cost is lower than a threshold value (generally between 0 and 0.1) all the identified fractures are removed from the original data and are associated to the selected tectonic phase solution. Steps 1 to 6 are repeated until a major part of the fracture data is associated to a tectonic phase.

An optional step can be applied if the recovered tectonic phases seem unrealistic. In such case, the full process should be repeated with a different proportion of fracture types at step 1.

Confidence criterion

It is common that when inverting for the tectonic stress using small subsets, these might give wrong results. This can be due to misinterpreted fracture type (step 1), and consequently, some subsets can

represent spurious stress regimes. In order to refine the polyphase solutions, a confidence criterion for each subset of fractures is defined:

$$C_1 = \sqrt{(found_j - n_j)^2 + (found_s - n_s)^2 + (found_c - n_c)^2} \quad (1)$$

where $found_j$, $found_s$ and $found_c$ are the number of fracture successfully clusterized of type joint, stylolite and conjugate, respectively. The corresponding number of joints, stylolites and conjugate faults are denoted n_j , n_s and n_c respectively.

If all joints, stylolites and conjugate fractures are explained, then $C_1 = 0$, which represents the ideal case.

Once all data are clusterised in subsets the second confidence criterion for a given subset is used and is defined as:

$$C_2 = H \left(\frac{n}{C_1 - \min(C_1) + 1} \right)^2 \quad (2)$$

where $\min(C_1)$ is the minimum value of C_1 for all the processed subsets and n is the total number of fractures in the original dataset (i.e., $n = n_j + n_s + n_c$). H is a parameter that depends on the number of fractures of each type. If the original dataset are chosen to contain all three types of fractures, then H is defined as:

$$H = nb_j \times nb_s \times nb_c \quad (3)$$

If, for a given fracture type, the number is zero, then it is not taken into account in (3).

Synthetic model for validation

2.1.4. Synthetic Fault Model and generated fractures

To validate the procedure, we use a synthetic model which consists of 5 intersecting active faults (Figure 1). The normal component of displacements on the fault plane are locked to prevent any opening or interpenetration of the fault walls, but they are free to slip.

In our mechanical models, a homogeneous and isotropic elastic whole space is used. Poisson's ratio and Young's modulus are 0.25 and 1GPa, respectively.

We impose three tectonic phases (see Table 1) and for each tectonic phase, we randomly generate 1/3 of joints, 1/3 of stylolites and 1/3 of conjugate fractures on the grid shown in figure 1 (black dots). The fracture orientation is provided by the computed principal directions of the local stress.

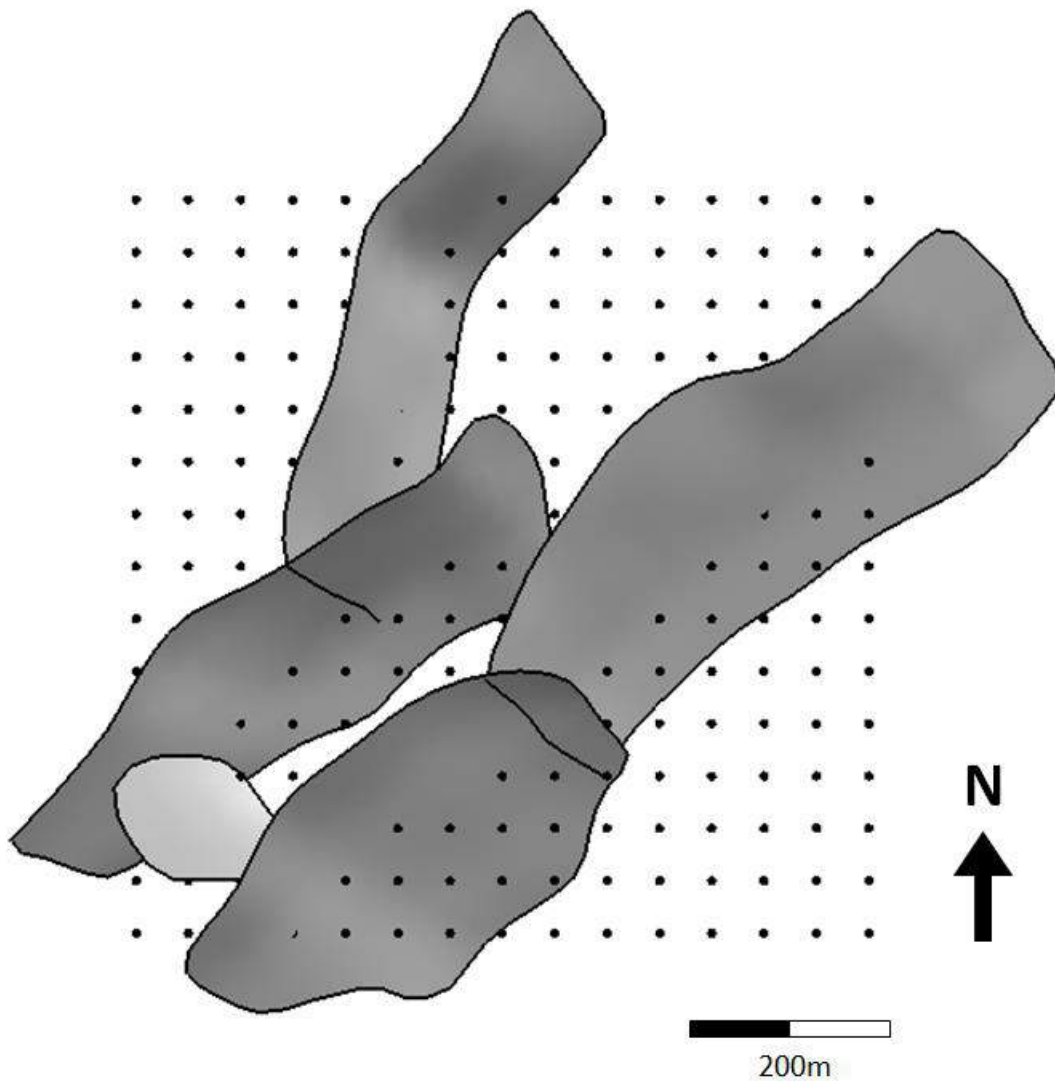


Figure 1. Fault model used for testing the polyphase stress inversion and type separation. The 3D fault geometry is represented in gray color). The grid is represented in black dots, contains 225 randomly generated fracture data with random type.

At the end of this process, we end up with a unique grid which includes the orientation of the randomly generated joints, stylolites and conjugate planes from 3 tectonic phases. The mechanical type of each fracture is then removed so that only spatial coordinates, strike and dip angles are available for each data point.

Our goal now is to invert for the parameters of the 3 tectonic phases (see table 1) to invert for the fracture type, and to classify each fracture in its respective tectonic phase.

Table 1: Definition of the 3 imposed Andersonian tectonic phases

Tectonic phase	R	θ
1	0.5	90
2	1.5	145
3	2.5	0

2.1.5. Data clustering and stress inversion validation

Figure 2a, displays the clusterization result using no confidence criterion. The points size is function of the number of data in each clusterized subset. This result shows that the imposed tectonic phases are hardly visible among all subsets.

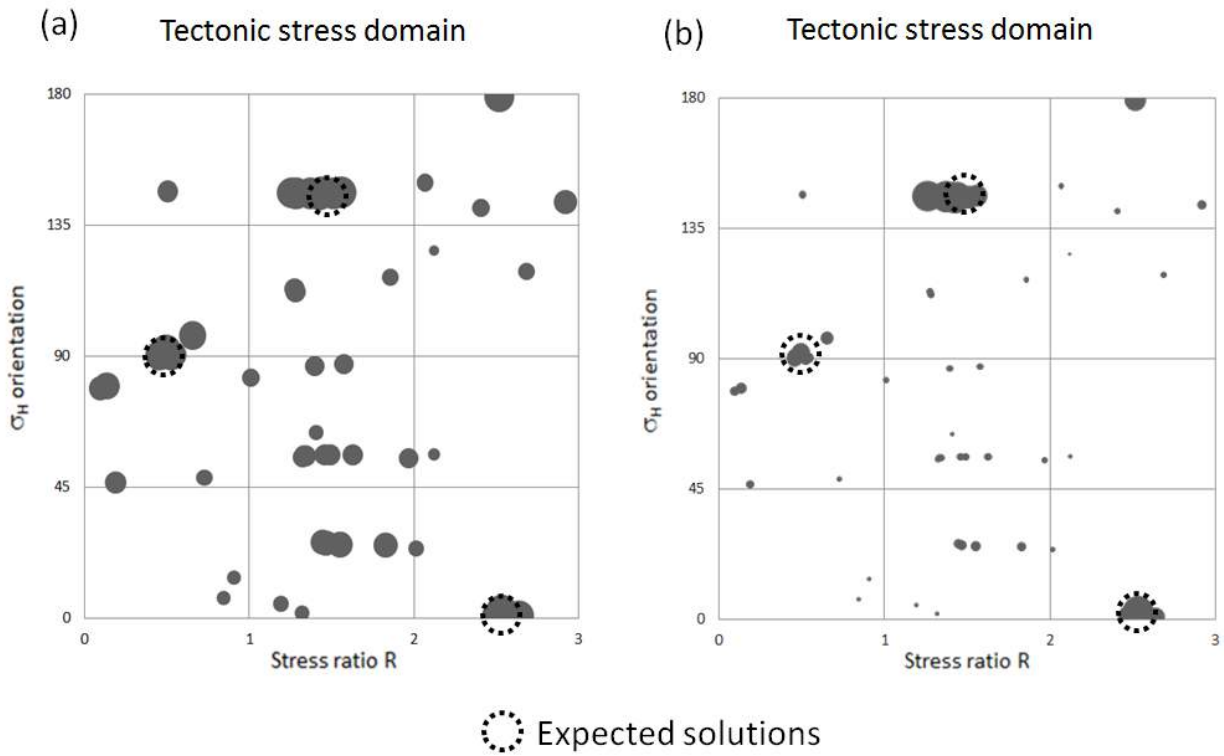


Figure 2. Clustering and inversion solutions for the synthetic model. The dashed circles are for the expected solutions (a) Without confidence criterion and (b) with confidence criterion C_2 where three main expected solutions are recovered.

figure 2b, displays the clusterization result using the C_2 criterion and where the three imposed tectonic stresses are clearly identified. These results (figure 2b) show the necessity to use the confidence criterion to recover the tectonic stresses.

2.1.6. Type separation validation

To test the mechanical type separation, the same model and parameters are used. For a better reading of the type separation results, only the tectonic phases 1 and 2 from table 1 are imposed (note that the algorithm is not restricted to three tectonic events).

To generate the synthetic fracture data, the first tectonic phase is imposed to the model. Using the stress field associated to this tectonic phase, fractures with random mechanical type are generated at each 'blue point of the grid (see Figure 4a).

Using the same procedure, the second phase is imposed to the model, and fractures are generated at 'red' points of the grid (see Figure 4a).

For the two tectonic phases, and in order to study the accuracy of both the polyphase stress inversion and the fracture type separation, a "random noise" is added for the strike and dip angles of the generated fractures. The following maximum "noise" values will be studied : 0°, 5° and 10° for the strike angle and 0°, 2.5° and 5° for the dip angle.

We run the polyphase stress inversion (steps 2 to 5) and the recovered tectonic phases are shown in figure 3 for different values of the "noise".

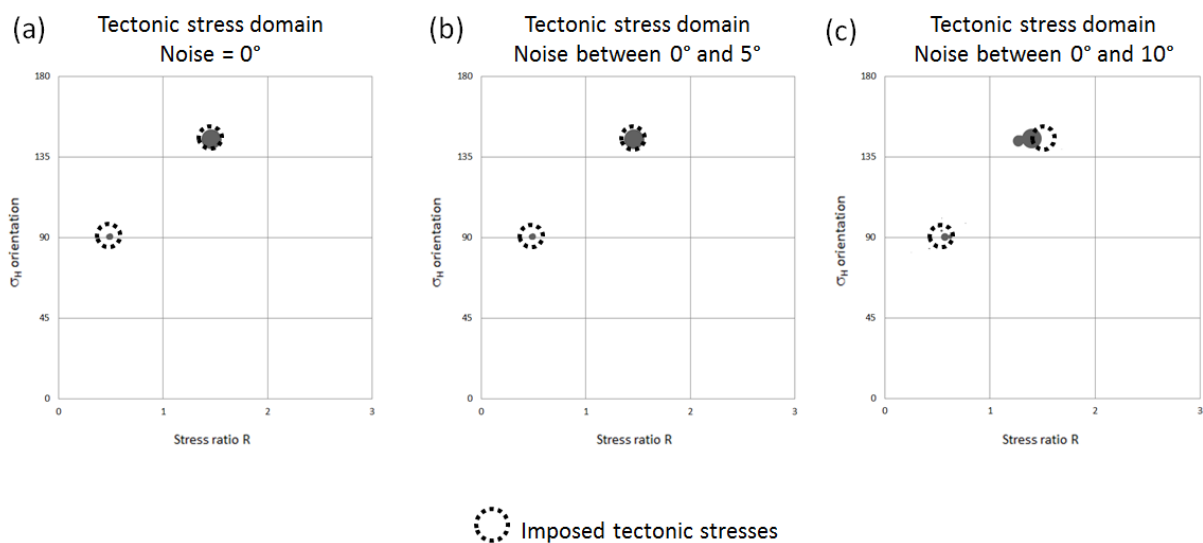


Figure 3. Clustering and stress inversion solutions using the confidence criterion C_2 two main solutions are recovered as well as one artifact solution. (a) is for 0° noise, (b) is for 5° noise and (c) is for 10° noise on the generated fracture data.

It is shown that the polyphase inversion gives the same results even if the generated synthetic fractures orientation is blurred. Then, each correct tectonic phase solution plotted in the tectonic stress domain (Figure 3) is thus applied in a forward sense in order to recover the fractures mechanical type (step 6.a of the algorithm). Using an appropriate cost function (see General introduction, section 5.2), we compute the affinity of a fracture plane to the 3 possible mechanical types. The lowest of these 3 costs yields the most plausible mechanical type of the fracture for a given tectonic phase. When the cost is lower than a threshold value (generally less than 0.1) the fracture is said to be associated to the tectonic phase solution. Figure 4b shows in green color the fractures successfully associated to the correct tectonic phase, in red color the fractures that have been associated to the wrong tectonic phase, and in white color for the fractures that could not be associated to any tectonic phase (meaning that these fractures were associated to a wrong stress field). To assess for the mechanical fracture type recovery accuracy, Figure 4a shows the imposed randomly generated joints (blue color), stylolites (red color) and conjugate fractures (green color) at each point of the grid. Each fracture is related to a unique tectonic phase (1 or 2). Figure 4d shows the recovered mechanical type. A comparison of Figures 4c and 4d shows that most of the fracture types have been recovered successfully. The white color is for fractures for which the type was not recovered.

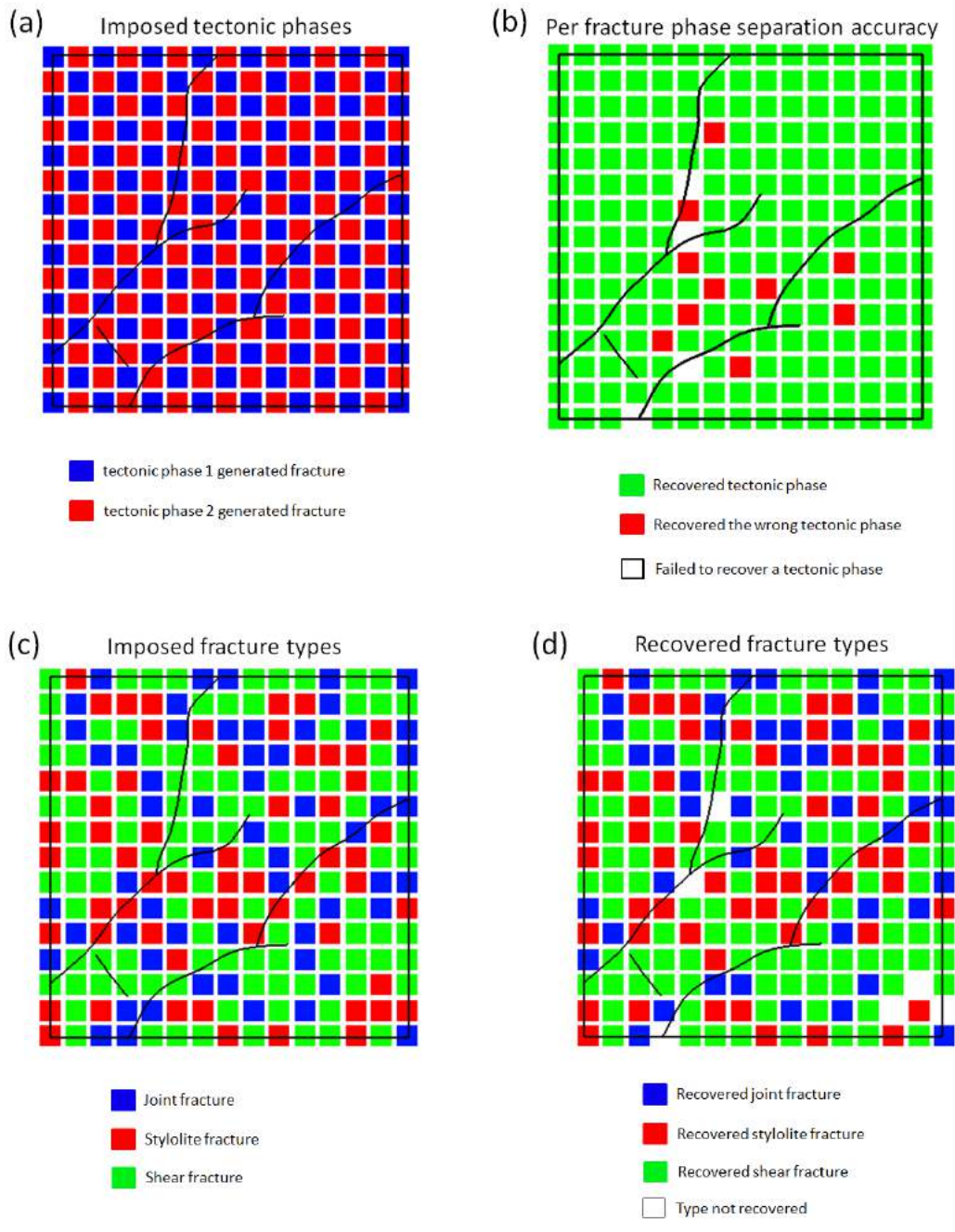


Figure 4. A synthetic examples of polyphase inversion and fracture type separation accuracy. Top view of the grid and representation of: (a) the imposed tectonic phases, (b) the successfully associated fractures to each retrieved tectonic phase. (c) the randomly generated fracture types on each point of the grid (d) the recovered fracture types.

The synthetic example (figure 4) shows that, during the fracture type separation process, 94% of the fractures have been successfully associated to the right tectonic phase, 4% to the wrong phase, and 2% have not been identified.

3. Case Study: La dalle des Matelles

The algorithm described in section 2.2. is now applied to “La dalle des Matelles”. This outcrop is located close to the village called Les Matelles, 15 km North of Montpellier, France (longitude 3°48’E, latitude 43°43’N) (Figure 5). A large number of features such as faults, stylolites, joints and veins filled with calcites exposed which make this outcrop well suited for the study of brittle tectonics in limestones around meso-scale faults (Rispoli, 1981; Petit & Mattauer, 1995; Soliva et al., 2010).

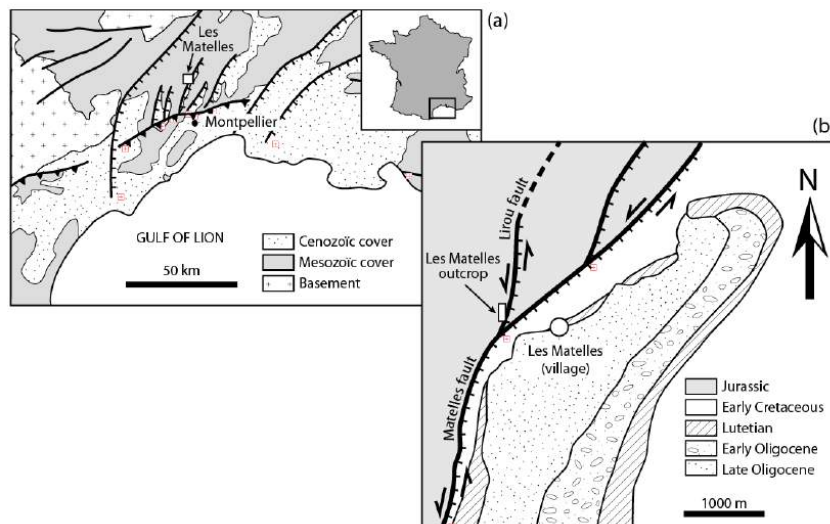


Figure 5. Location and geological context of the Matelles study area. (a) Regional structural scheme of the study area. (b) Structural sketch map showing the geological setting of the Matelles Fault and the Lirou fault branch (from the 1:50,000-scale geological maps of Montpellier and Saint Martin de Londres), with location of the presented outcrop.

Geological setting

Located along the Lirou fault, the outcrop consists of very gently tilted ($<10^\circ$) Jurassic micritic limestone layers. The Matelles fault is a NE-trending half-graben fault (see Figure 5) that has been affected by two successive tectonic events: (i) an Eocene NS-trending contraction related to the Pyrenean orogeny that triggered a left-lateral strike-slip movement and (ii), a late Oligocene-early Miocene SE-trending extension

related to the rifting of the Gulf of Lion continental passive margin that triggered a normal dip-slip movement. The observed sub-horizontal and steeply pitching slickenlines along the Lirou fault are directly related to these two successive contractional and extensional events (Petit and Mattauer, 1995).

Three types of brittle tectonic structures are observed on the outcrop: the long and straight faults, attributed to reactivated joints, the shorter and sinuous veins filled with calcite, and the stylolites. These structures have been described in previous studies (e.g. Rispoli, 1981; Taha, 1986; Petit and Mattauer, 1995; Petit et al., 1999; Watkinson and Ward, 2006; Soliva et al., 2010). Petit and Mattauer (1995) mapped these tectonic structures in detail and proposed a mechanical interpretation to explain the relationships. Here we base our analysis on their work in addition to our own field observations (chap 3).

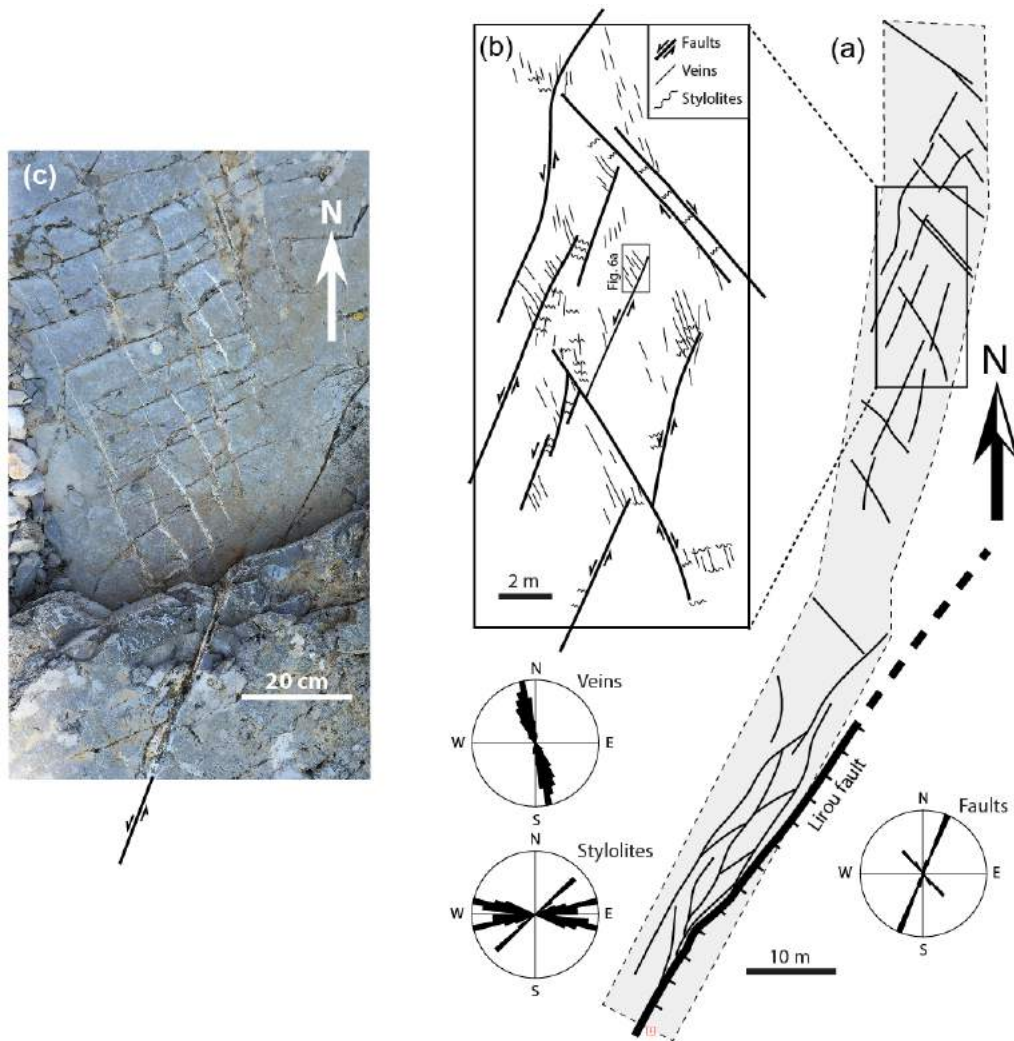


Figure 6. Interpreted fractures at the Matelles outcrop. (a) Map of the main fault pattern along the Lirou fault. (b) Detailed map of mesoscale structures used for the simulation (used for the model construction). (c) Photograph of a strike-slip fault termination showing tail cracks (veins). The maps are modified from Petit and Mattauer (1995).

Two conjugate fault sets are located at the Matelles outcrop, a $N20^{\circ} \pm 10^{\circ}$ trending left-lateral set and a $N140^{\circ} \pm 10^{\circ}$ trending right lateral set (see Figure 6ab). Petit and Mattauer (1995) suggested that and these two sets are former joint sets that have been reactivated during the Pyrenean orogeny compressive event.

The veins have a mean strike around $N170^{\circ} \pm 10^{\circ}$ with local variation and follow almost systematically (points A in Figure 6a) the wing crack or horse tail pattern around fault extremities (Pollard and Segall, 1987; Granier, 1985). Some veins are located between intersecting fault with an acute angle, where their general

orientation tendency is to converge towards the fault intersection points (point E in Figure 6a). The remaining veins are located at extensional jogs where they tend to be perpendicular to the overlapping fault traces (points C in Figure 6a). Since veins seem to be systematically located near the reactivated joints, and show a perturbed orientation, they have a clear genetic link with the faulting.

The outcrop also contains two different sets of stylolites. Throughout the entire outcrop, the first set is regularly oriented N55°-60°, and seems to have no clear genetic link with the faulting. Thus it is called 'background stylolites' set. A second N100° ±15° trending set of stylolites is observed locally especially near contractional jogs along the N20° faults (points B in Figure 6a), between acute angle intersecting faults (point E in Figure 6a) and occasionally near the tip of faults (point D in Figure 6a). Similarly, the nearly N50° trending dense stylolites observed between the two parallel N140° fault in the northern part of the outcrop could be partially linked to the stress reorientation triggered by the reactivation these N140° trending faults during the latest compressional event. All the stylolites located in the Matelles outcrop exposure have sub-perpendicular peaks to the stylolite surfaces. Fletcher and Pollard, (1981) interpreted these stylolites as anti-cracks or compression fractures perpendicular to the most compressive stress.

As suggested by Petit and Mattauer (1995), the brittle deformation can be decomposed into four stages. The first and second stages consist of two successive N20° and N140° trending jointing of the Jurassic limestone layers. The third stage is related to the generation of the N55°-60° trending 'background stylolite' (figure 6a). The fourth stage, is the reactivation of the N20° and N140° trending joints as both right-lateral and left-lateral strike slips faults due to the latest shortening event accompanied by the creation of wing cracks, en echelon veins and a second generation of stylolites which follows the perturbed stress field around the reactivated joints.

Model configuration

The detailed interpretation of the fault traces Figure 6a allows to build the 3D fault model (see Figure 7). Since the greatest vertical extent of observed faults in the outcrop reaches a maximum height of 3 m, the fault traces have been vertically extruded in order to have sub-vertical faults. Faults are set to freely slip but not to open or close.

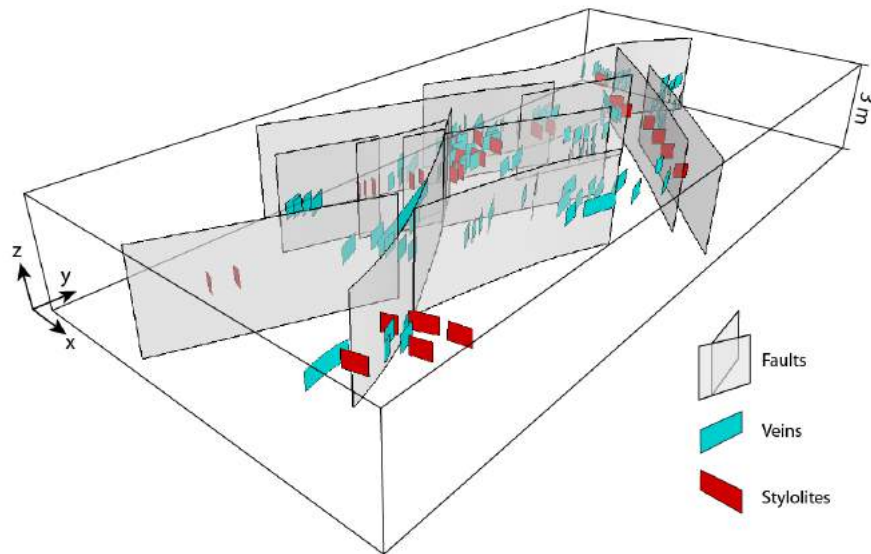


Figure 7. The Matelles model configuration. 3D model made of sub-vertical faults and interpreted veins and stylolites. Y-axis points to the North.

As for the synthetic models, a homogeneous and isotropic linear elastic whole space is used. We considered a value of 0.25 for Poisson's ratio (ν), 50 GPa for Young's Modulus (E), which are the mean values representative for the limestone (Clark, 1966).

Our goal is to test first the polyphase stress inversion. For this purpose, the polyphase inversion is set up to run using both the mapped vein and stylolite traces (see Figure 6). The algorithm allows to classifying each fracture into its respective recovered tectonic phase.

The second goal is to test the polyphase inversion using unknown mechanical type. For that purpose, all the mechanical types are removed. The algorithm allows to classifying each fracture into its respective recovered tectonic phase and to recover the fracture type.

The results are compared to the tectonic phases described by Petit and Mattauer (1995). Then, if necessary, these tectonic phases are used to recover for the fracture types. The recovered fracture types are then compared with the observed fracture types. The main goal here is to check if the polyphase inversion and the fracture type separation yield consistent solutions.

Model results

3.3.1. Known mechanical type

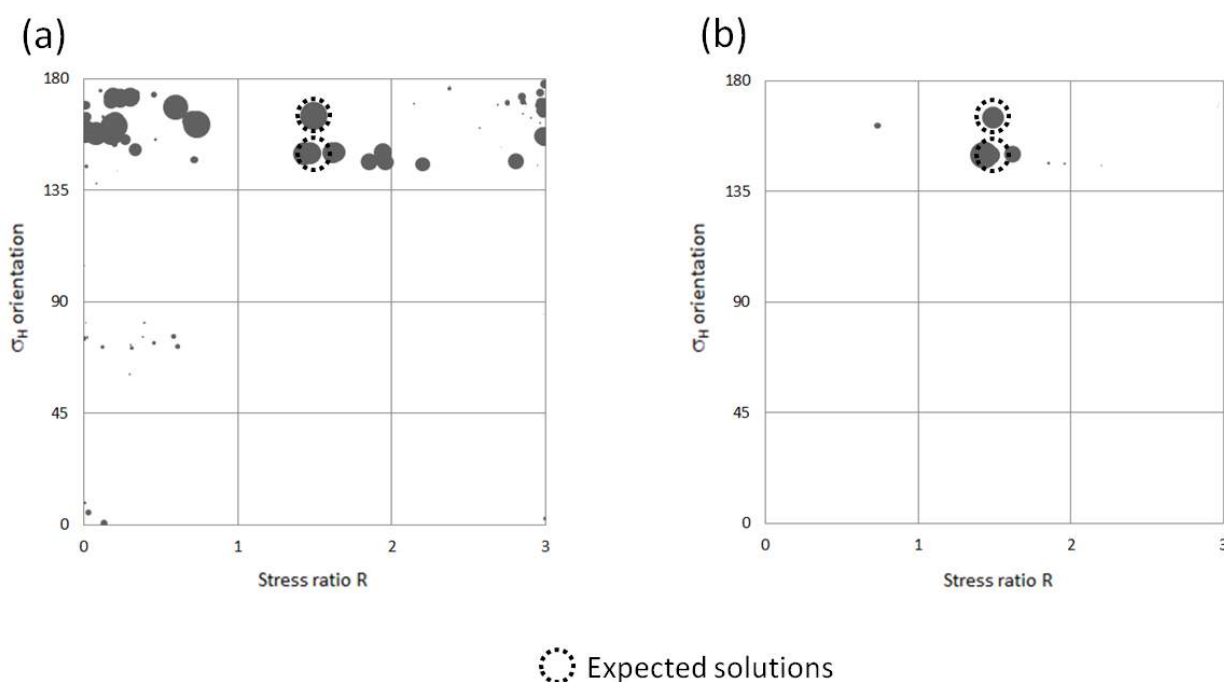


Figure 8. Polyphase stress inversion for les Matelles using known fracture type (a) with no confidence criterion and (b) using the confidence criterion C_2 . Using C_2 , the two best solutions are identifiable.

Using the fracture data with known mechanical type, the polyphase stress inversion, consisting of 150 x 50 000 geomechanical simulations, has been run in less than 84 minutes. Figure 8a shows the stress inversion

solutions for all the subsets with no confidence criterion. While most of the inverted tectonic stresses are oriented $N165^\circ$ and $N150^\circ$ there is an uncertainty along \bar{R} that covers both the normal, wrench and reverse fault regime (see Chapter III). Figure 8b shows the tectonic stress found using the C_2 criterion. Optimum solutions are found for $\theta = N165^\circ, \bar{R} = 1.49$ and $\theta = N150^\circ, \bar{R}$ between 1.42 and 1.63.

3.3.2. Unknown mechanical type

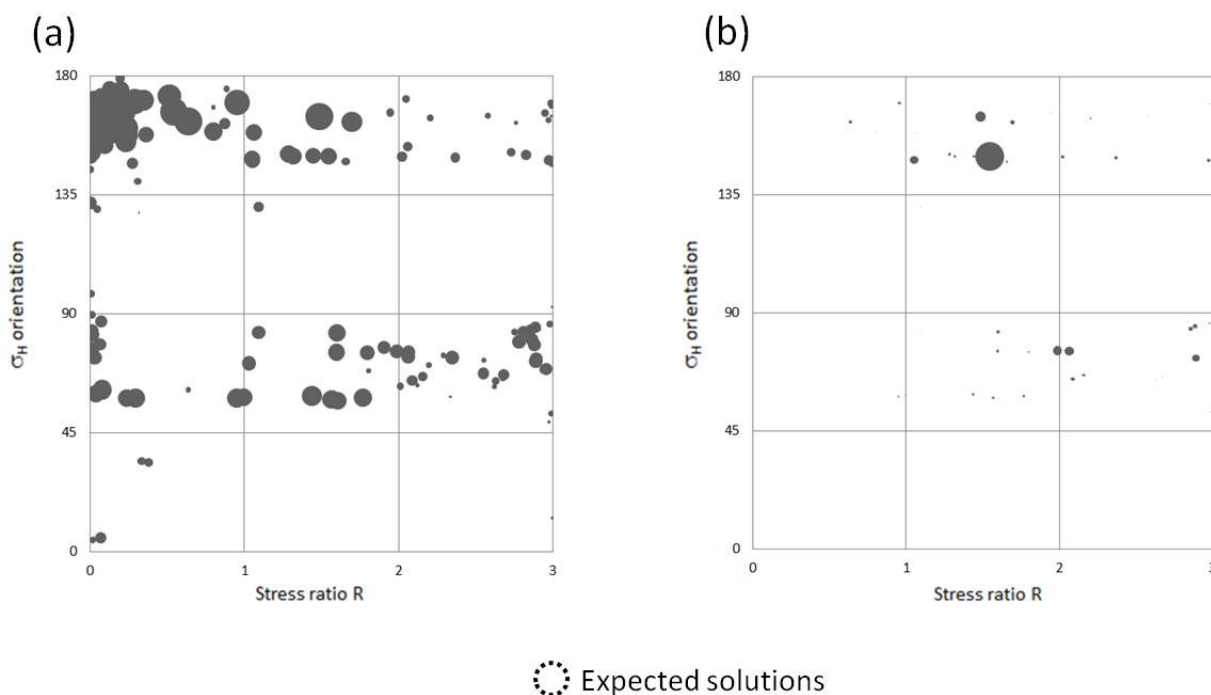


Figure 9. Polyphase stress inversion for les Matelles using unknown fracture type (a) without confidence criterion, (b) with confidence criterion C_2 . (b) shows the best solutions.

Using the fracture data with unknown fracture type, the polyphase stress inversion, has been run in 96 minutes.

Figure 9a shows the stress inversion solutions for all the subsets with no confidence criterion. Most of the inverted tectonic stresses are oriented $N165^\circ$ and $N150^\circ$ (θ) (as in figure 8a) and $N75^\circ$ and $N60^\circ$. The same uncertainty is found for \bar{R} . Figure 9b shows the tectonic stresses found using the C_2 criterion. Optimum solutions are found for $\theta = 149^\circ N$ and $\bar{R} = 1.54$, $\theta = 149^\circ N$ and $\bar{R} = 1.05$, $\theta = 164.7^\circ N$ and $\bar{R} =$

1.48. More solutions are found close to $\theta = 75^\circ N$ and \bar{R} between 1.59 and 2.89, and close to $\theta = 60^\circ N$ and \bar{R} between 2.08 and 2.15. In both cases (Figure 9a and Figure 9b), pair of solutions are separated of 90° (see Discussion for explanation).

3.3.3. Type separation

Each tectonic phase solution plotted in the tectonic stress domains (Figure 8b and Figure 9b) is applied in a forward sense in order to recover the fracture mechanical types (step 6.a of the algorithm). The affinity of each fracture plane to the 3 possible mechanical types is computed, and then the lowest of these 3 costs gives the mechanical type of the fracture for a given tectonic phase. When the cost is lower than the threshold value (e.g. here 0.05), the fracture is associated to this tectonic phase. Figure 10c shows in green color the fractures successfully associated to the correct tectonic phase, in black color the fractures that have been associated to the wrong tectonic phase, and in gray color, the fractures that could not be associated to any tectonic phase.

Figure 10b shows the fractures for which the mechanical type has been recovered successfully. Recovered veins are in blue color, recovered stylolites (e.g. associated to the faulting and the 'background') are in red color and the non-recovered fracture types are in gray. This highlights the efficiency of the mechanical fracture type recovery as most of the fracture types have been recovered successfully. This is to be associated to Figure 10c as some fractures have been associated to the wrong tectonic phase (black color in Figure 10c) while their mechanical type have been correctly recovered. For The Matelles example, 476 over 697 (68%) fractures have been successfully associated to the correct tectonic phase, 12% to the wrong tectonic phase, and 20% have not been associated to any tectonic phase.

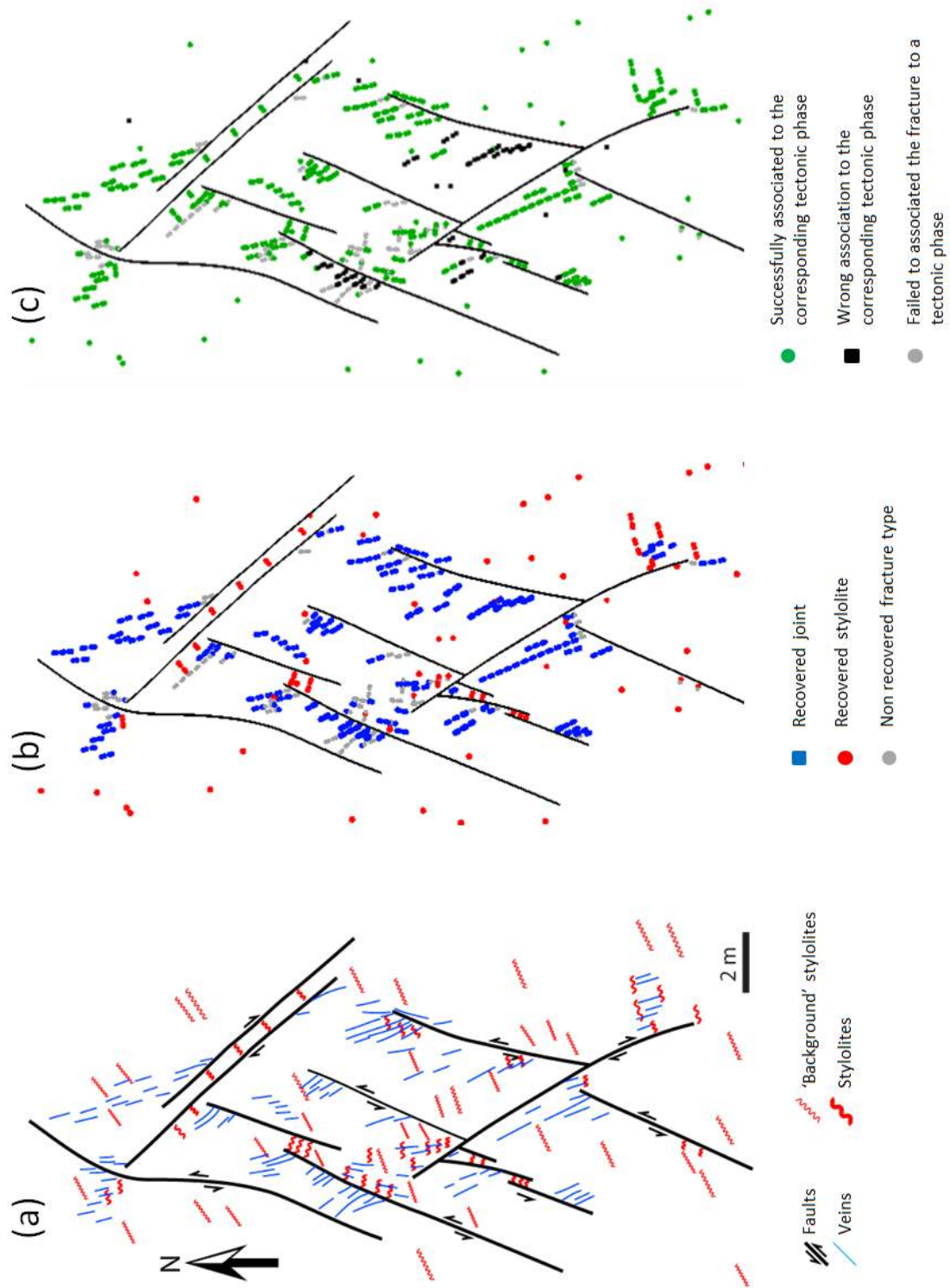


Figure 10. Fracture Type separation. (a) Top view of the interpreted faults and fractures : (b) the recovered fracture types (c) accuracy of the polyphase inversion for each fracture.

4. Discussion and conclusions

The proposed method inverts for both multiple tectonic events and fracture mechanical type, and classifies the fractures into homogeneous subsets regarding their affinity to a given inverted tectonic stress. This method avoids the problem of the mean stress solutions found by conventional stress inversions using heterogeneous data.

In the presented synthetic model, the polyphase stress inversion yields results in agreement with the imposed far field stresses (Table 1) when the fracture type percentage (step 1 of the algorithm) is close to the imposed percentage. This raises the question of how sensitive is the result with respect to a change in the fracture type percentage. Adding a random noise, as high as 10° , to fracture orientation (both for the strike and dip angles) in the synthetic model (Figure 3) does not seem to alter the results. However it is expected that higher values of random noise might lead to wrong solutions. The type separation (Figure 4) performs well in recovering the fracture type and the associated tectonic phases. Wrong results are potentially due to BEM singularities close to the faults (which can be improved by increasing mesh density for faults, although this will increase the processing time) or to a high computed cost that does not fit to the user selected threshold. It is expected that the fracture type separation accuracy depends on the number of tectonic phases and the 'distance' between these tectonic phases (Nemcok and Lisle 1995, see Lejri 2015 (chapter I)), such as the higher the number of tectonic phases and the closer to each other, the lower accuracy. In our synthetic model, the best accuracy was around 95% while the worst was around 30% for ambiguous tectonic phases (very close regimes in terms of \bar{R} and θ). It is also expected that, depending on the selected cost threshold, part of the fractures can be associated to the wrong tectonic phase.

For 'Les Matelles' outcrop, when the fracture type is known, the polyphase stress inversion and the fracture classification yield very good results, consistent with the geological context (Figure 8). The 165°N compression accounts for the joints and stylolites, while the $\text{N}150^\circ\text{N}$ compression account for the

background stylolites. This last result reinforces the use of mechanical models to recover tectonic stresses using fractures genetically linked to fault interactions as well as tectonic stresses using homogeneous background fractures. When the fracture type is unknown, some results might correspond to “shifted” scenario (Figure 9b). For example, a joint associated to a strike slip regime with $\theta = 140^\circ N$, when used as a stylolite in the stress inversion, will yield a strike slip or a reverse regime with $\theta = 50^\circ N$ (which is at a 90° angle of expected 140° orientation). The same joint, used as a conjugate fracture will yield a strike slip regime with $\theta = 110^\circ N$ or $170^\circ N$ depending on the friction angle ($\delta = 30^\circ$ for $\mu = \sim 0.6$). Although the method is automatic, it is clear that a geological and a structural knowledge of the studied area is a plus. The geologist needs to carefully choose the threshold value for polyphase inversion and the confidence criterion to differentiate actual tectonic phases from spurious results. Also a comparison with the geological setting is important to filter shifted solutions and uncertainty on \bar{R} (if any), and to choose the most consistent tectonic phases.

In further studies, a probability attribute in the tectonic domain should be investigated. Combined to the confidence criteria, this attribute might help to filter more wrong solutions, especially when there is a lot of uncertainty from step 1 of the algorithm). It will be necessary to test the fracture type separation with a number of tectonic phases greater than three.

Acknowledgements:

We would like to thank Emmanuel Malvesin and Azddine Benabbou for their support during this work. We thank the reviewers for their diligent review of the manuscript. Jean-Pierre Petit is thanked for providing us with his detailed fracture maps of the Matelles outcrop and Roger Soliva for guidance in the field. This study is part of M. Lejri’s PhD thesis, granted by both the French Ministry of Research and Schlumberger. These are deeply acknowledged.

References:

- Anderson, E.M., 1951. *The Dynamics of Faulting and Dyke Formation with Applications to Britain*, 2nd Edition. Oliver and Boyd, Edinburgh.
- Anderson, E. M., The dynamics of faulting, *Transactions of the Edinburgh Geological Society*, 8, 387–402, 1905.
- Angelier, J., 1979a. Determination of the mean principal directions of stresses for a given fault population. *Tectonophysics* 56, T17–T26.
- Angelier, J., 1994b. Fault slip analysis and palaeostress reconstruction. In: Hancock, P.L. (Ed.), *Continental Deformation*. Pergamon Press, Oxford, pp. 53–100.
- Angelier, J., 2002a. Détermination du tenseur des contraintes par inversion de mécanismes au foyer de séismes sans choix de plans nodaux. *Comptes Rendus Geoscience*
- Angelier, J., 2002b. Inversion of earthquake focal mechanisms to obtain the seismotectonic stress IV — a new method free of choice among nodal planes. *Geophysical Journal International* 150 (3), 588–609.
- Angelier, J., 1984. Tectonic analysis of fault slip data sets. *Journal of Geophysical Research* 89 (B7), 5835–5848.
- Angelier, J., 1991a. Inversion directe et recherche 4-D: comparaison physique et mathématique de deux modes de détermination des tenseurs des paléocontraintes en tectonique de failles. *C. R. Acad. Sci., Série II* 312 (10), 1213–1218.
- Angelier, J., Goguel, J., 1979. Sur une méthode simple de détermination des axes principaux des contraintes pour une population de failles. *C. R. Acad. Sci. Série D* 288, 307–310
- Angelier, J., Manoussis, S., 1980. Classification automatique et distinction des phases superposées en tectonique de failles. *C. R. Acad. Sci. Série D* 290, 651–654.

- Angelier, J., Mechler, P., 1977. Sur une méthode graphique de recherche des contraintes principales également utilisable en tectonique et en sismologie: la méthode des dièdres droits. *Bull. Soc. géol. de France* XIX (6), 1309–1318.
- Angelier, J., 1979. Determination of the mean principal directions of stresses for a given fault population. *Tectonophysics* 56, T17–T26.
- Armijo, R., Cisternas, A., 1978. Un problème inverse en microtectonique cassante. *C. R. Acad. Sci. Série D* 287, 595–598.
- Armijo, R., Carey, E., Cisternas, A., 1982. The inverse problem in microtectonics and the separation of tectonic phases. *Tectonophysics* 82, 145–160.
- Bott, M.H.P., 1959. The mechanics of oblique slip faulting. *Geological Magazine* 96, 109–117.
- Bourne, S. J., and E. J. M. Willemse, 2001, Elastic stress control on the pattern of tensile fracturing around a small fault network at Nash Point, UK: *Journal of Structural Geology*, v. 23, p. 1753-1770.
- Bourne, S. J., Rijkels, L., Stephenson, B. J., Willemse, E. J. M., 2000, Predictive modeling of naturally fractured reservoirs using geomechanics and flow simulation: *GeoArabia*, v. 6, p. 27-42.
- Burg, J.-P., Célérier, B., Chaudhry, N.M., Ghazanfar, M., Gnehm, F., Schnellmann, M., 2005. Fault analysis and paleostress evolution in large strain regions: methodological and geological discussion of the southeastern Himalayan fold-and-thrust belt in Pakistan. *Journal of Asian Earth Sciences* 24 (4), 445–467.
- Carey, E., Brunier, B., 1974. Analyse théorique et numérique d'un modèle mécanique élémentaire appliqué à l'étude d'une population de failles. *C. R. Acad. Sci. Série D* 279, 891–894.
- Carey, E., Vergely, P., 1992. Graphical analysis of fault kinematics and focal mechanisms of earthquake in terms of stress; the right dihedra method, use and pitfalls. *Annales Tectonicae* VI (1), 3–9.
- Carey, E., 1979. Recherche des directions principales de contraintes associées au jeu d'une population de failles. *Revue de Géographie physique et de Géologie dynamique* 21 (1), 57–66.

- Célérier, B., Séranne, M., 2001. Breddin's graph for tectonic regimes. *Journal of Structural Geology* 23 (5), 789–801.
- Celerier, B., Etchecopar, A., Bergerat, F., Vergely, P., Arthaud, F., Laurent, P., 2012. Inferring stress from faulting: from early concepts to inverse methods. *Tectonophysics*, Volume 581, 18 December 2012, Pages 206-219
- Delvaux, D., Sperner, B., 2003. Stress tensor inversion from fault kinematic indicators and focal mechanism data: the TENSOR program. In: Nieuwland, D. (Ed.), *New Insights into Structural Interpretation and Modelling*, 212. Geological Society, London, Special Publication, pp. 75-100.
- Diday, E. , Une nouvelle méthode de classification automatique et reconnaissance des formes: La méthode des nuées dynamiques, *Rev. Stat. Appl.*, 19(2), 283-300, 1971.
- Etchecopar, A., Mattauer, M., 1988. Méthodes dynamiques d'analyse des populations de failles. *Bull. Soc. géol. de France* IV (2), 289–302.
- Etchecopar, A., 1981. An inverse problem in microtectonics for the determination of stress tensors from fault striation analysis. *Journal of Structural Geology*, Vol. 3, No. 1, pp. 55-65.
- Etchecopar, A., 1984. Étude des états de contrainte en tectonique cassante et simulations de déformations plastiques (approche mathématique). Thèse d'État. Ph.D. thesis, Université des Sciences et Techniques du Languedoc.
- Fletcher, R. C. and Pollard, D. D., 1981, Anticrack model for pressure solution surfaces. *Geology*, v. 9, p. 419-424.
- Fry, N., 1999. Striated faults: visual appreciation of their constraint on possible paleostress tensors. *Journal of Structural Geology* 21, 7–21.
- Fry, N., 1992. Stress ratio determinations from striated faults: a spherical plot for cases of near-vertical principal stress. *Journal of Structural Geology* 14 (10), 1121–1131.
- Galindo-Zaldívar, J., González-Lodeiro, F., 1988. Faulting phase differentiation by means of computer search on a grid pattern. *Annales Tectonicae* II 2, 90–97.

- Gephart, J.W., 1990a. FMSI: a Fortran program for inverting fault/slickenside and earthquake focal mechanism data to obtain the regional stress tensor. *Computers & Geosciences* 16 (7), 953–989
- Gephart, J.W., 1990b. Stress and the direction of slip on fault planes. *Tectonics* 9 (4), 845–858.
- Gephart, J. W., Forsyth, D. W., 1984. An improved method for determining the regional stress tensor using earthquake focal mechanisms data: Application to the San Fernando earthquake sequence, *J. Geophys. Res.*, 89, 9305-9320.
- Granier, T., 1985, Origin, damping and pattern of development of faults in granite, *Tectonics*, v. 4, p. 721-737.
- Hammah, R.E., Curran, J.H., 1998. Fuzzy cluster algorithm for the automatic identification of joint sets. *International Journal of Rock Mechanics and Mining Sciences* 35, 889e905. doi:10.1016/S0148-9062(98)00011-4.
- Hardcastle, K.C., Hills, L.S., 1991. BRUTE3 and SELECT: QUICKBASIC 4 programs for determination of stress tensor configurations and separation of heterogeneous populations of fault–slip data. *Computers & Geosciences* 17 (1), 23–43.
- Hardcastle, K.C., 1989. Possible paleostress tensor configurations derived from fault–slip data in eastern Vermont and western New Hampshire. *Tectonics* 8 (2), 265–284. Huang, Q., Charlesworth, H., 1989. A FORTRAN-77 program to separate a heterogeneous set of orientations into subsets. *Computers & Geosciences* 15 (1), 1–7.
- Huang, Q., 1989. Modal and vectorial analysis for determination of stress axes associated with fault slip data. *Mathematical Geology* 21 (5), 543–558.
- Kattenhorn, S.A., Aydin, A., Pollard, D.D., 2000. Joints at high angles to normal fault strike: an explanation using 3-D numerical models of fault-perturbed stress fields. *Journal of Structural Geology* 22, 1–23.
- Kaven J.O., Maerten F., Pollard, D.D., 2011. Mechanical analysis of fault slip data: Implications for paleostress analysis. *J. Struct. Geol.* 33, 78-91.

- Lejri, M., Maerten, F., Maerten, L., Soliva, R., 2015. Paleostress inversion: A multi-parametric geomechanical evaluation of the Wallace-Bott assumptions. *Tectonophysics* 657, 129–143.
- Liesa, C.L., Lisle, R.J., 2004. Reliability of methods to separate stress tensors from heterogeneous fault–slip data. *Journal of Structural Geology* 26, 559–572.
- Lisle, R.J., 1988. ROMSA: a basic program for paleostress analysis using fault-striation data. *Computers & Geosciences* 14 (2), 255–259.
- Lisle, R.J., Vandycke, S., 1996. Separation of multiple stress events by fault striation analysis: an example from Variscan and younger structures at Ogmere, South Wales. *Journal of the Geological Society* 153 (6), 945.
- Lisle, R.J., 1987. Principal stress orientations from faults: an additional constraint. *Annales Tectonicae* 1 2, 155–158.
- Maerten, F., and L. Maerten, 2011, Stress and fracture modeling using the principle of superposition, Slb Patent declaration and assignment for docket no. 94.0276.
- Maerten F., Maerten L., Pollard D.D., 2014. iBem3D, a three-dimensional iterative boundary element method using angular dislocations for modeling geologic structures. *Computers & Geosciences* 72, 1-17.
- Maerten F., Madden, B., Pollard, D. D., Maerten, L., 2015, Accounting for fault mechanics in the inversion of geophysical data for the tectonic driving stress: Application to the 1992 Landers, California earthquake, Accepted to JGR.
- Maerten F., 2010. Geomechanics to solve geological structure issues: forward, inverse and restoration modeling. Thesis. Universite Montpellier II.
- Maerten, L., 1999, Mechanical interaction of intersecting normal faults: theory, field examples and applications: Ph.D. thesis, Stanford University, Stanford, California, U.S.A., p. 167.
- Maerten F., Maerten L., Cooke M., 2010b. Solving 3D boundary element problems using constrained iterative approach. *Computational Geosciences*. 14, 551-564.

- Martel, S.J., Boger, W.A., 1998. Geometry and mechanics of secondary fracturing around small three-dimensional faults in granitic rock. *Journal of Geophysical Research* 103,21299-21308.
- Mercier, J.L., Carey-Gailhardis, E., 1989. Regional state of stress and characteristic fault kinematics instabilities shown by aftershock sequences: the aftershock sequences of the 1978 Thessaloniki (Greece) and 1980 Campania-Lucania (Italia) earthquakes as examples. *Earth and Planetary Science Letters* 92 (2), 247–264
- Nemcok, M., Lisle, R.J., 1995. A stress inversion procedure for polyphase fault/slip data sets. *Journal of Structural Geology* 17 (10), 1445–1453.
- Nemcok, M., Kovac, D., Lisle, R.J., 1999. A stress inversion procedure for polyphase calcite twin and fault/slip data sets. *Journal of Structural Geology* 21 (6), 597–611.
- Pecher, A., 1989. SCHMIDTMAC: a program to display and analyze directional data. *Computers and Geosciences* 15, 1315e1326. doi:10.1016/0098-3004(89) 90095-2.
- Peel, D., Whiten, W.J., McLachlan, G.J., 2001. Fitting mixtures of Kent distributions to aid in joint set identification. *Journal of the American Statistical Association* 96, 56e63. doi:10.1198/016214501750332974.
- Petit, J.-P., Mattauer, M., 1995. Palaeostress superimposition deduced from mesoscale structures in limestone: the Matelles exposure, Languedoc, France. *Journal of Structural Geology* 17, 245–256.
- Petit, J.P., Wibberley, C.A. J., Ruiz, G., 1999. ‘Crack-seal, slip’: a new fault valve mechanism? *Journal of Structural Geology* 21, 1199–1207.
- Phan-Trong, T., 1993. An inverse problem for the determination of the stress tensor from polyphased fault sets and earthquake focal mechanisms. *Tectonophysics* 224 (4), 393–411.
- Pollard, D. D. and Segall, P, 1987, Theoretical displacements and stress near fractures in rocks: with applications to faults, joints, veins, dikes, and solution surfaces. In: *Fracture Mechanics of Rock* (edited by Atkinson B. K.). Academic Press, London, 277-349.

- Pollard, D.D., Saltzer, S.D., Rubin, A.M., 1993. Stress inversion methods: are they based on faulty assumptions. *J. Struct. Geol.*, 15, 1045-1054.
- Rispoli, R., 1981. Stress fields about strike-slip faults inferred from stylolites and tension gashes. *Tectonophysics* 75, T29–T36.
- Shan, Y., Suen, H., Lin, G., 2003. Separation of polyphase fault/slip data: an objectivefunction algorithm based on hard division. *Journal of Structural Geology* 25 (6), 829–840.
- Shan, Y., Li, Z., Lin, G., 2004. A stress inversion procedure for automatic recognition of polyphase fault/slip data sets. *Journal of Structural Geology* 26 (5), 919–925.
- Shanley, R.J., Mahtab, M.A., 1976. Delineation and analysis of clusters in orientation data. *Mathematical Geology* 8, 9e23. doi:10.1007/BF01039681.
- Simon-Gomez 1986 Analysis of a gradual change in stress regime (example from the eastern Iberian Chain, Spain). *Tectonophysics*, 124, 37-53.
- Soliva, R., Maerten, F., Petit, J.-P., and Auzias, V., 2010. Field evidences for the role of static friction on fracture orientation in extensional relays along strike-slip faults ; comparison with photoelasticity and 3D numerical modelling. *J. Struct. Geol.* 32, 1721–1731, doi:10.1016/j.jsg.2010.01.008.
- Sperner, B., Zweigel, P., 2010. A plea for more caution in fault–slip analysis. *Tectonophysics* 482 (1–4), 29–41.
- Sperner, B., Ratschbacher, L., Ott, R., 1993. Fault-striae analysis: a Turbo Pascal program package for graphical presentation and reduced stress tensor calculation. *Computers & Geosciences* 19 (9), 1361–1388.
- Taha, M., 1986, Apport de la microtectonique cassante au problème des trajectoires de contraintes et de leurs perturbations. Exemples du Nord de Montpellier, thèse d’E tat, Université de Montpellier, pp. 155.

- Thomas, A.L., 1993. Poly3D: a three-dimensional, polygonal-element, displacement discontinuity boundary element computer program with applications to fractures, faults, and cavities in the Earth's crust. M.S. thesis, Stanford University, California.
- Vasseur, G., Etchecopar, A., Philip, H., 1983. Stress state inferred from multiple focal mechanisms. *Annales Geophysicae* 1, 291–298
- Wallace, R.E., 1951. Geometry of shearing stress and relation to faulting. *J. Geol.*, 59, 118-130.
- Watkinson, A. J. and Ward, E., M., G., 2006, Reactivation of pressure-solution seams by a strike-slip fault-sequential, dilational jog formation and fluid flow, *AAPG Bulletin*, v. 90, p. 1187-1200.
- Will, T.M., Powell, R., 1991. A robust approach to the calculation of paleostress fields from fault plane data. *Journal of Structural Geology* 13 (7), 813–821.
- Yamaji, A., 2000. The multiple inverse method: a new technique to separate stresses from heterogeneous fault–slip data. *Journal of Structural Geology* 22 (4), 441–452.
- Yamaji, A., 2003. Are the solutions of stress inversion correct? Visualization of their reliability and the separation of stresses from heterogeneous fault–slip data. *Journal of Structural Geology* 25 (2), 241–252.
- Yamaji, A, Sato, K., 2011. Clustering of fracture orientations using a mixed bingham distribution and its application to paleostress analysis from dike or vein orientations. *Journal of Structural Geology* 33, 1148-1157.
- Yamaji, A., Otsubo, M., Sato, K., 2006. Paleostress analysis using the Hough transform for separating stresses from heterogeneous fault–slip data. *Journal of Structural Geology* 28 (6), 980–990.
- Zalohar, J., Vrabec, M., 2007. Paleostress analysis of heterogeneous fault–slip data: the Gauss method. *Journal of Structural Geology* 29 (11), 1798–1810.

Conclusions

The essence of this thesis was to improve the modeling of natural fractures in sub-surface oil and gas reservoirs by using numerical models of rock deformation based on continuum mechanics. Indeed, one of the main challenges in the oil industry is the exploitation of new resources in naturally fractured reservoirs often located in structurally complex areas, and while geomechanical methods are becoming the industry standard to solve such issues, they are still highly dependent on the knowledge of the tectonic stress field that needs to be applied as boundary condition in numerical simulations. The tectonic stress field characteristic (e.g. type - normal, wrench or reverse - orientation and magnitude) being often unknown or badly approximated, my primary objective was to find methods to improve its assessment.

I first reviewed the existing historical methods for recovering the paleostress field, and decided to evaluate to what extent the Wallace and Bott assumptions, which are the basis for these paleostress inversion methods, are reliable. This study complements the work done by several authors, who, over the last three decades, have shown that the validity of the Wallace and Bott assumptions could be questionable with respect to their geomechanical simplification. In the first chapter, I showed that specific tectonic stress conditions applied to corrugated faults and intersected fault geometries, as well as increasing fault fluid pressure, could generate high stress perturbations that increase the misfit between the resolved shear stress and the modeled slip vector (ω), invalidating the WB assumption, which assumes that slip vector must be collinear to the resolved shear (regional) stress on the fault plane. I also demonstrate that when the friction coefficient increases, the misfit ω decreases. However, as many authors emphasize that fault reactivation occurs for low friction ($\mu \leq 0.4$), friction should not have a significant effect in reducing ω . I therefore conclude that the Wallace and Bott assumptions for paleostress inversion from fault slip data should be used with care.

In the second chapter, I wanted to evaluate the real impact of the misfit ω on the slip data inversion results using two stress inversion methods: (1) a method based on the Wallace and Bott assumption (WB) and (2), a geomechanical method based on the boundary element method (BEM). It was shown that the stress inversion solution accuracy can be inversely correlated to ω for specific tectonic stress conditions, which counterintuitively goes against the results of the first chapter. This demonstrates that, depending on the stress configuration, the misfit angle ω is not always correlated to the WB stress inversion solution accuracy. This goes against the idea that suggests filtering the data with high misfit prior to performing stress inversion. It was also shown that the WB and BEM-based stress inversion methods generally yield good results and are complementary depending on the sliding fault friction. Indeed, the BEM-based frictionless stress inversion performs well for faults with sliding friction and even better when sliding friction is low ($\mu \leq 0.4$), which seems to be the general case in nature for reactivated faults. It was also noted that WB-based stress inversions, using diverse data orientations (including stress perturbation), implicitly include an average friction inversion of $\mu=0.5$, which contributes to a better approximation of the solution for low sliding frictions. However, the lack of diversely oriented slickenlines as well as stress regimes near pure stress regime regions (e.g. normal, wrench and reverse), affects both stress inversion method inherent indetermination. On the other hand, explicitly integrating the locally perturbed slickenline orientations allows the BEM-based stress inversion method to be more efficient than the WB-based stress inversion methods.

Since slip markers on faults are hardly observed in core or image log from the oil and gas industry, I showed, in the third chapter, that to use observed natural fracture data as main drivers for the inversion of the paleostress using new generation technique based on geomechanics could be efficient. I have demonstrated that it is possible to reduce uncertainty in the paleo-tectonic stress determination (style, orientation and relative magnitude) needed to efficiently constrain geomechanical simulations used for modeling natural fractures in the subsurface. The method is based on the physical fact that any large scale

rock discontinuities such as faults, salt bodies, décollement layers or cavities, subjected to far field stresses, generate local stress perturbations that in turns can be the drivers for the development of secondary structures such as smaller scale fractures. Knowing the location and characteristics of these secondary fractures as well as the kind and geometry of the large scale discontinuities, helps recovering the far field stress responsible for the development of the smaller scale fractures. Therefore, the method depends upon the assumption that, for instance, in a growing and active fault system, the orientation of natural fractures will be influenced by the the perturbed stress field nearby active larger faults. As opposed to most paleostress inversion techniques, which are mainly based on measured fault slip data, our method takes into account any type of observed and measured deformation that can be associated to a local state of stress. I have demonstrated that the three mechanical fracture types, extension, compression and shear fractures, can be efficiently used to constrain the paleostress inversion. The proposed method, which takes into account the heterogeneous state of stress that can be found around active faults, has been successfully tested against three natural geological examples.

As it is sometimes difficult to determine the mechanical fracture type from wellbore images, and that very often the studied regions experienced a complex tectonic history with multiple tectonic phases, I finally developed and tested, in the fourth chapter, an algorithm that allows to inverting for both multiple tectonic events and fracture mechanical types. I successfully demonstrated the efficiency of the technique through a synthetic model and the natural example of The Matelles outcrop. This should greatly help improve the modeling of the natural fractures in reservoirs.

Perspectives

Even though the geomechanically-based stress inversion appears as a promising approach, there is space for theoretical improvements and for developing other applications for both the industry and the academic world.

Within the field of linear elastic stress inversion, one primary new objective would be to extend the functionality of such tool in order to incorporate the fault activity inversion. Indeed, faults are not always synchronously active through time and some faults might be reactivated while others are not. This spatial variation of fault activity can be registered within the observed secondary fracture characteristics (distribution and orientations) and can be used to automatically recover the corresponding fault activity for each dataset.

Another hot topic that can benefit from such stress inversion technique is the modeling of in-situ stress field around salt diapirs as well as around magma chambers and volcanoes. Indeed, stress or deformation measurement sampled around such structures, which reflects the highly perturbed stress field could be used to perform mechanical stress inversions that should also incorporated the inversion of the pressure inside such geological structures.

Finally, as preliminary shown in the second and third chapters, research investigation should be done in order to develop techniques for optimally inverting for the fault sliding friction. This would have an important application to earthquake studies.

Benefits for Schlumberger

Most of the research described in this thesis has been and will be integrated in the Schlumberger's Petrel™ software in the module dedicated to the natural fracture modeling in reservoirs.